

# THE SEA

**Ideas and Observations on Progress in the Study  
of the Seas**

Edited by

**E. D. GOLDBERG**

**I. N. McCAVE**

**J. J. O'BRIEN**

**J. H. STEELE**

**VOLUME 6**

Marine Modeling

**A Wiley-Interscience Publication**

**JOHN WILEY & SONS · New York · London · Sydney · Toronto**

Copyright © 1977 by John Wiley & Sons, Inc.

All rights reserved. Published simultaneously in Canada.

No part of this book may be reproduced by any means, nor transmitted, nor translated into a machine language without the written permission of the publisher.

*Library of Congress Cataloging in Publication Data:*

Main entry under title:

The Sea: ideas and observations on progress in the study of the seas.

General editor, v. 1-3: M. N. Hill; v. 4, pts. 1-  
A. E. Maxwell; v. 5-6: E. D. Goldberg.

Vol. 4, pts. 1- have imprint: New York, Wiley-Intersciences; v. 5: New York, Wiley.

Includes bibliographies and indexes.

CONTENTS: v. 1. Physical oceanography.—v. 2. The composition of sea-water. Comparative and descriptive oceanography.—v. 3. The earth beneath the sea. History.—v. 4. New concepts of sea floor evolution. pt. 1. General observations. pt. 2. Regional observations, concepts.

1. Oceanography. I. Hill, Maurice Neville, 1919- ed. II. Maxwell, Arthur Eugene, 1925- ed. III. Goldberg, Edward D., ed.

GC11.S4      551.4'6      62-18366

ISBN 0-471-31091-3(V.6)

Printed in the United States of America

10 9 8 7 6 5 4 3 2 1

## 7. THE DYNAMICS OF UNSTEADY CURRENTS

PETER B. RHINES

### 1. Summary

This is an account of the dynamics of quasi-geostrophic flows of a wavelike or turbulent nature. An *historical review*, Section 2, is followed by a section on *kine-matics*, Section 3, which illustrates the characteristically different appearance of the fields of pressure, velocity, vorticity, and density, even though they are linearly related. The spectral breadth is the important quantity distinguishing them. Their different natural weighting with respect to length scale leads to simple experimental tests of the  $(\omega, k)$  (i.e., frequency, wave number) relation from single moorings. These make use of an empirical "turbulent" dispersion relation,  $\omega \propto Uk$ , where  $U$  is the root-mean-square (rms) fluid velocity. The spectra and correlation functions useful for nondivergent fields are reviewed.

Section 4 is a review of the *lowest-order dynamics* of a wedge-shaped analogue of a  $\beta$  plane ocean, stressing the nearly geometrical nature of Sverdrup flow and long, baroclinic waves. An impedance is defined to quantify the vertical stiffness of rotating fluids, and these classical flows occur when forcing is so gentle that fluid columns can resist vertical stretching and compression.

Section 5 is a review of *topographic Rossby waves*, which occur when the potential vorticity balance is linear, for small wave steepness,  $\varepsilon/\omega$ , where  $\varepsilon$  is the Rossby number and  $\omega$  the wave frequency divided by the Coriolis frequency. Attention centers on (1) barotropic, (2) fast baroclinic, and (3) slow baroclinic waves; type 2 relies on the slope of the bottom. All three are important to the nonlinear dynamics that follow. The partition of initially prescribed flow among the types, and a steady flow, is demonstrated.

Oceanic observations are given in support of the gross properties, particularly westward propagation (types 1 and 3), intensification near the bottom (type 2), and the inverse nature of the dispersion relation (type 1).

Section 6 gives a new treatment of *nonlinear cascades* that occur in a *flat-bottom ocean* when  $\varepsilon/\omega$  is not small. For oceanic energy levels it is shown that energy may travel faster through wave number space than physical space, in the sense that significant horizontal and vertical eddy-eddy interactions can occur before propagation has moved the energy a single wavelength.

The cascades carry barotropic (depth-independent) energy toward large scale. However, geophysical flows find many ways to counter the lateral expansion of eddies, for example, Rossby-wave propagation may take hold, while developing persistent anisotropy that favors zonal currents. (This is related to the induction of mean circulation by eddies; see Section 8.)

Baroclinic energy (currents with vertical shear) moves toward the Rossby deformation scale from either smaller or larger scales; there the eddies above and below the thermocline lock together, producing a barotropic state with surprising efficiency. A proof of the migration from baroclinic toward barotropic flow is given. Once this transformation has occurred, the theory for a simple homogeneous fluid applies.

This chain of events means that, for example, a slowly propagating, long baroclinic Rossby wave with modest currents fragments into deformation scale eddies (in a

generalized baroclinic instability), jumps to the barotropic mode, expands to larger scale again, and propagates away much more quickly, as a barotropic Rossby wave, whose currents are much swifter. A Gulf Stream meandering experiment is described, which involves the same cascades. The meteorological analogue is discussed.

Section 7 adds to these "primary" cascades the effect, crucial to the oceans, of a *rough bottom* and *coastal boundaries*. Both act (via simple formulas given here) as sources of enstrophy which can grossly alter the energy cascades. In addition, they suggest the relatively small-scale flows found in the deep water and near western boundaries.

Sea-floor roughness (at scales greater than the deformation radius) is found to be essential in preserving the vertical shear of currents found in the oceans; without this topography, the cascade toward depth-independent flow would operate within a few months [with the caveat that disequilibrium (forcing or damping) of the field, or severe spatial intermittency, such as found in Gulf Stream rings, can also preserve baroclinity]. Computer experiments show this control of the vertical structure to occur when  $\epsilon/\delta \lesssim 0.5$ , where  $\delta$  is the rms topographic height, say, in a 500-km region of interest. Baroclinic instability of large-scale flows is altered by bottom topography, which severely inhibits the "occlusion" stage. Topography generally whitens the wave number spectrum, whereas the nonlinear cascades, alone, tend to sharpen it.

Over topography the energy develops a patchy distribution, even after time averaging. Such "fine structure" in the intensity has recently been discovered at sea. At the same time a steady component of flow develops spontaneously, about  $f/h$  contours in the deep water ( $f$  is the Coriolis frequency and  $h$  is the depth).

Linear wave theory with a rough bottom is reviewed, and a simple baroclinic "double Kelvin wave" derived, which is trapped both horizontally and vertically. The wave theory lends insight to the behavior of the nonlinear, rough-bottom ocean, for the linear waves themselves exhibit spatial intermittency, a cascade toward small scale, a predilection for vertical shear, and an inability to carry energy efficiently in the horizontal.

In all, the oceanic case contrives to make horizontal energy flux in eddies triply dependent on the energy level. Only the more intense baroclinic flows succeed in switching from baroclinic to barotropic modes, and expanding in the horizontal. Both such changes act to increase the group velocity, and the concurrent release of potential energy increases the kinetic energy being transported. Horizontal propagation experiments are shown as illustration. Baroclinic energy, in the nonlinear, rough-bottom case, moves principally westward from its source (less than 1 km/day in other directions), qualitatively as in linear theory.

The fluid tends to adjust toward states near the transition between waves and geostrophic turbulence. Ideas of linear propagation still have value; combined with knowledge of the nonlinear changes in structure, they predict qualitatively the movement of energy about these model oceans. Yet the transfer spectra verify that quasi-equilibrium of an eddy field involves a continuing conflict among the cascades due to advection and topography.

Section 8, a discussion of *mean flows*, begins with a formula (related to an early model of Kolmogorov) for the difference between ensemble-averaged Eulerian and Lagrangian mean flow, which is

$$\langle u_i \rangle = \frac{\partial}{\partial x_j} \kappa_{ij}$$

where  $\kappa_{ij} = \int_0^t R_{ji}(\tau) d\tau$ , is the diffusivity integral of the Lagrangian correlation

function. Particles on the average are attracted to regions of intense eddies (large  $\kappa_{ij}$ ); oceanic evidence is given for important gradients in eddy intensity.

Holland and Lin's (1975) simulation of eddy interaction with the mean ocean flow is described. Then a simple vorticity-flux theory is given for mean-flow generation by turbulent eddies (or waves), which accounts for  $f/h$ -contour-following currents found in the laboratory and computer simulations. In the simplest case, isolated forcing of a barotropic  $\beta$  plane fluid, a westward zonally ( ) averaged flow,

$$\bar{u} = -\frac{\beta}{2} \overline{\eta^2}$$

develops in the far field, where  $\eta$  is the displacement, north and south, of particles from their point of origin. This applies to either wavelike or turbulent inviscid flow, and leads to a prediction of both the eastward jet and westward-flowing far field found experimentally by Whitehead (1975). With weak bottom friction, coefficient  $D$ , a nondiffusive ( $\kappa_{22} = 0$ ), wavelike field induces flow with speed ranging from the above value to twice it, depending on the correlation time of the velocities. If, instead, particles wander freely in latitude, then

$$u = -\frac{\beta \kappa_{22}}{D}$$

The Lagrangian drift is compared with these Eulerian values.

Generalizations are given, and related to Green's and Welander's work. The time-dependent theory here involves both positive and negative diffusivity of potential vorticity. The curl of these stresses,  $(\partial/\partial x_i)(\kappa_{ij}\partial Q/\partial x_j)$  where  $Q$  is a slowly varying mean potential vorticity distribution, is a likely source of surface and abyssal circulation, both in regions immediate to intense currents, and also in random eddy fields. The argument combines with others to predict, especially, elongated bands of zonal, or  $f/h$ -following currents in the oceans. The gradients of diffusivity,  $\kappa_{ij}$ , may in many regions provide the dominant driving.

Section 9 is a further discussion of *recent observations*, of *sources* and of *sinks*.

This paper is arranged, first, with flows that would be driven by gentle and slowly varying forces and then, successively, by quickly varying and vigorous forcing. The set of parameters that determines the evolution of a field of quasigeostrophic eddies is:  $L/L_\rho$ , the ratio of the horizontal scale of the dominant eddies, and  $L_\rho$ , the Rossby deformation scale;  $\beta L^2/U$  where  $U$  is the vertical-average rms velocity;  $\varepsilon/\delta$ , the ratio of Rossby number and topographic height variations found between scales  $L$  and  $L_\rho$ ; and  $P/K$ , the ratio of available potential and kinetic energies in the eddy field. In addition, the level of external forcing, the strength of mean currents and their associated potential energy, the bottom drag, internal-wave interaction rate, and degree of intermittency may occur, if they are not negligible. In some interesting cases the turbulent dynamics alter the parameters toward  $L/L_\rho \sim 1$ , then  $P/K \rightarrow 0$ ,  $\beta L^2/U \rightarrow 1$ .

## 2. Historical Introduction

The kinetic energy of the oceans takes four dominant forms: surface waves, inertial (or near-inertial) and tidal oscillations, the climatological mean circulation, and unsteady currents of period greater than one-half pendulum day. The latter, particularly the nearly geostrophic eddies of roughly 200 km diameter, are the concern of this chapter. I have sought to make this a self-contained account, and yet to include

recent results on the nonlinear dynamics of eddies. Doing so has severely limited its breadth, and in particular many important investigations of Rossby wave propagation have had to be omitted. Sections 2–5 are in part a review of classical ideas, whereas Sections 6–9 are new or recently published material. A broader discussion of ocean variability is given by Monin, Kamenkovich and Kort, 1974.

### A. Observational History

The beginnings of concentrated investigation of transient ocean currents came in the 1950s with a series of cruises led by Fuglister to map the instantaneous form of the Gulf Stream and the rings of current that are thrown off it, to the north and south. Earlier, those who looked closely at other parts of the Stream (e.g., Bache, 1846; Pillsbury, 1890) found unsteadiness and spatial complexity to be the rule. Turbulence in concentrated streams (recorded in sketches by Leonardo da Vinci) at one extreme, and seasonal reversals of the Somali Current, at the other, were familiar long ago. But eddy motion was generally related in the observer's mind to nearby intense currents. The notion that the ocean interior is populated by chaotic, variable currents is recent (excepting ancient speculations, like those of Plato, about bodies of water oscillating deep within the earth, feeding the seas, and about the occasional, malign Charybdis).

Perhaps self-protection causes the human mind to imagine unknown regions to be simply structured, or structureless. Thus in the early nineteenth century, before even the mid-oceanic depth had been determined, it was held that below the first few hundred meters the ocean was stagnant and lifeless. The notion of inert abyssal regions was reinforced by the incorrect observation of frequent 4°C temperatures (measured with unprotected thermometers), combined with the incorrect notion that seawater has its maximum density at this temperature.

The zoologist, in search of the beginning of this lifeless (azoic) zone, gradually pushed downward the known limits of both life and dynamic activity. Finally, benthic animals were dredged from the sea floor in increasing quantities. Broader scientific interest in the abyssal ocean grew when Darwin suggested it might contain a living record of early animal evolution, and technical interest came with the laying of telegraph cables.

Physical oceanography often bootlegged on geographical or biological cruises. Complexity and variability of the deep-temperature field quickly became apparent. Thomson and Carpenter on the *Lightning* (1868), for example, measured temperatures to 1000 m near the Faeros Bank: "it had been shown that there are great masses of water at different temperatures moving about, each in its particular course, maintaining a remarkable system of ocean circulation, and yet keeping so distinct from one another that an hour's sail may be sufficient to pass from the extreme of heat to the extreme of cold." The use of density structure to infer horizontal current came with gradual appreciation for the intensity of the Coriolis force. Routine dynamic computations followed Bjerknes' circulation theorem at the beginning of this century.<sup>1</sup>

The dominant concern of the hydrographic work that followed was the climatological mean circulation. Fuglister and Worthington's (1951) explorations were the first to capture the instantaneous picture of the transient meanders and eddies. The enormity of the task is obvious, requiring vast numbers of ships or moored instruments. Reproduced in Fig. 1 is a map of the mean temperature in the upper 200

<sup>1</sup> Two interesting histories of the general subject are those of Deacon (1972) and Schlee (1973).

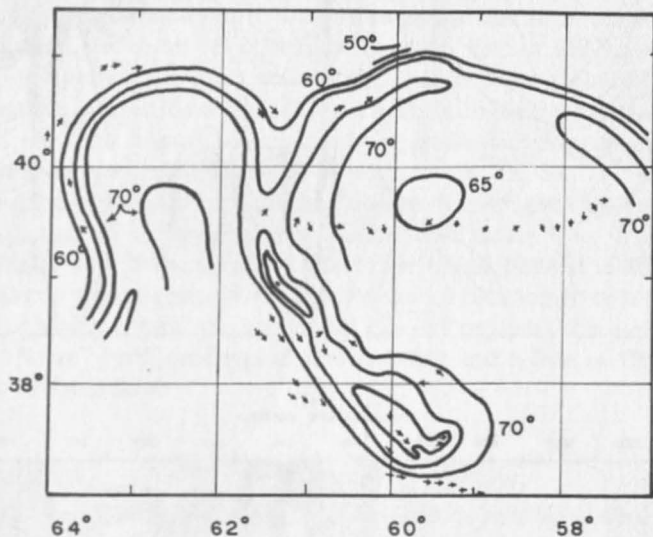


Fig. 1. A Gulf Stream ring at the moment of detachment (Fuglister and Worthington, 1951). Mean temperature in the upper 200 m, in degrees Fahrenheit. Current directions from towed electrodes (GEK). See also Figs. 28, 57.

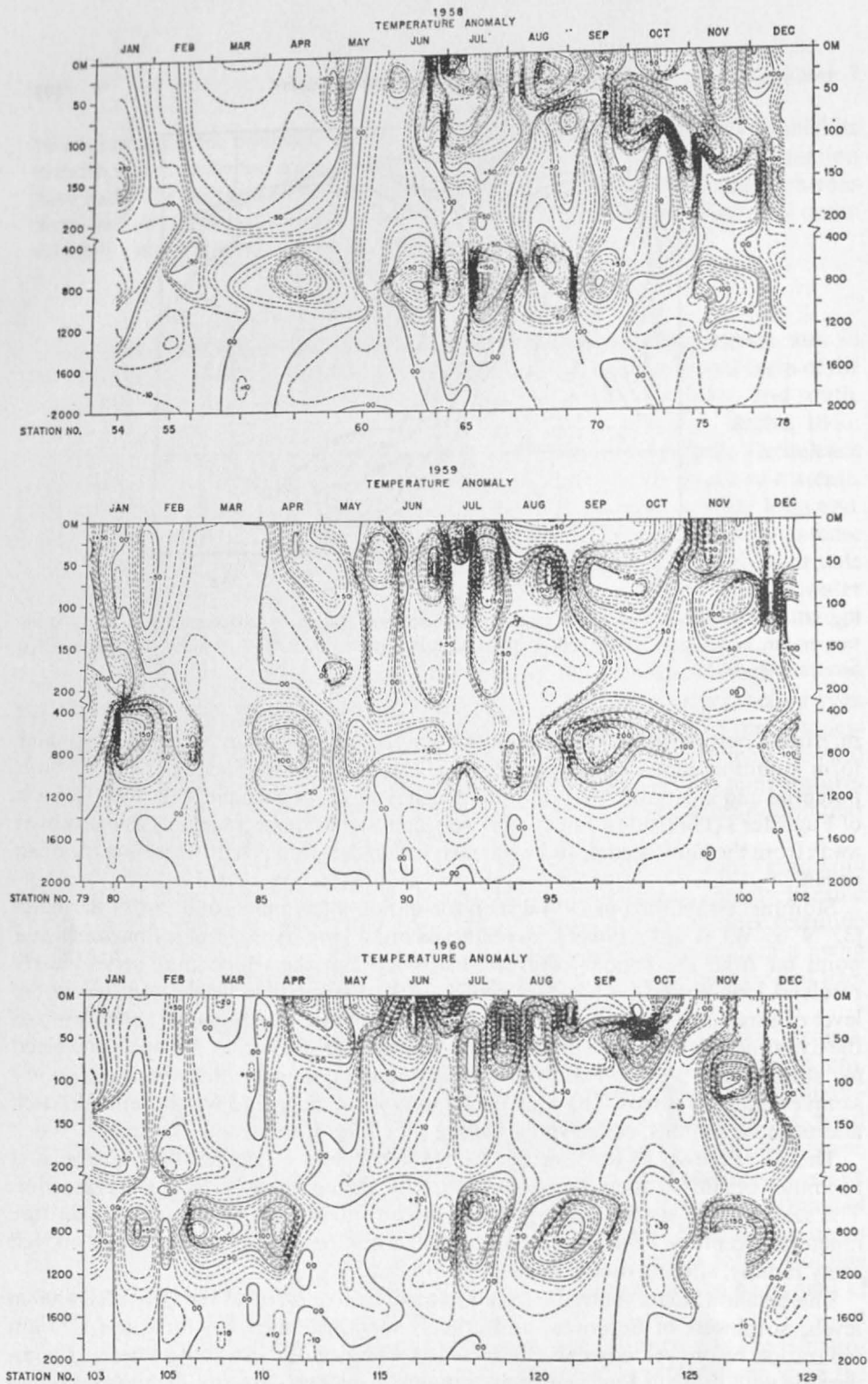
m, from a part of the 1950 survey. A 500-km-long meander has begun to detach and form an autonomous, cold, cyclonic ring. The effect of this nucleus of energy, both potential and kinetic, on the adjoining ocean is clear, for example in the long sections of Fuglister's (1960) atlas. But typical isopycnal slopes decrease rapidly as one moves away from the Gulf Stream, and we are left to wonder what activity there is in the open ocean.

Stommel established in 1954 a monitor station a few miles southeast of Bermuda (32°N, 65°W). It was a novel prospect to record a long hydrographic time series at a point far from the regions of greatest activity. But the temperature series clearly resolved long-period (~150-day) eddies in the thermocline height, well below the level of direct seasonal penetration (Fig. 2). Schroeder and Stommel (1969) showed the dynamic height variations to be coherent with the sea level at Bermuda (corrected for atmospheric pressure) and thus eliminated the possibility that they were poorly sampled internal waves. The only uncertainty is the degree to which Bermuda itself affects these stations, conceivably casting off eddies into passing currents.

The *Aries* cruises in 1955 seemed to be the conclusive step. Swallow, Crease, and Stommel organized them to measure directly the currents below the thermocline. The search for a slowly moving, steady ocean interior ended as surely as did the nineteenth-century belief in an azoic zone, when neutrally buoyant floats moved away rapidly, altering direction every few weeks.

The Swallow floats showed currents exceeding 10 cm/sec (at the 2000 and 4000 m levels, southwest of Bermuda) and crudely identified their length scale (~70 km separation before velocity coherence is lost). The size of these deep eddies was comparable with those in Fuglister's and Stommel's shallow data, but the time scale and intensity were far smaller. In the succeeding sections we hope to show convincing dynamic reasons for the generic differences and similarities among these eddies.

Little was known before this decade about the geographic distribution of eddy energy. It is easy to appreciate that wiggleness of isotherms in classical sections



diminishes away from coasts and intense currents, but it is difficult to produce satisfying maps of perturbation energy from them. Parker (1971) used the bathythermograph archives to produce an interesting map of the distribution of shallow, intense thermal features in the western North Atlantic. Again, the decrease in numbers as one leaves the Gulf Stream is clear, but the spatial irregularity of the data base makes further interpretation difficult.

Only now is the proliferation of moored current meters and thermistors yielding a quantitative picture of the geography of eddies and mean flow. We have come to realize that really very little is known about the broad pattern of these quantities; even the dynamic topography of the time-mean circulation in a region so widely traveled as the North Atlantic is unreliable, beyond verifying the western-boundary activity, the "polar" front, and equatorial currents, and a hint of the nature of the broad, shallow return flow.

### *B. Dynamic Background*

It is the fault of eddies that the general circulation is hard to observe, but they are more than just observational noise. Stommel (1957) discussed how precarious was the dependence of linear, steady models on the Sverdrup interior flow. It may be that such circulation models, together with their time-dependent counterpart, the linear Rossby wave, are sufficiently inspired to hold true beyond their strict limits of validity. But there is increasing evidence that deeper understanding will come from nonlinear, interactive models of eddies and mean flow.

The atmospheric circulation gives a precedent. There, one would like to have dismissed fronts, internal waves, cyclones, and monsoon and orographic circulation to find a simple theory of the maintenance of the zonal winds, but Jeffreys (1926) and Starr (e.g., 1968) showed some of these to be essential in redistributing mean angular momentum. The physical source and nature of the "eddies" that produce the relevant Reynolds' stresses are complex and include both classical baroclinic instability and large-scale orographic and thermal contrasts.

The ocean contains many similar elements; the energy-containing eddies, though less than 1/10 as big as those in the atmosphere, are roughly the same size if rescaled by the density structure (the Rossby radius). Oceanic flow speeds are perhaps 1/25 as big, yet again appear the same, relative to the ratio of the beta effect and square of the Rossby radius. But the absence of unobstructed paths for zonal flow (everywhere but, possibly, in the Southern Ocean) is likely to make very different the driving or retarding of the mean circulation by eddies.

The ocean basins, in addition, are perhaps 20–60 eddy diameters wide, whereas the atmospheric domain is rather small, measured against the size of cyclones. This, together with the confinement of the intense mean flow to a far smaller region in the oceans, suggests that inhomogeneity is the greater, and that the nature of lateral influences is more crucial there, than in the atmosphere.

There is, then, a competition between the response as local flow to local external forcing by winds and heating, on the one hand, and the necessity that unusual clumps of energy and density anomalies spread themselves about, on the other. The classical mean circulation presumes that lateral influence is powerful, and the constitutive relation of the fluid somehow allows forces excited, say, on the Labrador Sea to be felt off Cape Hatteras. A picture of rubbery seas, propagating energy about, is incomplete without actual circulation. As in striking an elastic wheel, which is free to spin about its hub, the signaling process distributes angular momentum until internal friction dissipates all but the new rigid-body rotation. An important parameter of this analogue is the travel time for waves, relative to the time characteristic

of the forcing. If the forcing is slowly varying, measured in these terms, the transients are insignificant and the body effectively rigid. But in the other extreme, a flaccid material will have gross undulations superimposed on the steady mode. It is this latter case that appropriately describes the oceanic response to weather and the seasons: the speed of travel for the energy-containing eddies is probably less than 5 km/day.

Unfortunately, however, these strongly excited transients (and those generated by internal instability) are so energetic, and the medium itself is so irregular, that linear superposition fails. We must then consider carefully the nature of geostrophic and topographic turbulence in altering the horizontal transports, and driving circulation wherever they are found.

### 3. Kinematics of Eddy Fields

The difficulties posed by complex, variable fields of current, density, and pressure are not merely analytical and instrumental. One's judgment and memory of the simplest qualities of an eddy field can fail, and two observers rarely seem to agree upon, say, the dominant scale or period of a flow, however perfectly it has been measured. The problems of description lead to vagueness in all later stages of analysis. The object of this section, therefore, is to review some of the descriptors of eddies, and some of their immediate application to observations.

#### A. Space

Consider an example, Fig. 3, of instantaneous maps of some artificially produced eddies. Each of the three major boxes, Figs. 3a-3c, shows four fields corresponding to a two-dimensional, nondivergent flow; counterclockwise from the lower right, these are  $\psi$  (stream function or pressure),  $\partial\psi/\partial x$ ,  $-\partial\psi/\partial y$  (velocity components), and  $\nabla^2\psi$  (vorticity). The maxim, "integration smooths, differentiation roughens," applies. Observations using current meters would identify a smaller dominant length scale than those from pressure gauges, and a vorticity meter would be the most confusing of all.

The Fourier coefficients  $\hat{\psi}_{\mathbf{k}}$  of the instantaneous stream function are defined by

$$\psi(\mathbf{x}) = \sum_n \sum_m \hat{\psi}_{\mathbf{k}} e^{i\mathbf{k}\cdot\mathbf{x}} \quad (\hat{\psi}_{\mathbf{k}} = \hat{\psi}_{-\mathbf{k}}^*)$$

where  $\mathbf{k} = 2m\pi/L, 2n\pi/L$ ;  $n, m = 1, \infty$ , periodic over a large domain, width  $L$ . Let  $L$  become large, and imagine an equivalent continuum of wave numbers obtained by blurring the discrete  $k$  over a fixed, small interval (or see Batchelor, 1953, p. 30). Then the power spectra of the various fields, with respect to vector and scalar wave number, are, for geostrophic flows,

$$\begin{aligned} P(\mathbf{k}) &= \rho_0 f_0 |\psi_{\mathbf{k}} \psi_{\mathbf{k}}^*| & \mathcal{P}(k) &= \int_0^{2\pi} P(\mathbf{k}) k \, d\theta \quad (\text{pressure}) \\ E(\mathbf{k}) &= \frac{1}{2} \frac{|\mathbf{k}|^2 P(\mathbf{k})}{\rho_0^2 f_0^2} & \mathcal{E}(k) &= \frac{1}{2} \frac{k^2 \mathcal{P}(k)}{\rho_0^2 f_0^2} \quad (\text{kinetic energy}) \\ \Omega(\mathbf{k}) &= \frac{1}{2} \frac{|\mathbf{k}|^4 P(\mathbf{k})}{\rho_0^2 f_0^2} & \hat{\Omega}(\mathbf{k}) &= \frac{1}{2} \frac{k^4 \mathcal{P}(k)}{\rho_0^2 f_0^2} \quad (\text{enstrophy}) \end{aligned}$$

$$k = |\mathbf{k}|, \quad \tan^{-1} \theta = \frac{\mathbf{k} \cdot \text{north}}{\mathbf{k} \cdot \text{east}}$$

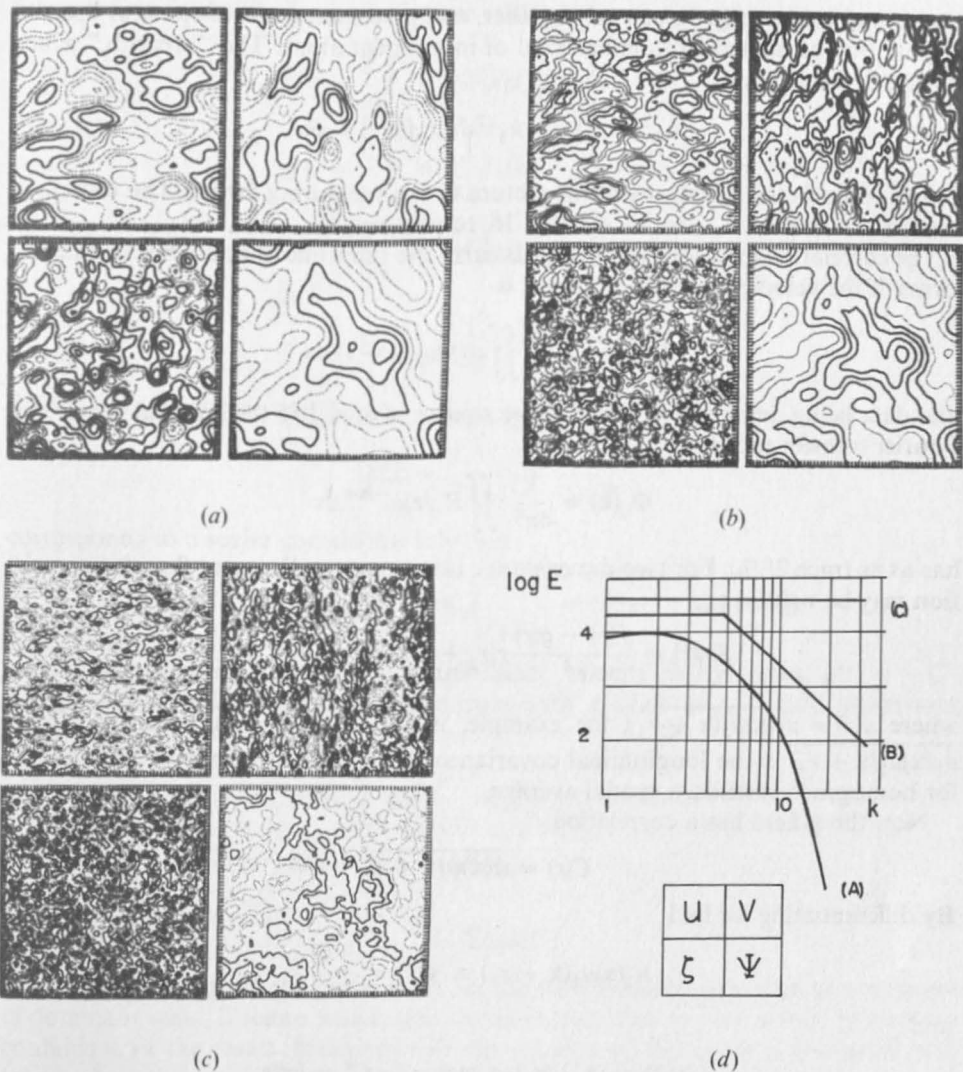


Fig. 3. Artificially generated fields of  $\psi$  (or pressure), velocity components  $u$ ,  $v$ , and vorticity  $\zeta$ . The azimuthal wave number dependence is fixed. (a) For scalar-wave number spectrum  $E = ke^{-2/3k}$ ; (b) for  $E = 1.0$  ( $k \leq 5$ ),  $E = (k/5)^{-3}$  ( $k > 5$ ); (c) for  $E = \text{const}$ . The discrimination between associated fields  $\psi$ ,  $u$ ,  $v$ ,  $\zeta$  increase with spectral bandwidth.

where  $\rho_0$  is density,  $f_0$  is Coriolis frequency. Successive differentiation in space corresponds to high-pass filtering of the spectrum. The *degree* to which this filtering affects the picture depends of course on the breadth of the spectrum. A monochromatic field will be unaltered in character by differentiation. The three realizations in Fig. 3 illustrate this. Each one has the same directional makeup in its spectrum, yet with different dependence on  $k$ , Fig. 3d. As one proceeds from relatively narrow to white spectra, differentiation has more and more of an effect. The dominant scale of the vorticity for a white velocity spectrum is infinitely small (limited here only by the  $64 \times 64$  grid). The distinction is experimentally useful because arrays of current

meters and pressure gauges, used together, can give a measure of spectral breadth beyond that estimated from either kind of instrument alone. The "breadth," which may be defined by

$$k_2^2 = \int |k - k_1|^2 \mathcal{E}(k) dk \bigg/ \int \mathcal{E} dk$$

clearly controls the sensitivity of the picture to the measuring device. The centers of mass of the spectra,  $k_1$ , are 3.1, 4.8, and 16, respectively.

The correlation functions of such fields carry the same information, but in different forms. If the velocity correlation tensor is

$$R_{ij}(\mathbf{r}) = L^{-2} \iint u_i(\mathbf{x}) u_j(\mathbf{x} + \mathbf{r}) d\mathbf{x}$$

(the data being defined over a very large square of area  $L^2$ ), the spectral tensor, the Fourier transform of  $R_{ij}$ ,

$$\Phi_{ij}(\mathbf{k}) = \frac{1}{4\pi^2} \iint R_{ij}(\mathbf{r}) e^{-i\mathbf{k}\cdot\mathbf{r}} d\mathbf{r}$$

has as its trace  $2E(\mathbf{k})$ . For two-dimensional, isotropic, nondivergent flow the correlation may be written as

$$R_{ij}(\mathbf{r}) = \frac{f(r) - g(r)}{r^2} r_i r_j + g(r) \delta_{ij} \quad r = |\mathbf{r}|$$

where  $g(r) = \overline{u_2(\mathbf{x})u_2(\mathbf{x} + r_1)}$ , for example, is the lateral covariance and  $f(r) = \overline{u_1(\mathbf{x})u_1(\mathbf{x} + r_1)}$  is the longitudinal covariance. The bar is a probability average or, for homogeneous fields, a spatial average.

Now the  $\psi$  field has a correlation

$$C(r) = \overline{\psi(\mathbf{x})\psi(\mathbf{x} + \mathbf{r})}$$

By differentiating we find

$$u_1(\mathbf{x})u_1(\mathbf{x} + r_1) \equiv f(r) = \frac{-C'}{r}$$

and

$$u_2(\mathbf{x})u_2(\mathbf{x} + r_1) \equiv g(r) = -C'' = (rf)'$$

Here the basic  $\psi$  field and velocity fields have correlation functions which themselves are related by differentiation. The lateral correlation  $g(r)$ , being a differentiated function of the longitudinal correlation,  $f(r)$ , generally has a smaller dominant scale. This distinction is made clear by the anisotropy in the maps (Fig. 3) of the velocity components. The spectrum with respect to scalar wave number is related to the covariances by various expressions,

$$\begin{aligned} \mathcal{E}(k) &= \frac{1}{4}\pi k \iint (f + g) e^{-i\mathbf{k}\cdot\mathbf{x}} d\mathbf{x} \\ &= \frac{1}{2}\pi k \int_0^\infty r(f + g) J_0(kr) dr \\ &= \frac{1}{2}\pi k^3 \int_0^\infty r C J_0(kr) dr \end{aligned}$$

for isotropic fields. The inverses of these relations are

$$f(r) = \frac{2}{r} \int_0^\infty k^{-1} \mathcal{E}(k) J_1(kr) dk$$

$$g(r) = \frac{2}{r} \int_0^\infty \mathcal{E}(k) \left[ J_0(kr) - \frac{1}{kr} J_1(kr) \right] dk$$

$$C(r) = 2 \int_0^\infty k^{-2} \mathcal{E}(k) J_0(kr) dk$$

$$= (\rho_0 f_0)^{-2} \int_0^\infty \mathcal{P}(k) J_0(kr) dk$$

A useful model energy spectrum,

$$\mathcal{E}(k) = \frac{1}{2} \frac{k^3}{[r_0^{-2} + k^2]^{\mu+1}}$$

corresponds to a scalar correlation function

$$C(r) = C(0) \frac{2^{1-\mu}}{\Gamma(\mu)} \left(\frac{r}{r_0}\right)^\mu K_\mu\left(\frac{r}{r_0}\right) \sim r^{\mu-1/2} e^{-r} \quad \text{for } r \rightarrow \infty$$

[and corresponding lateral and longitudinal velocity correlations,  $g(r) = -C''$ ,  $f(r) = -r^{-1}C'$ ]. For instance, a spectrum with a peak at  $r_0^{-1}$  and asymptotic tail  $\sim k^{-3}$  has a scalar correlation

$$C(r) = \frac{1}{2} C(0) \left(\frac{r}{r_0}\right)^2 K_2\left(\frac{r}{r_0}\right) \quad (\mu = 2)$$

The zero crossing of  $g(r)$  occurs at  $r = 1.34r_0$ .

### B. Scales

Above we have used the centroid,  $k_1$ , of the wave number spectrum as a measure of dominant scale. It seems wise to use the entire spectrum in such a way, to increase confidence in the result. Measures like the position of the spectral maximum will tend to be less stable. However, when comparisons of  $k$  are being made, one must take care that the range of wave numbers being considered, particularly at the low end, is the same.

The correlation function for scalar fields has associated with it the integral scale,

$$r_1 = \int_0^\infty C(r) dr$$

and the "microscale,"  $r_2 = [C''(0)]^{-1/2}$ . In terms of isotropic spectra,

$$r_1 = (\rho_0 f_0)^{-2} \int_0^\infty \mathcal{P}(k) dk$$

and  $r_2^2 = (\rho_0 f_0)^{-2} \int_0^\infty k^2 \mathcal{P}(k) dk$ ; these are very different scales from  $k_1^{-1}$ . For the velocity correlations of classical turbulence theory, the corresponding microscale is  $[f''(0)]^{-1/2}$ ;  $f''(0) = \frac{1}{10} \int_0^\infty k^2 \mathcal{E}(k) dk$  (proportional to the total dissipation) weights heavily the smaller scales.

Thus it is a rather different picture one gets from spectra on the one hand, by remembering the centroid  $k_1$ , breadth  $k_2$ , and perhaps asymptotic tail  $N(\mathcal{E}(k) \sim k^{-N})$ , than from correlations on the other hand, where the scale  $r_1$ ,  $r_2$ , and perhaps the position of the first zero crossing are kept track of. The use of spectra has the advantage that, if linear waves are present, a dispersion equation may associate particular wave vectors,  $\mathbf{k}$ , of spatial Fourier components with frequencies,  $\omega$ , of temporal Fourier components. If, instead, the flow is turbulent, there may still be a theory predicting the shape and dynamical role of the spectral tail. Neither kind of theory is readily applied to correlation functions.

### C. Time

In individual time series similar remarks hold, except that the temporal correlation functions are simple one-dimensional Fourier transforms of the spectra. For example, if  $C_\psi(t, \tau) = \overline{\psi(t)\psi(t + \tau)}$ ,  $C_u = \overline{u(t)u(t + \tau)}$ , then the spectrum of  $\psi$ , is

$$P_1(\omega) = \int C_\psi(t, \tau) e^{-i\omega\tau} d\tau$$

and the spectrum of the velocity is  $\mathcal{E}_1(\omega) = \int C_u(t, \tau) e^{-i\omega\tau} d\tau$ . Centroid frequencies,  $\omega_1$ , breadth  $[(\omega - \omega_1)^2]^{1/2}$ , spectral tails  $\omega^{-N}$ , integral time scales  $t_1 = \int_0^\infty C d\tau$ , and microscales  $t_2 = [C''(0)]^{-1/2}$  exist in analogy with their spatial counterparts. Here  $t_2^2$  is just twice the mean-square acceleration  $(\overline{(\partial u / \partial t)^2})$  and  $t_1$  is  $\lim_{\omega \rightarrow 0} \mathcal{E}(\omega)$  (this must not be confused with the mean, which is presumed to have been removed).

In temporal records there arise two natural reference frames: purely Eulerian records measured at a point fixed in space, and Lagrangian records measured from points moving with fluid parcels. For later reference we define the Lagrangian data as  $\mathbf{u}^L(t; \mathbf{x}_0)$ , depending on time and the initial particle position,  $\mathbf{x}_0$ , and Eulerian data  $\mathbf{u}^E(t, \mathbf{x})$ , depending on the fixed observation point  $\mathbf{x}$ . The corresponding spectra are  $\mathcal{E}_i^L(\omega; \mathbf{x}_0) = \int R_{ij}(\tau, \mathbf{x}_0) e^{-i\omega\tau} d\tau$  and  $\mathcal{E}_i^E(\omega; \mathbf{x}) = \int R_{ij}^E(\tau; \mathbf{x}) e^{-i\omega\tau} d\tau$ .

### D. Dynamics

Some simple dynamic remarks are in order. First, if the complete space-time correlations or wave number-frequency spectra [corresponding to  $\mathbf{u}(\mathbf{x}, t)$ , say] can be measured, then a simple dynamic system might reveal itself by the appearance of spectral energy only along certain dispersion surfaces,  $\omega = \omega(\mathbf{k})$ . But usually this is neither observationally possible nor theoretically expected. Grosser dynamic comparisons can be made, however. For instance, the breadth or asymptotic tail of a wave number spectrum tells us whether or not there is dissipation occurring at small scales, that is, dissipation strong enough to damp actively and critically the energy-containing eddies. Violently energetic, three-dimensional turbulence has broad enough spectra (e.g.,  $k^{-5/3}$ ) to do this critical damping, but many flows such as geostrophic turbulence and plume convection have spectra too sharp (e.g.,  $k^{-3}$ ) to be dominated in this way by friction.

One of many ways to distinguish waves from turbulence is by the strength of the diffusivity of marked fluid particles. The diffusivity at long times, for a homogeneous, stationary field, is

$$\kappa_{ji} = \overline{u_i u_j} t_{ij}; \quad t_{ij} = \int_0^\infty R_{ij}(\tau) d\tau$$

(see Section 8), and one sees that a wave field in which particles do not stray far from their origins will necessarily yield a correlation function with deep negative lobes capable of making the integral scale,  $t_{ij}$ , vanishingly small, while diffusive turbulence will have a substantial  $t_{ij}$ .

Another wave/turbulence comparison can be made using the above discussion of spectral breadth. Suppose, first, that turbulence is endowed with a crude dispersion relation  $\omega \sim U|k|$ , where  $U$  is the root mean square (rms) particle speed. This is not Taylor's hypothesis, which is a more precise consequence of a strong mean current, but merely suggests that turbulent eddies advect one another past a fixed sensor in the advective time  $(|k|U)^{-1}$ . If this is so, then our remarks about the spatial filtering action of pressure sensors relative to current meters (in a geostrophic flow) apply also to temporal records: a pressure record at a single point should be of characteristically longer period than a velocity record at the same point. Figure 4, a computer experiment with two-dimensional turbulence, shows this to be true: the larger spatial scale of  $\psi$  or  $p$ , compared with velocity, maps onto a longer period, and the *extent* of the difference gives a measure of spectral breadth. If, instead, the motion had obeyed the dispersion relation of planetary waves,  $\omega \propto k^{-1}$ , the reverse would have occurred: longer waves would have the higher frequency, and a pressure time series would have

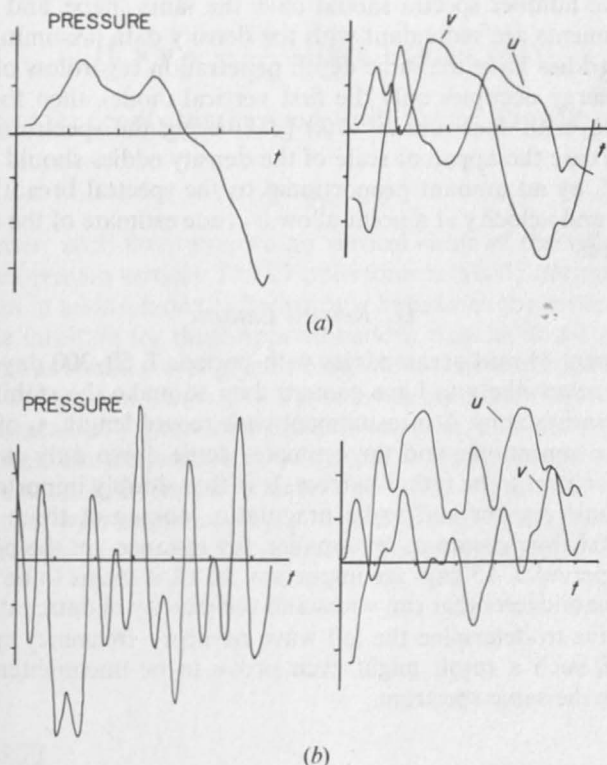


Fig. 4. (a) Pressure and velocity at a fixed point in a two-dimensional turbulence simulation (see Table I for details of computer experiment). The velocities are more rapidly changing than the pressure; this verifies that turbulence maps large wave-numbers on to large frequencies. (b) As in (a), but with a field of linear Rossby waves (for which  $\sigma = -\beta \cos \theta/|k|$ , where  $\theta$  is the angle of  $k$  from the east). The inverse dispersion relation causes velocities to change *less* rapidly than pressure.

been more quickly varying than current (Fig. 4b). A crude test of the dispersion relation is thus possible with a single pair of records from these different sensors.

Time series at fixed (or drifting) points seem to be easier to obtain than space series (although one cannot claim that the *Panulirus* time series preceded the discovery of eddies in classical sections). Further use of the advective dispersion relation thus may be of interest. For instance, Eulerian frequency spectra characteristically drop down steeply at frequencies above those of the dominant eddies, roughly like  $\omega^{-3}$ . A deep spectral valley separates the eddies from the inertial-tidal-internal wave band. Now the energetic eddies must sweep smaller eddies past a fixed sensor, and thus a wave number spectrum falling off something like  $k^{-3}$ , beyond *its* maximum, is expected, as is a real dearth of energy at scales (wavelength/2)  $\sim 2$ –10 km (corresponding typically to periods of 2–10 days, for  $U \sim 5$  km/day). The implication of this spectral valley (Rhines, 1973) is simply that no local cascade of energy is occurring from the eddies to small scales. If such a transfer happens at all, it must be jumping the valley via boundary turbulence, intermittent internal turbulence, or nonlocal cascade into internal waves. The rate of energy dissipation in the eddies is crucial, and at this point unknown.

What about temperature and salinity data, used in conjunction with current records? The thermal wind equation,  $f(\partial \mathbf{u} / \partial z) = -\mathbf{g} \times \nabla \rho / \rho$ , admits two possibilities. If eddies are geometrically similar, broader ones penetrating more deeply, the density and velocity wave number spectra should have the same shape, and the baroclinic velocity measurements are redundant with the density data (assuming geostrophy). However, if the eddies have the same depth penetration regardless of breadth (say, the baroclinic energy occupies only the first vertical mode), then the density field acts like pressure, with spectrum  $k^{-2} \mathcal{E}(k)$  [ $\mathcal{E}(k)$  being the spectrum of baroclinic velocity]. In this case the apparent scale of the density eddies should exceed that of the velocity field, by an amount proportional to the spectral breadth. Again, time series of density and velocity at a point allow a crude estimate of the corresponding dispersion relation.

#### D. Record Length

In the measurement of mid-ocean eddies with period,  $T$ , 50–300 days, scales  $\sim 40$ –100 km, we are never likely to have enough data to make the stability of spectral estimates really satisfactory. A measurement with record length,  $\tau$ , of more than 10 periods would be ambitious, and the estimates settle down only as  $(\tau/T)^{1/2}$ , even assuming the spectrum to be rather narrow. It is thus doubly important to focus on important dynamic regions and to be pragmatic, looking at those regions where the environmental time constants are smaller, for instance, on the continental rise, where waves of period 5–15 days are important. In all, it seems to be more useful to invent crude dynamic tests that can withstand the paucity of data, rather than make a monolithic drive to determine the full wave number—frequency spectrum of the eddies. By itself, such a result might even prove to be unenlightening, for many theories produce the same spectrum.

### 4. Dynamics of the Gentlest Kind

It is well to describe the ideal response of a gently driven rotating fluid, before examining the flows caused by stronger forcing, and in the presence of less simple boundaries and more complex density stratification. Indeed it is the linear Sverdrup

solution that is the heart of modern circulation theories, whether thermohaline or wind-driven, and its strength or weakness must be noted.

Here we describe a model that attempts to show in more intuitive form the basic solutions described by Stommel (1957). It reproduces a number of the known principal features of spherical geometry, yet in a wedge-shaped container, Fig. 5. The primitive Boussinesq equations for the velocity,  $\mathbf{u}$ , and pressure,  $p$ , are

$$\begin{array}{cccccc} 1 & 2 & 3 & 4 & 5 & 6 \\ \frac{\partial \mathbf{u}}{\partial t} + \mathbf{u} \cdot \nabla \mathbf{u} + f \hat{\mathbf{k}} \times \mathbf{u} = - \frac{\nabla p}{\rho_0} + \mathbf{g} \rho' + \nu \Delta \mathbf{u} & & & & & \\ \nabla \cdot \mathbf{u} = 0 & & & & \frac{\partial \rho'}{\partial t} + \nabla \cdot \rho' \mathbf{u} = 0 & \end{array} \quad (1)$$

where  $\rho \equiv \rho_0(1 + \rho')$  is the potential density,  $f$  is the Coriolis frequency,  $2\Omega$ ,  $\hat{\mathbf{k}}$  is a vertical unit vector,  $\mathbf{g}$  is the gravity field, and  $\nu$  is the kinematic viscosity. For flows describable by a single horizontal length scale  $L$ , vertical length scale  $H$ , time scale  $T$ , and velocity scale  $U$ , the ratio of typical sizes of terms 1 and 3 is  $(fT)^{-1} \equiv \omega$ , a scaled frequency; the ratio 2:3 is  $U/fL \equiv \varepsilon$ , the Rossby number; and 6:3  $\nu(H^{-2} + L^{-2})/f \equiv E$ , the Ekman number.

Basic geostrophy occurs when each of  $\omega$ ,  $\varepsilon$ , and  $E$  is small, whence

$$f \hat{\mathbf{k}} \times \mathbf{u} = - \frac{\nabla p}{\rho_0} + O(\omega) + O(\varepsilon) + O(E) \quad (2)$$

If we now neglect the density stratification, 5, the Taylor–Proudman approximation follows:

$$f(\hat{\mathbf{k}} \cdot \nabla) \mathbf{u} = 0 \quad (3)$$

to the same order; such flows involve no vertical shear of the velocities, and ideal vertical dye lines remain vertical. The Coriolis force acts only normal to  $\hat{\mathbf{k}}$ , and hence equation 3 relies in addition on the hydrostatic balance in the vertical.

Considerable intuition for these approximations may be found in linear internal wave theory, just as sound waves give us insight into “incompressible” fluids. Plane-wave solutions of equation 1 with  $E \rightarrow 0$  pass smoothly to the limit  $\omega \rightarrow 0$  where they take on the character of Taylor–Proudman flows, even while the energetics of wave theory still applies. The frequency over  $f$  is just  $\omega = \cos \theta$ , where  $\theta$  is the angle of the wave number vector,  $\mathbf{k}$ , from the vertical. The group velocity lies along the wave crests, normal to  $\mathbf{k}$ , with magnitude  $f|\mathbf{k}|^{-1} \sin \theta$ . Energy propagates, therefore, ever closer to the vertical as  $\omega \rightarrow 0$ , painting out Taylor columns induced, say, by a

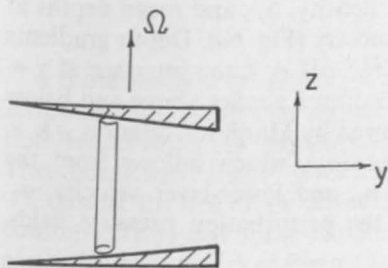


Fig. 5. Wedge-shaped container filled with homogeneous fluid uniformly rotating.  $y$  is analogous to north on a  $\beta$  plane.

disturbance below. Rigidity develops in fluid columns owing to the rapidity of this energy propagation, the group velocity approaching  $fL$  [and the time for signals to penetrate vertically through a distance  $H$  approaching  $f^{-1}(H/L)$ ] even as the frequency vanishes. In order that the fluid not be strained vertically, free motions in a container like that in Fig. 5 must be directed along the depth contours,  $h = \text{constant}$ .

### A. Hough, Goldsbrough, Sverdrup Flow

The lowest-order constraints due to strong rotation alone provide the solution to simple interior flows in the wedge-shaped model of the  $\beta$  plane. Imagine the response of the fluid to gentle downward motion,  $w_0$ , imposed at the upper surface (whether by Ekman convergence, fluid sources, or simply mechanical motion of the lid itself). Since equation 3 implies  $\nabla_H \cdot \mathbf{u} = 0$ , the only recourse for the fluid is to move toward greater depth, avoiding any vertical compression (the vertical velocity equaling  $w_0$  throughout the column). The "southward" velocity,  $-v$ , is given by

$$v = \frac{w_0}{\alpha} \quad (4)$$

where  $\alpha/2$  is the semi-angle of the wedge. In the case of an imposed stress,  $\tau$ , quasi-steady Ekman layers along the rigid boundaries produce interior vertical velocity,  $w_0 = \mathbf{k} \cdot \nabla \times \tau / \rho_0 f$ , and then renaming  $\alpha$  as  $\beta H / f$ , where  $H$  is the mean depth, equation 4 becomes

$$\beta v = \frac{\nabla \times \tau|_z}{\rho_0 H} \quad (5)$$

The horizontal flow is approximately nondivergent,  $\nabla_H \cdot \mathbf{u} = 0$ ; hence  $u = \int v_y dx$ , the limits of integration as yet unspecified.

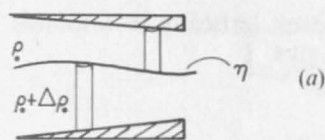
If the wedge geometry is complicated by adding rough-bottom topography, free geostrophic flows must still follow  $h(x, y)$  contours, and equation 5 generalizes to

$$hu \cdot \nabla \left( \frac{f}{h} \right) = \frac{\nabla \times \tau|_z}{\rho_0 H} \quad (6)$$

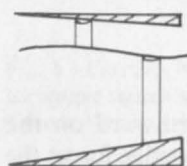
Either equation 5 or 6 puts severe constraints on the forcing pattern and basic geometry if violations of this level of geostrophy are to be avoided.

### B. Stratification

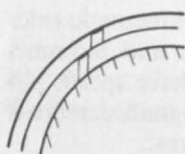
The principal effects of stratification can be included without loss of simplicity using two homogeneous layers of slightly different density,  $\Delta\rho$ , and mean depths at  $y = 0$  of  $H_1$  and  $H_2$ , respectively, in the same geometry (Fig. 6a). Depth gradients occur in both layers, in the rest state. (Provided  $f^2 L^2 / gH \ll 1$ , the interface at  $z = \eta(\mathbf{x}, t)$  is practically flat in the absence of flow.) Equation 2 applies above and below the interface, yet a jump in velocity across it is allowed by Margules' relation,  $g' \mathbf{k} \times \nabla \eta = -f[\mathbf{u}_1 - \mathbf{u}_2]$  ( $g'$  is the reduced gravity,  $g\Delta\rho/\rho_0$ ), which follows from the expression (equation 2) for upper-layer velocity,  $\mathbf{u}_1$ , and lower-layer velocity,  $\mathbf{u}_2$ , with the hydrostatic relation  $p_2 - p_1 = g'\eta$  for the perturbation pressure fields, respectively.



(a)



(b)



(c)

Fig. 6. Two-layer analogues of the  $\beta$  plane. (a) Equal mean depths of the fluid; (b) with a thin upper layer, the bottom sloping more steeply than the lid, for a uniform potential vorticity gradient; (c) on a rotating sphere, with columns remaining parallel to  $\Omega$  (yet the effect of continuous stratification in the oceans makes this less than a perfect idealization).

Now the same driving by a vertical velocity at the top causes, by the constraint of stiffness in each layer, a north-south transport

$$\frac{1}{2}(v_1 + v_2) = \frac{w_0}{\alpha} \quad \text{for } H_1 = H_2$$

This is the analogue of the stratified Sverdrup relation. For the flow to be steady,  $\partial\eta/\partial t = 0$ ,  $v_2$  must vanish, leaving the transport entirely confined above the thermocline, which tilts, preventing the upper-layer pressure gradients from reaching the depths.

However, the time required to set up such a flow is great, so that either unsteadiness of the winds or diffusive effects may modify the vertical structure. The latter lead to thermocline theories, which do not concern us here.

### C. Time Dependence

A more realistic resolution of the vertical structure with stratification, and a description of the setup time for steady flow, come from the approach to steady circulations found when the frequency of an oscillatory wind-stress pattern is led to vanish. Then linear wave theory gives a complete solution.

Consider the free motions possible ( $w_0 = 0$ ) beyond that of flow along geostrophic contours. Time and space variations are allowed, but they must be gradual. In the equal-depth geometry of Figure 6a north-south motion is possible without stretching

fluid columns, only if  $v_2 = -v_1$  and if the interface moves vertically in response. Combining with the equation for geostrophic thermocline tilts,

$$\frac{\partial \eta}{\partial x} = \frac{f}{g'}(v_2 - v_1) = \frac{-2f}{g'}v_1$$

and continuity,

$$\frac{\partial \eta}{\partial t} = v_1 \alpha$$

we find

$$\frac{\partial \eta}{\partial t} + \frac{\alpha g'}{2f} \frac{\partial \eta}{\partial x} = 0.$$

Where the thermocline is locally depressed, the upper flow is northward on the western side and southward to the east. This flow into and out of the wedge forces the thermocline downward in the west, upward in the east. It follows that an arbitrary pattern of interface displacements, varying in both  $x$  and  $y$ , moves "westward" without dispersion, at speed  $\alpha g'/2f \equiv \beta c_0^2/f^2$  where  $c_0$  is the speed of long internal waves without rotation, or equivalently,  $\beta L_\rho^2$ , where  $L_\rho$  is Rossby's internal deformation radius,  $c_0/f$ , and in doing so obeys the most trivial, nearly kinematic rules of Taylor-Proudman flow. This internal Rossby wave of Veronis and Stommel (1956) describes the baroclinic adjustment to unsteady winds. Its phase speed,  $\lesssim 4$  km/day at mid-latitudes, shows that many years must pass before signals can cross the ocean and complete the spin-up of a baroclinic circulation from rest.

It is now a simple matter to imagine the response to a wind stress of large scale, say, a steady pattern turned on at time zero. Let the imposed vertical velocity be

$$w_0(x, y, t) = \frac{\nabla \times \tau|_z}{\rho_0 f} = f_1(x)f_2(y) \quad t \geq 0$$

$$= 0 \quad t < 0$$

Including unequal layer depths  $H_1$  and  $H_2$  (Fig. 6b), the equivalent  $-\beta$  slopes are now  $\alpha H_1$  and  $\alpha H_2$ , where  $\beta = f\nabla h/h = f\alpha$ . Then,

$$\alpha H_1 v_1 = w_0 - \frac{\partial \eta}{\partial t}$$

$$\alpha H_2 v_2 = \frac{\partial \eta}{\partial t}$$

$$\frac{\partial \eta}{\partial x} = \frac{f}{g'}(v_2 - v_1)$$

and we find

$$\frac{\partial \eta}{\partial x} - c_0^{-1} \frac{\partial \eta}{\partial t} = -\gamma w_0 = -\gamma f_1(x)f_2(y)$$

where

$$\gamma = \frac{f}{g'\alpha H_1}$$

$$c_0 = \frac{\alpha g' H_1 H_2}{f(H_1 + H_2)} = \beta L_\rho^2$$

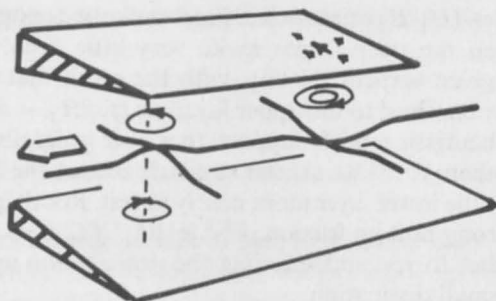


Fig. 7. Currents induced by steady localized wind stress turned on at  $t = 0$  (yet slowly enough that barotropic signals are negligible). The transient, circular baroclinic wave moves off to the west, leaving a steady Sverdrup gyre. This occurs without stretching or compression of fluid columns.

The solution is

$$\eta = -\gamma f_2(y) \int_x^\infty [f_1(x' + c_0 t) - f_1(x')] dx$$

If, for example, the stress curl has a dipole nature, say,  $w_0 = -x \exp[-(x^2 + y^2)]$ , the interface is

$$\eta = \frac{1}{2} \gamma \exp(-y^2) [\exp[-(x + c_0 t)^2] - \exp(-x^2)]$$

which is a steady, downward depression in the thermocline just beneath the stress, and its mirror image, propagating westward along  $y = 0$  (Fig. 7). The currents are initially barotropic, with an anticyclonic vortex at the origin. But as time progresses, this stationary circulation intensifies above the thermocline, and vanishes below it as the transient vortex moves off to the west. The currents in the transient vortex themselves are concentrated in the thin upper layer,  $v_2/v_1 = H_1/H_2$ . Lighthill (1969) has described in detail such events, particularly as applied to equatorial wave modes excited by the arrival of monsoon winds. Our major point here is that they fall within the range of interesting effects whose dynamics are so gentle that there is no vortex stretching; this is possible even near the equator, when the typical "impedance" of a rotating fluid with respect to vertical stretching, shown below to be  $f^2 L^2 T/H$ , becomes large.

It might seem that motions with such slow propagation would find difficulty in remaining linear, but the expected principal violation, the advection of density  $u \cdot \nabla \eta$ , vanishes identically. We may thus expect westward propagation of thermocline eddies of rather large amplitude.

If broad topography is added to the bottom, beyond that which is here imitating  $\beta$ , the free-wave equation becomes

$$\frac{\partial \eta}{\partial x} - \frac{f^2}{g'} \left( \frac{1}{\beta H_2 + \delta f} + \frac{1}{\beta H_1} \right) \frac{\partial \eta}{\partial t} = 0$$

where  $\delta$  is the true north-south bottom slope, here taken to be uniform. A strong slope thus *increases* the baroclinic wave speed to

$$\frac{f^2}{g'} \left( \frac{\beta H_1 (\beta H_2 + \delta f)}{\beta (H_1 + H_2) + \delta f} \right)$$

which approaches  $1 + (H_1/H_2)$  times the speed without topography. The change arises, as above, when the steep slopes make very little deep, horizontal motion necessary to yield a given vertical velocity, with the result that this slowly varying circulation is virtually confined to the upper layer, as  $\partial f/\beta H_2 \rightarrow \infty$ . Rhines (1970) has suggested, and these heuristic models support, that over generally rough topography (with slopes greater than  $10^{-3}$ ) we should similarly expect the baroclinic waves to propagate faster, with the lower layer more nearly at rest. Rooth (private communication) remarks that strong bottom friction,  $E^{1/2} \gg \beta L_\rho^2/fL$ , does just the same thing, bringing the deep water to rest and speeding the propagation up, while in the limit causing vanishingly small dissipation.

#### D. Spherical Geometry

These same arguments provide a local description of mid-latitude flows in a two-layer spherical ocean, (Fig. 6c) with rigidity imparted to the fluid parallel to the rotation axis. The wedge geometry is provided, in effect, by the northward gradient of the axial projection of the layer depths, equivalent to gradients of  $f/h_i$  where  $f = 2\Omega \sin(\text{latitude})$ . The inclusion of continuous stratification, the final link to the real oceans, is a difficult step. The integrity of fluid columns parallel to  $\Omega$  is then lost and scale analysis gives support to the "traditional approximation," the neglect of locally horizontal components of the earth's rotation, which makes our wedge geometry an analogue rather than a replica of the complete spherical ocean.

Finally we mention that other, more distant analogues may be of value to the intuition. For example, the nonrotating Boussinesq thermal convection of a fluid with strong basic temperature stratification,  $\bar{T}(z)$ , obeys

$$\frac{d\bar{T}}{dz} w = Q(x, z)$$

$$\frac{\partial u}{\partial x} + \frac{\partial w}{\partial z} = 0$$

for a gentle internal heat source distribution,  $Q(x, z)$ . This is a Hadley circulation in  $(x, z)$  fundamental to atmospheric modeling, and is formally the same as Sverdrup flow in  $(x, y)$  with  $\beta \equiv d\bar{T}/dz$ ,  $\nabla \times \tau|_z/\rho_0 f_0 \equiv Q$ . Fluid that is heated rises slightly to a new equilibrium level, without significantly altering the mean state. Simple gyres in  $(x, z)$  are possible in confined geometry, if only  $\int Q dx = 0$  at each level. Otherwise conductive boundary layers form at the side walls to close the vertical circulation.

By establishing that Sverdrup flow and long internal Rossby waves involve nearly inextensible translation of fluid columns in the wedge analogue, we can gauge the transition to more vigorous currents. To do so, we quantify the stiffness by solving for the flow induced by simple forcing with  $\beta = 0$ ; imposed vertical velocity must then produce relative vertical vorticity,  $\zeta$ , according to  $\partial\zeta/\partial t = -f(\partial w/\partial z)$ . Suppose  $w_0 = w_0 \sin(x/L) \sin(t/T)$ ; the resulting pressure field is

$$P = \frac{p}{\rho} = \frac{f^2 T w_0 L^2}{H} \sin \frac{x}{L} \cos \frac{t}{T}.$$

The oscillatory currents have an *impedance* with respect to vertical stretching,

$$\left| \frac{P}{w_0} \right| = \frac{f^2 L^2 T}{H},$$

here a reactance. The increased vertical stiffness at large scale or large rotation rate is evident.

The average kinetic energy produced here by pressure work,  $\overline{Pw_0}$ , below the lid is  $f^2 w_0^2 T^2 L^2 / 16H$ , which may be compared to the kinetic energy in a pure Sverdrup flow ( $v = w_0/\alpha$ ) driven by the same distribution of vertical velocity (but with sloping geometry), which averages to  $Hw_0^2/8\alpha^2$ . Now if the forcing becomes so rapidly changing as to make the ratio of these energies,  $(\alpha f TL/2H)^2 [\equiv (\beta LT/2)^2]$ , less than unity, the least work is expended if the fluid begins to yield to vertical stretching and compression, with less motion to the north and south. The less energetic choice is made, and Sverdrup flow gives way to Rossby waves, involving essential relative vorticity, when  $\beta LT$  falls below unity. If the forcing is more intense than this, so that nonlinearity is significant, nonnegligible vorticity appears when  $\alpha f L^2/HU < 1$  (i.e.,  $\beta L^2/U < 1$ ), and two-dimensional turbulence appears, instead of linear waves, to replace the classical circulation. These same conclusions follow from a more conventional scale analysis of the potential vorticity equation, which is developed in the next section.

### 5. Linear Potential-Vorticity Waves

The earliest explorations of long-period waves ("linearized eddies") on a rotating sphere followed the train of thought found in classical elastic oscillations of solids and membranes, and in the short-period tides, that is, dominance of grave modes of large scale. This seemed appropriate because the assumed forcing effect, the winds and sun, act on a large scale, and also because the natural frequencies and propagation speeds turned out to be the *largest* for the grave modes (with all "higher" modes contained at lower frequency). With the intellectual focus moving more or less continuously downward through the frequency spectrum, the grave modes were the first oscillations to be found at periods greater than one-half pendulum day. LaPlace's tidal equation, which reduces to the spherical form of the potential vorticity equation at small  $\omega$ , thus was divided by Hough (1898) into first- and second-class waves according to whether  $\omega$  was greater or less than unity. Longuet-Higgins (1964 et seq.) has produced the most thorough discussion of the second-class planetary waves on a sphere, as did Ball (1963 et seq.) for smoothly shaped rotating basins.

It was imagined that, in combination with classical circulation theory, the planetary waves would provide the complete solution to the currents forced by the real, unsteady winds and heating. In fact, the possibility of nonlinear interaction in a weak sense was recognized, and some calculations of weak rectified flows (wave-current interaction) and wave-wave resonant interactions were produced (e.g., Pedlosky, 1965; Veronis, 1970; Kenyon, 1964; Longuet-Higgins and Gill, 1966).

Now these grave-mode planetary waves may be relevant to oceanwide seiches of periods less than a month once the modifications owing to variable ocean depth are included (Rhines, 1969; Platzmann, 1974). However, despite recent measurements supporting their existence, they are most unenergetic, accounting for currents not exceeding 1 cm/sec or so. The evidence is now overwhelming that the scale of the dominant energy-containing eddies is 100 km or less, corresponding more closely

with the Rossby internal radius of deformation,  $L_\rho$ , than with the geometry of either the basin or the external forcing effects.<sup>2</sup>

Linear waves are worthy of study, even though the linear approximation is doubly bad at the mesoscale (the currents being far stronger there, and the phase speeds far slower than with the basinwide planetary modes). However, it turns out that vestiges of the linear theory apply well into the nonlinear range, even when energy transformations are becoming violent. In addition, powerful intuition about the spin-up of steady circulations (and the resolution of degeneracies in them) is provided by the group velocity of low-frequency waves, and this intuition provides rough upper bounds to the rate at which influence can propagate laterally, above and beyond any fluid advection velocity. Veronis and Stommel (1956) and Lighthill (1967, 1969) have emphasized this use of wave theory, and produced a rich picture of the regions of influence and rates of communication of currents forced on a  $\beta$  plane.

### A. Derivation of Equations

By centering attention on the  $O(100 \text{ km})$  scales, we can be less uneasy about the mid-latitude  $\beta$  plane approximation, which is essentially an expansion of the problem in terms of  $L/R_e$ ,  $R_e$  being the earth's radius multiplied by  $\tan(\text{latitude})$ . The traditional approximation is also taken. This neglects the upward Coriolis force  $2\Omega \cos \lambda u$  (due to overwhelming static stability) and the eastward Coriolis force  $2\Omega \cos \lambda w$  (due to the smallness of vertical velocity,  $w$ , in low-frequency motion of small aspect ratio,  $H/L$ ); see Miles (1974) and Needler and LeBlond (1973). The momentum and mass conservation equations for free adiabatic motions are

$$\frac{\partial \mathbf{u}}{\partial t} + (\mathbf{u} \cdot \nabla) \mathbf{u} + \mathbf{f} \times \mathbf{u} = -\frac{\nabla p}{\rho} - \mathbf{g} + \nu \Delta \mathbf{u} \quad (7)$$

$$\frac{\partial \rho}{\partial t} + \nabla \cdot \rho \mathbf{u} = 0$$

Here  $(x, y, z)$ ,  $(\hat{i}, \hat{j}, \hat{k})$  are Cartesian coordinates and unit vectors eastward, northward, and locally upward,  $t$  is time,  $\mathbf{u}$  is the velocity,  $f = 2\Omega \sin \lambda$  where  $\lambda$  is latitude,  $\mathbf{g}$  is the gravity vector, plus centrifugal acceleration,  $p$  is the pressure, and  $\nu$  is the kinematic viscosity. The Boussinesq approximation applies when the compressibility is slight enough that the density scale height far exceeds the fluid depth, and when temperature- and salinity-induced density variations are also small. For the oceans the pressure effect on density is not really negligible (fractional range of in situ density is  $\sim 3\%$ ) and deep-ocean vertical density gradients far exceed the gradients of potential density,  $\partial \rho_p / \partial z = (\partial \rho / \partial z) - (\rho g / c^2)$  (the dynamically relevant quantity), where  $c$  is the speed of sound. However, we henceforth ignore such effects, which mainly affect the calculation of static stability from vertical soundings.

<sup>2</sup> This chapter exclusively treats mid-latitude regions. Within a band of a few degrees north and south of the equator the waves are, on the whole, more rapidly propagating, particularly in the baroclinic modes due essentially to the reduced impedance of the fluid with respect to vertical stretching. The ocean may turn out to be rather like the atmosphere, in being largely nonlinear at middle latitudes, yet full of energetic linear waves near the equator. The zone of distinct equatorial dynamics is  $(gH)^{1/2} / \beta \sim \pm 2.5^\circ$  for the oceans ( $H =$  equivalent depth  $\sim 0.75 \text{ m}$ ), whereas for the atmosphere it is much greater,  $\sim \pm 33^\circ$  ( $H \sim 10 \text{ km}$ ). (Higher vertical modes, trapped within  $10^\circ$  of the virtual equator, are also of meteorological interest.)

Take the following nondimensionalization:

$$[x, y] = L, \quad [z] = H, \quad [t] = (f\omega)^{-1}, \quad [u, v] = U, \quad [w] = \frac{UH}{L},$$

$$[\zeta] = \frac{U}{L}, \quad [p'] = fUL\rho_0, \quad [\rho'] = \frac{\rho_0 fUL}{gH}, \quad [\zeta_H] = \frac{U}{H}$$

where  $(\zeta_H \cdot \mathbf{i}, \zeta_H \cdot \mathbf{j}, \zeta)$  is the vorticity,  $\nabla \times \mathbf{u}$ . The departures from mean hydrostatic values  $\bar{p}$  and  $\bar{\rho}$  of the pressure and density are  $p'$  and  $\rho'$ , respectively:  $p = \bar{p} + p'$ ,  $\rho = \bar{\rho} + \rho'$ . Let  $f = f_0[1 + (L/R)y]$ , where  $R = \text{earth radius} \times \tan(\text{mean latitude})$ . The vorticity equation, the curl of equation 7, is then

$$\omega \zeta_t + \varepsilon \mathbf{u}_H \cdot \nabla \zeta + \varepsilon \frac{H}{L} w \zeta_z - \left( \varepsilon \zeta + y \frac{L}{R} + 1 \right) w_z + \varepsilon (\zeta_H \cdot \nabla) w + \frac{L}{R} v$$

$$= \varepsilon \frac{\rho_0^2}{\rho^2} \frac{f^2 L^2}{gH} (p'_x \rho'_y - p'_y \rho'_x) \quad (8)$$

for the vertical component and

$$\omega \zeta_{H,t} + \varepsilon \mathbf{u}_H \cdot \nabla \zeta_H + \varepsilon \frac{H}{L} w \zeta_{H,z} - \varepsilon (\zeta_H \cdot \nabla) \mathbf{u}_H - (1 + yL/R + \varepsilon \zeta) \mathbf{u}_{H,z}$$

$$= \frac{\bar{\rho} \rho_0}{\rho^2} \left( 1 + \frac{\varepsilon \rho_0 f_0^2 L^2}{\bar{\rho} gH} p'_z \right) \mathbf{k} \times \nabla \rho' + \frac{\rho_0 H}{\rho H_s} \mathbf{k} \times \nabla p' \quad (9)$$

$H_s^{-1} = -(1/\bar{\rho})\bar{\rho}_z \equiv N^2/g$ , the density scale height, for the horizontal. With oceanic scaling the right side of equation 8, the creation of vertical vorticity by twisting,  $\nabla p' \times \nabla \rho'$ , is of relative order  $10^{-3}\varepsilon$ , and will be ignored. The term  $(H/H_s)\mathbf{k} \times \nabla p'$  in equation 9 is negligible ( $\sim 10^{-2}$  at most) relative to  $\mathbf{k} \times \nabla \rho'$ .

The vertical momentum and continuity equations are

$$\omega w_t + \varepsilon \mathbf{u} \cdot \nabla w = \frac{L^2}{H^2} (-p'_z - \rho') \quad (10)$$

$$\omega \rho'_t + \varepsilon (\mathbf{u} \cdot \nabla \rho) = \delta B^2 w \frac{\bar{\rho}}{\rho_0} \quad (11)$$

$$\nabla \cdot \mathbf{u} = 0 \quad (12)$$

where  $B = NH/f_0 L$ .

Now expand in  $\varepsilon$ , with  $\omega = O(\varepsilon)$  formally, and  $H/H_s \leq O(\varepsilon)$ ,  $f_0^2 L^2/gH \leq O(\varepsilon)$ .  $L/R = O(\varepsilon)$ ,  $(\bar{p} - \rho_0)/\rho_0 \leq O(\varepsilon^2)$  ( $u, v, w, p', \dots$ ) =  $(u^0 + \varepsilon u' + \dots, v^0 + \varepsilon v' + \dots, \dots)$   $O(\varepsilon^0)$ :

$$w_z^0 = 0 \quad (13a)$$

$$u_z^0 = \rho_y^0, v_z^0 = -\rho_x^0 \quad (13b)$$

$$u_x^0 + v_y^0 = 0 \quad (13c)$$

$$p_z^0 = -\rho^0 \quad (13d)$$

$$B^2 w^0 = 0 \quad (13e)$$

This says that the scaling was mistaken in one respect:  $w \sim \varepsilon(H/L)U$  rather than  $UH/L$ . The typical inclination of the velocity vector from horizontal is far smaller than the aspect ratio,  $H/L$ , would alone suggest. At this order, then, there exists a stream function for the horizontal velocities,  $u^0 = \hat{\mathbf{k}} \times \nabla\psi$ , which is simply proportional to the pressure field:

$$-\hat{\mathbf{k}} \times \mathbf{u}^0 = -\nabla p^0$$

The next order balance is of interest, not so much in giving small corrections, but in revealing the slow evolution of the dominant fields.

$$O(\varepsilon): w'_z = \frac{\omega}{\varepsilon} \zeta_t^0 + \mathbf{u}_H \cdot \nabla \zeta^0 + \frac{L}{R} v^0 \quad (14a)$$

$$\mathbf{u}'_{H,z} + \hat{\mathbf{k}} \times \nabla p' = \frac{\omega}{\varepsilon} \zeta_{H,t}^0 + (\mathbf{u}_H \cdot \nabla) \zeta_H^0 - (\zeta_H^0 \cdot \nabla) \mathbf{u}_H^0 \quad (14b)$$

$$u'_x + v'_y = 0 \quad (14c)$$

$$p'_z = -gp' \quad (14d)$$

$$\frac{D^0 \rho^0}{Dt} = \delta B^2 w' \quad (14e)$$

where

$$\frac{D^0}{Dt} = \frac{\omega}{\varepsilon} \frac{\partial}{\partial t} + \mathbf{u}_H^0 \cdot \nabla$$

The left side of the vertical vorticity equation 14a is eliminated with equations 14c and 13d:

$$\frac{D^0}{Dt} (\zeta^0 + (B^{-2} p_z^0)_z) + \frac{L}{\varepsilon R} v^0 = 0$$

In terms of the stream function,

$$\frac{D^0}{Dt} \left( \nabla^2 \psi^0 + (B^{-2} \psi_z)_z + \frac{\omega}{\varepsilon} f \right) = O \left( \varepsilon + \frac{H}{H_s} + \varepsilon \frac{f^2 L^2}{gH} \right) \quad (15)$$

with  $(D^0/Dt)\psi_z^0 = (\delta B^2/\varepsilon)\nabla\psi^0 \times \nabla h \cdot \hat{\mathbf{k}}$  on  $z = -H$ ,  $(D^0/Dt)\psi_z^0 = 0$  on  $z = 0$ . Here the fluid is confined between rigid flat top,  $z = 0$ , and rigid bottom,  $z = -H(1 + \delta h(\mathbf{x}))$ ,  $\delta \lesssim \varepsilon$ . This is the conservation of geostrophic potential vorticity, following nearly horizontal particle trajectories. In other situations more exact conservation laws exist; for instance, the barotropic potential vorticity law,

$$\frac{D}{Dt} \left( \frac{h \nabla \cdot h^{-1} \nabla \psi + f}{h} \right) = O \left[ \varepsilon^2 \left( \frac{H}{L} \right)^2 \right] \quad (16)$$

obeyed by uniform density fluid in a rapidly rotating container of depth  $h$ .<sup>3</sup> Here the vertical stretching term imposed by horizontal flow across an uneven bottom,  $f(D/Dt)h^{-1}$ , replaces the stretching of fluid between two, infinitesimally separated, isopycnal surfaces,  $(D^0/Dt)(B^{-2}\psi_z)_z$ , in equation 15. Ertel's (1942) relation,

$$\frac{D}{Dt} \left( \frac{(\nabla \times \mathbf{u} + \mathbf{f}) \cdot \nabla \rho}{\rho} \right) = 0$$

is the most exact of all, giving a potential vorticity that is conserved even in strongly ageostrophic, nondiffusive flows. For a more thorough account, see Phillips (1963).

### B. Linear Waves

The range of phenomena governed by equation 15 is vast. Taking the limit  $\varepsilon/\omega \rightarrow 0$ , we recover the purely linear wave regime. It cannot be overstressed that nonlinearities are rarely negligible in this sense, even though the momentum equation is quite accurately geostrophic [ $O(\varepsilon)$ ]. But linear theory is important just as, in the study of surface gravity waves in a full gale, the linear propagation theory would still hold in a gross sense for the dominant waves (and accurately for much longer waves). The smallness of the terms in equation 15 requires that we not forget for long diffusive effects and interaction with small-scale processes like internal waves.

Three distinct kinds of wave can be identified in the linear solutions of equation 15. To illustrate, take the boundary conditions to be free in the horizontal, rigid at the sea surface,  $z = 0$ , and at the sea floor, which slopes uniformly in the north-south direction:

$$\psi_z = 0 \quad \text{on } z = 0 \quad (17)$$

$$\omega B^{-2}\psi_{zt} = \delta\psi_x \quad \text{on } z = -1 \quad (18)$$

where the zero superscript has been dropped, and the bottom slope, of magnitude  $\delta L/H$ , is small  $\delta \sim \omega$ . The interior equation is

$$(\nabla_H^2\psi + (B^{-2}\psi_z)_z)_t + \left( \frac{L}{\omega R} \right) \psi_x = 0 \quad (19)$$

<sup>3</sup> In a case of particular interest, waves in homogeneous fluid on a thin spherical shell, care is required in applying equation 16. Though it is appropriate to discuss more gentle motions (as in Fig. 6c) in which fluid columns retain their integrity *parallel to the rotation axis*, such a model gives grossly incorrect results when used to develop a wave theory. This is because, on a sphere, the error in applying the Taylor-Proudman approximation is of order  $\omega H/L$  [whereas on a flat  $\beta$  plane the error is  $O(\omega H/L)^2$  only]. If, instead, the entire vector vorticity equation is expanded in  $\omega$ , rather than assuming away parts of it, the correct wave speeds result, and fluid columns retain their alignment with the *local* vertical. The solution agrees in the short-wave limit with the usual  $\beta$  plane formula. The mistake of assuming the Taylor-Proudman approximation to be exact seems to be common. Another illustration is the later interpretation of the wave pattern produced in experiments of Fultz and Frenzen (1955). When an obstacle was dragged westward about a latitude circle in the spherical shell, a distinct train of waves was produced that obeyed the planetary wave dispersion relation. When the obstacle was caused to move in the opposite (eastward) direction, no planetary waves should have been possible, yet there appeared a peculiar, periodic wave train with cusp-like particle paths. Though elaborate planetary solutions of equation 16 have been produced to explain the pattern, it is very likely that they were simply standing inertial oscillations (which have cycloidal particle paths). Once again, the *possibility* of  $\beta$  plane, Taylor-Proudman dynamics applying has spirited away the simpler  $f$  plane, nonhydrostatic flows from our minds. (The experiments are shown by Greenspan, 1968, p. 266.)

The problem is separable into vertical and horizontal parts. For uniform density stratification, plane-wave solutions are

$$\psi = e^{ikx + ly - \hat{\omega}t} \begin{Bmatrix} \cosh \mu z \\ \cos mz \end{Bmatrix}$$

already satisfying equation 17. Substituting into equations 18 and 19, we have

$$\hat{\omega} = \frac{-kL/R\omega}{k^2 + l^2 + B^{-2}m^2}$$

and

$$m \tan m = \frac{\delta R}{L} [(k^2 + l^2)B^2 + m^2] \quad (20)$$

or

$$\mu \tanh \mu = -\frac{\delta R}{L} [(k^2 + l^2)B^2 - \mu^2]$$

The solutions divide into those with vanishing vertical shear, those with oscillatory structure, and those which are evanescent in the vertical.

### Type 1. Fast Barotropic

For  $k^2 + l^2 \ll B^{-2}$  a solution with  $m^2 = O[(\delta R/L)(k^2 + l^2)B^2] \ll 1$  is (returning to dimensional variables)

$$\sigma = \frac{-k(\beta - f_0 \alpha/H)}{k^2 + l^2} = \frac{(\beta - f_0 \alpha/H) \cos \theta}{|\mathbf{k}|} \quad (21)$$

$$\beta = \frac{df}{d(\text{latitude})}, \quad \sigma = \hat{\omega} \omega f_0, \quad \alpha = \nabla h = \frac{\delta H}{L}$$

These familiar topographic Rossby waves involve only slight  $[O(\delta)]$  density perturbations, and are the same shearfree modes found on an unstratified  $\beta$  plane. Both the frequency and propagation speeds rise with wavelength, indefinitely in this model.

### Type 2. Fast Baroclinic

The above solution ceases to exist at scales as small as the Rossby radius,  $NH/f$ . There arises to replace it a wave confined within a layer of thickness  $fL/N$  above the sloping bottom. Its purest form has  $k^2 + l^2 \gg B^{-2}$  and  $\beta = 0$ . Then, in dimensional form, the dispersion relation is

$$\sigma = -N\alpha \sin \phi \quad (22)$$

where  $\phi$  is the angle of the wave vector  $(k, l)$  from  $Oy$ . The wave field, also in dimensional form, is

$$\psi = e^{i(kx + ly - \sigma t)} \cosh\left(\frac{zN}{f_0 L}\right)$$

This is a harmonic solution of  $\Delta\psi = 0$ , the rather passive form which equation 19 takes in the absence of  $\beta$ . The spatial scaling  $B \sim 1$  is ubiquitous to rotating, stratified fluids. The dispersion relation is that of a simple buoyancy oscillation. In common with other trapped solutions like Kelvin waves, it is independent of the very property,

$f$ , that causes its trapping. But this mode has a kind of dual nature. If we replace  $h$  in equation 21 by the penetration height,  $fL/N$  (with  $\beta = 0$ ), the dispersion relations 21 and 22 become the same. We may thus consider this to be a topographic Rossby wave, where density stratification provides a lid for vortex stretching.

### Type 3. Slow Baroclinic

At all scales, modes exist that are oscillatory in the vertical, in the presence of  $\beta$ . For small slopes (relative to  $H/R$ ,  $\sim 10^{-2}$ ) these obey equation 20  $\tan m \approx 0 \rightarrow m \approx n\pi$ , while for larger slopes,  $m \rightarrow (n + \frac{1}{2})\pi$ . The most quickly varying such wave (for  $\delta \rightarrow 0$ ),  $m = \pi$ , has a period of about 1 yr and horizontal scale  $L_\rho \sim 40$  km. At larger scales,  $|\mathbf{k}|^2 B \ll 1$ , the dispersion relation becomes

$$\begin{aligned} \hat{\omega} &= -\frac{kL/R\omega}{\pi^2 B^{-2}} \quad \left( \frac{\delta R}{L} \rightarrow 0, m \approx \pi \right) \\ &= \frac{4kL/R\omega}{B^{-2}\pi^2} \quad \left( \frac{\delta R}{L} \rightarrow \infty, m \approx \frac{\pi}{2} \right) \end{aligned}$$

This is the nondispersive, purely westward propagating mode derived in a simpler fashion in Section 4. The increase in frequency and propagation speed over a sloping bottom by a factor of four becomes somewhat less dramatic when realistic, nonuniform density stratification of the ocean is included.

The dispersion relation (Fig. 8) shows each of the three limiting types. Sketched on the figure is the corresponding vertical structure of the current. With realistic stratification, which is strongest in the upper ocean, the energy of type 3 waves is increasingly confined there. A fraction, roughly  $(L/L_\rho)^2$ , of the energy is potential. This normally exceeds unity in cases of interest, so it is appropriate to call these baroclinic motions "thermocline eddies."

The fast baroclinic waves (type 2) are, conversely, confined near the sloping bottom. Their inclusion here is of course schematic for those regions of ocean with complex topography. But it makes clear what was omitted from earlier wave models, that vertical shear (and density perturbations) with periods far shorter than 1 yr can exist under linear quasi-geostrophic dynamics.

How great must the bottom slope be for type 2 waves to occur? It turns out (Rhines, 1970, 1971a) that one may imagine there to be a competition for the highest frequency, among the basic planetary, topography, and buoyancy waves. The  $\beta$  effect alone provides a frequency  $\sim fL/R$ . Simple vortex stretching by the topography without stratification causes a frequency  $\sim f|\nabla h|L/H$ . Motion forced up a slope, disturbing the density field, suggests the frequency  $\sim N|\nabla h|$ . Predominance of bottom-trapped waves thus occurs if

$$\frac{NH}{fL} > 1 + \frac{H}{R|\nabla h|}$$

on the basis of scale analysis. If, therefore, the slope exceeds that equivalent to  $\beta$  ( $\sim 10^{-3}$ ), the type 2 wave may be expected at scales of order the Rossby internal radius,  $L_\rho \sim NH/f$ , and smaller. At slopes so large that  $\omega \gtrsim 1$  ageostrophic theory is required, yet the same, trapped buoyancy oscillation occurs.

The fast barotropic wave, type 1, is of course a  $\beta$  plane representation of the planetary wave on a sphere. In a forced problem, with wind blowing across the ocean surface, say, this mode is encountered alone at large frequency. The response, undiminished through the water column, is of crucial importance, and is one of the

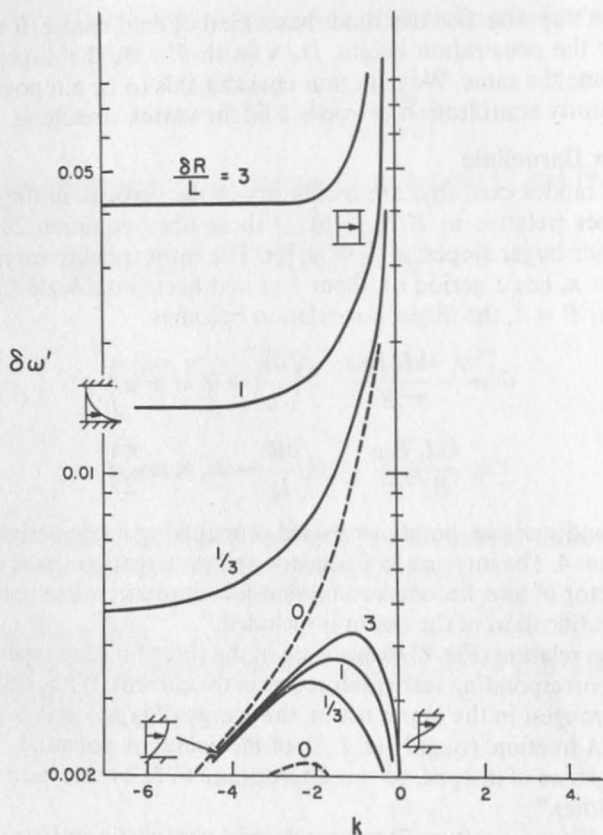


Fig. 8. Dispersion relation for linear topographic-Rossby waves ( $\beta$  plane, uniform upslope to the north), for several values of slope. Rossby waves,  $\delta = 0$ , are plotted with dashes. The sketches show the vertical structure. The three classes of structure are referred to as 1, 2, and 3 in the text.  $R = 6000$  km ( $43^\circ$  latitude), wave number normalized by  $NH/f = 120$  km.

striking predictions of linear theory, for “weatherlike” time scales over horizontal scales greater than  $L_\rho$ . Veronis and Stommel (1956) established the result for an ocean of constant depth, and it holds here with a sloping bottom, unless  $L \lesssim L_\rho$ .

Perspective views of the dispersion surface are shown in Figs. 9 and 10, and  $\delta > 0$  (upslope to the north). The double arrows give the direction and relative size of the horizontal group velocity,  $\omega f L (\partial \hat{\omega} / \partial \mathbf{k})$ . The transition from classical type 1 waves to bottom-trapped type 2 waves carries one from a situation in which the group velocity can point in any direction (yet the phase velocity always has a westward component) to one in which both group and phase velocities must have a westward component. For arbitrary orientation of the depth gradient, type 2 waves tend to move energy and phase to the left facing shallow water, while type 1 is a topographic Rossby wave, relative to a “pseudo-westward” direction along  $f/h$  contours, and type 3 tends still to favor actual westward propagation. The larger group velocities occur near the origin of Fig. 9, and these have a westward component. Conversely, those components, generated by a point excitation, say, which do radiate eastward have large amplitude, if anything like equal energy flux occurs with respect to direction.

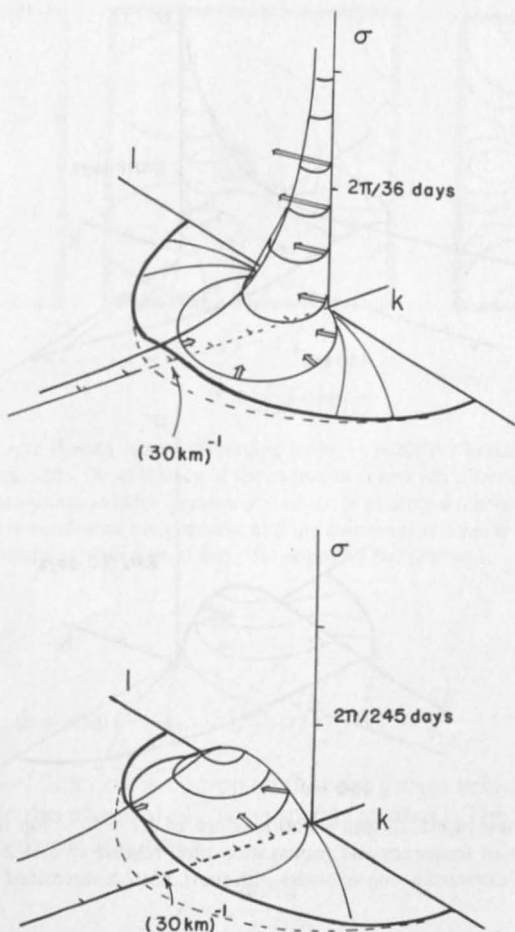


Fig. 9. Perspective view of dispersion surface,  $\sigma(k, l)$  (constant depth). Equal- $\sigma$  curves are shown. Double arrows indicate direction and (schematically) magnitude of group velocity. Upper portion is the barotropic mode, lower portion the baroclinic. Note different frequency scales.  $N/f$  is uniform, = 30.

Another immediate consequence of the linear theory is that thermocline eddies (type 3), already very slowly propagating, will be doubly inefficient at carrying energy north or south from a source. The greatest north-south component of group velocity is  $0.23\beta c_0^2/f_0^2$  (for  $\delta = 0$ ), whereas the westward velocity approaches  $\beta c_0^2/f_0^2$  in the entire set of long waves. For oceanic conditions these velocities are roughly 0.9 cm/sec and 3 cm/sec, respectively

Lighthill (1967, 1969) has emphasized the application of wave theory in the limit of vanishing frequency to the development of forced, steady flows. For instance, the Taylor column in a simple rotating fluid may be visualized as a region of influence of inertial waves of small frequency. In that limit the group velocity remains large ( $\sim f_0 L$ , where  $L$  is the horizontal scale of the "source") and acts to resolve a degenerate flow without the immediate need of invoking viscosity. Here the degenerate, free flows are those along geostrophic contours (for barotropic flow) or zonally (for large-scale baroclinic flow), or along depth contours (for small-scale deep baroclinic flow).

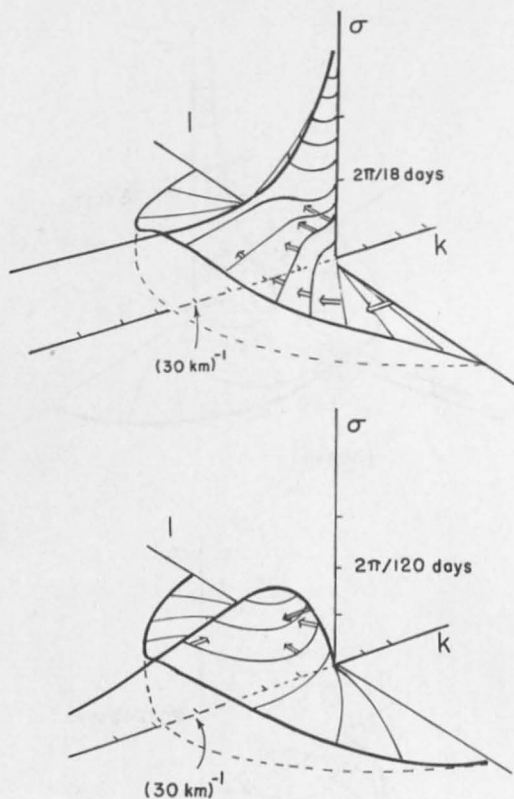


Fig. 10. Perspective view of  $\sigma(k, l)$ , with a bottom slope of  $1.7 \times 10^{-3}$  (up to the north). ( $\delta R/L = 2$ ). Both types have increased frequency and propagation rate, relative to  $\delta = 0$ . The constant-frequency loci show an absence of eastward group velocities with short, bottom-intensified waves.

Types 1, 3, and 2 show that the signal from a slowly oscillating forcing function propagates westward or pseudo-westward at rates  $(\beta + \alpha f_0)L^2$ ,  $\beta L_\rho^2$ , and  $N|\nabla H|/L$ , respectively, and in doing so carries with it the developing flow. This justifies the classical procedure of calculating Sverdrup flow by zeroing the disturbance to the east of the wind stress (Lighthill, 1967).

### C. Initial-Value Problems

The wave pattern (Fig. 11) arising from the dispersion of an initial Gaussian vortex shows some of these tendencies. There is no bottom slope, and the currents are infinitesimal and entirely barotropic. This computer realization shows the characteristic penetration of east-west crested waves due westward from the origin, while slower, shorter, stronger north-south crested waves appear east of the origin. The general picture agrees with far-field ray theory, and with the Green's function for a steadily oscillating delta-function source,<sup>4</sup>

$$\nabla^2 \psi_t + \beta \psi_x = \delta(\mathbf{x}) \exp(-i\omega_0 t)$$

<sup>4</sup> This canonical problem is slightly misleading, in that the right side is not the result of purely local forces; the stress,  $\tau$ , itself obeys  $\oint \tau \cdot d\mathbf{l} = 1$  about any circuit enclosing the origin. The difference in wave pattern between this and local forcing is probably small, but the difference in amplitude structure may not be.

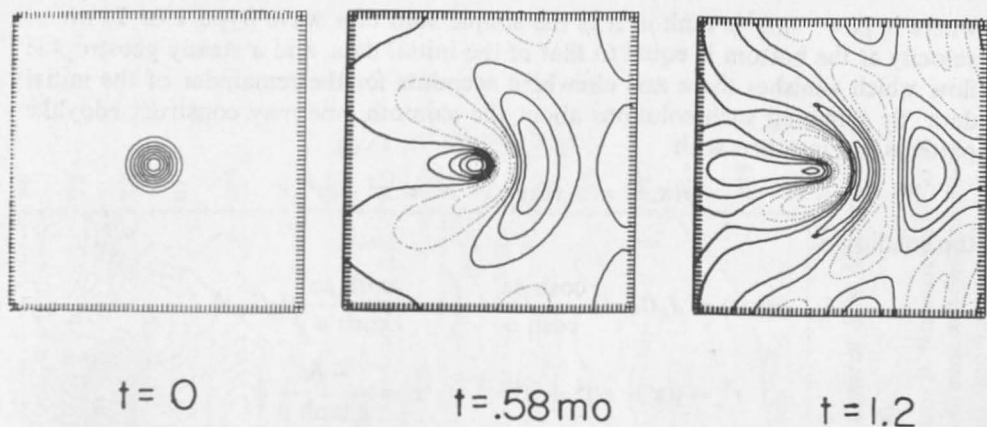


Fig. 11. Linear, barotropic Rossby waves dispersing from an initially Gaussian current pattern; for more than infinitesimal currents, the efficiency of the radiation is severely altered. In this and later computer simulations the contours are solid for *negative*  $\psi$ , dashed for positive  $\psi$  (choosing  $\psi$  to be proportional to pressure). The boundary conditions are periodic, and the numerical scheme is the spectral code (cutoff wave number 32, corresponding to  $64^2$  spatial map) developed by Dr. Orszag.

which is known to be

$$\psi = \exp(-ik_3 x) H_0^{(2)}(k_3 r) \quad k_3 \equiv \frac{\beta}{2\omega_0}$$

This particular Hankel function is chosen so that the group velocity points outward at large radius [while the phase of  $H_0^{(2)}(k_3 r)$  spirals inward]. The wave crests, in the stationary phase approximation, obey

$$r = \frac{\text{const}}{\cos^2(\frac{1}{2}\theta)}$$

( $r, \theta$ ) being polar coordinates relative to the origin. Longuet-Higgins and Gill (1966) have given the response to a space-time delta function of stress-curl, which also resembles these patterns.

Considering now the stratified case, the wave modes derived here, together with free geostrophic flow, completely describe linearized motions which develop from given currents and density. This is true provided that the initial data is itself sufficiently close to a state of geostrophy. The appearance of the frequency in the lower boundary condition renders the set of equations 20 nonorthogonal, but this may be circumvented as in the problem of a vibrating string with a nonrigid support (Morse and Feshbach, 1953, p. 1343).

To illustrate the role of the bottom-trapped type 2 we consider (with  $\beta = 0$ ) an initial current of arbitrary vertical structure, but limited to a single horizontal Fourier component,

$$\psi(\mathbf{x}, 0) = e^{i(kx + ly)} F(z)$$

The solution to equations 15, 17, and 18, derived by Suarez (1971), is

$$\psi = e^{i(kx + ly)} \left[ (e^{-i\sigma t} - 1) \frac{\cosh \mu z}{\cosh \mu} F(-1) + F(z) \right]$$

where  $\sigma/f_0 = -kB^2/\mu \tanh \mu$ . It is the simple sum of a wave (type 1 or 2) whose velocity at the bottom is equal to that of the initial data, and a steady geostrophic flow which vanishes there and elsewhere accounts for the remainder of the initial data. By summing such solutions about the azimuth, one may construct eddylike patterns; for instance, with

$$\psi(\mathbf{x}, 0) = J_0(k_0 r) \quad r^2 = x^2 + y^2$$

the solution is

$$\psi(\mathbf{x}, t) = J_0(k_0 r^1) \frac{\cosh \mu z}{\cosh \mu} + \left(1 - \frac{\cosh \mu z}{\cosh \mu}\right) J_0(k_0 r)$$

$$r^1 = ((x - ct)^2 + y^2)^{1/2} \quad c = \frac{-B^2}{\mu \tanh \mu}$$

This represents a steady circular flow at the origin, which decreases toward the bottom, as a bottom-trapped circular pattern creeps out from beneath it, along the depth contours to the "left." The difficulty with such solutions is that they are not truly local, and rely on inward radiation from infinity to defeat the natural dispersive nature of the waves.

The role of a weak  $\beta$  effect would be to cause the "steady" component to propagate itself, as a type 3 wave. Howard and Siegmann (1969) have discussed in general terms the possible steady geostrophic flows in such cases.

#### D. Observations

The observations made in the introduction fixed the gross time and length scales of the energy-containing eddies, both deep and shallow. We are rapidly obtaining refined measurements to improve upon this picture, which bring observations and theory somewhat closer together.

##### Type 1. Fast Barotropic

The Mid-Ocean Dynamics Experiment (MODE-I) covered a  $(200 \text{ km})^2$  region centered on  $28^\circ\text{N}$ ,  $69^\circ 40'\text{W}$ , in the Sargasso Sea, Spring 1973. Rossby and Webb's neutrally buoyant SOFAR floats drifted with the currents at 1500 m. Characteristics of the floats were unusual accuracy (roughly 1 km absolute,  $< \frac{1}{2}$  km relative position fixing) and longevity (the observations in this area began in September 1972 and continue at the time of this writing, May 1975).

There were often more than 10 floats present in the area, and they allowed rather accurate, objective stream function maps to be produced (in real time by Bretherton, and subsequently by Freeland and Gould). Figure 12a from Freeland, Rhines, and Rossby (1975), is an  $x-t$  plot of the stream function at  $28^\circ\text{N}$ ; Fig. 12b is a  $y-t$  plot taken along  $70^\circ\text{W}$ . There appears a persistent tendency for phase lines to move westward with time, but no striking north-south propagation. Thus the nearly ubiquitous property of westward phase propagation, found in the linear theory of Rossby waves, actually appears in currents below the main thermocline.

The phase speed ranges from 2 to 12 cm/sec in the figure, averaging about 5 cm/sec. This slightly exceeds the rms current speed, which is 4 cm/sec in the region, and far exceeds the mean flow. The horizontal length scale is also visible; the transverse spatial correlation function first crosses zero at 50 km. For linear theory, flat-bottom waves (equation 21) have a westward phase speed equal to  $\beta/|\mathbf{k}|^2$ . The estimate

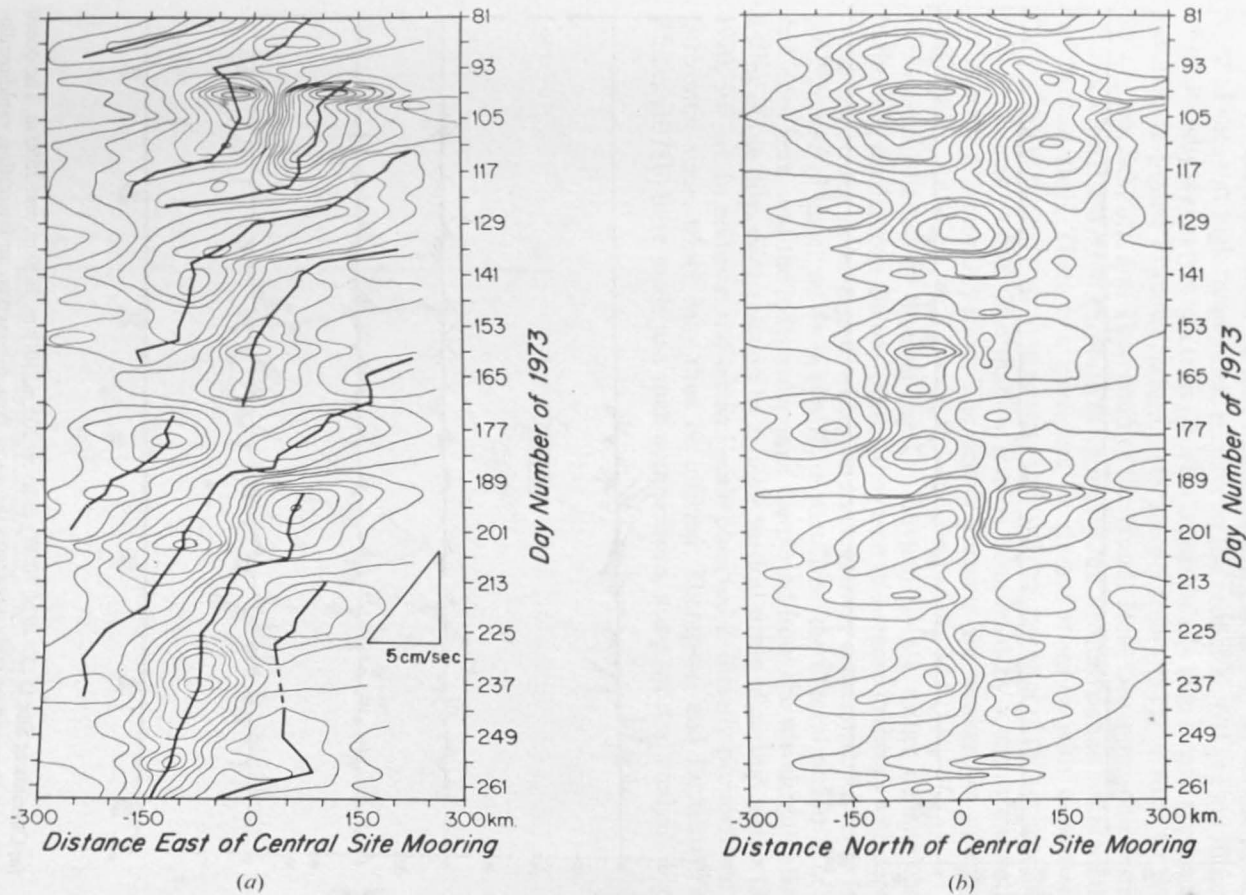
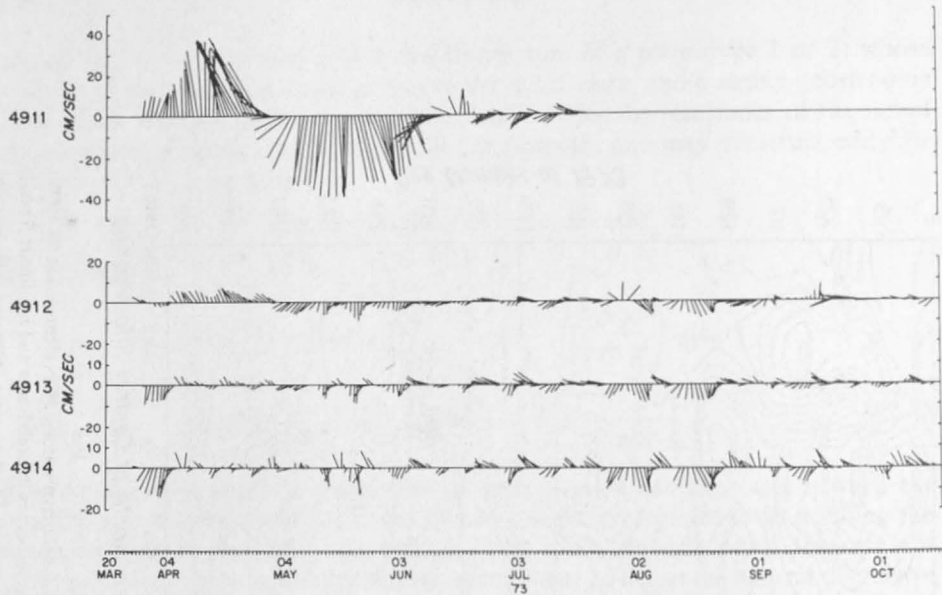
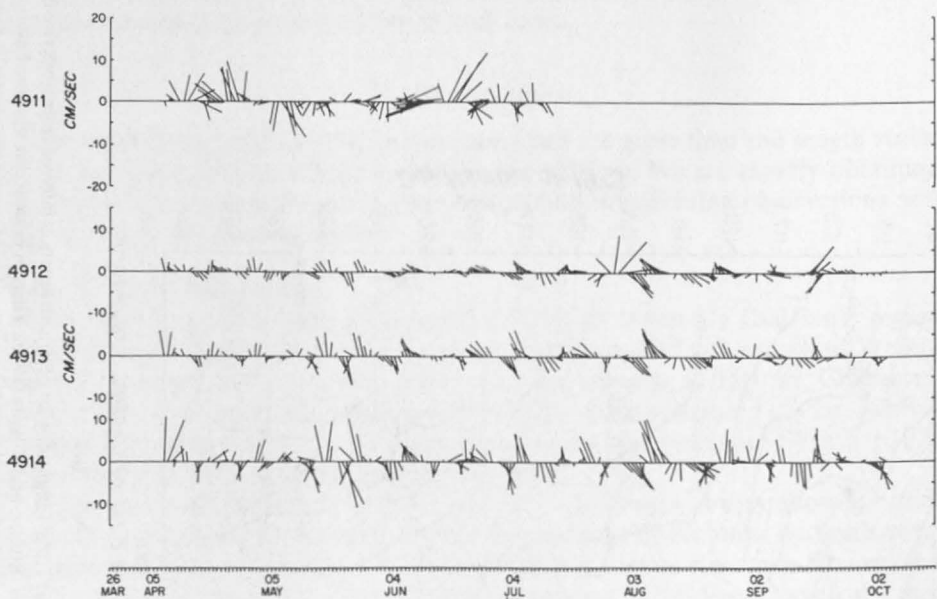


Fig. 12. (a) Time-longitude plot of stream function inferred from objective maps of 1500-m currents along  $28^{\circ}\text{N}$  (centered at  $69^{\circ}40'\text{W}$ ), by Freeland, Rhines, and Rossby (1975). There is evidence of westward motion of phase, as occurs in both linear and nonlinear  $\beta$  plane theory (compare Fig. 20b). The large-scale  $f/h$  contours in the region lie roughly east and west. The data came from neutrally buoyant SOFAR floats (Figs. 64-66). The currents at this depth are not dominated by thermocline eddies, but are more representative of the deep ocean. (b) As in (a), but time-latitude plot along  $69^{\circ}40'\text{W}$ .



(a)



(b)

Fig. 13. (a) Currents at Site D ( $39^{\circ}10'N$ ,  $70^{\circ}W$ ), at levels 205 m, 1019 m, 2030 m, and 2550 m. The ocean depth is 2650 m. A thermocline eddy dominates the upper flow, followed by an interesting, rapid oscillation. (b) High-pass filtered version of (a). The deep westward mean flow and upper-level thermocline eddy are thus removed. The deeper layers are dominated by fast oscillations with episodes of clear bottom intensification and polarization ( $\overline{w} < 0$ ).

5 cm/sec implies a rational scale,  $|k|^{-1}$ , of 50 km. More is said about these exceptional measurements below.

## Type 2. Fast Baroclinic

Cursory examination of current meter records frequently shows the existence of vertical shear at high frequencies, relative to the predicted,  $O(1 \text{ yr})$ , cutoff for baroclinic Rossby waves (yet less than  $f_0$ ). This is particularly true as one approaches the ocean floor. Figure 13 shows current meter records from site D ( $39^\circ 10' \text{N}$ ,  $70^\circ \text{W}$ ) taken by Luyten, Schmitz, and Thompson of the Woods Hole Oceanographic Institution. The location is some 100 km north of the mean Gulf Stream axis and 50 km south of the continental shelf. There is a persistent northward shoaling with slope  $8 \times 10^{-3}$ . First, observe the agreement in general terms of the character of the vertical structure with the linear picture. The shallow level is dominated by a strong current which varies with a 3-month period. The deeper currents are weaker, yet more quickly varying.

High-pass frequency filtering (by Dr. Luyten) gives a rather definite character to the deep oscillations. Below 1000 m, they tend to increase in energy with depth, and develop a strong polarization, with  $u$  and  $v$  negatively correlated. All these features are expected of linear waves of type 2; in particular, the natural period  $\geq 2\pi/N|Vh| \approx 6$  days here, and the independence of the period from the wavelength allows the testing of the dispersion relation by a *single* vertical string of current meters (Rhines, 1970, 1971a). In addition the vertical scale observed is directly proportional to the horizontal scale, which may thus be inferred. Thompson and Luyten (1976) and Rhines (1971b) have made just such comparisons, using spectral analysis. Figure 14

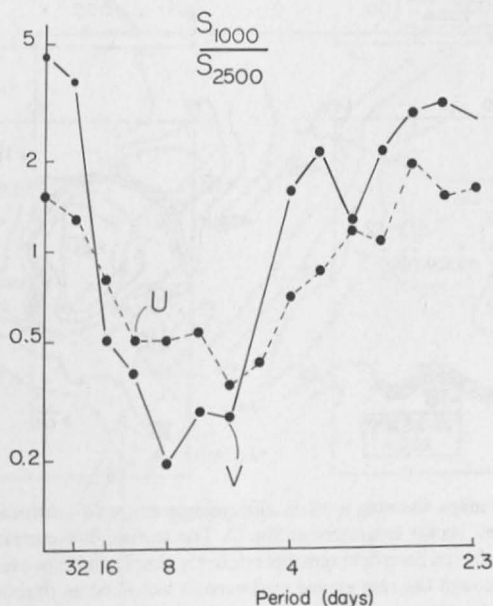


Fig. 14. Ratio of kinetic energy spectra between 1000 m and 2500' m at Site D versus frequency, from Thompson and Luyten (1976). The records occupied 10 months in 1972. Both  $u$  and  $v$  spectra are shown. Most of the energy in the  $v$  spectrum lies between 8 and 20 days. Energy in a significant band is bottom-intensified. The wavelength inferred from linear theory ranges from 90 to 160 km.

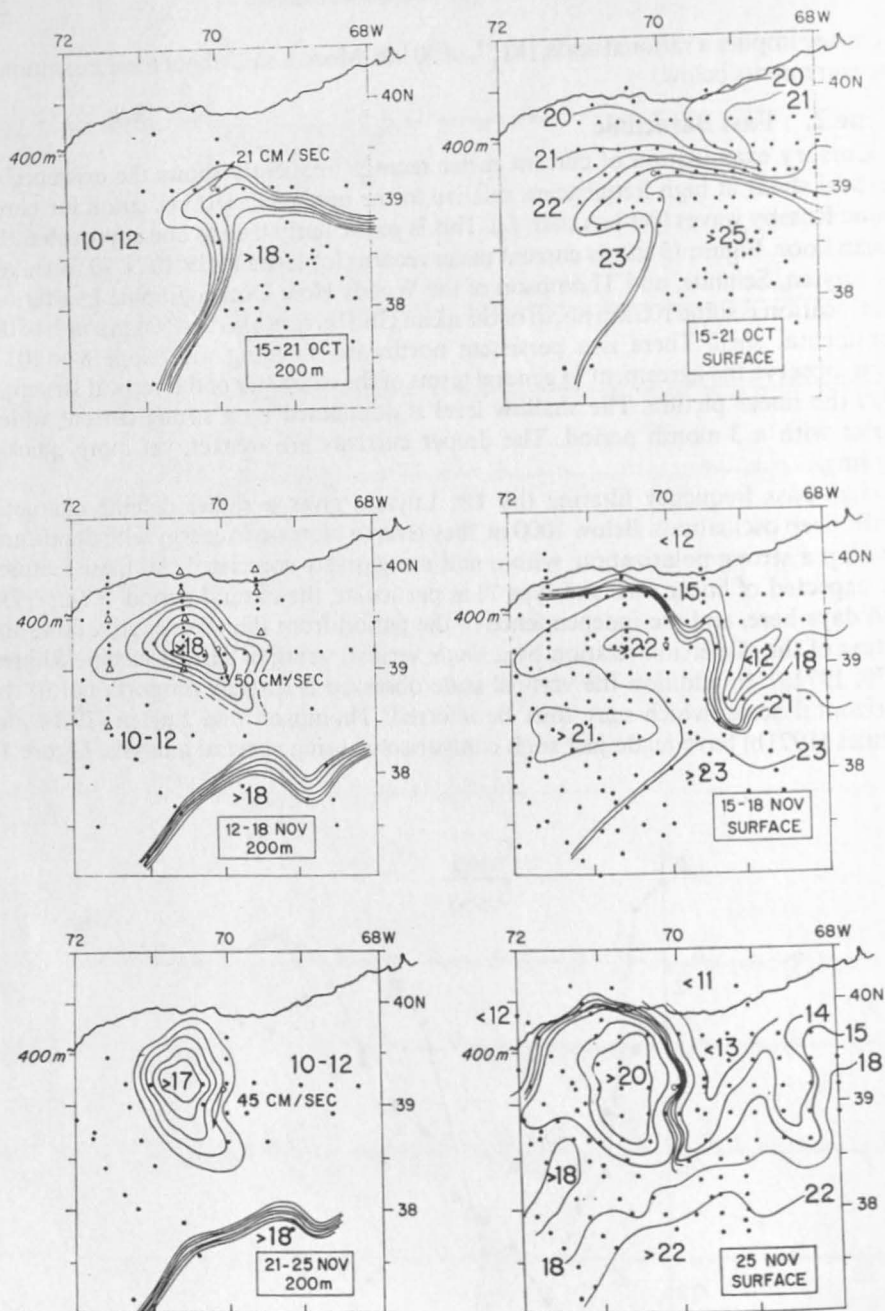


Fig. 15. Temperature ( $^{\circ}\text{C}$ ) maps showing a warm anticyclonic ring cast northward by the Gulf Stream (Saunders, 1971). The current vector originates at Site D. The surface flow entrains cold water from the shallow continental shelf while the deep field remains relatively simple. Such an event probably caused the 200-m flow in Fig. 13a. Although the ring moved westward, it would be an oversimplification to characterize it as a baroclinic Rossby wave.

shows how, in an intermediate band of frequencies, the spectral energy increases downward, as predicted.

What is particularly exciting is not only that the "waves" exist with apparently correct local behavior, but that their  $\bar{u}\bar{v}$  polarization implies group velocity with a component to the north. Thompson (1971) recognized that the nearby Gulf Stream was a likely source, and that this polarization would be expected with type 1 Rossby waves. Fortunately, the same behavior arises with type 2 waves; there is probably enough breadth to the distribution of scales that a range encompassing types 1 and 2 waves occurs.

### Type 3. Slow Baroclinic

These current data are a good example of the many levels of understanding that apply to ocean observations. Some features of the deep flow agree with type 1 Rossby wave theory, yet the addition of type 2 waves fills out the picture. The strong current at the upper level might be interpreted as a type 3 baroclinic Rossby wave, yet in fact it has the signature of cutoff Gulf Stream eddies. An event very like this one was documented by Saunders (1971), Fig. 15 (see also Fig. 57). That particular eddy in fact moved westward, at roughly the speed of the climatological mean flow, and rejoined the Stream. With this mixture of advection and propagation present, it would be unwise to say that type 3 waves had been seen, so for better evidence we turn to the open ocean, far from intense currents. The POLYGON group (Brekhovskikh, Federov, Fomin, Koshlyakov, and Yampolsky, 1971), Bernstein and White (1975), and the MODE group have each witnessed the slow westward movement of thermocline eddies. The MODE observations are summed up in Fig. 16, and  $x-t$

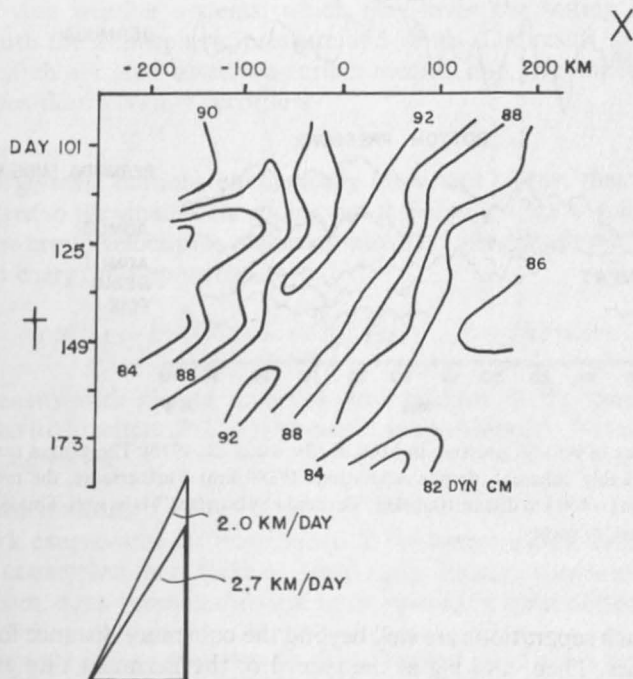


Fig. 16. Time-longitude diagram of dynamic height (501-1500 dbar) along  $28^{\circ}\text{N}$ , from the Mid-Ocean Dynamics Experiment. There is increasing evidence of such westward phase propagation in thermocline eddies, at a rate comparable with the linear speed (see also Fig. 41); note that this is significantly slower than the observed phase motion in 1500-m currents (Fig. 12a).

diagram, again along  $28^{\circ}\text{N}$ , of the dynamic height anomaly across the main thermocline. This measure of the density field shows a clear westward movement at a rate 2 cm/sec. It is less likely than Gulf Stream eddies to have involved net westward movement of the water, although this is not yet certain. In fact, it is the very slowness of the propagation of thermocline eddies that makes it hard to resolve the mean flow (for one must average over many eddy periods).

### Type 1. Fast Barotropic (Ultralong)

It is shown in Section 6 that the use of linear theory is marginal, at best, in studying the above observations. But a "benthic" group in MODE-I provided observations of sea-floor pressure that are much more likely to relate to linear waves. It was discovered that the pressure records were surprisingly coherent ( $>0.95$ ) over 200-km separations in the MODE region (Fig. 17; Brown, Munk, Snodgrass, Mofjeld, and

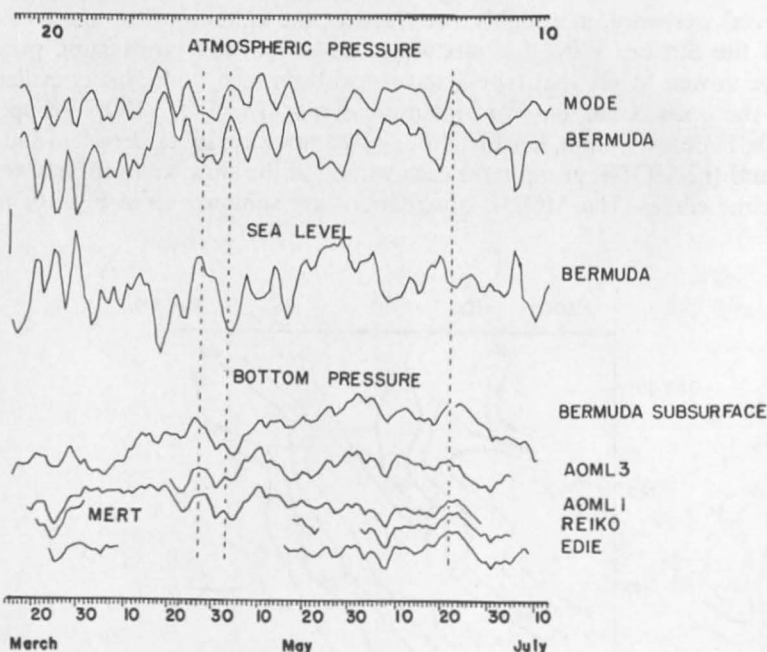


Fig. 17. Time series of bottom pressure in MODE (Brown et al., 1975). The gauges centered on  $28^{\circ}\text{N}$ ,  $69^{\circ}40'\text{W}$  are remarkably coherent, despite separations  $O(180\text{ km})$ . Furthermore, the pressure-corrected sea level at Bermuda ( $\sim 650\text{ km}$  distant) (labeled "Bermuda Subsurface") is as well. This is strong evidence for fast, type 1 planetary waves.

Zetler, 1975). Such separations are well beyond the coherence distance for the energy-containing eddies. Then, looking at the record of the Bermuda tide gauge 700 km away, they found that it too was remarkably coherent ( $\geq 0.8$ , once the inverted barometer effect of atmospheric pressure had been subtracted). This established that the pressure just below the sea surface is coherent both vertically with the sea floor, and also horizontal, over 700 km.

It may be the first observation of "ultralong" planetary waves, of the kind anticipated many decades ago.<sup>5</sup> To see whether the observed large scale is indeed consistent with wave theory, we converted the observed  $P(\sigma)$  frequency spectrum to a wave number spectrum, assuming a model dominated by a single orientation (say,  $k = l$ ). Let

$$\hat{P}(k) = \frac{P(\sigma) d\sigma}{dk}$$

where  $\sigma = -\beta/2k$ ,  $d\sigma/dk = -\beta/2k^2$ . Although the frequency spectrum is "red," increasing toward small frequency, the estimated wave number spectrum is flatter, with a central peak at  $k \sim 2\pi/7000$  km. The large scale is sufficient to explain the highly coherent records, with phase lag of less than a day. This is particularly so because it gives only a rough upper bound to the phase lag. The sense of the lag, though marginally determined, seems to have Bermuda leading, suggesting westward propagation. The atmospheric pressure patterns, conversely, move eastward across the region. The inferred energy spectrum [ $\propto k^2 P(k)$ ] is very "blue" and suggests that, indeed, the kinetic energy in the deep-ocean peaks near the 50–100 km (rational) scale.

This example verifies the almost inescapable result, discussed in Section 3, that pressure gauges see longer scales than current meters, but we could not have anticipated how great the difference would be. The observed association of higher frequencies dominantly with large scales gives support to the planetary "inverse" dispersion relation,  $\omega \propto k^{-1}$ , for ultralong waves as against the turbulent relation  $\omega \propto Uk$ , described in Section 3. The periods and scales of these waves are closer to the scales of moving weather systems, which may favor the setting up of planetary seiches by both the atmospheric pressure and winds. The result should motivate a systematic search of island-based sea-surface records, and give impetus to the refinement of the sea-floor pressure recorders.

### Energy Flux

Are the large-scale motions energetically important? True, their energy density is slight relative to the small-scale eddies, but their energy flux is in fact much larger. Given that the group velocity for planetary waves has magnitude  $\sigma/k = -\beta/|k|^2$ , one can define an energy flux spectrum,

$$\mathcal{F}(k) = \beta k^{-2} \mathcal{E}(k) = \frac{\beta}{\rho_0 f^2} \hat{P}(k) \quad (k = |\mathbf{k}| \text{ here}),$$

giving the density with respect to scalar wave number of the kinetic energy flux, without regard to direction.  $\mathcal{F}(k)$  is thus simply proportional to  $\hat{P}(k)$  and is dominated by the ultralong waves.

### Scale Transformations

This remark exaggerates the importance of the longer waves, unless mechanisms exist for the conversion from large to small scale. Bottom roughness provides one such mechanism, but a simpler, classical feature works in a flat bottom, linear ocean.

<sup>5</sup> Thus the Bermuda tide gauge has helped in establishing both type 1 waves, and at longer periods type 3 waves, in collaboration with the *Panulirus* stations. In either case there is significant concern over such use of island stations, for local island dynamics could conceivably have dominated the sea-level records. Happily, this result shows that the higher-frequency components are indeed of large scale. This was predicted by Rhines (1969) for the linear theory, but he gave no reasons why nonlinear, unsteady "island wakes" might not add significant noise.

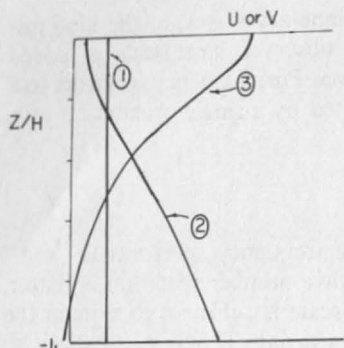


Fig. 18. Typical vertical structure of the linear waves, types 1, 2, and 3 for exponential stratification  $N \propto \exp(2z/H)$ .

This is the striking fact (Pedlosky, 1965; Phillips, 1966) that the reflection laws for Rossby waves cause fast, long, weak, westward-propagating waves to reflect at a western boundary into slow, short, strong, eastward-propagating waves. It can be verified, in Fig. 9, by finding two waves of the same frequency and north-south wave number. The ratio of  $|k|$  of the reflected wave to that of the incident wave exceeds unity and the ratio of energy densities is the square of this ratio. Any reasonable model of the dissipation then leaves the western region filled with energetic eddies fed by a nearly invisible, ocean wide source. This occurred clearly in the laboratory (Phillips and Ibbetson, 1967). We return to the topic in Section 7.

### Synthesis

Using linear building blocks we can produce current and density fields that contain a number of observed features. McWilliams and Flierl (1975) gave done so, to produce an optimal linear description of the fields in MODE-I. It should already be clear that the decrease in characteristic time scale with depth and the great decrease in kinetic energy with depth, followed by a gradual increase, are consistent with a superposition of wave types 1, 2, and 3, such that type 3 dominates the flow above the thermocline, type 1 the flow at mid-depth, and type 2 the flow in the lowest kilometer. Figure 18 shows this schematically, using an exponential stratification and a bottom slope of  $8 \times 10^{-3}$ . The thermocline eddies are disposed this way by the concentration of the density gradients in the upper ocean. Away from the western regions of the oceans, particularly, where the  $18^\circ$  water provides a deep thermocline, the type 3 waves would be strongly confined near to the ocean surface, where they could intermingle with the directly driven wind-mixed layer.

The picture may be refined by allowing the modes to interact weakly, and by including a large-scale mean current. But this might deflect us from the central issue: the thermocline eddies, even in a quiet part of the ocean like the MODE area, are sufficiently strong to blow the tops off barotropic waves, trying to propagate through them. This is the subject of the next section.

## 6. Nonlinear Waves and Turbulence: Primary Cascades

A classical ocean filled with linear waves would present us with a problem in spectral discrimination and synthesis. All that would remain would be the identification of sources and sinks. The basic gradient of mean potential vorticity dominates in that case, and provides a smooth restoring force. Based on typical mid-ocean

conditions, however, none of the three principal wave types has a steepness that is small. Take an upper ocean velocity of 10 km/day and deep-ocean velocity of 4 km/day; the particle excursion during a wave period  $\div 2\pi$ , or ratio of particle speed to theoretical phase speed,  $\hat{\epsilon} \equiv \epsilon/\omega$ , is,

$$\hat{\epsilon}_1 = \frac{2Uk^2}{\beta} = 2 \quad (\text{deep-ocean } U, k = k_\rho \equiv 1/45 \text{ km})$$

$$= 5 \quad (\text{shallow } U, k = k_\rho)$$

$$\hat{\epsilon}_2 = \frac{2Uk}{N\alpha} = 0.8 \quad (N = 2.6 \times 10^{-3}, \alpha = 5 \times 10^{-3}, k = 1/15 \text{ km})$$

$$\hat{\epsilon}_3 = \frac{3Uk_\rho^2}{\beta} = 7$$

for the barotropic, fast baroclinic, and slow baroclinic types, respectively. The numerical factors allow the criteria to apply to the average wave speed, rather than an extreme value. Although special solutions can be found whose nonlinear advection is far smaller than these numbers suggested, the interactions between different Fourier components must, on the average, be strong, particularly in regions of more vigorous currents than these. Such a situation is remarkable, when it is remembered that for deep-ocean velocities any less than these, the current-meter rotors would be stalled a significant fraction of the time. However, all the forces acting to accelerate the fluid are weak and a state of horizontal turbulence is readily reached. A persuasive picture of the wave steepness (Fig. 64) is the ensemble of tracks of the SOFAR float experiment in MODE, Rossby, Voorhis, and Webb (1975). Even at 1500 m, the slowest level in the ocean, the tracks show particles not to be confined near latitude lines, but chaotically traveling distances far greater than the dominant length scale, say 50 km, of the flow.

### A. The Diagram

Figure 19 shows schematically the nonlinear cascades that occur in a flat-bottom ocean. We have plotted turbulent states on this dispersion diagram by endowing turbulent fluid of dominant wave number  $k$  and rms particle speed  $U$  with a frequency  $kU$ . There is some reality in this, (Section 3), as a crude representation of the concentrated frequency-wave number spectrum. The vertical axis is a crude two-point representation of the vertical wave number. Thus baroclinic modes appear on the upper plane, barotropic modes on the lower plane. For linear waves,  $U < \omega(k)/k$ , the exact dispersion relation  $\omega(k)$  applies instead. This delineates the wave regime to the left of the solid curves. As suggested by the shortness of trajectory  $a$ , interactions in the linear region are slow. A cursory look at the other trajectories shows a general movement toward the deformation radius on the baroclinic plane, downward to the barotropic plane, and then to the left. Taken literally it would say that in a freely evolving ocean vertical shear would disappear, and the horizontal size of eddies would at first approach the deformation radius, and then increase. We first describe the individual elements of this statement, and then in the succeeding section modify it to account for the real, rough-bottom ocean.

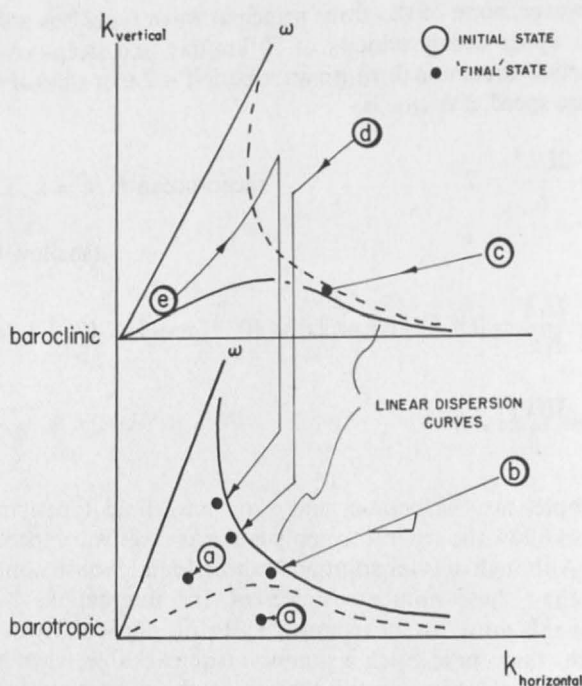


Fig. 19. Schematic representation of freely evolving, nonlinear eddy fields in a flat-bottom ocean. Turbulent states are plotted on this  $\omega, k$  diagram by ascribing to them a frequency  $kU$ , where  $k$  is the centroid of the energy spectrum, and  $U$  the rms particle speed. The position of these states relative to the linear dispersion relations (below solid curves) is crucial. Energy-preserving changes of scale occur, within baroclinic eddies, toward the deformation radius from either side. This same scale is an aperture through which energy passes, downward from baroclinic to barotropic states, followed by cascade to small wave number. Wherever energy meets a dispersion region it tends to stagnate.

### B. Barotropic Cascade, Path b

The behavior on the lower plane is just the same as if the ocean were unstratified; under the Boussinesq approximation, arbitrary barotropic motion itself satisfies the equations. This case is described in detail by Rhines (1973, 1975). The essential result (Batchelor, 1953) follows from the integral constraints on total energy and squared relative vorticity, or enstrophy, in purely two-dimensional flow:

$$\begin{aligned} \frac{\partial}{\partial \tau} \int_0^{\infty} \mathcal{E} dk &= -2\nu \int k^2 \mathcal{E} dk - 2R \int \mathcal{E} dk < 0 \\ \frac{\partial}{\partial \tau} \int_0^{\infty} k^2 \mathcal{E} dk &= -2\nu \int k^4 \mathcal{E} dk - 2R \int k^2 \mathcal{E} dk \end{aligned} \quad (23)$$

There is no forcing and an Ekman drag,  $R\mathbf{u}$ , acts at the base of the fluid. As in Section 3, the domain is taken to be periodic, of very large size, and Fourier coefficients are blurred into a continuous function. If initial values  $\psi_0(\mathbf{x})$  are specified and then allowed to evolve freely, both right sides are negative. For a finite initial scale of motion they both vanish with  $R, \nu$  (for all finite time), leaving  $(\partial/\partial t) \int \mathcal{E} dk = 0, (\partial/\partial t) \int k^2 \mathcal{E} dk = 0$ .

The argument proceeds by assuming that an initially narrow spectrum spreads in time, about its mean wave number,

$$\frac{\partial}{\partial \tau} \int (k - k_1)^2 \mathcal{E} dk > 0$$

where  $k_1 = \int k \mathcal{E} dk / \int \mathcal{E} dk$ . It follows immediately that

$$\frac{\partial k_1}{\partial t} < 0 \quad (24)$$

This "red" cascade toward small wave numbers may be appreciated by imagining possible redistributions of a "mass"  $\mathcal{E}(k)$  along the  $k$  axis, such as to conserve the moment of inertia of  $\mathcal{E}$  about  $k = 0$ . If a unit amount of  $\mathcal{E}$  is taken from a narrow peak at  $k = k_0$  to twice  $k_0$ , then the equivalent of *four* units of  $\mathcal{E}$  must move to  $\frac{1}{2}k_0$  to compensate. Given an initially narrow concentration, no more than one fourth of the total energy can move to  $2k_0$ , for the entire remainder must then move to  $k = 0$  to preserve the second moment.

The transfer of energy out of small eddies into larger ones, when 3D vortex stretching is suppressed, is a feature having links with many kinds of fluid flows. The transfer from cyclones to the zonal-average winds in the atmosphere may be considered a special case, and in terms of westerly momentum, appears as a negative eddy viscosity (Starr, 1968). The corresponding spectral transfer function  $T_{\psi}(k)$  shows the nonlinear contribution to  $\partial \mathcal{E}(k)/\partial t$  at each wave number; more complex flows with stratification and topography continue to have a "red"  $T_{\psi}(k)$  (Figs. 31, 38), but the velocity components normal to isopleths of density and topography yield competing transfer spectra, that may reverse this trend.

The absence of vortex-stretching in two dimensions (2D) prevents high-Reynolds number turbulence from dissipating energy at all efficiently. Whereas the  $e$ -folding time for energy decay in 3D is approximately  $L/U$  regardless of how fine the dissipation scale, here a viscous time of order  $(\nu/L^2 + R)^{-1}$  is required. The presence of strong eddy motions cannot, therefore, be taken as an indication that dissipation is occurring, in the gross sense encountered, for instance, in a laboratory jet.

Enstrophy,  $k^2 \mathcal{E}$ , on the other hand, must in the mean be carried to small scale to balance the expansion in size of the dominant eddies. The notion that an inertial subrange will form at large wave number, to carry enstrophy, dominates the literature (e.g., Kraichnan, 1967). However, the similarity of this process to the energy-carrying Kolmogorov inertial range of 3D turbulence breaks down when rates are considered: 3D energy can apparently reach infinitesimal scale during a single revolution of an eddy ( $\sim L/U$ ). Yet the time required for 2D enstrophy to do so is logarithmically infinite, as the Reynolds number increases without bound. This is because the time for enstrophy to double its characteristic wave number is of order  $(\int_0^k k^2 \mathcal{E} dk)^{-1/2}$ , which is strictly bounded in two dimensions. A high-Reynolds number, 2D fluid is thus inviscid for all finite time, given energy initially at finite scale. The fact that the effective Reynolds number *is* large is plausible once one views the wealth of fine structure in, say, sea-surface temperature photographs. In spite of blurring of temperature gradients by exchange with the atmosphere, strong contrasts persist down to a scale of 1 km and less. Clearly there is a wide gap between the energy-containing scale, say,  $k_1^{-1}$ , and the scale of significant thermal dissipation. Less is known about the velocity fine structure, but current records on fixed moorings, low-passed to remove internal waves, do show frequent rapid accelerations as if a corresponding jaggedness in the velocity distribution were present.

The removal of viscosity from the dominant dynamics at large Reynolds number suggested to Batchelor (1969) a similarity solution for the time evolution of the energy-containing eddies. If details of the initial conditions are eventually forgotten in the evolution the only external parameter is the rms particle speed,  $U$ . This suggests a shape-preserving solution,

$$\mathcal{E}(k, t) = \frac{1}{2}U^3 t g(Ukt) \quad (25)$$

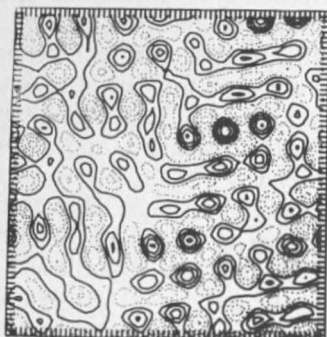
where  $g$  is a normalized, unknown shape function ( $\int_0^\infty g(\xi) d\xi = 1$ ). Solution 25 exhibits both rightward enstrophy flux and leftward energy flux. The dominant scale,  $k_1^{-1}$ , of this eddy field expands according to

$$\frac{dk_1^{-1}}{dt} = TU \quad (26)$$

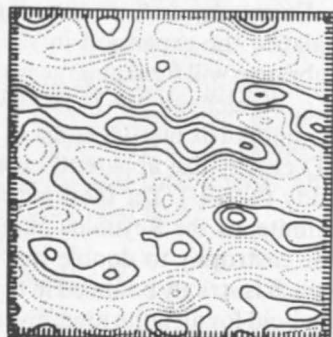
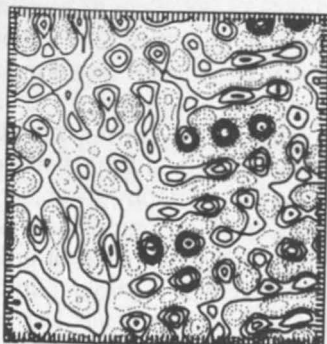
where

$$T^{-1} = \int_0^\infty \xi g d\xi, \text{ a constant}$$

$\beta=0$



$\beta \neq 0$

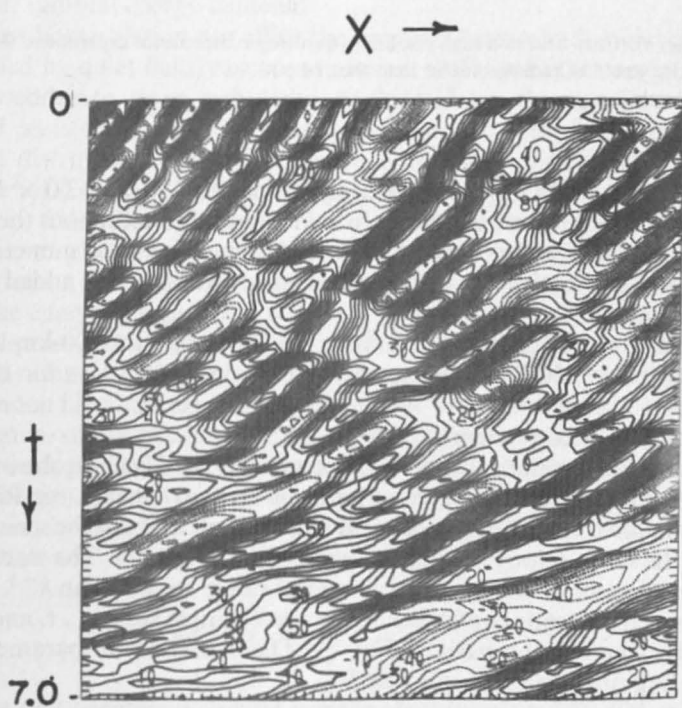
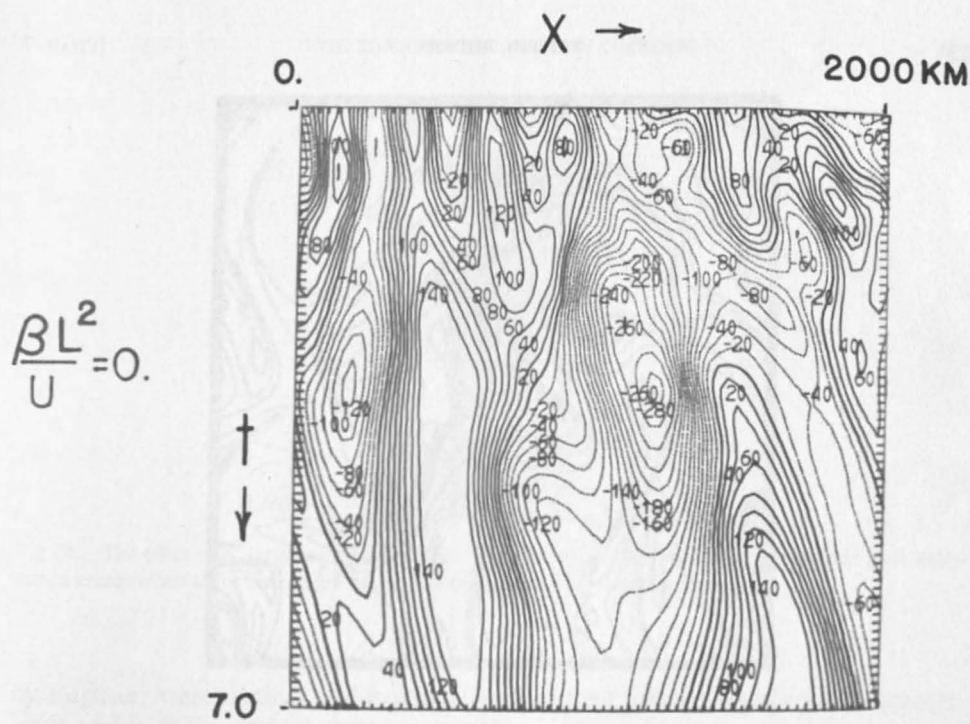


$t=0$

$t=5 \text{ mo}$

(a)

Fig. 20. (a) Streamlines in barotropic evolution experiments with and without the  $\beta$  effect. Beside keeping the scale small,  $\beta$  tends to produce a striated pattern of shifting, principally zonal, flows. (a) Contour interval 0.11 at  $t=0$ , 0.16 at  $t=5$ .



(b)

Fig. 20. (b) contour interval 0.11 at  $t = 0$ , 0.06 at  $t = 5$ . (See Table I for parameters.) (b) Time-longitude diagrams for  $\psi$ , from the barotropic runs in (a). The cascade to large scales occurs in either case; with beta, it leads to increasingly fast propagation, until being halted at  $\kappa \sim \kappa_\beta$ .



(c)

Fig. 20. (c) Vorticity field in a high resolution barotropic turbulence experiment. With a strong  $\beta$  effect this vorticity would be radiated rather than sheared out.

Experimental values for  $T$  are given by Rhines (1975);  $T = 3.0 \times 10^{-2}$  for initially narrow spectra. Thus we are closer to having useful results about the evolution of the energy-containing eddies in two than in three dimensions, and numerical computation is far more economical in two dimensions, so we have the added benefit of many simulations.

If these results are applied directly to the ocean, say, the 200-km-wide thermocline eddy viewed in MODE-I, equation 26 gives about 100 days for the time required to double its size (taking  $U \sim 10$  cm/sec). But this certainly did not occur, for reasons that will soon become clear.

A numerical simulation of pure, barotropic 2D turbulence is shown in Fig. 20a. The computation uses a  $64^2$  degree-of-freedom spectral scheme (see Rhines, 1975). The dominant scale increased rapidly, and its evolution may also be seen in the  $x-t$  plot of stream function (along a single latitude line), Fig. 20b. The corresponding wave number spectrum is sharp, with an inertial range steeper than  $k^{-3}$ . This narrowness of the spectrum lends confidence to the use of single scales  $L$ ,  $\tau$ , and  $U$  in describing the field, which is the basis of Fig. 19. The experimental parameters for this and succeeding runs are given in Table I.

### C. Obstacles to the Red Cascade

Evidence from mid-ocean observations is that the eddies are closely packed and not very intermittent. But the mechanism of thin-jet instability makes the field more erratic nearby the Gulf Stream or other intense currents. The eddies followed

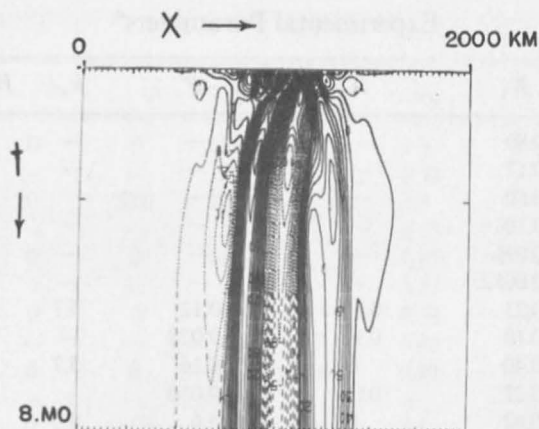


Fig. 21. The effect of isolating a patch of eddies with surrounding, still fluid (time-longitude plot). Interaction ceases when there are too few eddies to act as turbulence (roughly four).

by Fuglister were distinct and isolated, both in their foreign water-mass characteristics, and in their unusual energy content.

Figure 21 shows how isolation can affect the simple 2D cascade. A initial cluster of eddies, surrounded by quiet fluid, cascades to longer scale, until the energetic patch contains too few eddies to act as turbulence. At this point in the experiment further evolution ceased, as is clear in the  $x-t$  diagram. A number of integral properties of such an isolated distribution must be conserved: the total vorticity, the center of vorticity  $\iint \mathbf{x}\zeta \, d\mathbf{x}^2 / \iint \zeta \, d\mathbf{x}^2$ , and the dispersion  $\iint |\mathbf{x}|^2 \zeta \, d\mathbf{x}^2 / \iint \zeta \, d\mathbf{x}^2$  about the center (Batchelor 1967, p. 528). These guarantee that the "size" of a cluster of turbulence remain about the same as it evolves, if the net vorticity is significantly nonzero. In the present experiment, however, the net vorticity vanishes identically, and there is no guarantee that the energetic region will remain confined. In some other realizations, in fact, vortex dipoles (which are self-propelled) managed to escape the cluster. Regardless of the ultimate detail, the initially isolated cluster must eventually cease to act as turbulence.

A second, and more subtle, obstacle to the 2D cascade is the restoring force provided by the  $\beta$  effect, or its topographic equivalent (owing to gradients of ambient potential vorticity). The energy and enstrophy integrals, equation 23, are unaltered (in an unbounded domain) by  $\beta$ , indicating that the direction of the cascade should be the same as before. Scale analysis of the equation,

$$\frac{D}{Dt} \nabla^2 \psi + \beta \psi_x = 0$$

however, suggests that eventually the red cascade (path  $b$  in Fig. 19) will carry the flow into the regime of linear waves, no matter how intense or how small the initial eddies. The relative strength of nonlinearity  $\hat{\epsilon}_1 \equiv 2Uk_1^2/\beta$ , decreases like  $2/\beta U t^2 T^2$ , according to equation 26. When it passes through unity, radiation of vorticity begins to supplant advection, and interactions between different wave numbers demand frequency resonance obeying the dispersion relation of type 1 waves if they are to develop fully. This requirement of physical coincidence plus spectral resonance

TABLE I  
Experimental Parameters<sup>a</sup>

Figure	$t$	$K_1$	$K_2$	$P$	$k_p$	$H_2/H_1$	$dt$	$v$
20a	0	0.80	—	—	—	—	0.004	0.004
	4.0	0.17	—	—	—	—	—	—
20b	0	0.80	—	—	—	—	0.004	0.004
	4.0	0.10	—	—	—	—	—	—
21	0	0.036	—	—	—	—	0.004	0.0025
	2.5	0.0082	—	—	—	—	—	—
22a	0	0.23	0.23	0.12	5.7	1	0.016	0.003
	4.8	0.10	0.11	0.023	—	—	—	—
22b	0	0.40	0	0.16	5.7	1	0.008	0.002
	4.8	0.22	0.054	0.056	—	—	—	—
23, 24	0	0.62	0	5.6	8.0	3.57	0.004	0.004
	6.2	0.64	1.5	1.97	—	—	—	—
25	0	1.0	0.33	20.4	8.0	3.57	0.006	0.004
	3.0	5.0	8.4	3.3	—	—	—	—
27-29	0	0.24	0	2.11	5.0	3.17	0.008	0.006
	3.2	0.26	0.064	1.95	—	—	—	—
	8.5	0.46	0.52	0.74	—	—	—	—
31	0	1.2	0.70	1.8	8.0	3.57	0.008	0
	5.1	0.57	1.64	0.24	—	—	—	—
34	0	1.1	0	1.9	8.0	3.57	0.008	0.004
	3.0	0.53	0.40	0.81	—	—	—	—
35, 41	0	1.2	0.30	2.4	8.0	3.57	0.008	0
	7.0	0.33	1.0	0.48	—	—	—	—
39, 40	0	0.25	0	3.1	8.0	3.57	0.008	0.004
	2.6	0.48	0.80	1.7	—	—	—	—
	5.1	0.38	0.61	0.95	—	—	—	—
39	0	0.25	0	3.1	8.0	3.57	0.008	0.004
	2.6	0.43	0.64	2.1	—	—	—	—
39	0	0.25	0	3.1	8.0	3.57	0.008	0.004
	2.6	0.20	0.05	3.1	—	—	—	—
39	0	0.25	0	3.1	8.0	3.57	0.008	0.004
	2.6	0.20	0.05	3.1	—	—	—	—
39	0	$2.6 \times 10^{-11}$	0	$3.1 \times 10^{-10}$	8.0	3.57	0.008	0.004
	5.1	$3.7 \times 10^{-11}$	$2.0 \times 10^{-11}$	$5.0 \times 10^{-11}$	—	—	—	—
42	0	0.48	0	0.16	6.0	1.0	0.008	0.003
	3.5	0.16	0.016	0.096	—	—	—	—
43b, e	0	0.49	0	0.79	8.0	3.57	0.008	0.004
	8.8	0.046	0.035	0.16	—	—	—	—
43c	0	0.50	1.5	2.0	8.0	3.57	0.008	0
	7.0	0.21	0.85	0.30	—	—	—	—
43d	0	0.60	0.15	1.21	8.0	3.57	0.008	0
	7.0	0.19	0.44	0.30	—	—	—	—
45	0	$1.1 \times 10^{-4}$	0	$3.0 \times 10^{-4}$	8.0	3.57	0.008	0.006
	7.0	$2.8 \times 10^{-5}$	$6.0 \times 10^{-6}$	$1.6 \times 10^{-4}$	—	—	—	—

<sup>a</sup>In "computer" units such that the box width is  $2\pi$ . In the later simulations this corresponds to 2000 km, with the time unit 1 month, and velocity unit 10 cm/sec (then  $\beta = 17.8$  and  $f = 200$ ). Energies ( $K_1$ ,  $K_2$ ,  $P$ ) are in velocity units; multiply by  $H_1$  to get energy.  $k_p$  is the inverse Rossby deformation radius,  $(F_1 + F_2)^{1/2}$ .  $v$ ,  $R$ , and  $Q$  are lateral, bottom, and  $k^4$  friction coefficients;  $\delta$  is the rms topographic height/ $H_2$ ;  $k_1^{(1)}$  and  $k_1^{(2)}$  are

$R$	$Q$	$\delta$	$\beta$	$k_1^{(1)}$	$k_1^{(2)}$	$U_1$	$U_2$	Experiment
0	0	0	0	10.4	—	1.3	—	2DT5
—	—	—	—	3.5	—	0.58	—	
0	0	0	52.0	10.4	—	1.3	—	$\beta$ T5
—	—	—	—	5.7	—	0.45	—	
0	0	0	0	14.0	—	0.27	—	Entrain-1
—	—	—	—	—	—	0.13	—	
0	0	0	0	8.5	8.5	0.68	0.68	2LT-2
—	—	—	—	4.6	3.7	0.45	0.47	
0	0	0	0	6.5	6.4	0.89	0	2LT-1
—	—	—	—	—	—	—	—	
0	0	0	20.0	2.7	—	1.1	0	BE
—	—	—	—	4.6	3.9	1.1	1.7	
0	0	0	20.0	2.2	2.9	1.4	0.43	BCRW
—	—	—	—	6.3	4.6	3.2	2.2	
0	0	0	0	—	—	0.69	0	GS3-2
—	—	—	—	2.6	3.8	0.71	0.20	
—	—	—	—	3.0	2.4	0.96	0.57	
0.04	$10^{-5}$	0	17.8	6.5	6.3	1.5	0.65	MODE 4B
—	—	—	—	4.7	4.2	1.1	0.96	
0.04	0	0.053	17.8	5.5	—	1.5	0	MODE 3B
—	—	—	—	6.3	7.2	1.0	0.47	
—	—	—	—	5.8	7.0	0.51	0.24	
0.04	$10^{-5}$	0.053	17.8	5.6	5.6	1.5	0.41	MODE 4A
—	—	—	—	6.4	6.2	0.81	0.76	
0	0	0.053	20.0	2.0	—	0.71	0	MODE 2 <sub>1</sub>
—	—	—	—	4.9	5.5	0.98	0.67	
—	—	—	—	5.5	6.2	0.87	0.58	
0	0	0.027	20.0	2.0	—	0.71	0	MODE 2 <sub>2</sub>
—	—	—	—	4.6	4.5	0.92	0.60	
—	—	—	—	5.4	5.0	1.0	0.70	
0	0	0	20.0	2.0	—	0.71	0	MODE 2 <sub>3</sub>
—	—	—	—	2.1	2.6	0.64	0.17	
—	—	—	—	4.9	5.1	0.81	0.48	
0	0	0.053	20.0	2.0	—	$7.2 \times 10^{-6}$	0	MODE 2 <sub>3</sub>
—	—	—	—	3.5	6.0	$6.3 \times 10^{-6}$	$5.3 \times 10^{-6}$	
0	0	0.11	0	7.5	—	0.98	0	2LT-5
—	—	—	—	6.2	8.2	0.56	0.18	
0.04	0	0.053	17.8	5.7	5.7	0.99	0	HORIZ-1
—	—	—	—	5.6	6.9	0.30	0.14	
0.04	$2 \times 10^{-5}$	0.053	17.8	5.8	5.7	1.0	0.92	HORIZ-2
—	—	—	—	5.8	5.9	0.64	0.69	
0.04	$1 \times 10^{-5}$	0.053	17.8	5.7	5.7	1.1	0.29	HORIZ-2
—	—	—	—	6.2	6.7	0.62	0.50	
0	0	0.053	17.8	5.5	—	0.015	0	MODE 3A
—	—	—	—	5.1	7.3	0.0074	0.0018	

the first moments of the upper and lower kinetic energy spectra, respectively.  $U_1$  and  $U_2$  are rms velocities. Note that in the experiments with regions of empty ocean these will be less than the typical velocities.

The early runs, using lateral friction, were heavily damped by friction, but these have all been repeated with the more effective (less devastating)  $k^4$  friction.

reduced the cascade rate  $T$  by a factor of five in the numerical simulations. The result was a slowly evolving Rossby wave field of scale given by

$$k_{\beta}^2 = \frac{\beta}{2U}$$

and steepness  $\hat{\epsilon}_1$  slightly below unity. The action of turbulence as a source of wave motion (with no loss of energy to dissipation) is one of the ironies of geostrophic flow.

The numerical experiment is shown in Fig. 20. For comparison, the  $\psi$  field at an intermediate time, 5.1 months, taking  $U \sim 5$  cm/sec and a domain 2000 km wide, with and without  $\beta$ , is shown. Within the time of a single eddy revolution the differences become apparent. The growth of energy in the smallest wave numbers is inhibited by  $\beta$ , as is the leftward migration of the spectral maximum. The  $x-t$  plots in Fig. 20b show how the initial clustering occurs as before, but both the slower advection time of the bigger eddies [ $\sim(k_1 U)^{-1}$ ] and the ever greater frequency of Rossby waves of scale  $k_1^{-1}$  continue to make the transition to wave motion a quick one. The westward phase propagation, at a rate comparable with  $U$ , takes over, and further changes of scale occur only gradually. For this reason, the constant energy trajectory  $b$  in Fig. 19 is shown to terminate at the threshold of the wavelike region. The vorticity field, (Fig. 20c) in pure 2D turbulence shows contours elongated by the shear, in exactly the pattern of a passive dye trace. In more complex experiments below, this shearing action shows reliably when horizontal advection dominates the dynamics.

#### D. Anisotropy

An interesting feature of 2D turbulence with  $\beta$  is the development of anisotropy in which eddies are elongated along latitude lines. This preference for flow along geostrophic contours is a common thread running through the remainder of this chapter, including the consideration of mean-flow generation by eddies. It may be anticipated by realizing that a general feature of weak-wave interactions seems to be that they cascade predominantly toward small frequency, proofs of the initial tendency having been given by Hasselmann (1967) for single triads. Combined with the 2D cascade to small wave number, this rules out continuing isotropy, for the type 1 dispersion relation associates small frequencies with *large* wave number, if we fix the mix of propagation directions. The end state of this cascade was speculated (Rhines, 1975) to be a nearly steady pattern of zonal current, alternating with scale  $k_{\beta}^{-1}$ . There is some controversy about whether the tendency proceeds this far, but at the intermediate times of interest for the ocean, it is clearly effective. When energetic eddies do not show this tendency (for instance, those observed along 70°W in the deep water are anisotropic in the opposite sense) other constraints (e.g., the proximity of a continental margin) must be suspected.

For typical deep-ocean velocities (5 cm/sec) the scale of these waves of unit steepness is  $\sim 70$  km (wavelength 440 km), which is comparable with estimates from the observed correlation functions. Although there is much more to the story, it appears that the planetary restoring force contributes to the smallness of mesoscale eddies.

#### E. Baroclinic Cascades; Path c

The remaining initial-value problems involve baroclinity. For comparison with experiments we approximate the full potential vorticity equation 15 by a two-layer model, similar to that used by Phillips in early atmospheric models and theory. The

equations for the upper and lower layer in dimensional variables, are

$$\begin{aligned} \frac{D_1}{Dt} [\nabla^2 \psi_1 + F_1(\psi_2 - \psi_1)] + \beta \psi_{1,x} &= v \nabla^4 \psi_1 + Q \nabla^6 \psi_1 \\ \frac{D_2}{Dt} [\nabla^2 \psi_2 + F_2(\psi_1 - \psi_2)] + \beta \psi_{2,x} &= v \nabla^4 \psi_2 + R \nabla^2 \psi_2 + Q \nabla^6 \psi_2; \end{aligned} \quad (27)$$

$D_i/Dt \equiv \partial/\partial t + J(\psi_i, \quad)$ ,  $F_i = f_0^2/g'H_i$ ,  $g' = g\Delta\rho/\rho$ . Here the interface height is  $f_0(\psi_2 - \psi_1)/g'$ . (In an  $n$ -layer model, the interior layers have thickness  $\propto \psi_{n+1} - 2\psi_n + \psi_{n-1}$ , from the hydrostatic relation. This approaches  $\psi_{zz}$ , equation 15, in the limit.) Hydrostatic, quasi-geostrophic motion is assumed. A distinct change in dynamics occurs between scales on either side of the Rossby deformation radius,  $(F_1 + F_2)^{-1/2} \equiv k_\rho^{-1}$ . When  $k_\rho L \gtrsim 1$  the layers are strongly coupled by interfacial motion and the attendant vortex stretching [the term  $F_i D_i(\psi_2 - \psi_1)/Dt$ ]. At scales far smaller than  $k_\rho^{-1}$ , on the other hand, the coupling terms are negligible, and the interface is effectively rigid. In later runs a high-order friction ( $Q\nabla^6\psi$ ) is used.

Thus the initial behavior of a field of eddies of scale  $k_\rho L \ll 1$  is just that of two decoupled layers of 2D turbulence. The cascade labeled *c* in Fig. 19 has this character, following a constant-energy trajectory until it meets the edge of the wave regime, where it stagnates. The waves themselves, in this extreme ( $\beta/2Uk_\rho^2 \gg 1$ ), have the same nature, being effectively two decoupled layers of barotropic Rossby waves; that they may be expressed as baroclinic modes of odd vertical symmetry obscures this independence.

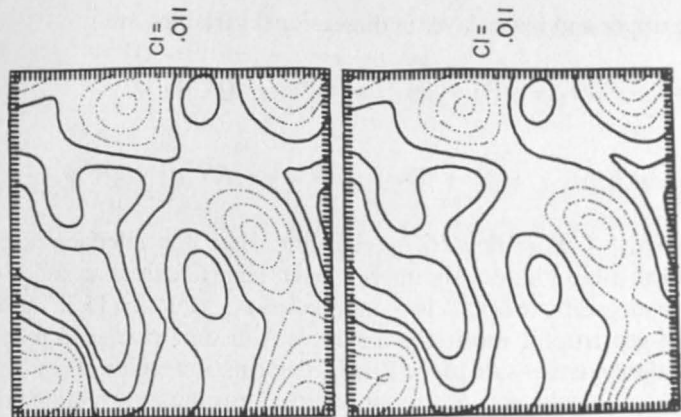
### F. Path *d*

Imagine now, the more interesting case, Fig. 19, path *d*, in which the energy level is greater, so that the initially small eddies reach the wave number  $k_\rho$  before feeling the  $\beta$  effect. As they expand toward the deformation scale the pressure perturbations build up (for the eddies are geostrophic and  $U$  remains fixed) and the layers begin to communicate. Where there is a strong cyclonic vortex in the upper layer, the interface is elevated by the low pressure, and vorticity of the same sign is induced in the fluid below. This tendency was noted long ago by Prandtl (see Prandtl, 1952, p. 386) and by meteorologists studying the development and occlusion of mature cyclones in the atmosphere (e.g., Wiin-Nielsen, 1962).

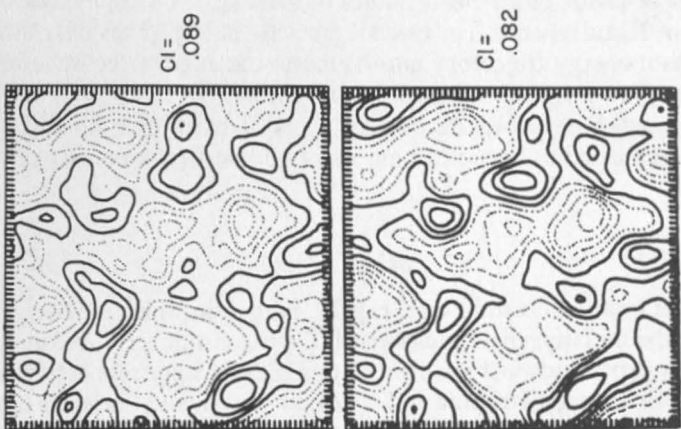
But what is striking about the experiments (Fig. 22), is the totality of the process. Very quickly, eddies of like sign, above and below the thermocline lock together to produce a barotropic field: if there are none present initially, in one layer, they will soon be produced by this process. In doing so the cascade goes far beyond the "equivalent barotropic" state familiar in the atmosphere. The 2D results again become relevant, for once the solutions have dropped to the barotropic plane in Fig. 19, they are indistinguishable from experiment *b*.

The necessity of these events can be established for path *d* by noting that *no state other than near-barotropy* is consistent with these initial values of potential vorticity, for energy that reaches small wave number. For example in the experiment with eddies of small scale ( $k_0 \gg k_\rho$ ) initially confined above the thermocline, the lower layer potential vorticity is nearly zero:

$$\nabla^2 \psi_2 - \frac{f\eta}{H_2} = O\left(\frac{k_\rho}{k_0}\right)$$

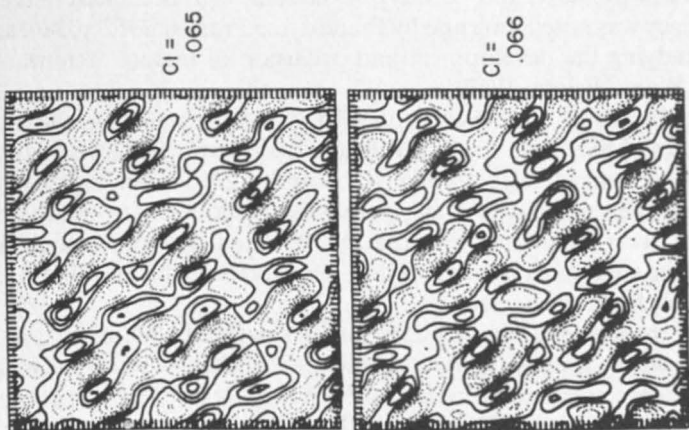


$t = 12.4$



$t = 3.2 \text{ mo}$

(a)



$t = 0.$

$\Psi_1$

$\Psi_2$

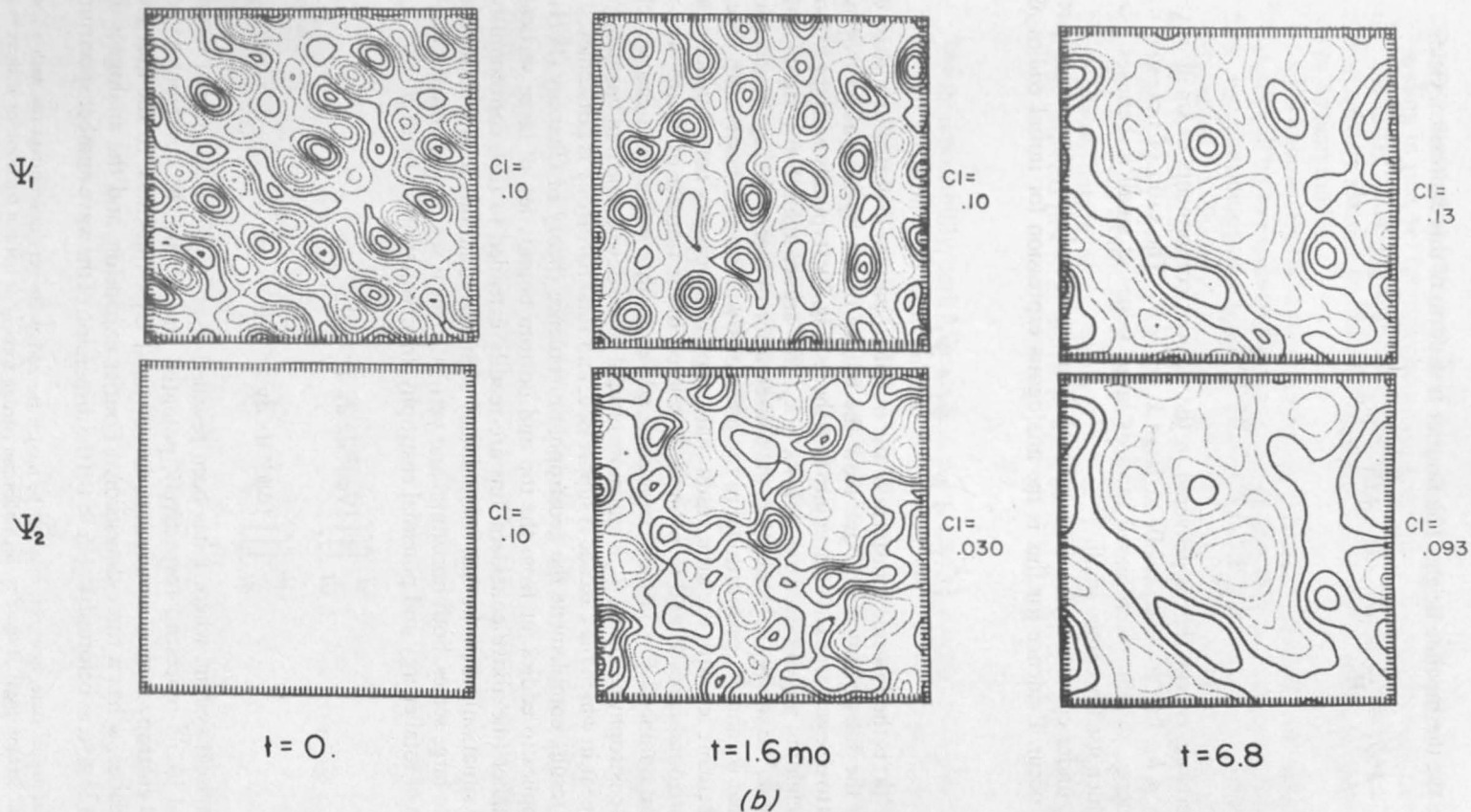


Fig. 22. (a) Sequence of two-layer streamline fields in a free spin-down experiment. The initial field has equal energy in either layer (at "box" wave number  $\kappa = 7-9$ , near  $\kappa_p = 7$ ) but with *random* phase relation. The box width is 2000 km, and  $\beta = 0$ . After locking together in the vertical, the eddies behave as 2D turbulence. CI means contour interval. (b) As in (a), but with the lower layer initially at rest. Energy is now communicated downward as a part of the cascade toward barotropy and large horizontal scale.

where  $\eta$  is the thermocline height. The Fourier transform of this expression yields

$$-k^2 \hat{\psi}_2 = \frac{f \hat{\eta}}{H_2} \equiv (\hat{\psi}_2 - \hat{\psi}_1) + O\left(\frac{k_\rho}{k_0}\right) \hat{k}_\rho^2; \quad \hat{k}_\rho^2 \equiv k_\rho^2 \frac{H_1}{H_1 + H_2}$$

or

$$\left(\frac{k^2}{\hat{k}_\rho^2} + 1\right) \hat{\psi}_2 = \hat{\psi}_1 + O\left(\frac{k_\rho}{k_0}\right)$$

Later, therefore, energy that is delivered to the Fourier components of small wave number  $k \ll k_\rho$ , has  $\hat{\psi}_2 \rightarrow \hat{\psi}_1$ , while at large  $k$ ,  $\hat{\psi}_2 \ll \hat{\psi}_1$ . The ratio of potential to kinetic energy, though often biased towards large values at small  $k$ , behaves like  $(k/k_\rho)^2$ , which itself becomes small.

In fact, under conditions far more general than  $(k_0/k_\rho) \gg 1$ , the same events are found to occur. Evidence for this is the analogous expression for initial eddies of any size:

$$\left(\frac{k^2}{\hat{k}_\rho^2} + 1\right) \hat{\psi}_2 = \hat{\psi}_1 + \hat{\psi}_1^0$$

where  $\hat{\psi}_1^0 | \mathbf{k} |$  is the Fourier transform of the initial  $\psi_1$  pattern *distorted as a passive tracer* by the subsequent deep flow. Now the nature of the horizontal enstrophy cascade is to elongate a passive tracer into thin sheets (Fig. 20c) typically with spectrum  $\propto k^{-1}$  weighting heavily the large  $k$ . If  $k_0 \sim k_\rho$ , this argues against any significant cascade of  $\hat{\psi}_1^0$  to smaller  $k$ . In addition, the conservation of energy during the cascade implies that  $\hat{\psi}_2$  and  $\hat{\psi}_1$ , proportional to the pressures, will increase vastly with time. We are therefore left with the same result: barotropy is a necessary consequence of a "red" horizontal cascade and is intrinsically related to the transfer of enstrophy to large wave number.<sup>6</sup> For initially large-scale eddies (path *e* below), the cascade of potential enstrophy to large  $k/k_\rho$  is still more crucial to the development of barotropy. Cases appear in which the cascade is suppressed, and total barotropy is not achieved.

These results complement the geostrophic turbulence theory of Charney (1971), which applies to eddies far from the top and bottom boundaries, of large vertical wave number (the above considerations are readily extended to this, continuously stratified situation); then the full, continuously stratified equations tend to exhibit a cascade to large scales, both horizontal and vertical. This is seen by writing the conservation of total energy and potential enstrophy, from equation 15 (with  $\beta = 0$ ):

$$\begin{aligned} \frac{d}{dt} \iiint |\nabla \psi|^2 dx dy dz &= 0 \\ \frac{d}{dt} \iiint |\Delta \psi|^2 dx dy dz &= 0 \end{aligned} \quad (28)$$

for an inviscid system, where  $z$  has been rescaled by  $fL/N$ . The additional terms  $|\psi_z|^2$  and  $|\psi_{zz}|^2$  represent, respectively, potential energy and the contribution to potential enstrophy from the variations in isopycnal layer thickness. In the absence of boundaries,  $\psi$  has a three-dimensional Fourier expansion, and the analogues of equation 23 give, as before,  $d| \mathbf{k} | / dt < 0$  if the dispersion of the wave number spectrum

<sup>6</sup> The barotropic state, however, may not be total if the eddies are very intermittent (as with a few distant Gulf Stream rings), if there is disequilibrium (strong forcing or bottom friction), or if there is a very shallow thermocline or strong bottom topographic roughness (see Section 7).

about its mean is to increase. This is a self-similar cascade, with ellipsoidal eddies expanding in size, yet keeping the same eccentricity. The red cascade again suggests the similarity solution 25 for the evolving wave number spectrum. The theory provides basic reasons for the predominance in the ocean and atmosphere of rather grave vertical modes.

We have shown that when top and bottom boundaries are encountered, the interior fluid will still try to expand its vertical scale, and thus develop into depth-independent flow. The continuing equipartition of energy between the potential and two kinetic components, in Charney's cascade, must then be lost, for the cascade  $d$  efficiently converts potential energy to kinetic. Once  $d$  reaches the barotropic plane, the system again enters into the wave-turbulence conflict described for  $b$ . The predicted spectra are very different from Charney's  $k^{-3}$  (for both velocity and temperature); here the uncorrelated nature of the layers at  $k \gg k_\rho$  suggests  $K(k) \propto k^{-3}$  and  $P(k) \propto k^{-5}$  roughly, whereas in  $k < k_\rho$  the barotropy suggests a red  $K(k)$ , yet blue or white  $P(k)$ .

### G. Path e

The final possibility, path  $e$ , for these initial value experiments is a field of baroclinic eddies far larger in scale than the deformation radius. At small amplitude these states would simply propagate as type 3 baroclinic Rossby waves, due westward at speed  $\beta k_\rho^{-2}$ . In fact the waves are unstable and quickly break down into eddies of scale  $\sim k_\rho^{-1}$ .

This is the first violation of the "red" cascade so far encountered. The constraints 23 are now relaxed by production of relative enstrophy. The analogues of equation 23 follow from conservation of total energy

$$\frac{1}{2}[H_1(\Delta\psi_1)^2 + H_2(\nabla\psi_2)^2 + H_1F_1(\psi_2 - \psi_1)^2]$$

[whose spectra are  $K_1$  (upper kinetic),  $K_2$  (lower kinetic), and  $P$  (potential)], and potential enstrophies

$$H_1[\nabla^2\psi_1 + F_1(\psi_2 - \psi_1)]^2, \quad H_2[\nabla^2\psi_2 + F_2(\psi_1 - \psi_2)]^2$$

With  $\beta = 0$  for simplicity, and  $F_1 = F_2 = F$ , we have, analogous to equation 23

$$\frac{d}{dt} \int (K_1 + K_2 + P) dk = 0 \quad (29)$$

$$\frac{d}{dt} \int [k^2(K_1 + K_2) + 2(F + k^2)P] dk = 0 \quad (30)$$

$$\frac{d}{dt} \int (k^2 + 2F)(K_1 - K_2) dk = 0 \quad (31)$$

When  $F \rightarrow 0$ ,  $P \rightarrow 0$  we recover equations 23. Otherwise, equations 29 and 30 yield

$$\frac{\partial}{\partial t} \int E dk = 0$$

$$\frac{\partial}{\partial t} \int k^2 E dk = - \int (k^2 + 2F) \frac{\partial P}{\partial t} dk \quad (32)$$

$$E = K_1 + K_2 + P$$

Comparing with equations 23, we find that the second moment of  $E(k)$  can increase if potential energy is released,  $\partial P/\partial t < 0$ , in the weighted sense of the integral. A wave number region of significantly growing eddies with  $\partial P/\partial t > 0$  cannot occur far above  $k = k_p$ , for it would tend to change the right side back to negative. This amounts to an integral statement, valid for turbulence, of the favoring of wave numbers  $k^2 \lesssim 2F$  for the growing eddies. The energy and enstrophy invariants thus permit a "blue" cascade, in which the dominant wave number, say,  $\int kE dk / \int E dk$ , increases spontaneously. Path  $e$  follows, as do  $a$  to  $d$ , if particles tend to separate with time.

Equations 29 and 30 are the two-layer analogues of the invariants 28 for the continuously stratified model. They can be rewritten as

$$\frac{\partial}{\partial t} \int \sum_{i=1}^2 (k^2 + m_i^2) \tilde{\psi}_i^2 dx = 0$$

$$\frac{\partial}{\partial t} \int \sum_{i=1}^2 (k^2 + m_i^2)^2 \tilde{\psi}_i^2 dx = 0$$

where  $m_0 = 0$ ,  $m_1 = (2F)^{1/2}$  appear as the vertical wave numbers and  $\tilde{\psi}_1, \tilde{\psi}_2$  are the Fourier transforms of the barotropic and baroclinic modes,  $\psi_1 + \psi_2$  and  $\psi_1 - \psi_2$ , respectively. This version emphasizes that to violate the red cascade in the horizontal sense with baroclinic instability, the motion must evolve toward larger vertical scales to compensate for the growth of smaller horizontal scales. For  $d|k_1|/dt < 0$  still, based on the total wave number  $(k, m_i)$ . Bass (1974) has discussed the  $n$ -layer case.

Though baroclinic instability is well-known in the study of nearly zonal mean flows, its appearance as a turbulent cascade from big eddies to small, is less familiar. Yet it is the *primary* nonlinear effect in large baroclinic eddies. The cascade rate can crudely be inferred from the linearized stability theory, which yields growth rates  $\sim Uk_p$ ,  $U$  being the large-scale baroclinic velocity. If we scale the small eddy velocities with  $U$  as well (implying a well-developed cascade), the energy flux to them is roughly  $U^3 k_p$ .

An experiment following path  $e$  (Fig. 23) involves a set of big eddies (of widths  $\sim 200$ – $1000$  km), initially above the thermocline. The successive streamline contours show meanders developing locally, where the flow is particularly intense. This first occurs in the region of southwestward flow (Fig. 23b). The shallowness of the upper layer makes westward currents,  $U_w$ , more unstable than eastward currents,  $U_E$ , if  $|U_w|/|U_E| > H_1/H_2$  (see Section 8). The situation changes in time owing to westward propagation. Later the band of east-northeastward current near the north end of the box breaks down in a well-defined instability, developing four wavelengths along the current (Fig. 23c).

At the end stages, the meanders collapse and produce an intensified band of zonal flow (Fig. 23c). By this time a considerable amount of barotropic, nearly zonal flow has developed. Arguments for the production of anisotropy and zonal-averaged east–west flow, which varies only slowly in time, were given in the purely barotropic case above. Here the generalized baroclinic instability augments these effects, producing even more striking "mean" flow. This occurs, first, owing to the greater instability of meridional flows, which break down into preferentially zonal eddies (the perturbation currents are then unopposed by  $\beta$ ), and second, owing to the finite amplitude eddy–eddy induction of zonal flow, to be discussed in Section 8. The strength and persistence of the zonal velocities may be seen in a time–latitude plot of stream function (Fig. 24). The upper-level flow in the north central region intensifies and endures throughout the 9-month experiment. Ocean observations (Section 9) hint at such a banded current structure.

$\Psi_1$ 

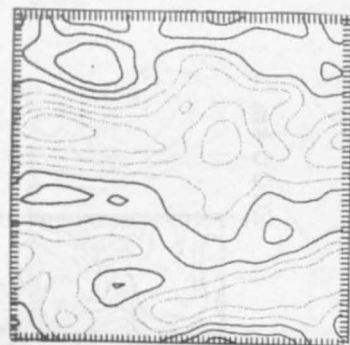
CI = .32



CI = .23



CI = .27



CI = .28



t = 0



CI = .13

t = 2.1 mo



CI = .21

t = 6.2



CI = .20

t = 7.7

245

 $\Psi_2$ 

Fig. 23. Evolution of large-scale eddies, initially confined to the upper layer, a mixture of (box) wave numbers 1 and 3. The field has local episodes of baroclinic instability that in turn reduce the scale, develop deep flow, and increase the scale again. The final, banded zonal pattern of flow is evident.

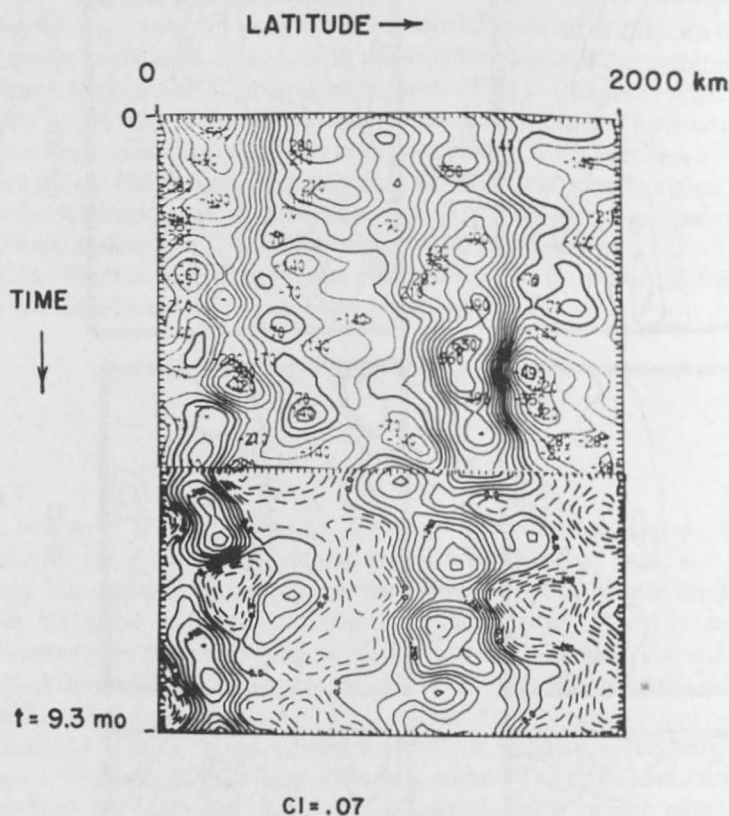


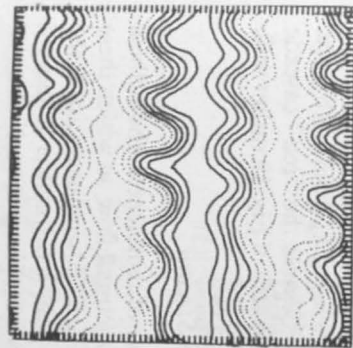
Fig. 24. Time-latitude plot of upper-layer  $\psi$  (actually  $-\psi$ ) (or pressure), at mid-longitude. The persistence and growth in strength of the zonal flow are evident. (At the end viscosity finally damps the current.)

The end state of this unforced flow has in it some uncertainty: though the barotropy that developed in experiments with smaller eddies, with a lesser store of potential energy, was often total, here we cannot be sure that all the large-scale potential energy will be tapped (the ratio of potential to kinetic energy started at 9.0, and dropped to 0.83 after 8.7 months). If a zonal configuration develops soon enough, vertical shear  $\Delta U$  can remain, and is stable, if  $\beta L_\rho^2 / \Delta U >$  about 1 (the classical result). The zonal configuration of the currents, in other words, can defeat the potential enstrophy cascade which is a prerequisite for barotropy. Indeed, this seems to be happening in Fig. 23*d*. But the nature of an equilibrium or near equilibrium end-state in these, or in steady forced experiments, is uncertain and must depend critically on the method of damping and driving the flow. The rms velocities certainly grow during the instability, but in a range of such experiments, they rarely exceeded the speeds of the initial flow by a factor of three. Even this required rather special, vulnerable flows, such as in the succeeding two examples. The rate of cascade toward  $k_\rho$  must be studied in detail, and compared with the other transfer spectra, and dissipation, to see how much of the energy completes the journey along path *e*.

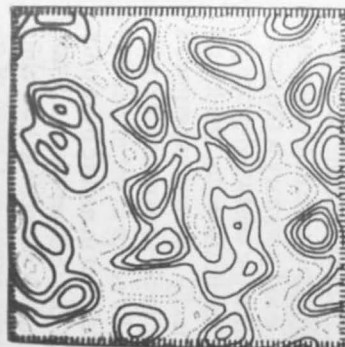
These events amount to a statement that the classical baroclinic Rossby wave, so often used to describe oceanic adjustment processes, is unstable. To isolate the simplest case, I looked at a single Fourier mode (wavelength 1000 km) combined with

$\Psi_1$ 

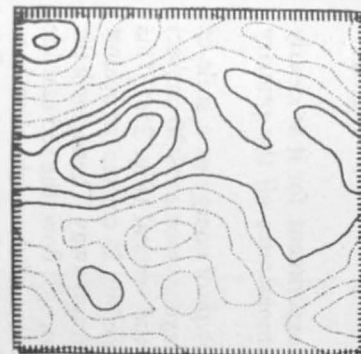
Cl = .26



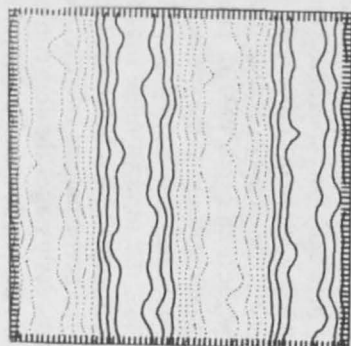
Cl = .27



Cl = .47



Cl = .72

 $\Psi_2$ 

(a)

Cl = .077

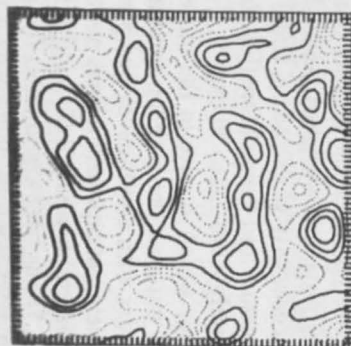
t = 0



(b)

Cl = .11

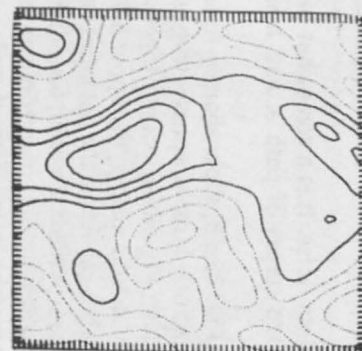
t = 1.5 mo



(c)

Cl = .33

t = 2.5



(d)

Cl = .68

t = 5.2

Fig. 25. Instability of a single baroclinic Rossby wave with a weak noise field. This is path *e* of Fig. 19. The initial behavior is a quasi-linear eddy-mean field interaction, yet mutual eddy interactions quickly take command.

a weak field of random noise. It is a somewhat bizarre experiment, for it so clearly passes through all the stages of path  $e$ , and hence demonstrates *all* the primary cascades!

The streamlines (Fig. 25a, b) show sharply tuned growth of energy at a scale of  $(1.3-1.6)L_\rho$ . After reaching large steepness (with upper layer velocities  $\sim 30$  cm/sec) the eddies interact laterally while locking together in the vertical (Fig. 25c). This yields a final surge of kinetic energy, the upper layer exceeding 35 cm/sec (as against 14 cm/sec initially), when the last of the potential energy drains away. Thenceforth the dynamics are just those described earlier, for purely barotropic flow: the red cascade continues until transforming into barotropic mode 1 waves, after which anisotropy builds up, favoring nearby zonal flow of scale  $\sim k_\beta^{-1}$  (Fig. 25d). The entire affair occupied 6 months, during which the ratio of potential to kinetic energies dropped from 15.7 to 0.03, the wave field switched modes from baroclinic to barotropic, and the initial meridional flow gave way to nearly zonal flow. A good summary is the time-longitude plots of pressure and temperature (Fig. 26), in which the westward propagation speed rises abruptly from 2.6 to 50 cm/sec. This has implications for the lateral propagation of energy which survive in the more oceanically relevant experiments (Section 7). The flow patterns that develop spontaneously in these experiments may seem unreal to a reader with a well-developed picture of the ocean in his mind; they are certainly incomplete, yet represent oceans not terribly distant in nature from ours.

The instability is tractable analytically, and Kim's (1975) treatment is a relevant model for the ocean. It has been common in the past to apply baroclinic instability theory based on "meteorological" flows which are steady, zonal, and often of infinite horizontal extent. In its most general form the Rossby-wave model develops both baroclinic and barotropic instabilities and transfer toward  $k_\rho$  from both sides. It shows  $\beta$  to inhibit all but zonal perturbations and to depress the "red" cascade when  $k < k_\beta$ . If extended to finite amplitude, it will model much of Fig. 19 rather well.

### H. Meanders in a Two-Layer Gulf Stream

These broad, homogeneous fields of eddies have an air of remoteness about them that, I believe, can be dispelled by describing a highly structured flow, in which these same interactions are found to occur. Consider a thin, zonal jet flowing eastward at the surface, through the periodic box. Its thinness (half-width  $\sim L_\rho$ ) makes it more a model of the Gulf Stream than of the atmospheric westerlies (at least in their classical conception). The initial field (Fig. 27) contains a weak, broad-band noise. There is also a slight counterflow such that no  $y$ -averaged transport passes through the section. The exact form chosen is  $\psi_1 = \tanh(y/a) - y/L + \text{noise}$ , where  $a = 78$  km, and  $L$  is the half-width of the box. This is now a smaller domain,  $2L = 1250$  km, with the thermocline at 960 m, and the total depth 4000 m. The deformation scale is 40 km,  $\beta = 0$ , and  $U_1 \sim 50$  cm/sec, averaged across the stream (by rescaling the time, this is equivalent to a very fast flow in the presence of  $\beta$ ,  $\beta L_\rho^2/U \ll 1$ ).

In less than 20 days, the random noise organizes into a meandering instability with a regular set of elliptical eddies below the thermocline. The deep motion and its phase shift (leading the perturbations overhead) are known to be essential to baroclinic instability. At the early stages, the deep currents are predominantly north-south, and the whole pattern moves downstream as it intensifies.

After the meander steepness exceeds unity, the independently growing eddies begin to interact with one another; here the turbulence theory becomes relevant. A symptom of the eddy-eddy interactions beginning to compete with eddy-mean flow

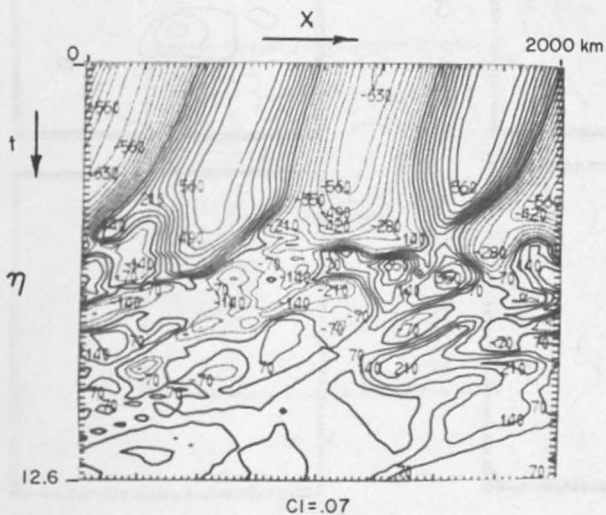
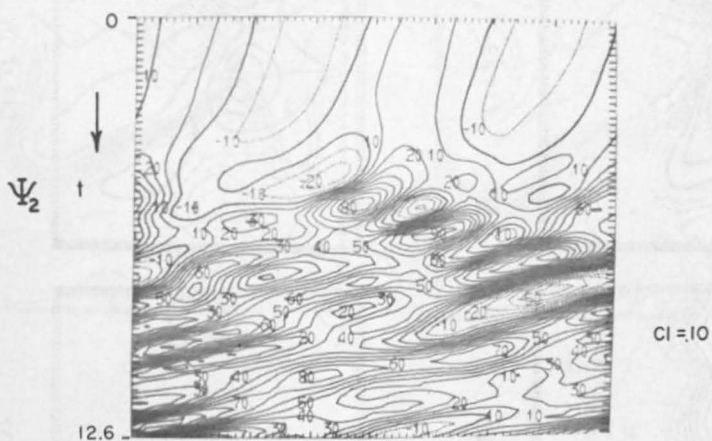
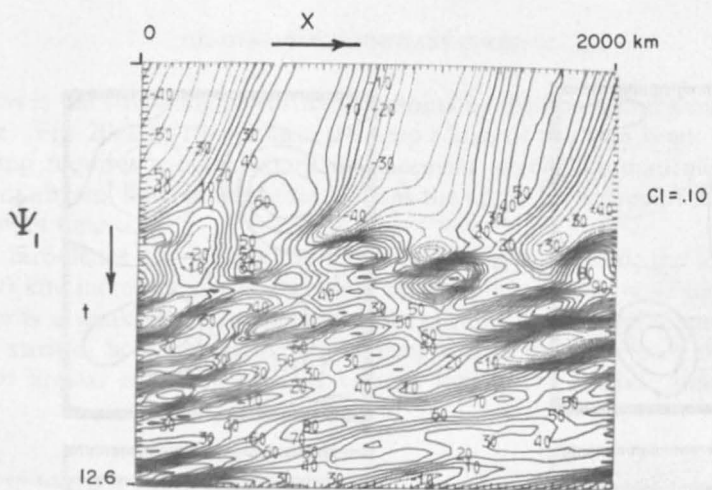


Fig. 26. A time-longitude representation of stream function and interface height ("temperature") shows the rapid breakdown of the field, which jumps from baroclinic to barotropic modes, increasing its propagation speed by a factor of 20. The temperature structure vanishes.

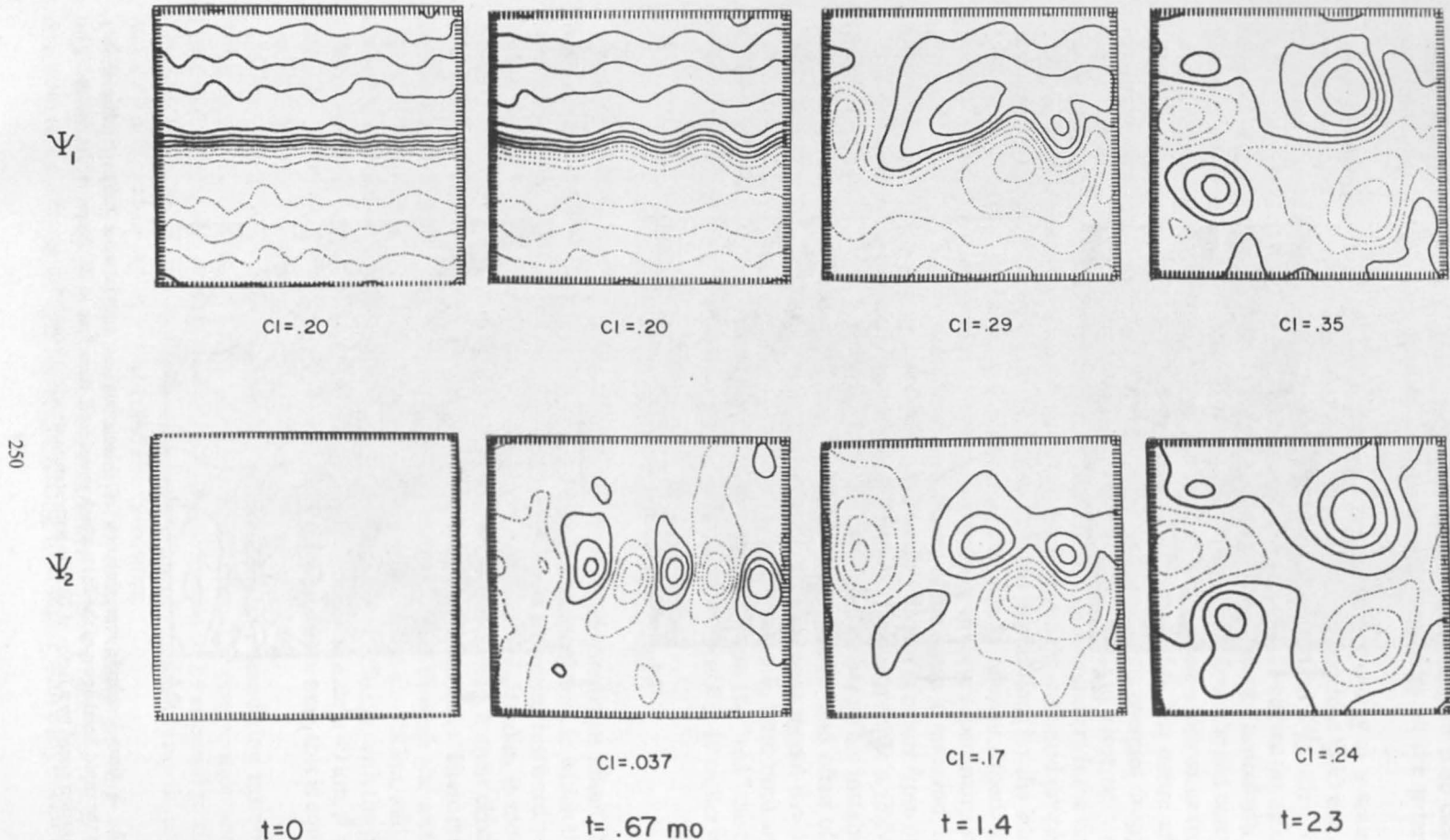


Fig. 27. Meandering instability of a thin zonal jet, initially flowing in the upper layer, passes through the stage of path e, Fig. 19. After linear growth, which involves immediately the deep water (producing predominantly north-south flow there), the eddy field interacts, expanding horizontally and "occluding" in the vertical. The box width is 1250 km,  $\beta = 0$ .

interactions is the stretching of vorticity contours by the horizontal shear (as in 2D turbulence) (Fig. 20c). At  $t = 42$  days the deep eddies of like sign begin to coalesce. This pairing requires a north-south displacement which automatically creates a zonal-mean abyssal flow, in the same sense as the upper level stream; the transport increases with time.

Lateral turbulence also causes the horizontal scale to expand; the initial wavelength, 330 km, increases as the meanders begin to break up ( $t = 42$  days). At this stage there is a weak lateral convergence of eastward upper-level momentum into the mean stream. Soon thereafter, the stream almost vanishes from the  $\psi$  fields, seeming to appear and disappear at various longitudes, as the cascade toward

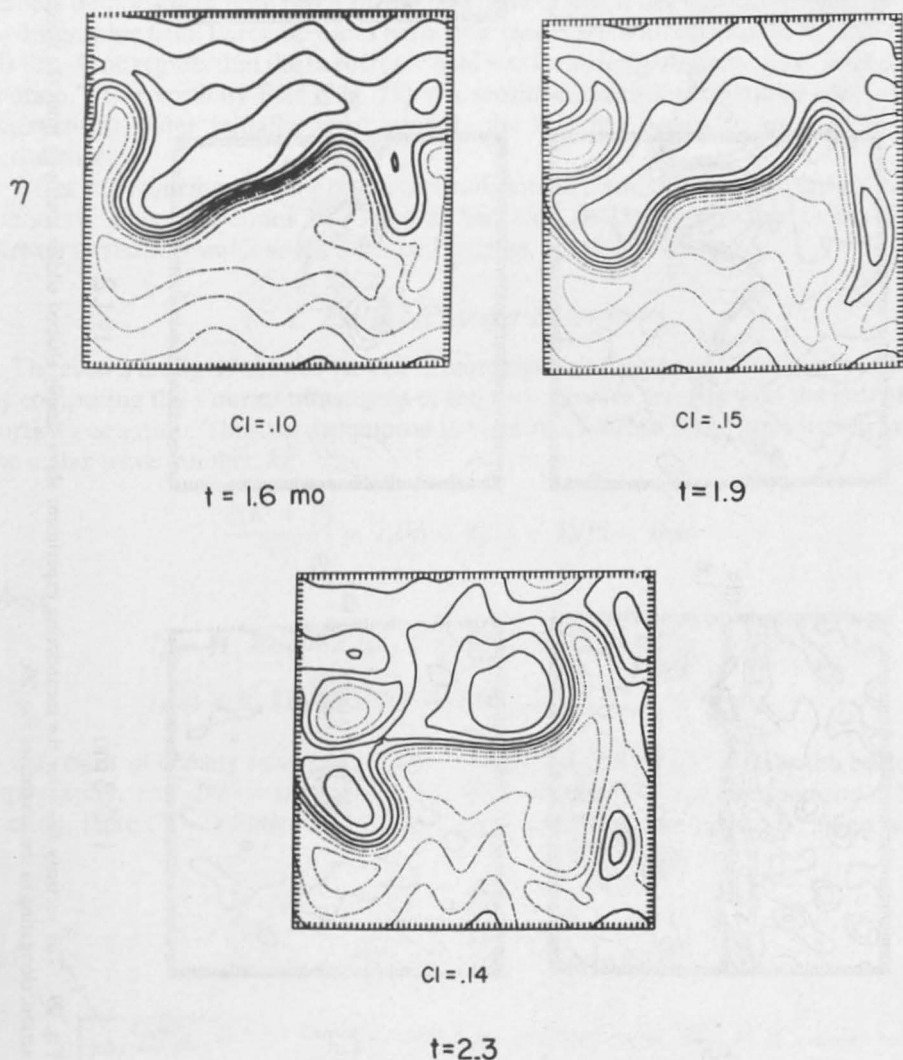


Fig. 28. None of the velocity events in Fig. 27 are visible in the "hydrographers'" Gulf Stream. There the jet remains identifiable for longer. An elongated meander detached to form a closed ring. Some of the flavor of Fig. 1 is thus reproduced in a hydrostatic two-layer model.

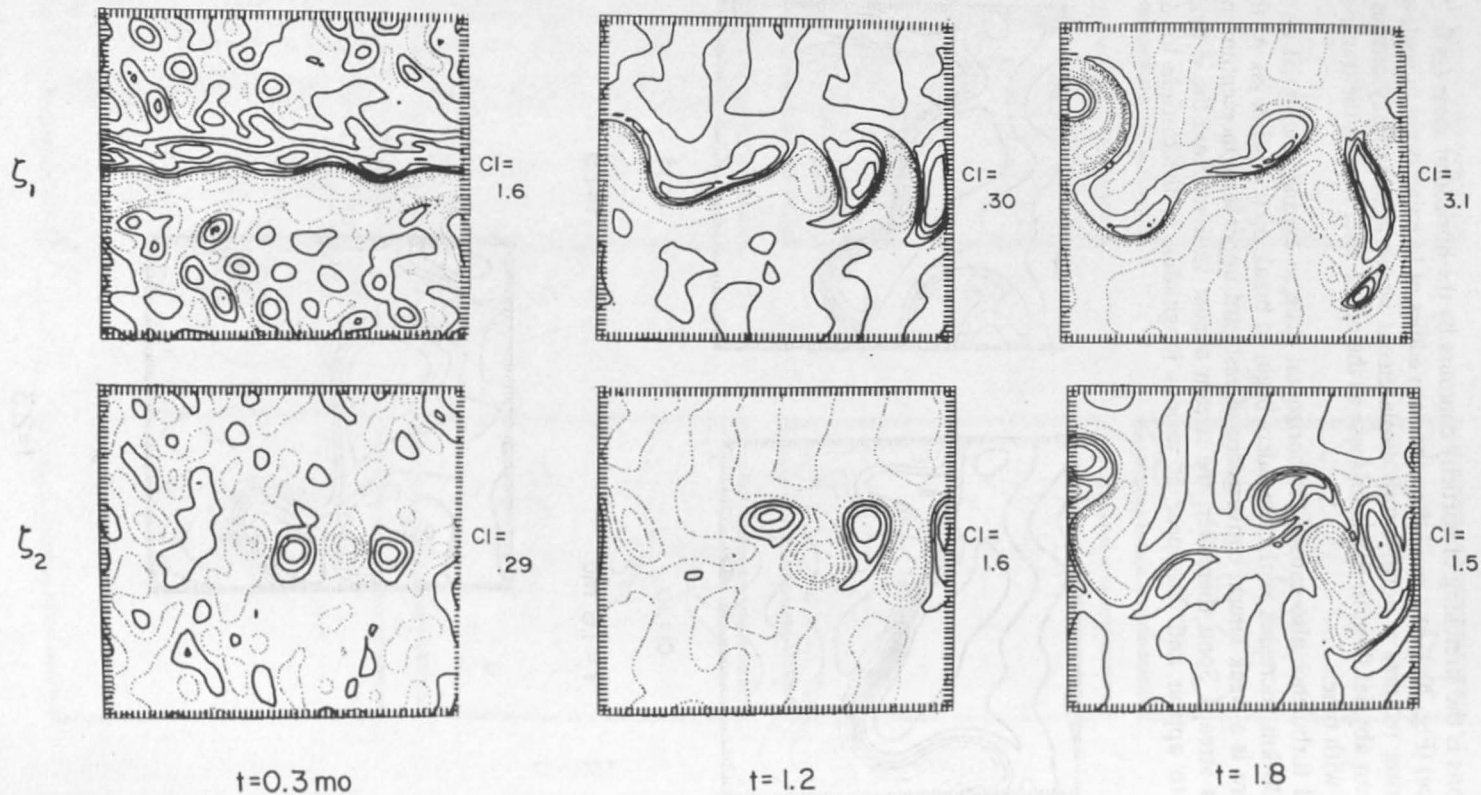


Fig. 29. The vorticity fields for the meandering experiment show simply shaped eddies emerging from the noise field, but at the stage of horizontal interaction, elongating in the manner of Fig. 20c.

barotropy takes hold, beginning to lock together the upper- and lower-level eddies ( $t = 68$  days). The "hydrographer's" Gulf Stream, however, is still present in the density field (Fig. 28) long after it is disguised in the velocity fields by the growing barotropic turbulence. The sequence in fact catches the growth of a very deep "sock," and the birth of a detached ring, reminiscent of Fig. 1. The end result, a field of very large eddies with a strong, deep flow, may suggest the nature of the North Atlantic east of the Grand Banks. The temporal instability may best be related to spatially growing meanders in the ocean.

The example of jet instability contains numerous dynamic similarities with homogeneous turbulence (path  $e$  of Fig. 19). It also reminds one of the accounts of oceanographers like Fuglister and Luyten who, on their return from a Gulf Stream tracking expedition, paint a beautiful picture, but one also of frightening complexity. Also, the figures demonstrate how much of the flow field is lost if one has access only to the hydrographic field. Barotropic and baroclinic modes are both essential to the dynamic picture. One regrets that the barotropic field was for so long obscured as a "level of no motion." The vorticity field (Fig. 29) is a sensitive indication of lateral eddy-eddy interactions. After initially linear growth, the shearing begins to work as in 2D turbulence.

Other experiments, with the important additions of  $\beta$  and topography, appear in the literature. The simulations by Orlanski and Cox (1973), appropriate to the Gulf Stream in shallow water south of Cape Hatteras, are also of interest.

### 1. Energy-Transfer Spectra

The events in Fig. 19 may be viewed in more rigorous fashion in wave number space by computing the Fourier transforms of the various advective terms in the potential vorticity equation. Thus we decompose the contributions to the change in energy at the scalar wave number,  $k$ :

$$\frac{\partial(K + P)}{\partial t} = T_\psi(k) + T_p(k) + T_H(k) - D(k)$$

where

$$T_\psi = H_1 \text{Re} [\hat{\psi}_1^* \hat{J}_1(\psi_1, \nabla^2 \psi_1)] + H_2 \text{Re} [\hat{\psi}_2^* \hat{J}(\psi_2, \nabla^2 \psi_2)],$$

$$T_p(k) = \text{Re} [F_1 H_1 (\hat{\psi}_1^* - \hat{\psi}_2^*) \hat{J}(\psi_1, \psi_2)],$$

is the result of density advection,  $T_H(k) = \text{Re} [f_0^2 \hat{\psi}_2^* \hat{J}(\psi_2, h_2)]$  involves the bottom topography, and  $D(k) = (R + \nu k^2 + Qk^4)K(k)$  involves lateral, bottom and " $k^4$ " friction. Here  $(\hat{\quad}) =$  Fourier transform. This relation is shown in Fig. 30 along with

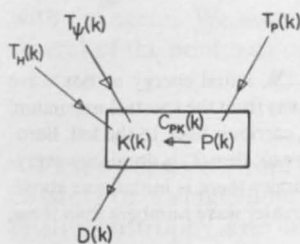


Fig. 30. Kinetic plus potential energy ( $K + P$ ) at a single scalar wave number,  $k$ , changes due to advection of vorticity ( $T_\psi$ ), advection of density ( $T_p$ ), flow across bottom topography ( $T_H$ ), and dissipation ( $D$ ). The internal conversion  $C_{PK}$  from  $P$  to  $K$  is unique if one defines  $T_p$  to be the only "direct" source of  $P$ .

the conversion between kinetic and potential energy at a single wave number,

$$C_{PK}(k) = T_P - \frac{\partial P}{\partial t}$$

[Note  $\int_0^\infty T_i(k) dk \equiv 0$ .] A similar format is used in meteorology (e.g., Smagorinsky, 1963) for analysis of general circulation dynamics. Here we recognize the signature of 2D turbulence (Fig. 31) as being a drain of energy by  $T_\psi(k)$  from the wave numbers at which it is concentrated, predominantly toward small  $k$ . The production of "barotropy" from moderate-scale eddies appears as a positive  $C_{PK}$ , conversion from potential to kinetic energy in the vicinity of the deformation radius together with the cascade of potential energy toward that wave number by  $T_p(k)$ . (The baroclinic instability of initially large-scale eddies is an approach to  $k_p$  from a larger reservoir

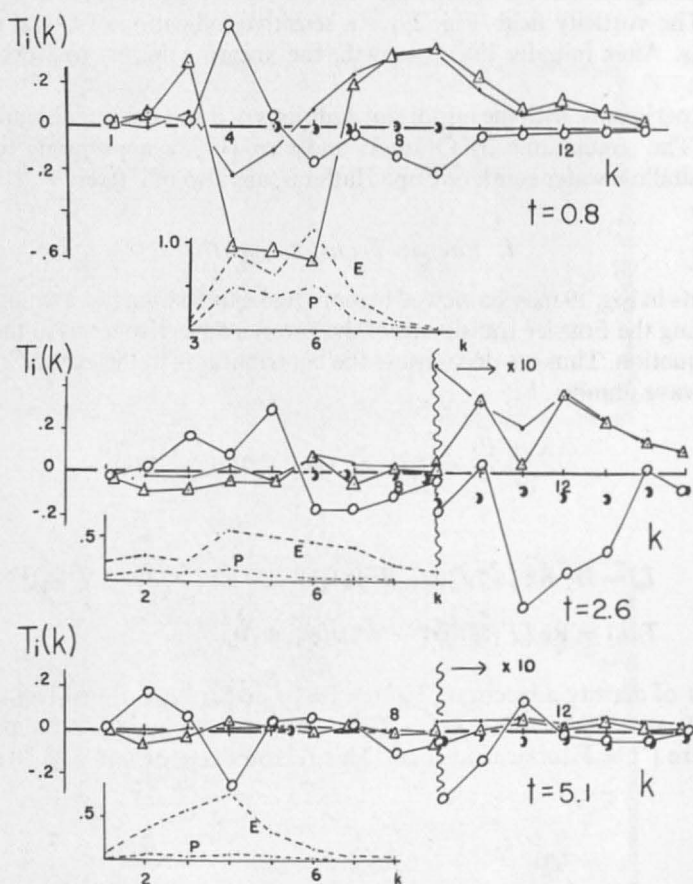


Fig. 31. Transfer spectra for a flat-bottom experiment similar to Fig. 22b, initial energy at box wave numbers  $k = 4-6$ , ( $U_1 = 14$ , deep layer at rest). At first  $T_p$  carries energy away from the spectral maximum, to the right. Near  $k_p (=8)$  it is converted to kinetic energy, whereupon  $T_\psi$  carries it back to the left. Barotropy is well-developed by  $t = 5.1$  (total potential energy,  $E$  and  $P$ , are shown); then  $T_\psi$  is dominant everywhere. The large-wave number "tail,"  $k = 10-14$ , is magnified. The dynamics there is initially as above, with  $T_p$  cascading to the right,  $T_\psi$  to the left. Dissipation dominates only greater wave numbers than these,  $k > 15$ . See also Steinberg (1973).  $\circ = T$ ,  $\cdot = C_{PK}$ ,  $\Delta = T_P$ ,  $\text{---} = -D$ .

of energy at small  $k$ .) Near  $k = k_\rho$ ,  $C_{PK}$  produces kinetic energy which finally cascades back toward small  $k$  via  $T_\psi$ , a more exact description of path  $e$ .

The region beyond the spectral maximum (magnified) is of interest. The balance there is a (nearly) statistically steady microcosm of path  $e$ , with energy carried to the right by  $T_P$ , converted by  $C_{PK}$ , and then carried back to the left by  $T_\psi$ , lateral vorticity advection. The dissipation is small in  $K < 15$ . As Steinberg suggested from his more viscous runs, the dynamics is far different from a 2D spectral tail.

There is a strong analogy with the meteorologists' concept of cyclone growth, followed by occlusion (vertical uplifting of frontal density surfaces) which causes the upper-level flow to fall into an equivalent barotropic state (similar perturbation streamlines, yet less energy aloft). The transfer of kinetic energy, at the late stages, back to the zonal-average winds, is the analogue of the final red cascade by  $T_\psi$ , and its attendant anisotropy. The sequential nature of these events is related to the observed "index cycle." Steadily forced computer simulations by Steinberg (1973) and Barros and Wiin-Nielsen (1974) form an interesting complement to our spin-down experiments, and some of the energy cycles are very similar. The emphasis in these papers is the nature of the viscous-inertial subrange, which carries potential enstrophy toward dissipation at large wave number.

The character of the transfer spectra is rather insensitive to the physical configuration for given wave number spectrum; this agrees with the appearance of the same cascades in both homogeneous turbulence and an unstable Gulf Stream. An interesting line of theoretical research involves the prediction of transfer spectra from instability analysis, or with turbulent closure models.

The vertical eddy-eddy interactions found here are striking, but they must now be examined in a model with better vertical resolution. A reassuring sign is the recent work of Bass (1974), who has simulated baroclinic instability with channel geometry. His resolution varies from 2 to 16 levels, yet in all cases the development of barotropy may be seen at interior levels. The fluid nearest the rigid top and bottom contains chaotic, energetic "pseudo"-fronts. Bass's experiment, though framed in a meteorological setting, shows some of the richness of vertical structure that we may anticipate in the ocean. Bretherton and Owens (private communication) have also been making multilevel simulations for oceanic turbulence, which will be interesting to compare with the present work.

## 7. Basins and Bottom Topography

The picture developed to this point of the free geostrophic-turbulence cascade would be simple enough to suggest ocean experiments, and to fit directly into a theory that contained forcing, mean flows, and dissipation; however, there are effects of ocean-basin geometry that work against the homogeneity and "narrow-band" evolution of those models. As an example, the vertical structure in the primary experiments developed toward a barotropic state far more rapidly than is consistent with the ocean. We demonstrate here that topography and side walls act to counter several of the nonlinear cascades, and to alter the nature of horizontal propagation.

### A. Coastal Boundaries

First we describe, from the aspect of turbulence theory, the role of idealized slippery coasts. For a single-fluid layer on a  $\beta$  plane the energy invariant remains, yet the relative enstrophy is no longer conserved (although potential enstrophy,  $[\nabla^2\psi + f]^2$ ,

is). Instead (Rhines, 1975), integration over the basin yields

$$\frac{\partial}{\partial t} \int \mathcal{E} dk = \frac{1}{2} \frac{\partial}{\partial t} \iint |\nabla\psi|^2 dx dy = 0 \quad (33)$$

$$\frac{\partial}{\partial t} \int k^2 \mathcal{E} dk = \frac{1}{2} \frac{\partial}{\partial t} \iint |\nabla^2\psi|^2 dx dy = -\frac{1}{2} \beta \oint_{\mathcal{C}} |\nabla\psi|^2 \sin \theta_b ds \quad (34)$$

where  $\theta_b$  is the angle from east of a positive unit vector tangent to the boundary,  $\mathcal{C}$ , upon which  $\psi = 0$ . The source term allows the second moment of  $E(k)$  to increase wherever shoreline lies to the west of moving fluid, and conversely. The "red" cascade, besides being blocked by Rossby wave propagation, can thus be reversed near a western boundary, where eddies or circulation of large scale are transformed to small scale. It amounts to a generalization to unsteady, nonlinear flow of classical arguments for western intensification; with linear Rossby waves, western-wall reflection converts long waves to short, increasing the enstrophy. Combined with the knowledge that small-scale [large-enstrophy/energy] motions propagate slowly, this favors the concentration of both energy and enstrophy in the west, and their removal from the eastern ocean.

In the linear frictional "Gulf Stream" the enstrophy produced according to equation 34 maintains its narrowness while, in a steady state, being dissipated by bottom friction (yet such a current at the eastern side would lose its enstrophy to the coast). The generation of enstrophy by wind stress is negligible in this case. Finally, in the nonlinear, frictionless, free gyres of Fofonoff (1954) a steady solution is made possible by east-west symmetry, enstrophy inflow and outflow just canceling one another.

With two-layer stratification (equations 29-31) the result becomes

$$\frac{\partial}{\partial t} \int (X_1^2 + X_2^2) dx dy = -\beta \oint_{\mathcal{C}} (\hat{K} + \hat{P}) \sin \theta_b ds$$

where

$$X_i = \nabla^2\psi_i + F(\psi_j - \psi_i), \quad j = 3 - i$$

and

$$\hat{K} = \frac{H_1}{2} |\nabla\psi_1|^2 + \frac{H_2}{2} |\nabla\psi_2|^2, \quad \hat{P} = \frac{1}{2} \frac{f_0^2}{g'} |\psi_1 - \psi_2|^2$$

Energy of either form at the coast alters the net "nonplanetary" enstrophy. The cascade arguments, equations 29 and 30, become

$$\frac{\partial}{\partial t} \int E dk = 0$$

$$\frac{\partial}{\partial t} \int k^2 E dk = \frac{-\partial}{\partial t} \int (k^2 + 2F)P dk - \beta \oint_{\mathcal{C}} \hat{E} \sin \theta_b ds$$

$$\hat{E}(\mathbf{x}) = \hat{K}(\mathbf{x}) + \hat{P}(\mathbf{x}), \quad E(k) = K_1(k) + K_2(k) + P(k)$$

The combined effect is clear: both potential-energy release within the body of the fluid and energy at its western periphery can increase the second moment of  $E$ , and move the center of mass of  $E(k)$  to larger wave number.

### B. Rough Bottoms

The final and most difficult topic in the dynamics of eddies is the effect of an irregular sea floor. This works through vertical vortex stretching produced by currents flowing across slopes. The sensitivity to this effect is clear in the intrinsic smallness of the vertical velocity ( $\sim U\varepsilon H/L$  or  $U\omega H/L$ ) under geostrophic scaling, and by the picture of vertical stiffness developed in Section 3. The effect is easiest to see in a hydrostatic, quasi-geostrophic layered model, where equation 16 becomes the conservation law for potential vorticity,

$$\frac{D}{Dt} \left( \frac{h_i \nabla(h_i^{-1} \nabla \psi) + f}{h_i} \right) = O\left(\varepsilon \frac{H}{L}\right)^2$$

for the  $i$ th layer. The two-layer model (equation 27) becomes, in the dimensional variables,

$$\begin{aligned} \frac{D_1}{Dt} [\nabla^2 \psi_1 + F_1(\psi_2 - \psi_1)] + \beta \psi_{1,x} &= \nu \nabla^4 \psi \\ \frac{D_2}{Dt} \left( \nabla^2 \psi_2 + F_2(\psi_1 - \psi_2) - \frac{\delta f_0 \hat{h}_2}{H} \right) + \beta \psi_{2,x} &= \nu \nabla^4 \psi_2 - R \nabla^2 \psi_2 \end{aligned}$$

where

$$F_i = \frac{f_0^2}{g'H_i}, \quad \frac{D_i}{Dt} = \frac{\partial}{\partial t} + J(\psi_i, \quad), \quad h_2(\mathbf{x}) = H_2 + \delta \hat{h}_2$$

The scaling has typical topographic heights ( $\sim H_2 \delta$ ) of order  $\varepsilon$  or  $\omega$ , whichever is larger, and this leads to the retention of depth variations only in the vortex stretching terms (neglecting for example,  $(D/Dt)(\Delta h_2^{-1} \cdot \nabla \psi_2)$ ). As before,  $\delta \sim L/R$  in order that the dynamics include both planetary and topographic waves. In order to consider islands and continental margins,  $\delta \sim 1$ , the depth should be allowed to vary throughout the equations.

### C. Effect on the Primary Nonlinear Cascades

The topography can generate relative enstrophy, fragmenting large eddies into small ones, and thus counter the red cascade of 2D turbulence. The process with weak currents resembles wave scattering by a random medium, but this gives a convergent result only when  $\varepsilon \ll \delta \ll L/R$ , plane Rossby waves being the first approximation. But neither inequality is valid for the energy-containing eddies. Figure 32 is a schematic diagram of the parameter space ( $\varepsilon, \delta R/L_H, kL_H$ ) for a single-layer fluid with topography of dominant horizontal scale  $L_H$ . Near the base plane are found linear solutions, with weakly scattered Rossby waves at the left (I) (Thompson, 1975; Rhines, 1970) and topographic Rossby waves (geometrical optics, short waves) (Smith, 1971) at the far right (III). The range II,  $\varepsilon \ll \delta \gtrsim L/R, kL_H \sim 1$ , represents linear oscillations in a very irregular medium, in the worst case being a kind of topographic "turbulence" (Rhines and Bretherton, 1974).

Above the base plane nonlinearity acts, approaching 2D turbulence above  $\varepsilon \sim \delta + (kR)^{-1}$ . The evolution of solutions is, as in Fig. 19, to the left in the turbulent region (arrows), until meeting the transition surface where they tend to stagnate. Yet below, solutions tend to move to the right by scattering and refraction. The representation of a wave number spectrum by a single length scale is less convincing here, however, than

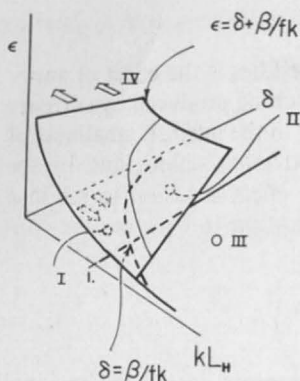


Fig. 32. The role of rough-bottom topography (for simplification, with single scale  $L_H$ ) in homogeneous fluid motions. Sufficiently intense flows ( $\varepsilon \gg \delta + \beta/k$ ), region IV, act as 2D turbulence, cascading to the left (arrows). Gentler flows are increasingly fragmented by roughness and migrate to the right.  $\beta = f_0/R$ .

in Section 6. For spectral broadening develops from interaction of energy at wave number  $k$  and topography at wave number  $\mu$ , producing energy at wave number  $k \pm \mu$ . Typically, topography has a rather flat spectrum,  $H(k) \sim k^{-1.5}$  or  $k^{-2}$ , which quickly "whitens" the energy spectrum, although favoring transfer to large  $k$  (in fact,  $H \propto k^{-2}$  is a white slope spectrum).

In the stratified problem, topography may affect the structure in the vertical as well as the horizontal. Though the nonlinear effects direct energy toward large vertical scale in the interior, the coup de grace, the destruction of vertical shear (path  $d$  and  $e$  in Fig. 19) is no longer so likely; the disappearance of the barotropic wave type 1 when  $kL_\rho \gtrsim 1$ ,  $\varepsilon \ll \delta$  is evidence. In its place arise baroclinic waves 2 and 3, of both large and small frequency.

I carried out a series of spin-down experiments to explore the rough bottom eddies, and these have revealed a number of properties of relevance to the ocean. The topography, of rms amplitude 200 m (Fig. 33a) is randomly generated with a  $k^{-1.5}$  scalar-wave number spectrum, cut off at  $k > 8$  (relative to the domain width of  $2\pi$ ). This is just at the deformation scale,  $L_\rho = (F_1 + F_2)^{-1/2}$ , set to be 40 km, with the "ocean" width 2000 km. The contours of  $f/h_2(x)$  (Fig. 33b) show the potential vorticity gradients due to  $\beta$  and  $h_2$  to be comparable, with occasional closed contours appearing. The degree of openness of these contours is crucial to the processes of horizontal propagation and mean-flow induction (Section 8). As in many of the earlier experiments, an initially narrow-band field of eddies was allowed to evolve freely for 200–500 days, with mild damping, and without driving. Here the evolution of deformation-scale eddies, very large initial eddies, and linear waves are separately described, as is another series of inhomogeneous runs in which horizontal propagation is important.

#### D. Deformation-Scale Eddies

A typical case (Fig. 34) starts with eddies slightly bigger than the deformation radius above the thermocline and still fluid below. In this instance the currents are not strong, ( $U_1 \sim 15$  cm/sec,  $U_2 = 0$  at  $t = 0$ ) but still significantly nonlinear, representative of the western Atlantic at  $30^\circ\text{N}$ . The initial adjustment phase occupies about 3 months [ $\sim (U_{\text{rms}} k_\rho)^{-1}$ ], during which the deep ocean is set into motion. But unlike the flat-bottom case, this development is halted by the irregularity of  $f/h$  (even though the "islands" of  $f/h$  are few). The layers become detuned by the topography so that the barotropic mode is a stable vertical structure only at large

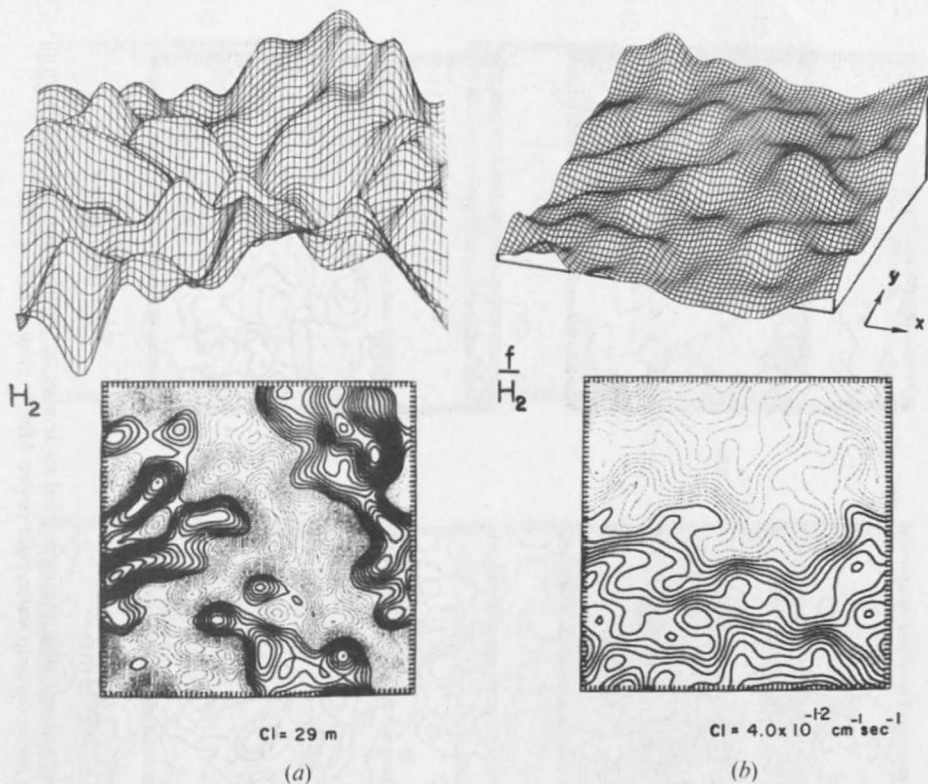


Fig. 33. Perspective plot and contours of topography (a) and  $f/h_2$  (b) for succeeding experiments. The depth has standard deviation 200 m ( $\delta = 0.053$ ), or a typical bottom slope equivalent to  $\beta$ . (Actually (a) shows minus the topography; a ridge runs southeast through the central region.) Later, flows will be shown responding to the large rise seen at the western end of  $y = 0$ . The box is 2000 km wide. The domain is 2000 km across. Topography of scale smaller than 40 km was omitted, even though it may be important.

scales, far from the activity at  $k_\rho$ . If in the theory, Section 6, demonstrating the necessary increase in barotropy, we add a fine-grained pattern of topographic potential vorticity with  $\delta \gtrsim \varepsilon$ , the argument is destroyed.

To grasp the gross sensitivity of these results to energy level, compare the evolution in Figs. 34 and 35. The sole difference is the addition of an initially weak eddy field below the thermocline, in Fig. 35. The more energetic run has rms  $|U_1| = 15.3$  cm/sec,  $|U_2| = 4.1$  cm/sec, and no great reservoir of potential energy. It is still a plausible intensity for the oceans. Yet the eddies succeed in interacting vertically, tending toward barotropy, expanding horizontally, and developing stronger anisotropy and  $f/h$  contour flow, practically oblivious to the roughness.

As it is, in the weakly energized flow (Fig. 34) one can spy the primary cascade working in limited regions for limited times, over unusually flat  $f/h$  topography, or in a region of unusually strong current (see also Fig. 37). A remarkable feature of this flow, and those seen earlier, is the persistence of westward phase propagation well into the nonlinear regime (Fig. 41). This is particularly so in the thermocline eddies, type 3, which dominate the upper level currents and the thermocline height. There the phase

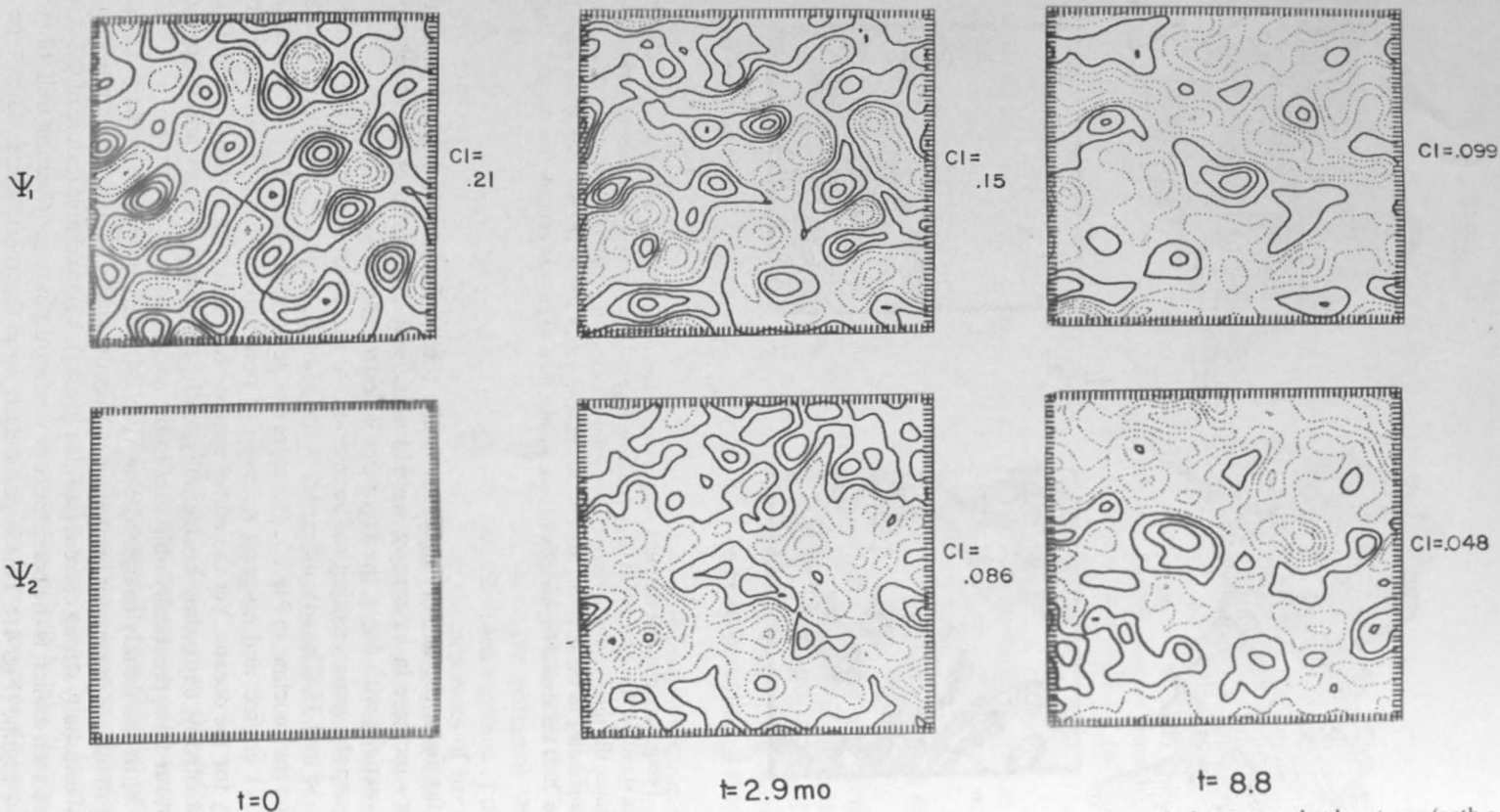


Fig. 34. Spin-down of deformation-scale eddies,  $U \sim 15$ , deep layer initially at rest. The uneven sea bed so detunes the vertical structure that barotropy (path  $e$ , Fig. 19) is now prevented. Note the anticyclone trapped over a predominant rise in the deep water, right center. After 7 months,  $K/P = 0.85$ .

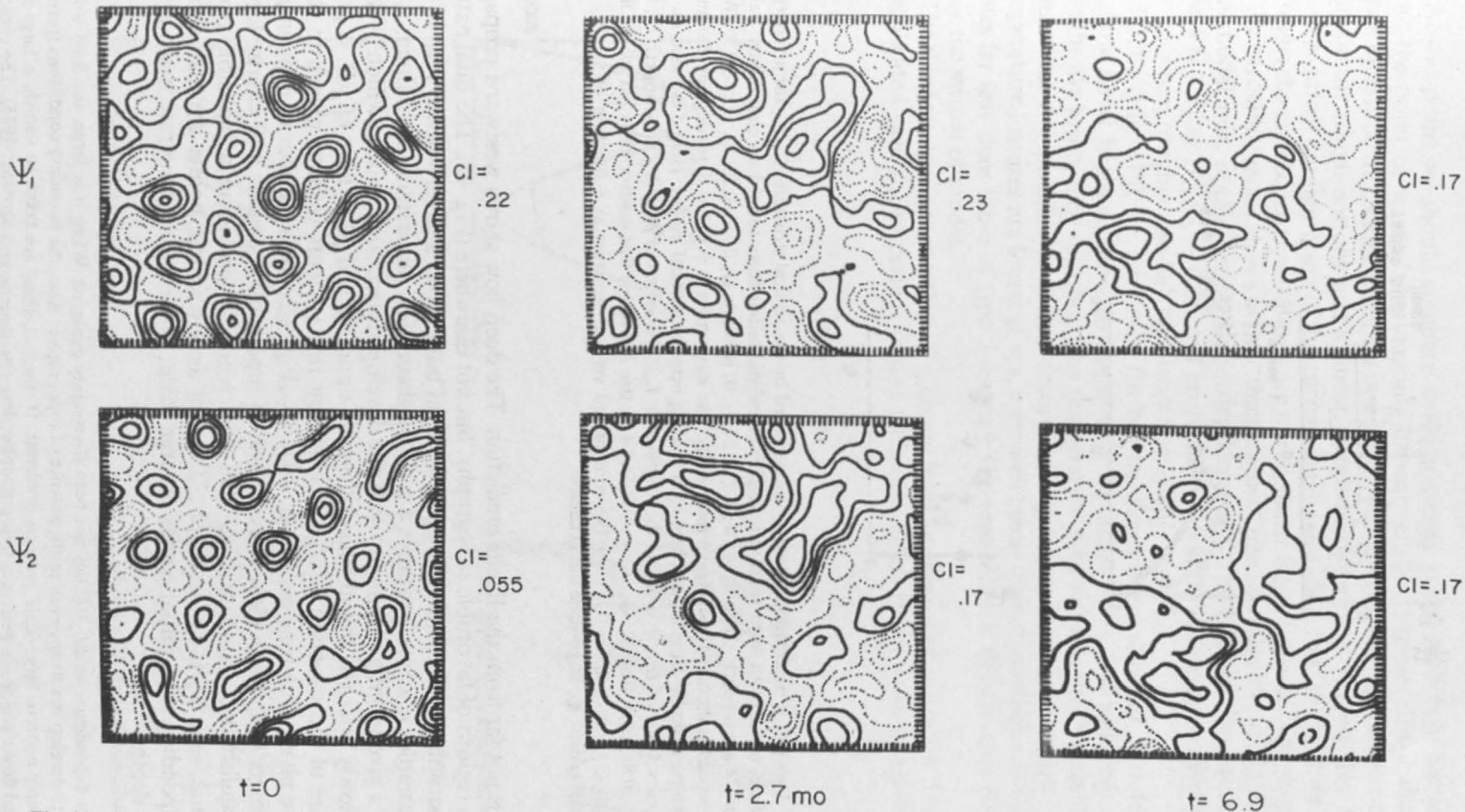


Fig. 35. When a 4-cm/sec eddy field is added to the deep layer, it raises the energy level enough to regain the "flat-bottom" cascade. After 7 months,  $K/P = 12.3$ .

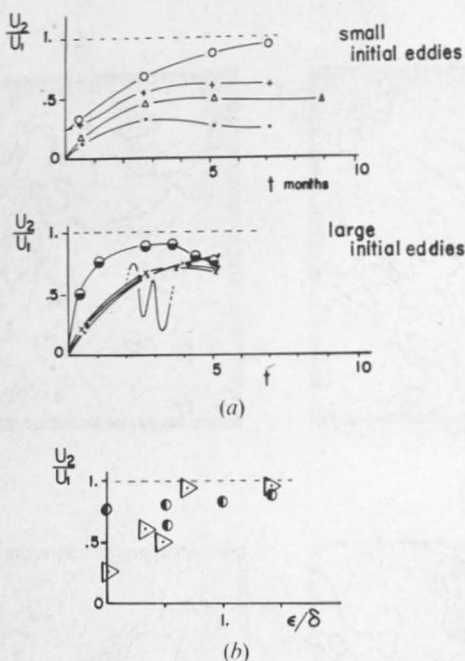


Fig. 36. Downward penetration of energy, as measured by the vertical structure,  $U_2/U_1$  for a variety of values of  $\epsilon/\delta$ . (a) Growth from small-scale highly baroclinic initial flows toward an equilibrated value. Values of  $\epsilon/\delta$  are (upper):  $\circ$ , 0.70;  $+$ , 0.34;  $\triangle$ , 0.51;  $\cdot$ , 0; (lower):  $\ominus$ , 0;  $\times$ , 0.50;  $\nabla$ , 1.0;  $\cdot$ , 0.50. With large initial eddies the energy penetrates more easily. The wavy curve ( $\epsilon = 0$ ,  $\delta = 0$ ) reminds us that linear effects can periodically alter  $U_2/U_1$ , here by a beating between vertical modes. Here  $\epsilon$  is based on the vertical r.m.s. value of  $U$  at  $t = 0$ , and the length-scale  $L_\rho$ . The values of  $\beta L_\rho^2/U_2$  are, (upper):  $\circ$ , 0.6;  $+$ , 0.8;  $\triangle$ , 0.8;  $\cdot$ , 0.8; (lower):  $\ominus$ ,  $\infty$ ;  $\times$ , 0.9;  $\nabla$ , 1.4;  $\cdot$ , 0.6. A triangle was inadvertently left off the final graph, ( $U_2/U_1 = 0.31$ ,  $\epsilon/\delta = 0.17$ ). (b) The equilibrated vertical structure as a function of  $\epsilon/\delta$ .  $\triangleright$ ,  $L_\rho$ -scale initial eddies;  $\bullet$ , large-scale initial eddies.

speed is not far from the linear prediction. The deep flow shows westward propagation in regions of favorable topography, but not elsewhere (Fig. 41). The dual nature of geostrophic eddies, exhibiting properties of both waves and turbulence even in the most complex of cases, promises a growing theoretical understanding of them.

For a given configuration at  $t = 0$ , the developed vertical structure (which evolves very slowly after the initial phase) depends upon  $\epsilon/\delta$  and  $\beta L_\rho^2/U \equiv \epsilon L_\rho/R$ . A gross measure of the structure is  $U_2/U_1$ , based on rms currents without regard to their relative phase. The time evolution of  $U_2/U_1$  (Fig. 36a) for a number of experiments (with fixed  $\beta$ ) shows a clear dependence on topographic heights and energy level.<sup>7</sup> The equilibrated structure (Fig. 36b) rises with  $\epsilon/\delta$ , providing a plausible ocean structure, say,  $U_2/U_1 = \frac{1}{3}$ , at  $\epsilon/\delta \lesssim 0.5$ . But as a warning, points are also shown corresponding with initial eddies of large scale; these clearly penetrate more easily to the depths.

<sup>7</sup> The dependence on  $\beta L_\rho^2/U$  has not been thoroughly explored. When it is large, the fluid will be unable to develop barotropy even in the absence of topography. Also, the boundary conditions (periodic in  $\psi$ ) imply nonzero large-scale pressure gradients. If, instead, these are taken to vanish, a large-scale westward flow develops in response to topographic drag (Bretherton and Karweit, 1975). The choice of boundary conditions (periodic  $\psi$  or periodic velocity) is moot.

At this point we should compare fields predicted in the models of Sections 5-7 from the point of view of the seagoing experimentalist. Figures 37*a-d* show time series measured at a single mooring in a linear, flat-bottom, a nonlinear flat-bottom, a nonlinear rough-bottom, and a linear, rough-bottom ocean, respectively. In each case the initial configuration of the current is the same as in Fig. 34. First, with weak currents the subsequent oscillations are purely linear Rossby waves. The long period of the baroclinic mode shows in the "temperature" (the interface elevation), and, with this modal mix, dominates the upper-level currents. The average vertical structure obeys  $U_2/U_1 = H_1/H_2 \sim 0.28$ , and evolves as soon as the two modes separate from one another, roughly one-half barotropic period.

Second (Fig. 37*b*), the bottom is flat but the currents are stronger. The deep and shallow flows begin to move in apparently unrelated ways, but suddenly, after 4 months the layers lock together. The temperature field exhibits much faster oscillations than are possible in linear theory, owing to horizontal advection. [Sharp temperature features are found at sea, even well below the surface (Fig. 63) with time scales far less than those of type 3 waves.] The time scale of the currents decreases after the switch of modes.

The third comparison run (Fig. 37*c*) comes from an ocean with  $\varepsilon/\delta \approx 0.4$ . This most complicated case shows periods during which the layers begin to lock together, but

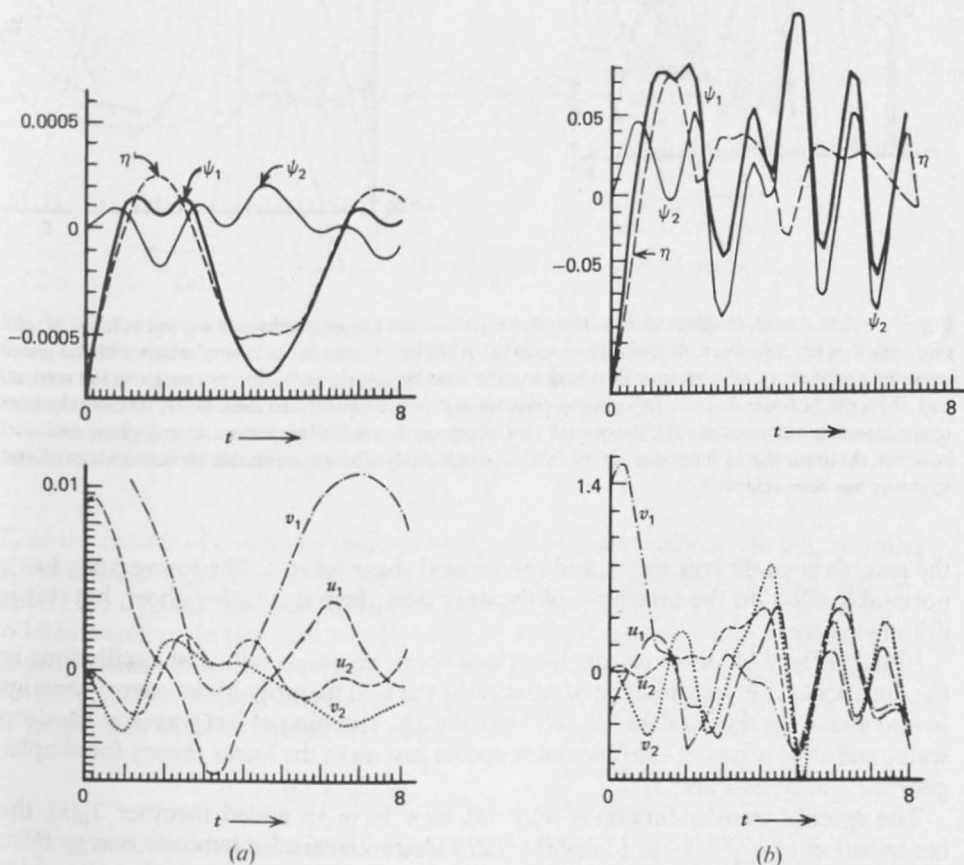


Fig. 37. "Mooring" records from computer experiments. (a) A linear constant-depth ocean; (b) nonlinear, constant depth.

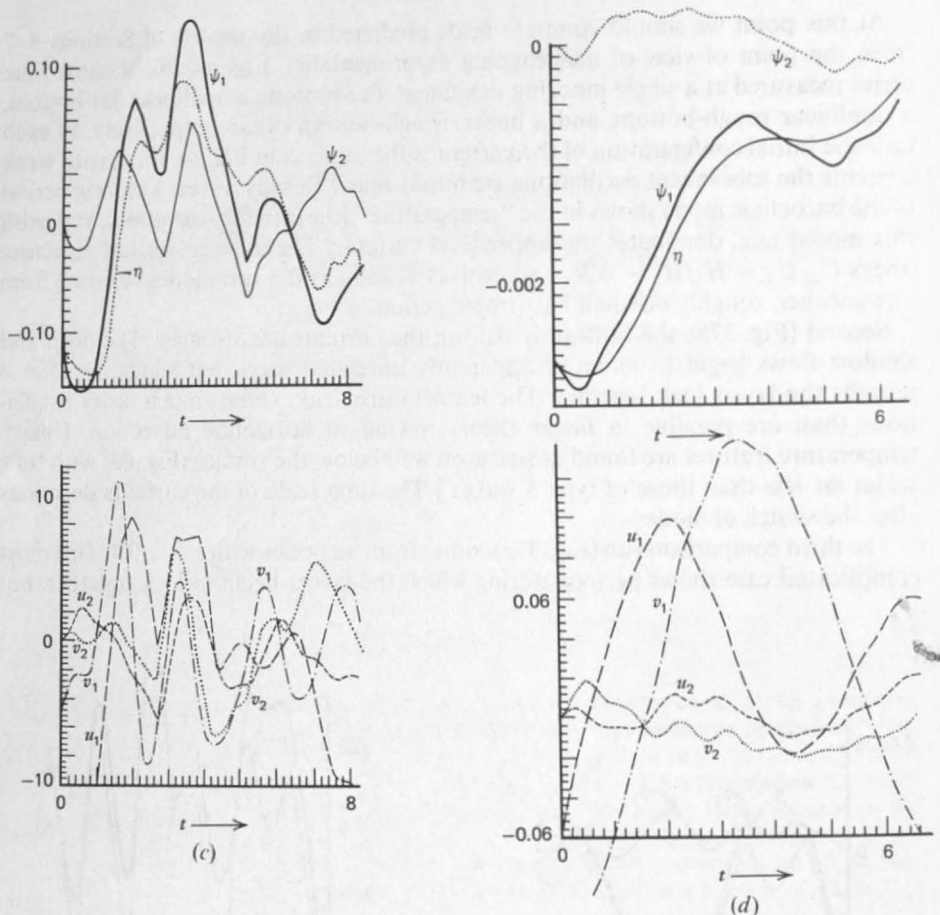


Fig. 37. (c) nonlinear, rough bottom; (d) linear, rough bottom. Upper graphs give  $\psi_1$ ,  $\psi_2$ ,  $\eta$ ; lower graphs give velocities (cm/sec). Note different abscissa in (d). Although there are crude similarities with the linear solution, nonlinearity adds shorter time scales to the density signals, redistributes energy in the vertical, and alters the horizontal scale; topography confines fast oscillations to the deep layer, whitens the horizontal spectra, and counters the downward flow of energy from shallow water. At any given moment, however, the linear theory has some partial validity, particularly after a comfortable vertical and horizontal structure has been achieved.

the records soon diverge again, and the vertical shear returns. The topography has a noticeable effect on the time scale of the deep flow; here it is rather short, but this is not always true.

Finally (Fig. 37d), a *linear* rough-bottom ocean responds with fast oscillations in the deep water. Yet for these initial conditions the vast majority of the energy remains in and above the thermocline ( $U_2/U_1 \sim 0.33$ ). The trapping of fast waves in the deep water and slow waves in shallow water occurs just as in the linear theory for simpler geometry, in types 2 and 3.

The spectral transfer functions (Fig. 38), now have an added member  $T_H(k)$ , the contribution of  $U_2 \nabla \cdot h_2$  to  $(\partial/\partial t)E(k)$ .  $T_H(k)$  characteristically removes energy from the spectral maximum of  $K(k)$ , sending it predominantly to large  $k$ . The dynamics of the spectral tail is different from the flat-bottom ocean (Fig. 31). Now  $T_H$  replaces

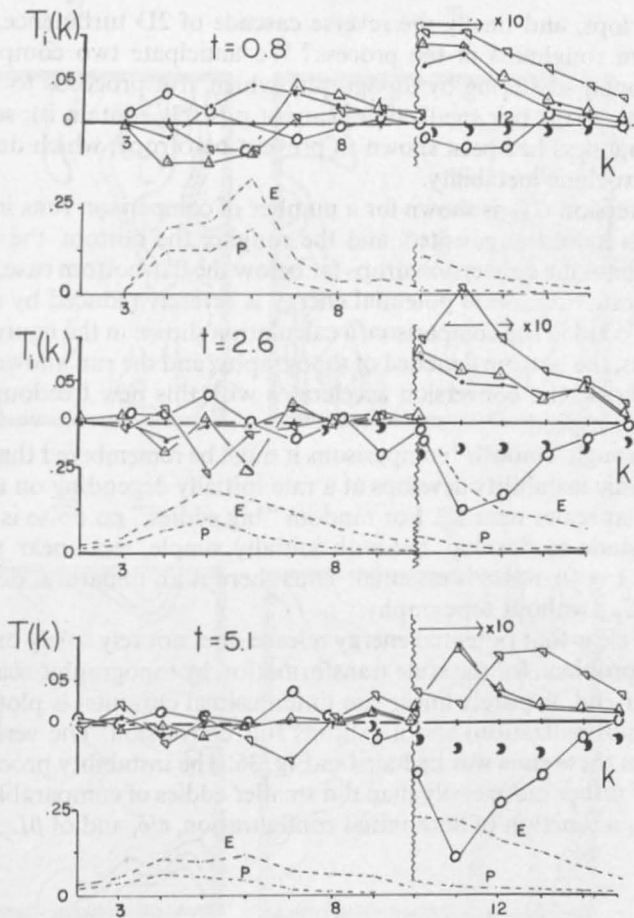


Fig. 38. Transfer spectra with topography, for an experiment with  $L_p$ -sized eddies, initial  $U_2 = 8.0$ ,  $U_1 = 2.7$  cm/sec. Compare Fig. 31 (here  $\nabla$  is  $T_H$ ). The basic shapes of  $T_\psi$ ,  $T_p$ , and  $C_{PK}$  are as before, yet they are relatively smaller, and barotropy fails to develop (compare  $E$  and  $P$  spectra). Topographic scattering broadens the spectra, relative to Fig. 31, sending energy to large wave number. The spectral "tail" (magnified) now has totally different dynamics:  $T_H$ , rather than  $T_p$ , carries the energy to the right and  $T_\psi$  returns it to the left. Dissipation is small throughout  $K < 14$ .

$T_p$  as the carrier of energy to large  $k$ , yet  $T_\psi$  still carries it back to the left, allowing a quasi-steady "topographic" subrange. It reduces the amount of energy carried to small  $k$  (by  $T_\psi$ ), and seems to reduce both the magnitude of  $T_p$  and the conversion  $C_{PK}$  to kinetic energy. In this manner, the progress of the fluid along the paths in Fig. 19 is impeded, and sometimes reversed. The flow evolves slowly after initial adjustment, but the persistent broadening due to  $T_H$  suggests that a true equilibrium spectrum will be impossible without forcing and dissipation.

### E. Initially Large-Scale Eddies

Those baroclinic eddies with diameter greater than about 150 km contain an excess of potential energy. Conversion into deformation-scale flow is the dominant non-linear process, followed, with bottom flat, by further conversion to kinetic energy as

barotropy develops, and finally the reverse cascade of 2D turbulence. What is the effect of bottom roughness in the process? We anticipate two competing effects: first, the horizontal scattering by topography which, if it proceeds to large  $k$ , must release potential energy (for small eddies cannot possibly contain it); second, and in opposition, roughness has been shown to prevent barotropy, which develops in the late stage of baroclinic instability.

The net conversion  $C_{PK}$  is shown for a number of comparison runs in Fig. 39. The initial release is indeed augmented, and the rougher the bottom, the more so. But in the second phase the conversion drops far below the flat-bottom case, as suggested. The time-integrated release of potential energy is severely reduced by the inhibition of barotropy. To aid in the comparison, a calculation shown in the figure was stopped at  $t = 2$  months, the bottom denuded of topography, and the run allowed to proceed. After a brief shock, the conversion accelerates with this new freedom, as the deep layer comes up to speed.

In making "rough-smooth" comparisons it must be remembered that the smooth-bottom baroclinic instability develops at a rate initially depending on the amount of noise specified at scales near  $L_p$ . For random "big eddies," no noise is necessary for the energy cascade to develop, but with initially simple, rectilinear patterns (here  $\psi_1 \propto \sin 2x$  at  $t = 0$ ), noise is essential. Thus there is an unnatural delay in the development of  $C_{PK}$  without topography.

It should be clear that potential energy release does not rely solely on nonlinearity ( $\mathbf{u} \cdot \nabla \eta$ ) in this problem, for the scale transformation by topographic scattering brings about a similar end. A purely linear run (infinitesimal currents) is plotted in Fig. 39 (with its own normalization) and it exhibits this conversion. The vertical structure resulting late in these runs was included in Fig. 36. The instability process penetrates the deep water rather more easily than did smaller eddies of comparable energy, thus making  $U_2/U_1$  a function of both initial configuration,  $\varepsilon/\delta$ , and of  $\beta L_p^2/U$ .

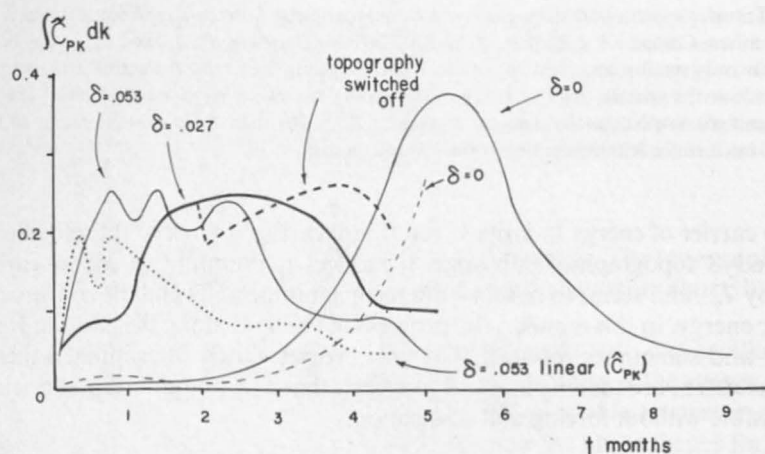


Fig. 39. Total conversion from potential to kinetic energy versus time, for three values of topographic height,  $\delta$ ; large-scale initial eddies. The stronger the topography, the greater the initial conversion (due to deep scattering) yet the less the total conversion (the area beneath the curves).  $C_{PK}$  is a nonlinear effect in a flat-bottom ocean, but here occurs also with purely linear motions.  $\tilde{C}_{PK} = C_{PK} P_0^{-3/2} k_p k_0^{-2}$ , ( $P_0$  = initial potential energy), ( $k_0$  = initial wave number)  $\hat{C}_{PK} = C_{PK} P_0^{-1}$ .

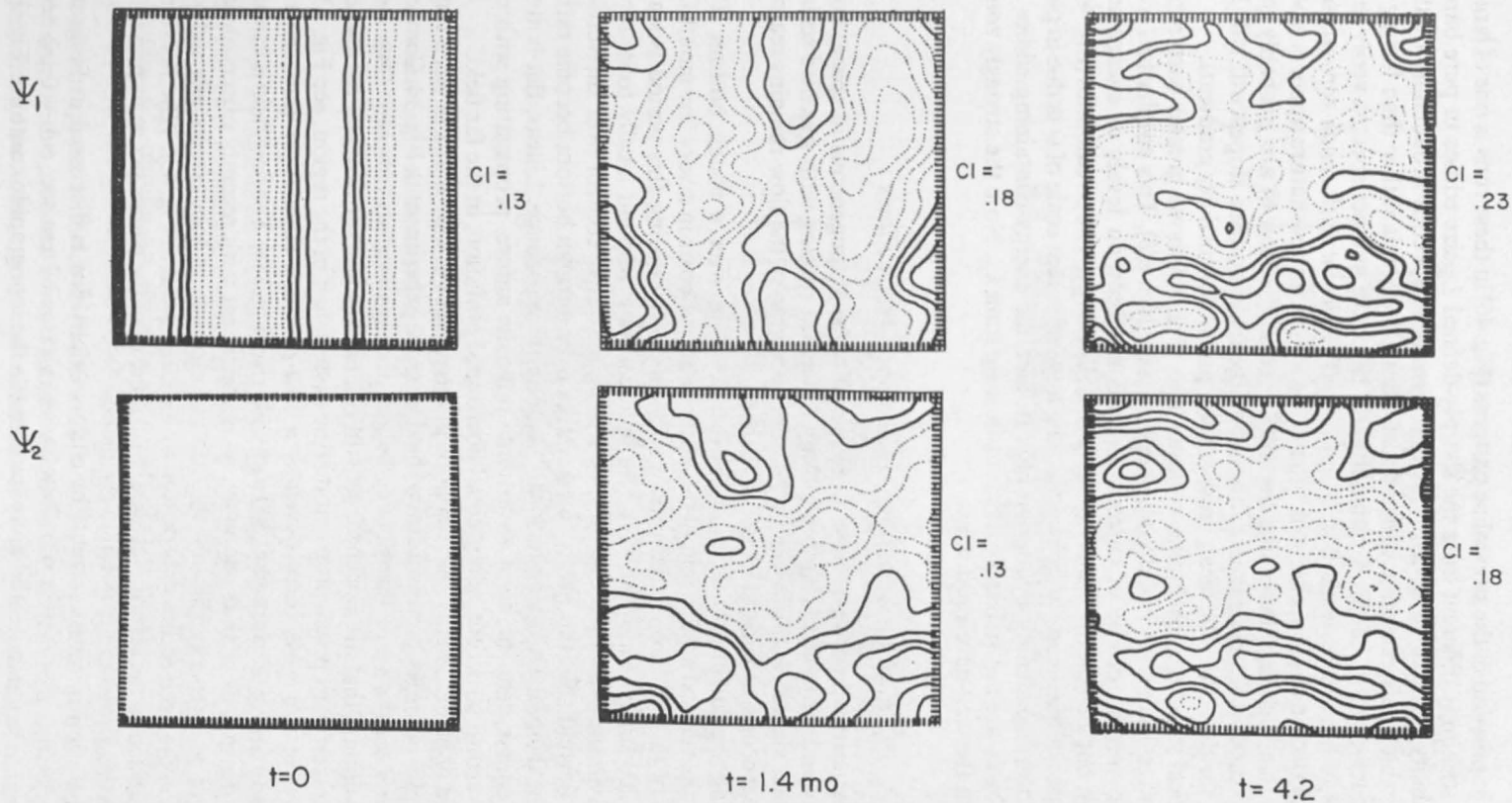


Fig. 40. Flow patterns for rough-bottom baroclinic instability,  $\delta = 0.027$ ,  $\varepsilon/\delta \approx 1.0$ . The large scale of the developing flow (relative to Fig. 25, flat bottom) comes as scattering carries energy continuously toward large  $k$  rather than jumping to  $k = k_p$ .  $f/h$ -Contour flow and a significant amount of deep-water energy develops ( $U_2/U_1 \rightarrow 0.7$ ).

A visual impression of the streamline patterns (Fig. 40) in these runs is one of large-scale flow, strikingly different from the sharply defined  $L_\rho$ -size eddies in pure baroclinic instability (compare Fig. 25). This is the result of spectral broadening by the roughness, which carries energy continuously along the  $k$  axis rather than having it leap to the deformation radius. Examination of the wave number spectra verify that the process of baroclinic instability is *intrinsically different with rough topography*, even though the  $f/h$  contours are still "open." As above, its new nature appears when  $\epsilon/\delta \lesssim 1$  so that vigorous flows like the Gulf Stream (Section 6) are probably less affected by small-scale roughness (although large-scale bottom slopes will still be important, for they alter the mean cross-stream potential-vorticity gradient).

The vertical structure developing in these flows (Fig. 36) shows greater barotropy, on the average, than with initially small eddies (for given  $\epsilon/\delta$ ). This emphasizes that the oceanic vertical profile of current depends not only on levels of energy and topography, but also on the *manner of supplying the energy*. The streamlines (Fig. 40), show a degree of barotropy at large scale. The huge apparent scale of  $\psi$  is due in part to the spectral broadening by topography. In fact, the energy-containing eddies as measured by  $k_1$  are not strikingly different in scale from  $k_\rho$ . Note the strongly zonal character to the well-developed flow.

### F. Fine Structure, Anisotropy, Mean Flows

The experiments described above were meant to be homogeneous in space; both topography and initial fields have randomly generated spectra, with specified scalar-wave number shape. Without uneven bottom topography the flow remains reasonably homogeneous, at least in its energy density.

A striking spatial intermittency, however, develops over a rough bottom. The result that the vertical adjustment of the water column occurs in a very few months, is suggestive of this, in that spatial propagation of energy during this period is small (less than 200 km in 2 months, say). The fluid can thus respond locally to its topographic environment, which Fig. 36 shows to be a decisive control over the vertical structure. Beyond this, the purely linear waves over a rough bottom become rather intermittent themselves, owing to local "seamount" resonance. Linear, flat-bottom waves, of course, tend to be of an extreme opposite nature, propagating with unchanging vertical structure, and gradual horizontal evolution, in the far field.

The kind of heterogeneity that develops in the current is shown in Fig. 41, a time-longitude plot of the deep pressure (or  $\psi$ ) field from the experiment in Fig. 34. Compare it with the smoothness of thermocline-height propagation, also shown. Over geostrophic contours that are bunched, yet still run east-west, there are fast oscillations and a clear westward phase propagation (the eastern half of the region; see Fig. 33b). Conversely, in the west there develops a low-pressure circulation that remains nearly steady, above the dominant 300-km-wide rise (Fig. 33b). The flow field is variable in energy density, as well as character, as is consistent with recently observed fine-structure of eddy energy (Section 9). Another example of topographically induced spottiness in the deep eddies may be seen by looking ahead to Fig. 43f. Whether or not one is interested in the erratic statistical distribution of the eddies per se, it presents a severe aliasing problem for ocean experiments.

The generation of mean currents by eddy vorticity-flux is discussed in Section 8. An example with  $\beta = 0$  (Fig. 42) shows a weak ( $U_2 \sim 2$  cm/sec,  $\epsilon/\delta \sim 0.14$ ) deep-current field to begin more and more to resemble the topographic contours (Fig. 33a) with time. G. Holloway (private communication) has shown this condition to be

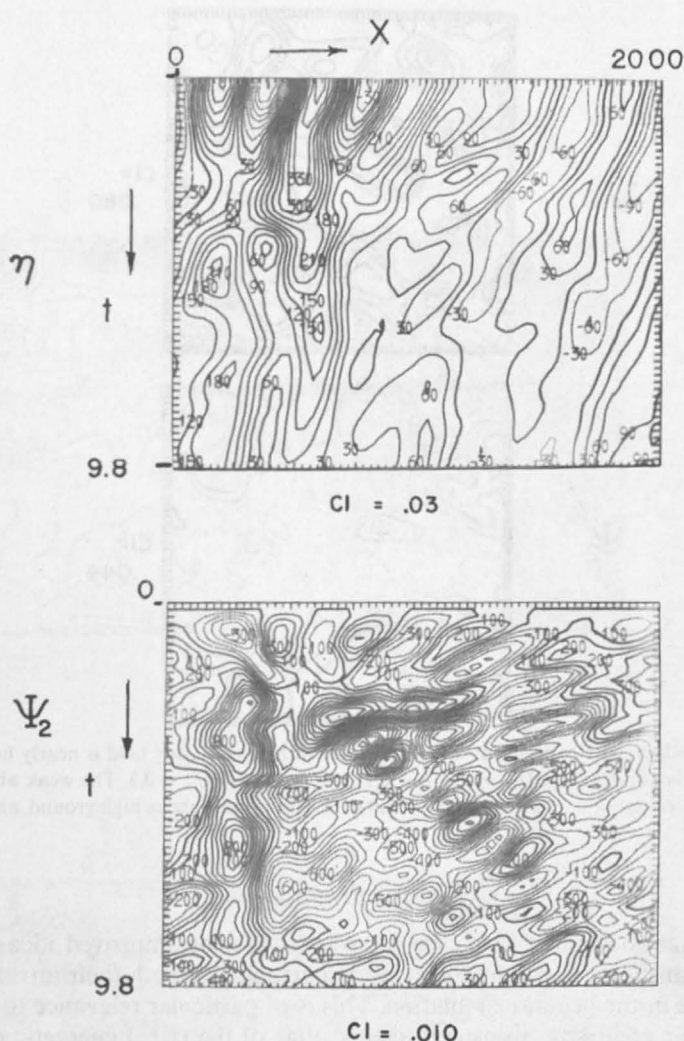


Fig. 41. Time-longitude plots of  $\psi_2$  and  $\eta$ , from the southernmost latitude shown in Fig. 33. The topography causes a natural inhomogeneity in the deep water: unusually fast oscillations in one area, yet a strong anticyclone trapped above a ridge in another. The thermocline eddies are less disturbed, and propagate westward with occasional episodes of vertical interaction.

reliable in a single-layer fluid, and it seems to be the generalization to  $f/h$  flow of the zonal currents appearing spontaneously throughout Section 6. He points out that, with  $(\zeta + fH/h)^2$  conserved for at least the initial period, an increase in relative enstrophy,  $\overline{\zeta^2}$ , implies an initially growing negative correlation between  $\zeta$  (and hence  $\psi$ ) and the geostrophic contours,  $(\partial/\partial\tau)\overline{\zeta f/h} < 0$  (the overbar is integration throughout space). In fact, we have shown  $\overline{\zeta^2}$  to increase owing to either topographic scattering or the presence of energy at a western boundary. This suggests both the appearance of persistent gyres about small seamounts and, on the large, appearance of basin-scale circulation with  $\overline{\zeta y} < 0$  ( $f = f_0 + \beta y$ ); see Section 8.

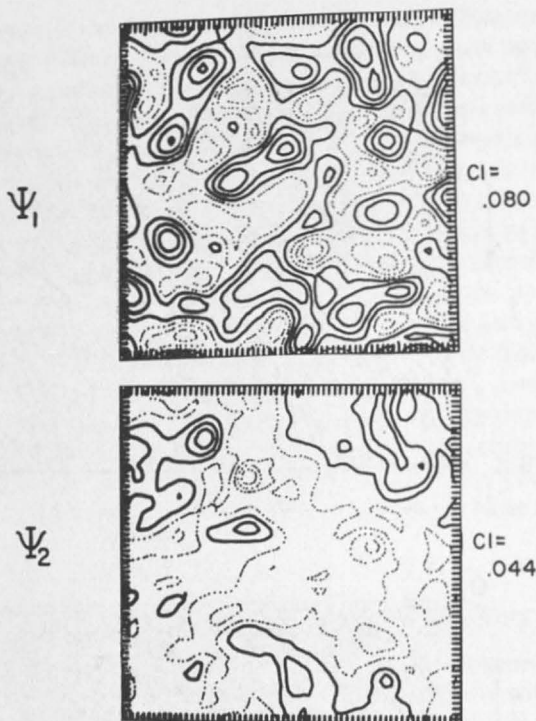
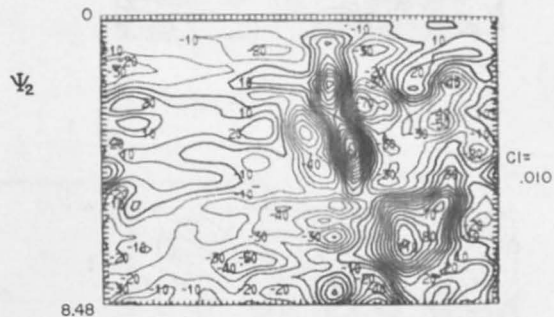
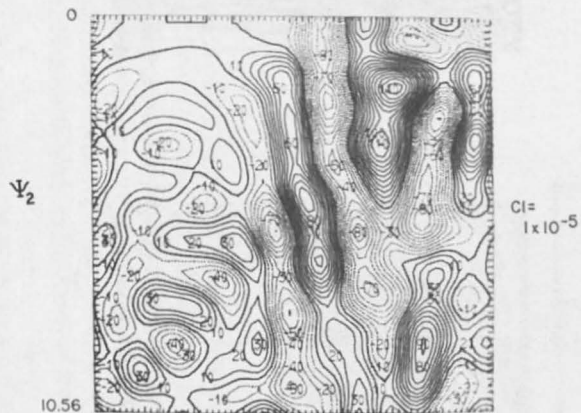
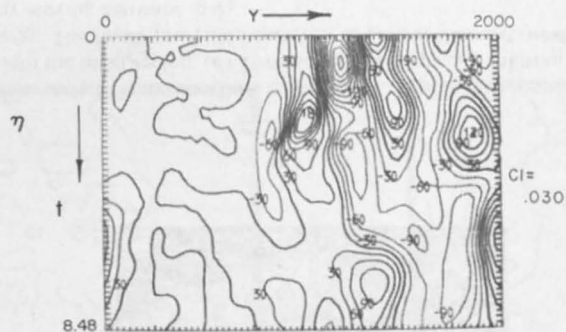
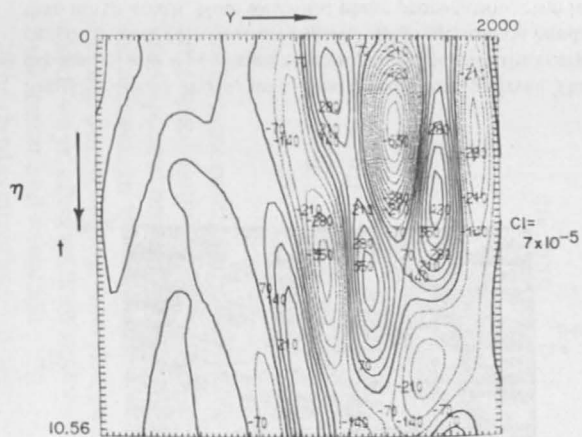


Fig. 42.  $\psi$  fields late in an experiment with  $\beta = 0$ . The rather weak eddy field is nearly held above the thermocline by the topography,  $U_1^0 = 9.3$ ,  $\delta = 0.11$ ,  $v/\delta = 0.4$ ,  $U_2/U_1 \rightarrow 0.3$ . The weak abyssal current develops toward a contour circulation (see Fig. 33a) with anticyclones above high ground, and conversely.

### G. Lateral Propagation

One motivation for this kind of work was to develop improved ideas about the horizontal transports of energy by unsteady currents, for both their intrinsic interest and their role in the general circulation. This is of particular relevance to the oceans owing to their great size, measured against that of the  $O(L_p)$  energetic eddies, and to the sparse distribution of really active energy sources. Estimates of travel time from a conjectured source of energy are often made from linear, flat-bottom theory. But what the experiments have shown most conclusively is that nonlinearity and topography can act to transform these scales, and the mix of vertical modes, in a rapid fashion.

We have initiated some further experiments with oceans initially one-half full of eddies, to provide information about the energy velocity and to suggest what the appearance of eddies arriving from a distant source should be. The energy was initially placed above the thermocline in deformation-scale eddies, occupying 1000-km bands separated by equal areas of quiet ocean. Time-latitude sections, (Figs. 43a-c) show the intrusion of energy from the north and south. Figure 43a is linear, with a flat bottom; the tilted contours indicate northward phase propagation, hence southward group velocity. After 250 days the barotropic mode has brought some energy into the quiet region, but the baroclinic mode has made only a meager contribution (the largest north-south group velocity of the baroclinic mode is  $\beta/4(F_1 + F_2) \sim 0.8$  cm/sec).



(a)

(b)

Fig. 43. Time-latitude plots of  $\eta$ ,  $\psi_2$ , showing propagation from an active east-west band into a quiet one (periodic boundary conditions). (a) Linear flat bottom. The greater speed of barotropic waves is visible in  $\psi_2$ . (b) Nonlinear, rough bottom. The north-south propagation is somewhat inhibited.

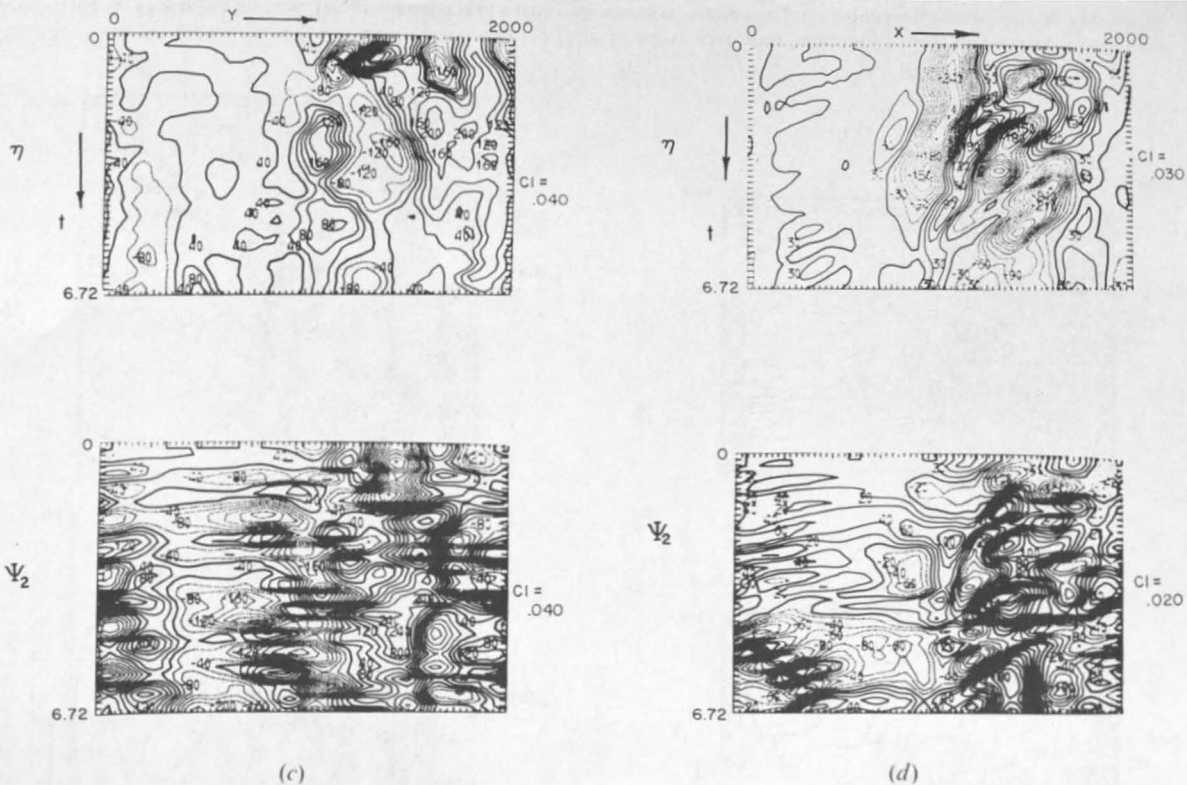


Fig. 43. (c) As above, yet a greater initial energy level. The nonlinear switch from baroclinic to barotropic modes, horizontal expansion, and  $C_{PK}$  release all combine to increase the energy flux into the quiet region. (d) Time-longitude maps of nonlinear, rough-bottom, east-west propagation from meridional bands of energy. The linear prediction survives, of greater flux east-west than north-south. Note westward phase propagation, even for energy moving eastward in  $\psi_2$ .

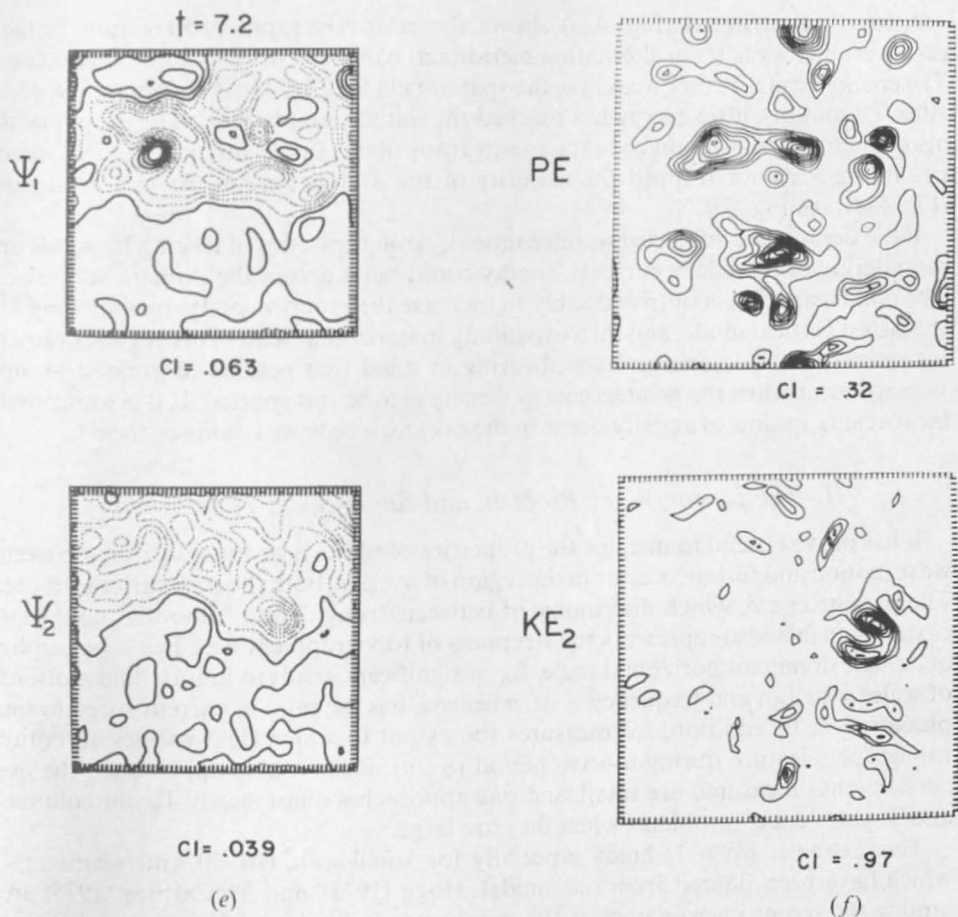


Fig. 43. (e)  $\psi$  Fields for experiment (b). Southward propagation has been slight after 7 months. There is a zonal-average Eulerian zonal flow in both layers, related to the eddy-flux of potential vorticity (Section 8). (f) Maps of potential and deep-kinetic energy in the east-west experiment in (d),  $t = 6.9$ . A 250-km-wide seamount has trapped 95% of the deep energy in a single eddy (it also affects (e)).

The same configuration of currents was set off over a rough bottom, with rms upper-level speed initially of 7.4 cm/sec (Fig. 43b). The propagation is less orderly, as the usual spectral broadening occurs. The thermocline eddies are at least as slow as in the linear case. In the deep water, rather less energy reaches the empty region than before, due to topographic backscatter and distortion. The topography works in subtle ways, affecting both vertical and horizontal scale of the fluid, as well as causing backscatter and refraction.

The third comparison run (Fig. 43c) illustrates the crucial influence that nonlinear scale transformations can exert. Here the current speed is initially 14 cm/sec in the upper ocean, 13 cm/sec below, so that the topographic resistance to barotropy is ineffective. The eddies switch modes and in doing so augment greatly their group velocity. The empty region is filled within 200 days, suggesting an effective north-south group velocity of about 5 cm/sec.

A fourth experiment (Fig. 43d) shows the relatively rapid propagation in the east-west direction, from alternating meridional bands of energetic and quiet ocean. The energy level is rather weak, yet the spatial field for Fig. 43c is shown in Fig. 43e. After 7.2 months, little energy has reached the initially empty fluid. The deep flow is again intermittent, with much of the energy trapped in a single anticyclone. This same rise in the sea floor trapped the majority of the deep energy in the east-west run (Fig. 43d); see Fig. 43f.

If the ocean were subjected to intermittent, strong episodes of forcing by winds or meandering of boundary currents, energy could burst across the domain with ease. The nonlinear effects contrive doubly to increase the group velocity, by switching to the fastest vertical mode, and then expanding in horizontal scale. This suggests rather intermittent far-field energy levels, bearing in mind that periods of greatest group velocity occur when the greatest energy density is to be transported. Is it possible that far-reaching spasms of activity occur in the oceans, if only we could see them?

#### H. The Linear-Wave Problem and Small-Scale Topography

It has proved useful to imagine the properties of eddies near the transition between wave motion and turbulence, for in the region of overlap, both theories can contribute. The parameter  $\varepsilon/\delta$ , which discriminated between "rough" and "smooth" nonlinear cascades, in fact also represents the steepness of topographic waves. For topography of a single dominant horizontal scale,  $L_H$ , if significant, tends to induce fluid motions of scales near  $L_H$ , and frequency  $\sim \delta f$ , whence  $\varepsilon/\delta$  is the ratio of current speed to the phase speed. In addition,  $\varepsilon/\delta$  measures the extent to which fluid crosses an entire topographic feature during a wave period ( $\div 2\pi$ ); linear waves apply when the excursions thus measured are small, and one approaches quasi-steady Taylor column- and Taylor "cone" problems when they are large.

This extreme,  $\varepsilon/\delta \gg 1$ , holds especially for small-scale (10–30 km) seamounts, which have been filtered from our model. Hogg (1973), and McCartney (1975) are among the recent investigators of the purely steady limit, and Huppert and Bryan (1975) have looked at the crucially important "start-up" problem. Recent ocean measurements (Section 9) emphasize that the larger-scale flow shifts sufficiently often in the deep water that the steady, potential-vorticity conserving deflections are a poor description of the effects of topography, even at the smallest scales relevant to geostrophic flow ( $\sim 10$  km). The transient-flow problem is complex, and it is essential to decide whether flow, starting from rest, causes just a single starting vortex to be swept from above the bottom feature (leaving behind the steady, bound vortex), or whether a continual train of shed vortices is created, as in a classical cylinder wake. (The author believes he has seen vortex shedding from a Taylor column in the laboratory, and there are numerous satellite photographs of vortex streets in the lee of islands, occupying either fluid.) The parameterization of small-scale topography, and its wave drag (including internal waves) on the mesoscale eddies is crucial; our present practice of removing all topography with  $L_H < L_\rho$ , and replacing it with a linear drag, may be severely in error.

We return to the larger scales, where  $\varepsilon/\delta \lesssim 1$  frequently (if only by inference from the observed baroclinity of ocean currents). There the wave theory has already suggested some of the turbulent cascade results. First, linear scattering of long waves provides a model for  $T_H(k)$ , the topographic energy transfer spectrum, in the general case. This may allow a quantitative estimate of spectral broadening and fragmentation, of even nonlinear eddies. Second, the occurrence of the bottom-trapped type 2 is

consistent with high-frequency oscillations found in the deep water (but not above the thermocline) in the simulations. Third, the disappearance of the barotropic type 1 at  $L \lesssim L_p$  suggests, in the turbulent runs, the sustenance of vertical shear (the defeat of barotropy), for it is the scales near  $L_p$  that form the aperture through which the different levels communicate. Fourth, the prediction from theory of horizontally trapped waves over rough topography is suggestive of the immobility of energy found in the nonlinear cases. This argues further that spatial intermittency of energy and "local" equilibrium of the eddies should develop in both linear and nonlinear oceans.

The linear-wave theory becomes difficult in the most relevant case of topographic "turbulence,"  $kL_H \sim 1$ ,  $\varepsilon \ll \delta \gtrsim L_H/R$ . Some closed-form solutions have been found but there is much to be done. A relevant idealization is that of isolated bottom features, which occur when  $f/h$  contours are packed together (as at the continental margins and Mid-Atlantic Ridge), or when they form closed "islands."

The simplest such wave, which we derive for illustration, is that found at a near-discontinuity in the depth, say, along  $y = 0$ ,  $h_2 = H_2$  for  $x < 0$ ,  $h = H_2(1 + \delta)$  for  $x > 0$ . This provides a delta function of the restoring effect, the slope. The two-layer equations (linear,  $\beta = 0$ ) become, in dimensional variables,

$$\begin{aligned} [\nabla^2 \psi_1 + F_1(\psi_2 - \psi_1)]_t &= 0 \\ [\nabla^2 \psi_2 + F_2(\psi_1 - \psi_2)]_t - \frac{f}{H_2} h_{2,y} \psi_{2,x} &= 0 \end{aligned}$$

for  $\delta \ll 1$ . Trapped waves exist of the form

$$\begin{aligned} \psi_1 &= (a_1 e^{-k|y|} + a_2 e^{-\kappa|y|}) e^{i(kx - \sigma t)} \\ (1 + \gamma) \psi_2 &= (a_1 e^{-k|y|} - a_2 e^{i\kappa|y|}) e^{i(kx - \sigma t)} \end{aligned}$$

They satisfy the exterior equations if  $\kappa^2 = k^2 + F_1 + F_2$ ,  $\gamma = H_2/H_1 = F_1/F_2$ . The interface height ( $\propto e^{-\kappa|y|}$ ) is tent-shaped, with its scale being the smaller of  $k^{-1}$  and the deformation radius  $k_p^{-1}$ . At  $y = 0$  we must match normal flux and pressure; integration of the lower-level equation across the step determines the discontinuity in  $\psi_{2,y}$ :

$$\begin{aligned} [\psi_1] &= 0 = [\psi_2] = [\psi_{1,y}] \\ [\psi_{2,y}] &= \frac{f}{\sigma} \delta \psi_{2,y} \quad (y = 0) \end{aligned}$$

An oscillatory vortex sheet occurs in the lower layer, driven by the upslope velocity (and has this strength even when the particle excursions are rather great). The matching conditions yield the dispersion relation

$$\frac{\sigma}{f} = -\frac{\delta}{2} \frac{\gamma}{1 + \gamma} \left( \frac{k}{\kappa\gamma} + 1 \right)$$

Large scales,  $k^2 \ll F_1 + F_2$  are barotropic "double Kelvin waves" (Rhines, 1969) with  $\sigma/f = -(\delta/2)(\gamma/(1 + \gamma)) = -\frac{1}{2} \times$  fractional change in total depth across the step, with  $\psi_1 = \psi_2$ . Waves shorter than the deformation scale become increasingly confined to the lower layer. In this limit they feel the interface as a rigid lid, and hence  $\sigma/f \rightarrow -\delta/2$ ,  $|\psi_1/\psi_2| \rightarrow k_p/k \ll 1$ . The topography provides trapping in vertical and horizontal directions. For the simplest case the group velocity,  $\partial\omega/\partial k$ , vanishes

at both extremes of  $k$ , but is significant near  $k = k_p$ . Phase and energy each move to the left, facing shallow water. Simple solutions also may be found for seamounts and islands, where the phase progresses clockwise (the analogue of westward-propagating Rossby waves).

The eigenvalue problem for sinusoidal depth variations (Suarez, 1971; McWilliams, 1974; Rhines and Bretherton, 1974) provides an interesting model of "roughness"

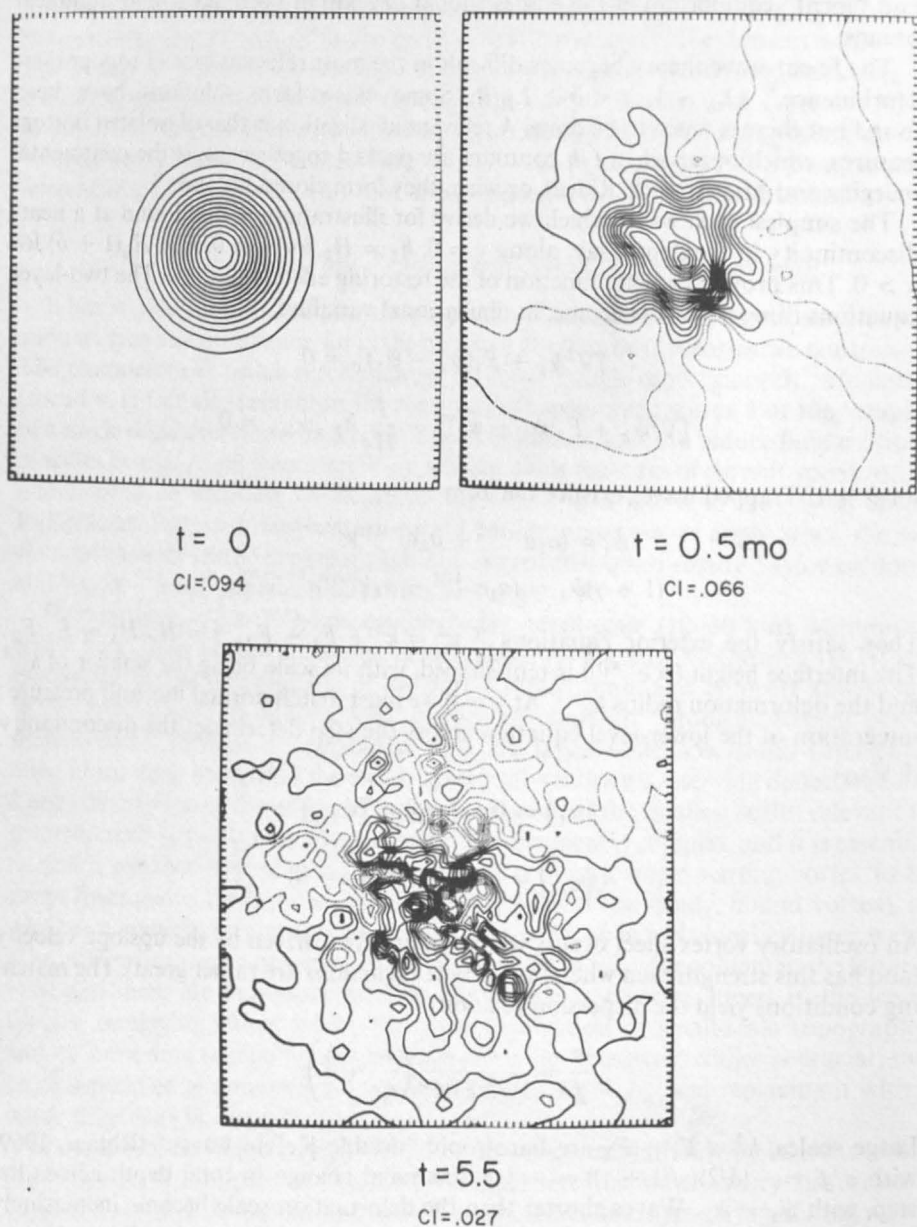


Fig. 44. Linear-wave dissolution of a circular vortex in a rough-bottom ocean (homogeneous fluid). The topography is confined to wave number 6–11. Compare Fig. 11. In spite of the spatial complexity, the pressure at a fixed point varies rather sinusoidally in time, as in a trapped "seamount" oscillation.

waves, the frequencies again being  $O(\delta)$ . For arbitrary depth in a one-layer ocean enclosed by a coast, upper bounds can be established for the frequency, and are of this same order:

$$\sigma \leq \left| f - \frac{f_0 h}{h_0} \right|_{\max}$$

where  $f_0$  and  $h_0$  are the mean values of  $f$  and  $h$ , respectively. If  $\delta R/L \ll 1$  this essentially sets the greatest planetary-wave frequency at  $|f - f_0|_{\max}$ .

If we fix the total rms derivation of  $f/h$  from its mean in a model basin, the average energy propagation tends to be faster, the more smoothly the topography is distributed. This is not quite the same as saying that the addition of rough topography to a smooth  $\beta$  plane must reduce the group velocity, for the group velocity eventually scales up with  $\delta$ , and hence must become large if  $\delta$  does.

Numerical experiments with a single-layer fluid exhibit some of the interesting horizontal-cascade effects. Figure 44, taken from a movie sequence, shows the fragmentation of a large Gaussian vortex by narrow-band bottom roughness. (See also Rhines, 1973, figure 5.) The energy gradually percolates outward from seamount to seamount, for there is no large-scale  $\beta$  effect to support fast, long waves. A natural fine structure builds up, even with these linear dynamics.

A linear experiment in the two-layer stratified ocean (Fig. 45) uses initial conditions and topography very like the nonlinear runs (Figs. 34, 35). The energy reaching down to the lower layer is rapidly "whitened," and again becomes severely intermittent

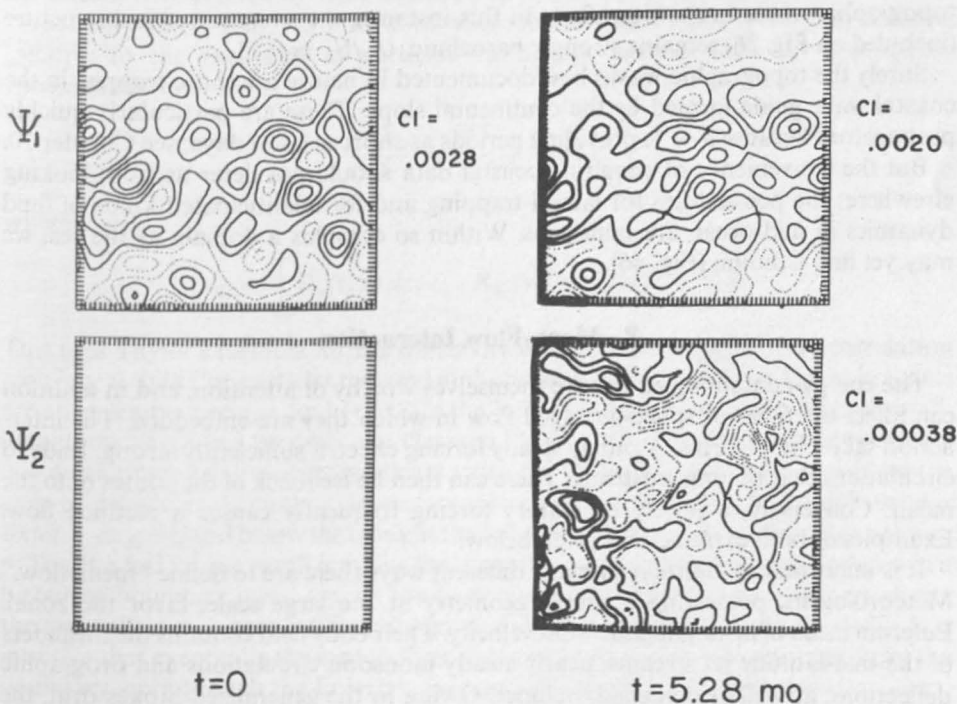


Fig. 45. Linear solution for a rough-bottom two-layer ocean (see time series, Fig. 37d). The wave number spectrum is very "white" in the deep water, although the finer scales are not evident in  $\psi_2$ .

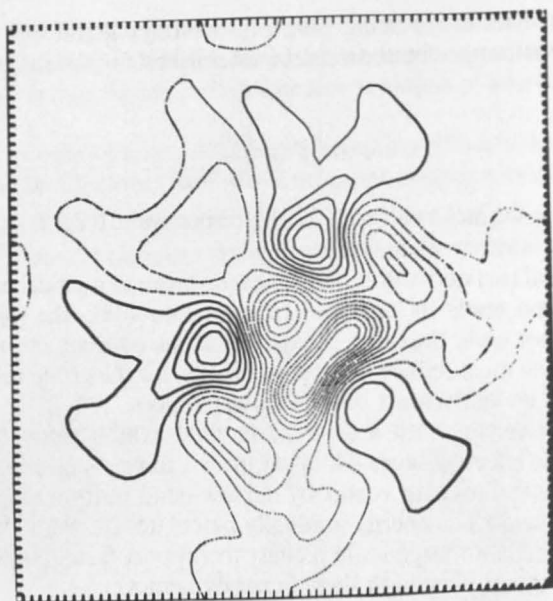


Fig. 46. The linear solution, after a Gaussian vortex is placed over a tessellated bottom,  $h \propto \sin x \sin y$ .

in space. The time series at fixed moorings, shown in Fig. 37*d*, are dominated by slightly modified baroclinic Rossby waves in the upper currents and temperature, yet fast topographic waves in the deep flow. In this instance, the average vertical structure (included on Fig. 36) remains strongly baroclinic,  $U_2/U_1 \approx 0.33$ .

Surely the topographic waves best documented in nature are those trapped in the coastal wave guide formed by the continental slope. These are particularly quickly propagatory because  $\delta \sim 1$ , providing periods as short as a few days; see Chapter 10.

But the convenience of acquiring coastal data should not deter us from looking elsewhere: the possibilities for lateral trapping and for unanticipated kinds of fluid dynamics in mid-ocean are numerous. Within so complex a domain as the sea, we may yet find Cthulhu (Fig. 46).

## 8. Mean-Flow Interaction

The energy-containing eddies are themselves worthy of attention, and in addition can affect the time- or space-averaged flow in which they are embedded. The interaction takes many forms. A purely steady forcing effect, if sufficiently strong, leads to circulations that become unsteady. There can then be feedback of the eddies onto the mean. Conversely, a purely oscillatory forcing frequently causes a rectified flow. Examples of both extremes are given below.

It is important to realize how many different ways there are to define "mean flow." Meteorologists, possessing a simple geometry at the large scale, favor the zonal, Eulerian mean of instantaneous wind velocity. Their eddy field contains the meanders of the mid-latitude jet streams, nearly steady monsoon circulations and orographic deflections, as well as detached cyclones. Owing to the generalized Stokes drift, the velocity averaged about fixed control surfaces does not accurately describe the average paths of fluid parcels, either in a meridional plane or a level surface. But

oceanographers, who are interested in the life history of salts, heat, and chemical tracers, as well as momentum, must pay more attention to such Lagrangian means, averaging over an ensemble of realizations. In the presence of coastal boundaries it is particularly difficult to find fixed control surfaces that yield useful overall statements about linear or angular momentum, or vorticity. The oceanographer's interest in the paths of fluid parcels is in part pragmatic: in much of the ocean the time-averaged current at a fixed point is nearly unmeasurable by direct means. (An illustrative example is given in Section 9.)

A simple calculation of the difference between Eulerian and Lagrangian mean flow can be made for a field of geostrophic turbulence. Imagine, as a model, that the dispersal of particles obeys a diffusion equation,

$$\frac{\partial C}{\partial t} = \nabla \cdot (\kappa \nabla C)$$

where  $C(\mathbf{x}, t)$  is the spatial concentration of fluid markers, and  $\kappa$  the diffusivity. Multiplying by  $\mathbf{x}$  and integrating, we find that the center of mass obeys

$$\frac{\partial \bar{\mathbf{x}}}{\partial t} = \bar{\nabla \kappa}$$

where  $(\bar{\quad}) = \int (\quad) C d\mathbf{x} / \int C d\mathbf{x}$ . If  $C$  is a delta function, this gives the most likely flow of a single particle. The particles move preferentially toward regions of large diffusivity, even in the absence of an Eulerian mean flow. The spread of the probability distribution about the expected path occurs, to a first approximation at rate  $\bar{\kappa}$ . This model was investigated by Kolmogorov (see Monin and Yaglom, 1972, p. 610).

It is very likely that, for a stationary, turbulent field of slowly varying statistics (relative to the excursion of particles during one eddy-period), the appropriate generalization is

$$\frac{\partial \langle \bar{x}_i \rangle}{\partial t} = \frac{\partial \bar{\kappa}_{ij}}{\partial x_j} + \langle u_i(\mathbf{x}) \rangle$$

where

$$\kappa_{ij} = \int_0^t R_{ji}(\tau | \mathbf{x}) d\tau, \quad R_{ij} = \langle u_i(t | \mathbf{x}) u_j(t + \tau | \mathbf{x}) \rangle$$

This uses Taylor's formula for the diffusivity in terms of the Lagrangian correlation function,  $R_{ij}(\tau | \mathbf{x})$  for particles released at the point  $\mathbf{x} \equiv (x_1, x_2)$  at  $t = 0$ . The brackets are an ensemble average, and  $\langle u_i(\mathbf{x}) \rangle$  is the Eulerian mean flow. In the limit of small-amplitude waves this becomes the classical Stokes drift. The difference between the two mean flows will be most significant when the eddy intensity varies greatly on the scale of the eddies themselves. In surface gravity waves, for example, the difference is  $\partial x / \partial t = \partial \kappa_{xz} / \partial z$ , and below the troughs the Eulerian average flow completely vanishes.

To get a feel for the result imagine the dispersion of neutrally buoyant particles in a turbulent boundary layer, say, at the base of the atmosphere. The boundary exerts the same effect as a strong diffusivity gradient (which also exists in the air itself). It is intuitive that eventually the center of mass of a marked region will rise away from the boundary, even though the Eulerian-average vertical velocity vanishes everywhere.

Taylor's (1921) formulation of turbulent diffusion (essentially the identity that  $(\partial / \partial t) \langle x_i x_j \rangle = \int_{-t}^t R_{ij}(\tau) d\tau$  in a homogeneous field) emphasizes also that in a given

region there are many different Lagrangian drifts and many different diffusivities, depending on the subset of particles being counted, and on the recent history of the field.<sup>8</sup> At small times a delta-function cloud disperses with  $\langle x_i^2 \rangle \propto \langle u_i^2 \rangle t^2$  (initially zero diffusivity) yet after the initial velocities are forgotten, the expansion slows toward a random walk,  $\langle x_i^2 \rangle \rightarrow 2(t \int_0^\infty R_{ii} d\tau - \int_0^\infty \tau R_{ii} d\tau)$ . Dyed patches of fluid of different sizes (marked with different colors) thus spread at rates inconsistent with a single diffusivity and their centroids move with different velocities.

This result suggested itself after neutrally buoyant SOFAR floats in MODE were observed to behave rather erratically in their mean drift, at times acting very unlike the mean flow seen by current meters moored nearby. In the same region, we found precipitous, permanent gradients in eddy intensity.

### A. A Whole-Gyre Model

The dynamical studies in Sections 5–7 focused for simplicity on homogeneous fields, without boundaries. But we know the ocean to be heterogeneous, and an independent line of attack includes an explicit source, here the meanders of a wind-driven circulation, which may in turn radiate to the central ocean. A number of investigators have been experimenting with such models reminiscent of Stommel's single-gyre circulation, yet with stratification and explicit eddies present. One such calculation, by Holland and Lin (1975), has reached an advanced stage,<sup>9</sup> and we describe their results in some detail.

Holland and Lin drive their ocean, in which there is simple lateral friction, by spinning up from rest with a steady wind stress, sinusoidally varying with latitude. At moderate Reynolds number the mean flow is highly inertial. The Gulf Stream (with free-slip boundary conditions) turns along the northern wall and then decelerates as fluid returns to the interior (Fig. 47). This is typical of inertial gyres; only at smaller Reynolds number, or with no-slip walls, do the more classical western boundary layer patterns return.

After 2 yr of driving by the wind (of amplitude 1 dyne/cm<sup>2</sup>) the circulation spontaneously begins to meander, and closed cells of transport move throughout the basin. Unlike our free initial-value experiments, the mean state here is continuously maintained and a statistically steady, fully interactive state is reached after about 3 yr (Fig. 47).

The time-mean and perturbation fields are at first sight surprising. The perturbations are strongest, not in the vicinity of the Gulf Stream, but in the westward return flow. There the upper layer meanders lag those in the lower layer by roughly 60°. This is a tilt of the phase of pressure in the  $xz$  plane opposite to the sense of the mean velocity, a familiar signature of baroclinic instability. The dominance of the open-ocean return flow is in part due to the stabilization provided by the northern wall, but more strongly due to the narrowness of the westward flow. For the intensity of the eastward-flowing Gulf Stream is about 20 cm/sec (averaged over its 80-km width), whereas that of the return flow is about one-third as great. Simple instability theory Section 6, which ignores horizontal shear, suggests that the eastward flow, to be unstable, must obey  $|U_E| > g'H_2\beta/f$  (in order that the mean potential vorticity gradient  $\bar{Q}_y$  have opposite signs in the two layers). The westward flow can more easily

<sup>8</sup> The identity in general involves  $\int_{t_0-\tau}^t (R_{ij}(\tau, t|\mathbf{x}, t_0) + R_{ji}(\tau, t|\mathbf{x}, t_0)) d\tau$ . If the statistics are stationary but inhomogeneous, however, this diffusivity is non-stationary.

<sup>9</sup> Others currently investigating this area include Haidvogel, Mintz, Robinson, and co-workers.

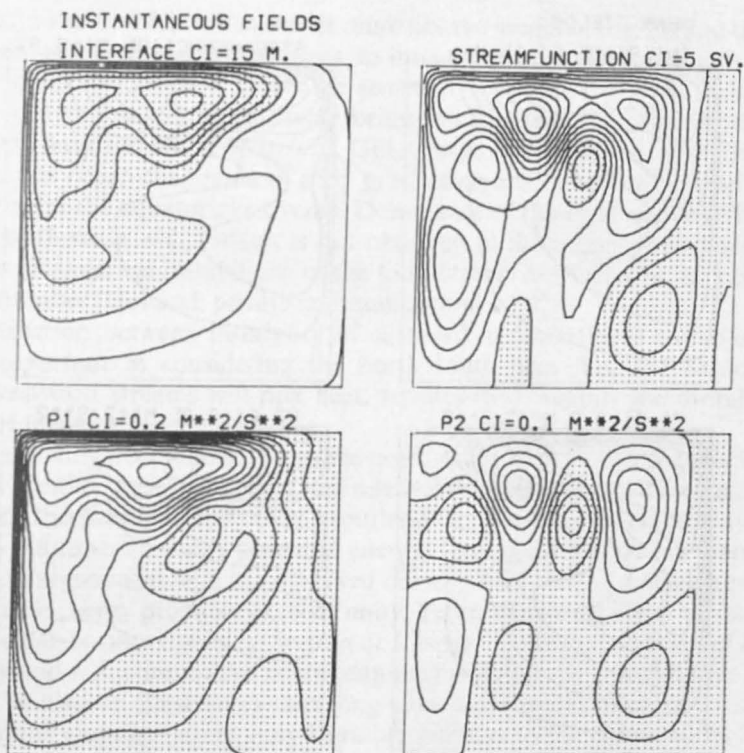


Fig. 47. Typical flow pattern from Holland and Lin's wind-driven ocean. P1 and P2 are  $\psi_1$  and  $\psi_2$  in our notation, PSI is  $\psi_1 + \psi_2$ , the total transport.

reverse the gradient in the thin upper layer, if only  $|U_w| > g'H_1\beta/f$ .<sup>10</sup> Thus if  $U_w/U_E > H_1/H_2$ , the return flow will be the more vulnerable, as it is here:  $H_1/H_2 \sim 0.2$ ,  $U_w/U_E \sim 0.3$  (averaging horizontally over the Rossby radius  $\sim 50$  km). When Holland doubled the north-south extent of the basin, so that the maximum westerly winds doubled at its middle latitude, a two-gyre circulation occurred (Fig. 49). With the restraint of the rigid wall removed, the separated Gulf Stream was weakly unstable, but the predominant energy conversion occurred, as before, in the return flow.

There is in the deep layer of Holland and Lin's ocean a time-mean flow (Fig. 48) including gyres both co- and counterrotating relative to the upper flow; here the eddies drive an abyssal circulation. Above the thermocline, however, Holland demonstrates that the flow is significantly weaker with eddies than without. Averaging over the water column, there is a net transfer of kinetic energy from mean to perturbations at a rate  $\frac{1}{2}$  the conversion from potential to kinetic energy. This remarkable braking action is suggested by Thompson's (1971a) qualitative argument, and our analysis below, that spontaneous wave radiation will intensify an eastward jet, yet weaken a westward jet. It is likely that, given a more realistic intensity of the separated Gulf Stream (which exceeds 100 cm/sec averaged over the upper kilometer) and of the return flow, which cannot far exceed 10 cm/sec, the center of energy release will move

<sup>10</sup> The wedge model of a two-layer  $\beta$  plane ocean (Fig. 6) shows this asymmetry simply, for the slope equivalent to  $\beta$  is greater in the thicker lower layer. Hence a rather steep uptilt of the thermocline to the north is required to cause  $dh/dy$  to have opposite signs in the two layers, yet a milder tilt in the opposite sense will manage to do so.

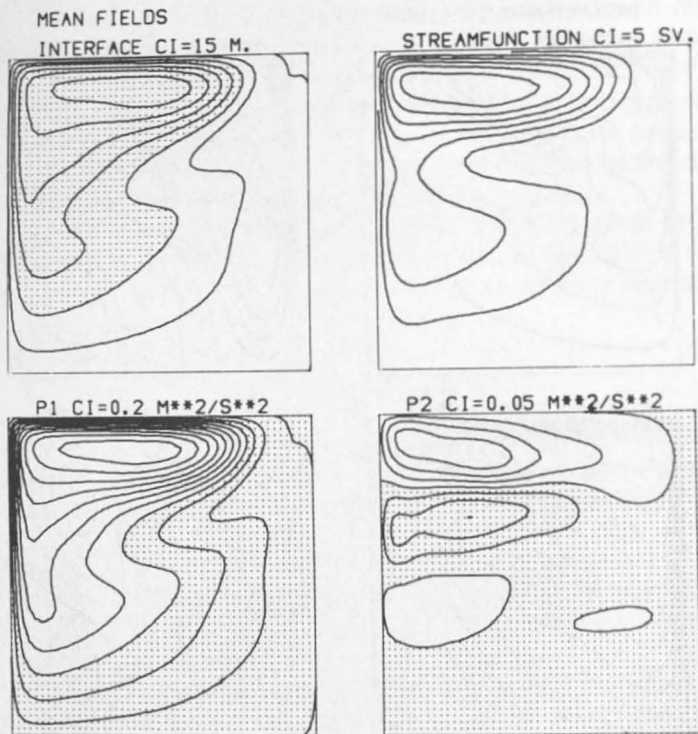


Fig. 48. Time-averaged flow, showing an abyssal circulation driven by the eddies.

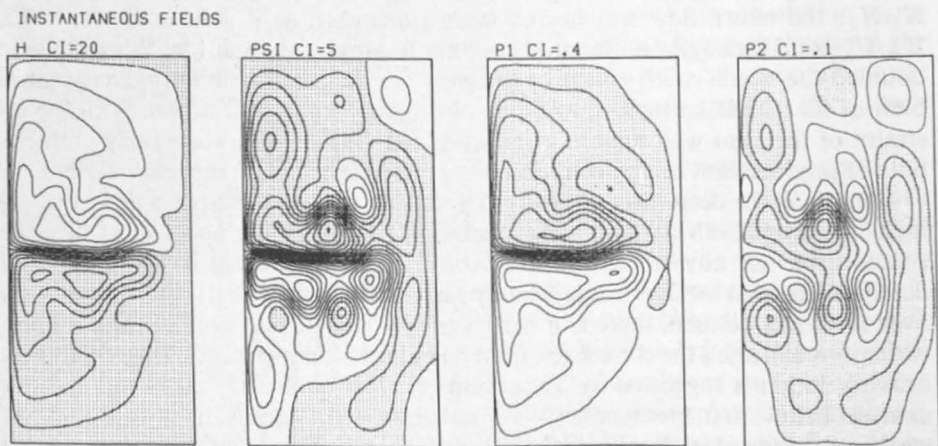


Fig. 49. As above, but in an elongated basin with the maximum eastward stress at mid-latitude. The separated Gulf Stream is now unstable, and becomes more so, the larger the Reynolds number.

to the Stream itself, which will meander more like the model in Fig. 27, and the eddies will then act, as in meteorological flows, to intensify the circulation in both layers.<sup>11</sup> The experiment nevertheless shows the sensitivity of westward flows to baroclinic instability (relying on the upper layer being thinner than the lower layer) which theoreticians have remarked upon (e.g., Gill, Green, and Simmons, 1974). It may be that in the real ocean the region of eddy production analogous to Holland's case is farther south in the equatorial currents. Dominance of the tight non-Sverdrup gyre of north-south scale  $\sim L_\rho$ , which is not observed in the oceans, may lessen when reasonable meandering instabilities of the Gulf Stream are included, by raising the Reynolds number (Holland, private communication).

The distinction between instability of eastward and westward currents is particularly important in considering the north-south heat flux, for baroclinically unstable westward streams will mix heat, equatorward, against the overall global gradients of temperature.

The distant eddy field radiated from the north in Holland's experiment is virtually barotropic. Neither mean advection nor relatively slow baroclinic propagation was able to carry thermocline eddies to the south (in fact, the basin-average eddy kinetic energy was 6.8 times the eddy potential energy). This dearth of strong thermocline eddies is in disagreement with the observed ocean, where the ratio of eddy potential to eddy kinetic energy probably exceeds unity. Yet the disparity is just the same one found in the flat-bottom cascades (Section 6). It is very likely that addition of realistic topography and reduction of the lateral damping will allow a baroclinic far field to develop. It is also an illustration that long-term experiments, involving a balance between forcing and dissipation, may be rather sensitive to the nature of the friction, more so than the short-term evolution in initial-value experiments. Heterogeneous experiments like this one also require accurate modeling of horizontal fluxes of energy, which in turn are themselves very dependent on both friction and bottom topography.

Despite these intricacies the calculations seem to be the first to include the entire list of ingredients (excepting rough topography) needed to understand the mean circulation.

### *B. Rectified Circulation on a Homogeneous $\beta$ Plane*

The problem of eddy-mean flow interaction needs the focus provided by simplified geometry and forcing, in addition to calculations like Holland's showing its role in complex ocean models. A laboratory experiment by Whitehead (1975) exhibits succinctly the rectified flow generated by localized forcing on a homogeneous  $\beta$  plane. The 2-m Woods Hole tank was rotated with its surface free (covered by a plastic "windscreen"), yielding a paraboloidal  $\beta$  plane. A circular disk was mounted in a horizontal plane, at mid-depth and mid-latitude. Forced vertical oscillation of the disk produced a mixture of waves and turbulence in the otherwise still fluid. Radial dye streaks revealed a persistent zonal circulation (Fig. 50) which was prograde ("eastward") at the latitude of the forcing and retrograde ("westward") elsewhere. Circulation in this sense occurred equally well when the disk was replaced by a source of small air bubbles. E. Firing, G. Williams, and E. Lorenz (private communications) have reported the analogous result from truncated numerical calculations on a rotating sphere covered by homogeneous fluid.

<sup>11</sup> In this case the eddies are likely to have a decisive effect on the upper-layer circulation, as well as abyssal flow, rather than altering it only slightly.

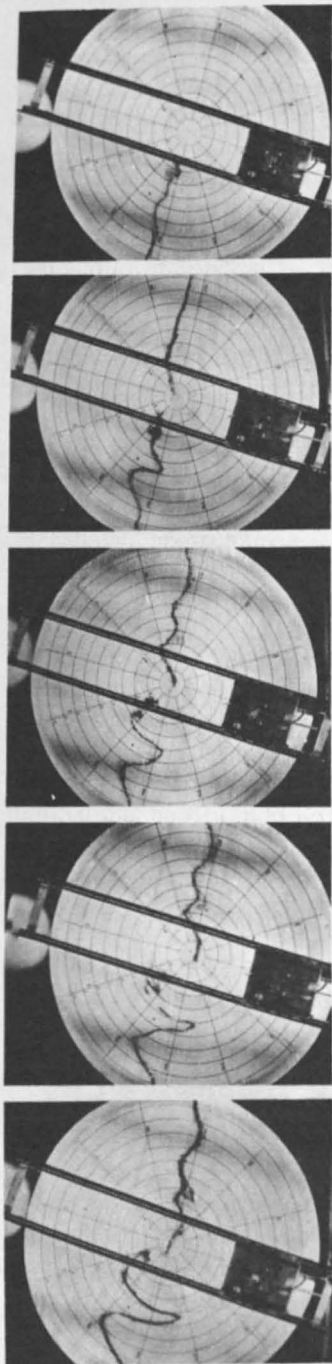


Fig. 50. Mean circulation induced by an isolated disturbance (beneath the black square) on a polar  $\beta$  plane (Whitehead, 1975). The dye streaks deforming with time show a prograde (eastward) jet at the forcing latitudes, with westward flow elsewhere.

C. Inviscid Theory

It is of interest to write an analytical expression for this mean flow which holds for both waves and geostrophic turbulence. Consider a polar  $\beta$  plane like Whitehead's but, for simplicity, with constant depth and Coriolis frequency,  $f$ , decreasing linearly away from the center (Fig. 51). Neglecting at first forcing and dissipation, we have simple conservation of barotropic potential vorticity,

$$q \equiv \beta y + \zeta \quad [\zeta \equiv (\nabla \times \mathbf{u})_z] \tag{35}$$

$$\frac{Dq}{Dt} = 0$$

Here  $y, v$  are the (inward) radial coordinate and velocity. Integrate over a region within a fixed latitude circle,  $\mathcal{C}$ . The Eulerian, zonally averaged  $u$  velocity is then given by

$$\frac{\partial}{\partial t} \bar{u}_e = \overline{qv}$$

where  $(\bar{\quad}) = \oint_{\mathcal{C}} (\quad) dx$  is the integral about the latitude circle. Now a fluid column which would have zero relative vorticity at latitude  $y_0$  has potential vorticity  $q = \beta y_0 \equiv \beta y - \beta(y - y_0)$ . With  $v = Dy/Dt$ ,  $\bar{v} = 0$ , and defining  $\eta = y - y_0$ , it follows that

$$\frac{\partial \bar{u}_e}{\partial t} = - \overline{\beta(y - y_0) \frac{D(y - y_0)}{Dt}} \tag{36}$$

$$= - \frac{1}{2} \beta \overline{\frac{D}{Dt} \eta^2}$$

which is an exact relation, regardless of the intensity or nature of the fluid motion. If the convective part of the right side is small, equation 36 becomes

$$\bar{u}_e = -\frac{1}{2} \beta \bar{\eta}^2 \tag{37}$$

for an initial state of rest. The neglect of the convective terms leading to equation 37 is not so severe as to require linear wave motion. It implies  $\overline{\mathbf{u} \cdot \nabla \eta^2} \equiv (\partial/\partial y) \bar{v} \eta^2 \ll (\partial \bar{\eta}^2/\partial t)$  or  $\gamma(U/c)[(\bar{\eta}^2)^{1/2}/L] \ll 1$  where  $\gamma$  is a correlation coefficient between  $v$  and  $\eta^2$ ,  $U$  is a scale particle speed,  $c$  a scale-phase speed, and  $L$  a length scale defining the

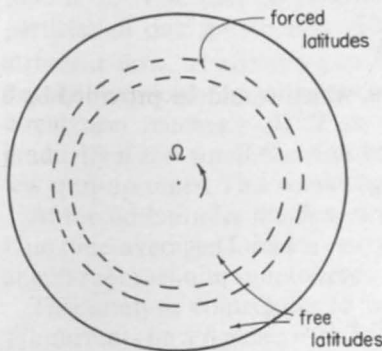


Fig. 51. Geometry for the circulation experiment.

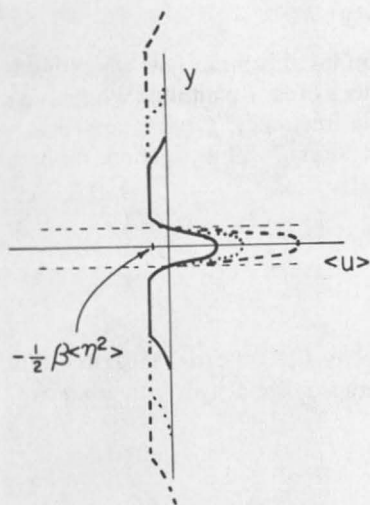


Fig. 52. Sketch of the inviscid solution for the Eulerian circulation due to random forcing confined to the dashed band. At successive times the jet strengthens, as the westward flow (of constant strength) fills an ever-greater region.

north-south envelope of variation of  $\overline{\eta^2}$ . Equation 37 is thus valid for either weak disturbances ( $U/c \ll 1$ ) or nonlinear fields in which the scale of variation  $L$  of the intensity is much greater than the typical north-south particle displacement.

Random trading of fluid particles across the latitude circle  $\mathcal{C}$  systematically decreases the net relative vorticity within  $\mathcal{C}$ , yielding an Eulerian mean circulation. This westward momentum appears at "free" latitudes for which equation 35 holds. At forced latitudes, where the wave maker was located in Whitehead's experiment, eastward momentum is left behind as a prograde jet whose strength depends upon the nature of the wavemaker: net angular momentum vanishes if the source (for example, the air bubbles used in some of Whitehead's runs) provides none. In the steadily excited inviscid case the westward circulation at a given latitude builds up to its asymptotic value  $-\frac{1}{2}\beta\overline{\eta^2}$  as soon as the disturbance arrives. The westward jet continues to accelerate indefinitely, to compensate for the presence of westward flow in an ever larger region. The solution is sketched in Fig. 52. The central result, which holds in more general circumstances, is that the depth-averaged flux of potential vorticity equals the force, plus the momentum influx, exerted along  $\mathcal{C}$  by eddies on the fluid instantaneously occupying the fixed contour,  $\mathcal{C}$ . Green (1970) made use of the steady form of this relation. Below, it is shown to shed light also on the eddy-forcing of flow, averaged in time at a point in space, rather than about a geostrophic contour.

#### D. Viscous Theory

Add to the problem a simple bottom drag,  $-Du$ , which would be provided by a linear Ekman layer. The vorticity equation,

$$\left(\frac{D}{Dt} + D\right)\zeta = -\beta v$$

has the formal solution, following a fluid parcel,

$$\zeta = -\beta \int_0^t v(t') e^{D(t'-t)} dt' + \zeta_0 e^{-Dt}$$

with initial value  $\zeta_0$  at  $t = 0$ . The northward flux of vorticity becomes

$$\overline{\zeta v} = -\beta v \int_0^t \overline{v e^{D(t-t')}} dt' + \overline{\zeta_0 e^{-Dt}}$$

which is simplified by defining  $\xi = \int_0^t v e^{D(t-t')} dt'$ , to

$$\overline{\zeta v} = -\beta \overline{\xi \left( \frac{D\xi}{Dt} + D\xi \right)} + e^{-Dt} \overline{\zeta_0 v}$$

The exact relation analogous to equation 36 is

$$\left( \frac{\partial}{\partial t} + D \right) \overline{u}_e = -\beta \overline{\left( \frac{1}{2} \frac{D}{Dt} + D \right) \xi^2} + e^{-Dt} \overline{\zeta_0 v} \quad (38)$$

Here,  $\xi$  is the north-south particle displacement weighted over the previous spin-up time, which expresses the fading memory that fluid has for its initial latitude. The second right side term gives the decaying dependence on initial relative vorticity. Again, if

$$\frac{U}{c} \frac{(\overline{\eta^2})^{1/2}}{L} \ll 1$$

the advective part of  $D/Dt$  may be neglected, and the explicit solution is

$$\overline{u}_e = -\frac{1}{2} \beta \left( \overline{\xi^2} + D \int_0^t \overline{\xi^2} e^{-D(t-t')} dt' \right) + e^{-Dt} \overline{\zeta_0} \int_0^t v dt$$

There are two interesting limits, the inviscid, which yields equation 36, or

$$\overline{u}_e = -\frac{1}{2} \beta \overline{\xi^2} \equiv -\frac{1}{2} \beta \overline{\eta^2} \quad (39)$$

(if  $\zeta_0 = 0$ ), and the steady, which yields

$$\overline{u}_e = -\left( \frac{\beta}{D} \right) \int_0^\infty R_{22}(\tau) e^{-D\tau} d\tau \quad (40)$$

If the spinup time,  $D^{-1}$ , far exceeds the time scale of the eddies, this simplifies to: (a)  $u_e = -\beta \kappa_{22}/D$  if the field is diffusive ( $\kappa_{22} \neq 0$ ); (b)  $u_e = -\frac{1}{2} \beta \overline{\eta^2}$ , if  $\overline{\eta^2}$  is bounded ( $\kappa_{22} = 0$ ) and the correlation  $R_{22}$  falls to zero rapidly, relative to  $D^{-1}$ ; or (c)  $u_e = -\beta \overline{\eta^2}$  (twice that of (b)) if  $\kappa_{22} = 0$  and  $R_{22}$  has long memory, relative to the time  $D^{-1}$ . Note that (a) resembles (b) if we replace  $\eta$  by the average excursion of particles in one spinup time. This illustrates the difference between wavelike and turbulent flow, as according to whether  $\overline{\eta^2}$  is bounded or not. Neither expression depends explicitly on the time or length scales of the eddies. In the solution, (c), the circulation reaches  $-\beta \overline{\xi^2}/2$  as soon as the disturbance is established but then, gradually if  $D$  is small, the circulation continues to increase to twice this value after a few spinup times. This would be a feature to look for in an experiment.

At forced latitudes the flow depends, as before, on the exact nature of the source. If no time-averaged forces are exerted on the fluid, the regions of positive and negative angular momentum sum to zero: each is not finite, being limited by friction.

This analysis contributes to earlier arguments for anisotropy, favoring zonal or  $f/h$  currents on a  $\beta$  plane, even without external forcing. Random increase or decrease

in  $\overline{\eta^2}$  will occur due to the eddy motion itself. The slowness of energy propagation north-south, relative to east-west, may enhance the effect by maintaining north-south gradients, yet smoothing out those east and west.

### E. Taylor's Formula

The derivation was suggested by a result in Taylor's remarkable 1915 paper which considered, among other things, the stability of a plane, nonrotating, inviscid flow in a channel. He finds (in our notation)

$$\frac{\partial U}{\partial t} = \frac{1}{2} U''(y) \frac{\partial \overline{\eta^2}}{\partial t} \quad (41)$$

as a consequence of conservation of relative vorticity. (See also Dickenson, 1969.)

Here  $U(y) \equiv \bar{u}_e$ ; Taylor's formulation is centered on slight deviations from a strong, parallel flow. In this case, unless  $U''$  is a constant, the displacements,  $\eta$ , and perturbation velocities must be assumed small. Equation 41 in effect equates the vorticity flux to the divergence of the momentum flux. When integrated across the channel the left side vanishes, there being no sources of momentum. This gives Rayleigh's criterion, that  $U''(y)$  must change sign somewhere for the spontaneous growth of disturbances, based on the novel definition of instability, that  $\overline{\eta^2}$  increase everywhere. [In our analogous  $\beta$  plane application, the integration of equation 37 (where  $\beta$  is a positive constant) across a zonal channel bounded by rigid walls (or, without walls, to distant latitudes which are quiescent) shows that  $\int \overline{\eta^2} dy$  must be constant in the absence of forcing or dissipation: on an *unforced*  $\beta$  plane random motion is ultimately limited in north-south excursion. External agents are required to mix the potential vorticity.]

Now a positive value of  $\frac{1}{2} \partial(\overline{\eta^2})/\partial t$ , which we henceforth call  $\kappa$ , acts (though not exactly) like a positive viscosity, reducing the momentum where  $U''$  is positive, and conversely (Fig. 53). This redistribution of momentum, on the whole, reduces the energy of the mean flow.

Two situations exist, however, in which the perturbations sharpen the jet and increase its energy. First, stable perturbations,  $\kappa < 0$ , can exist in a potentially unstable flow and they will increase  $U$  wherever the curvature  $U''$  is negative. Second, the flow may be absolutely stable,  $U'' \neq 0$  everywhere, and then the integral of equation 41 shows that  $\kappa$  must take on both signs within the fluid. Imagine, for example, a parabolic inviscid flow, with imposed initial values of  $\overline{\eta^2}$  that are large near its axis, and vanish towards the edges. It is most plausible that the disturbance will decrease where it is large and increase where it is small. If this is so, the flow will be intensified, with a flux of  $x$  momentum against its own gradient.

Starr (1968), in describing "negative viscosity," frequently invoked two-dimensional thought problems. Here we have shown in detail how such flows may redistribute momentum against its gradient, but only when, in some part of the flow, the eddy diffusivity of vorticity,  $\kappa$ , is negative.

Consider now the combined situation of a zonal current,  $U(y)$ , on a  $\beta$  plane. The equivalent of equations 36 and 41 is

$$\frac{\partial U}{\partial t} = (U'' - \beta) \frac{1}{2} \frac{\partial \overline{\eta^2}}{\partial t} \equiv (U'' - \beta)\kappa \quad (42)$$

The *unstable case* requires that the potential vorticity gradient vanish somewhere for  $\bar{\eta}^2$  to increase everywhere. By sketching the curvature of a typical jetlike profile, it becomes clear that westward jets are less stable than eastward jets of the same shape. During the instability the role of  $\beta$  is to cause westward accelerations of the mean flow in a broader band, and eastward accelerations in a narrower band, than in the comparison problem with  $\beta = 0$ .

In the *stable case*,  $U'' - \beta \neq 0$ ,  $\kappa$  must once again take both signs, and singling out the case where  $\kappa < 0$  near the jet axis and  $\kappa > 0$  elsewhere, we find a dramatic difference in the momentum redistribution. The stable, outward moving disturbance sharpens an eastward jet (in the sense that  $\partial U / \partial t > 0$  where  $\kappa < 0$ ), as it did with  $\beta = 0$ , but, by equation 42, a westward jet is now instead decelerated at the center. The westward momentum moves out to its flanks, where  $\kappa > 0$ .

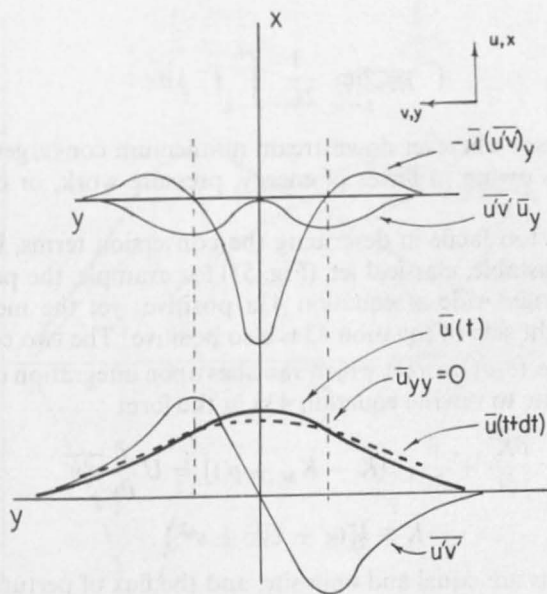


Fig. 53. Sketch of energy transformation terms and Reynolds' stress in a simple "laboratory" parallel jet. The perturbation field spreads the jet, reducing its energy. The conversion between  $x$ -mean and perturbation flow is clear, in an integrated sense, yet its local evaluation is obscured by spatial fluxes.

This shows the interplay between mean shear and  $\beta$  in deciding the redistribution of momentum.  $\beta$  takes the dominant role when  $\beta a^2 / U > 1$ ,  $a$  being the horizontal scale of  $U$ . The contribution of mean shear is in a sense included in the original derivation (equation 36) where it appears by altering the reference latitudes,  $y_0$ , of the fluid particles.

The descriptions show simply how a variety of up- and down-gradient momentum fluxes may occur in parallel flows; they are meant to contrast linear stability theory on the one hand (e.g., Howard and Drazin, 1964), with countergradient fluxes that may appear in a stable flow, on the other. It is significant that in unforced, stable flows the north-south diffusivity of fluid parcels,  $\kappa$ , must take both signs and average to zero.

### F. Energy Conversion to and from the Mean Flow

We have discussed the redistribution of momentum by eddies, without writing down the corresponding energetic relations. For two-dimensional inviscid channel flow, homogeneous in  $x$ , the usual equations for mean (in  $x$ ) and perturbation kinetic energy are

$$\frac{\partial \bar{K}_M}{\partial t} = -U \frac{\partial}{\partial y} \overline{u'v'} \quad (43)$$

$$\frac{\partial \bar{K}'}{\partial t} + \frac{\partial}{\partial y} [\overline{v'(K' + p')}] = \overline{u'v'} \frac{\partial U}{\partial y} \quad (43a)$$

where

$$u = U + u', \dots, K' = \frac{1}{2}(u'^2 + v'^2), \quad K_M = \frac{1}{2}U^2,$$

and

$$\bar{(\quad)} = \lim_{L \rightarrow \infty} \frac{1}{2L} \int_{-L}^L (\quad) dx$$

Mean energy increases wherever downstream momentum converges, and perturbation energy changes owing to fluxes of energy, pressure work, or conversion from mean energy.

One must not be too facile in describing the conversion terms, however. At the outer edges of an unstable, classical jet, (Fig. 53) for example, the perturbations are growing, with the right side of equation 43a positive; yet the mean flow is also growing, and the right side of equation 43 is also positive! The two conversion terms differ by a divergence,  $(\partial/\partial y)(\overline{u'v'U})$ , which vanishes upon integration over the domain. It may be appropriate to rewrite equation 43a in the form

$$\frac{\partial \bar{K}'}{\partial t} + \frac{\partial}{\partial y} [\overline{v'(K - K_M + p')}] = U \frac{\partial}{\partial y} \overline{u'v'}$$

$$K \equiv \frac{1}{2}[(u' + U)^2 + v'^2]$$

Now the conversions are equal and opposite, and the flux of perturbation energy is altered: the naming of  $v'(K - K_M)$  as perturbation energy flux seems appropriate, since  $K = K_M + K' + u'U$ , the final cross-term vanishing only after  $x$  averaging. The spatial flux terms are thus difficult to distinguish from the conversions between mean and perturbations. After integration over the entire domain the fluxes vanish, but it is not easy to ascribe the conversion to a particular region in space. Conclusions drawn from incomplete measurements, in only one part of the flow, may thus be ambiguous.

### G. Webster's Experiment

Apparently the first measurement of these fluxes and conversions in a large-scale ocean current was by Webster (1965). The Gulf Stream between Miami and Cape Hatteras frequently exhibits billowlike undulations on its inshore side. These are now a familiar sight, thanks to satellite-borne infrared photography (Fig. 58), but were once known only from sparse point measurements. The importance of turbulent-viscous theories of the Gulf Stream motivated this experiment in which towed

electrodes established the surface values of  $u'$ ,  $v'$ , and  $U$ , where  $Ox$  is downstream and time averages replace  $x$  averages in many experiments (although not in Fig. 54).

A typical cross-stream profile of near-surface values of the flux and conversion terms is shown in Fig. 54, from near Cape Hatteras. The persistently negative value of  $-U(\partial/\partial y)\overline{u'v'}$  nearest the shore, in the absence of other fluxes, indicates a retardation of the time-average flow there, whereas its positive value at the core indicates an intensification. This action may be related to the rather sharp inshore edge of the Stream. The net conversion in the region of measurement is directed into the mean kinetic energy, agreeing in sense with the computer simulation of Orlanski and Cox (1973), and the theoretical speculations of Starr (1968) and Green (1970). In each of these works, the energy source is the density structure below the surface.

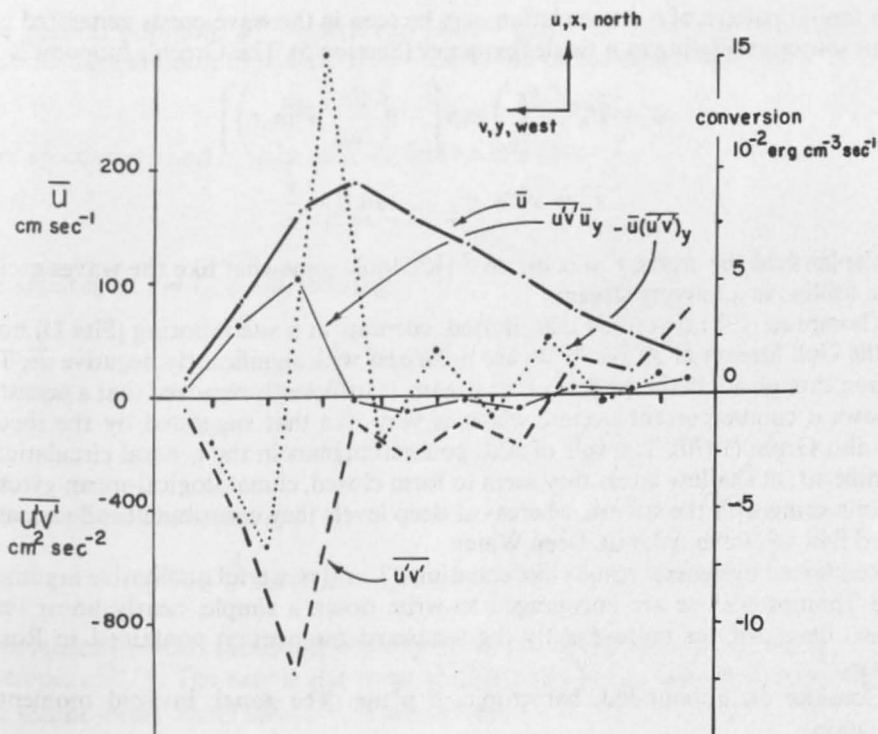


Fig. 54. The quantities analogous to Fig. 53 estimated by Webster for the Gulf Stream near Cape Hatteras. The energetic terms are very different, and both indicate net transfer from eddies to mean flow at the ocean surface. As above, the local evaluation of conversion is precarious.

This example reminds one of the difficulty in making energetic analyses when the measurements do not extend out to vanishing values of  $\overline{u'v'}$  or  $U$ . The integrated conversion terms between mean and perturbation kinetic energy are not then equal and opposite, when written as in equation 43. The common practice of using  $\overline{u'v'(\partial U/\partial y)}$  to sum up the mutual interaction of mean with fluctuations is therefore incomplete.

### H. Linearized Theory: Momentum Transport in Rossby Waves

Returning to the theory of zonal-flow generation, we concentrate on the role of  $\beta$ . We have shown that outward-moving disturbances in a basically stable flow necessarily sharpen an eastward jet while broadening a westward jet. But  $\beta$  also hastens the redistribution of  $\bar{\eta}^2$  itself by allowing waves to propagate. Thompson (1971b) first suggested this qualitative result on the basis of far-field, linear theory. As a consequence of their dispersion relation, equation 21, barotropic Rossby waves generated along an east-west line have crests arranged in a herringbone pattern which points to the east. The correlation of east and north velocities implied by motion to and fro along these crests represents a flux of westward momentum,  $uv$ , away from the source. The eastward momentum left behind in a force free environment would augment an eastward jet like the Gulf Stream beyond Cape Hatteras (see also Figs. 11, 55).

A similar pattern of  $u-v$  correlation may be seen in the wave-crests generated by a point source oscillating at a single frequency (Section 5). The Green's function is

$$\psi = H_0^{(2)}\left(\frac{\beta r}{2\omega_0}\right) \exp\left[-i\left(\frac{\beta x}{2\omega_0} + \omega_0 t\right)\right]$$

$$r^2 = x^2 + y^2, \quad \tan \theta = \frac{y}{x}$$

In the far field the crests,  $r = \text{const}/\cos^2(\frac{1}{2}\theta)$ , look somewhat like the waves excited by a fishline in a moving stream.

Thompson (1971a) verified that, indeed, currents at a site mooring (Site D) north of the Gulf Stream at  $39^\circ\text{N}$ ,  $70^\circ\text{W}$ , are polarized with significantly negative  $\overline{uv}$ . This region, though not in the far field of the stream, is sufficiently removed that a persistent westward countercurrent occurs, which is very like that suggested by the theory; see also Green (1970). The role of such countercurrents in the general circulation is significant; at shallow levels they seem to form closed, climatological-mean gyres by reconnecting with the stream, whereas at deep levels they contribute to the equatorward flow of North Atlantic Deep Water.

Reinforced by general results like equation 37, and powerful qualitative arguments like Thompson's, we are encouraged to write down a simple, nearly linear result which demonstrates more exactly the westward momentum contained in Rossby waves.<sup>12</sup>

Consider an unbounded, barotropic,  $\beta$  plane. The zonal, inviscid momentum equation,

$$\frac{\partial u}{\partial t} + u \frac{\partial u}{\partial x} + v \frac{\partial u}{\partial y} - fv = -\frac{\partial p}{\partial x}$$

yields upon averaging zonally, and expansion of the fields in powers of the non-linearity,  $\gamma \sim \varepsilon/\omega$ ,

$$\frac{\partial \overline{u^{(1)}}}{\partial t} = -\frac{\partial}{\partial y} \overline{u^{(0)}v^{(0)}}$$

where  $u = u^{(0)} + \gamma u^{(1)} + \dots$ . This gives the  $O(\gamma^2)$  induced Eulerian circulation due to the  $O(\gamma)$  wave field. Now imagine exciting the fluid with a moving corrugated wall

<sup>12</sup> Dr. Stern has recently reported a similar calculation (private communication).

at  $y = 0$ . A convenient artifice, the term  $e^{\alpha t}$  ( $\alpha \ll \gamma$ ), will be used to show the uniqueness of the wave-induced flow [otherwise, one can add an arbitrary steady zonal flow,  $\gamma^2 U(y)$ ].

The equation and boundary conditions, at lowest order, are

$$\frac{\partial}{\partial t} \nabla^2 \psi^{(0)} + \beta \frac{\partial \psi^{(0)}}{\partial x} = 0$$

$$\left. \frac{\partial \psi^{(0)}}{\partial x} \right|_{y=0} = A \cos k(x - c_x t) e^{\alpha t}, \quad \psi^{(0)} \rightarrow 0 \quad \text{as } \begin{cases} t \rightarrow -\infty \\ y \rightarrow \infty \end{cases}$$

with

$$(u^{(0)}, v^{(0)}) = \left( -\frac{\partial \psi^{(0)}}{\partial y}, \frac{\partial \psi^{(0)}}{\partial x} \right)$$

The general solution,  $\psi^{(0)} = \mathcal{R}\{B \exp [ik(x - c_x t) + i\ell y + \alpha t]\}$  is constrained by the boundary conditions to have  $B = -iA/k$ , and by the equation to have

$$\beta ik - (k^2 + \ell^2)(ikc_x + \alpha) = 0$$

Now specifying  $k$  and  $c_x$  to be real, we find  $\ell$  is complex,

$$\ell^2 = -k^2 + \frac{\beta ik}{ikc_x + \alpha}$$

For small  $\alpha$ , let  $\ell = \ell_0 + i\alpha\delta$ , yielding

$$\ell_0 = \left( -k^2 + \frac{\beta}{c_x} \right)^{1/2}$$

$$\alpha\delta = \frac{1}{2} \ell_0^{-1} \frac{\beta\alpha}{kc_x^2}$$

The complete linear solution,

$$\psi^{(0)} = \frac{A}{k} \sin [k(x - c_x t) + \ell_0 y] e^{\alpha(t - \delta y)} + O(\gamma) + O(\alpha)$$

automatically reveals the energy velocity by the rate of northward propagation of the envelope,  $e^{\alpha(t - \delta y)}$ . The rate is the same as that predicted by group-velocity theory.

The second-order zonal flow,  $\overline{u^{(1)}}$ , is found from

$$\frac{\partial \overline{u^{(1)}}}{\partial t} = \frac{\partial}{\partial y} \left( \overline{\frac{\partial \psi^{(0)}}{\partial y} \frac{\partial \psi^{(0)}}{\partial x}} \right)$$

$$= \frac{\partial}{\partial y} \left( \overline{\frac{A^2 \ell_0}{k} \cos^2 [k(x - c_x t) + \ell_0 y] e^{2\alpha(t - \delta y)}} \right)$$

or

$$\overline{u^{(1)}} = -\frac{\delta \ell_0}{2k} A^2 e^{2\alpha(t - \delta y)}$$

The solution to this order includes an outward propagating wave, growing everywhere because the boundary forcing is increasing, and a westward flow induced by it. For

this problem the Eulerian mean flow varies only slightly over a wavelength, and hence the Lagrangian (particle-drift) mean is identical, to  $O(\alpha)$ . Here, unlike the free jet models, there is an increase in total  $x$  momentum, owing to the external agent.

This total westward momentum may be found from an argument used by R. W. Stewart for the case of internal gravity waves (see Bretherton, 1969). The force, say,  $F$ , exerted westward to maintain the motion of the corrugated wall creates kinetic energy in the fluid at a rate  $Fc_x$ , and creates momentum (or more generally, impulse) at a rate  $F$ . Thus the average (in  $x$  and  $y$  directions) energy density  $E$  and momentum density  $M$  must obey

$$M = \frac{E}{c_x}$$

where  $c_x = -\beta/K^2$  for Rossby waves of total wave number  $K$ .<sup>13</sup> With  $E = \frac{1}{2}\beta^2\bar{\eta}^2/K^2$ , this becomes a special case of our result, equation 37.

### I. Rossby Waves in a Shear Flow

To this point we have omitted the classic eddy-mean flow interaction, that of linear waves moving through a slowly varying zonal flow, for reasons of appropriateness. Nevertheless the results of the theory are interesting. First, wave action,  $E/(\omega - \mathbf{U} \cdot \mathbf{k})$ , is a conservative property for a packet of waves. Here  $E$  is the integrated wave energy, measured by an observer moving with the mean flow,  $\mathbf{U} = U\hat{\mathbf{i}}$ , and  $\omega$  and  $\mathbf{k}$  are the frequency and wave number in an absolute frame of reference. Multiplied by  $\mathbf{k} \cdot \hat{\mathbf{i}}$ , this is the total westward momentum of the waves, which is invariant even though energy is being exchanged with the mean flow (a consequence of the constant wave momentum being carried up the gradient of ambient mean flow).

Now it seems to be less than well-known that this conservation property holds for more extreme, geophysically more interesting, variation in  $U$  with  $y$ . Imagine the case when  $U$  takes on two uniform values,  $U_1$  and  $U_2$ , on either side of a vortex sheet lying along  $y = 0$ . A steady train of Rossby waves approaches from the south. Ignoring possible instability, we can calculate the partial reflection that occurs at the interface. The fluid boundary between the two regions can be treated rather like the corrugated wall considered above; an observer in region 2, moving with speed  $U_2$ , sees the corrugations move steadily westward at speed  $c = \omega/\mathbf{k} \cdot \hat{\mathbf{i}}$ , and records that that material surface is doing work on region 2 at a rate  $-F(U_2 - c)$  where  $F$  is the  $x$  force exerted by fluid in region 1, on the interface. Similarly, an observer in region 1, moving with speed  $U_1$ , reports that the upper fluid is doing work at a rate  $F(U_1 - c)$  on the lower. The evidence implies that wave-energy fluxes  $\mathcal{F}_1$  and  $\mathcal{F}_2$ , measured in either case by observers riding on the mean flow, obey

$$\frac{\mathcal{F}_1}{\omega - kU_1} = \frac{\mathcal{F}_2}{\omega - kU_2}$$

by elimination of the force,  $F$ . Thus the wave action is conserved also in this rapidly varying medium, and is now partitioned among incident, reflected, and transmitted waves.<sup>14</sup> The argument applies to a large class of waves, including some with non-

<sup>13</sup> The work of Bretherton (1969) and McIntyre (1971) suggests extreme caution in the application of ideas of wave-momentum density; the mean flows associated with wave packets radiate far away from them. Here the  $x$  averaging conceals this.

<sup>14</sup> Yet an observer at rest, including as "wave energy" both the oscillatory and induced mean flow due to the waves, reports from the same argument that wave energy flux is conserved.

trivial structure normal to the propagation plane (e.g., short surface waves propagating among currents). It is related to the result of Eliassen and Palm (1960) for steady wave trains in a density-stratified atmosphere with horizontal winds of arbitrary vertical structure, that the momentum flux  $\overline{u\bar{w}}$  is independent of height.<sup>15</sup>

These results add further light to the discussion of jetlike mean flows. For waves propagating outward from the center of an eastward jet, where  $U - c$  ( $\propto E$ ) is large (recall that  $c < 0$ ), will transport westward momentum outward from the jet core, thus increasing the  $x$ -mean energy there, while  $E$  decreases. If  $U - c > 0$  everywhere in the corresponding westward jet, outward-propagating waves will still carry westward momentum, now at the expense of the zonal-average energy of the core as  $E$  increases. When the theory of critical-layer absorption is added in, covering flows where  $U - c$  vanishes at some latitude, the interactions can be calculated in detail, and are of relevance particularly to atmospheric flows (Dickenson, 1970).

### *J. Topographic Effects: Nonlinear Theory*

The theory of circulation induced by eddies given in most general form in equations 36 and 38 applies as well when the potential vorticity gradient is not simply a constant. The geostrophic contours of  $f/h$ , where  $h$  is the depth of a barotropic model, are generalizations of latitude circles, and the induced circulation obeys

$$\frac{\partial \bar{u}_E}{\partial t} = - \frac{h}{2} \overline{\left( \nabla \left( \frac{f}{h} \right) \times \mathbf{k} \right) \frac{D\eta^2}{Dt}}$$

for inviscid flow; a similar generalization of equation 38 follows with Ekman friction. Here  $\eta$  denotes the particle displacement normal to the contours, and the averaging bar is a line integral about a complete contour. The variations of  $\nabla(f/h)$  in space, over distances  $\sim L_h$ , however, impose the additional restriction that  $\eta \ll L_h$ .

We may expect to see anticyclonic circulation above seamounts and ridges in the deep ocean, when random forcing acts at a distance so that the region in question is "free." Such circulation has indeed been found in my numerical experiments (Section 7), and Holloway (private communication) has discovered similar contour currents in his barotropic model (Section 7).

An illustrative example from my early barotropic experiments (Fig. 55a) shows particle trajectories in finite-amplitude "roughness" waves above a sinusoidal bottom. The oscillations, in the mean, cause the fluid over ridges to have negative relative vorticity, and conversely. This yields contour currents of both Eulerian and Lagrangian flow, which are fully as strong as the currents associated with the primary wave.

An extreme example from the sea is the persistent anticyclonic current found above the Great Meteor Seamount by Meincke (1971), which occurred in the presence of fluctuations at tidal period and longer. The results apply not only to the deep ocean; the continental rise and shelf provide a systematic, strong potential-vorticity gradient, and shelf waves and turbulence are present in abundance. The above theory, which applies when lateral boundaries do not block the geostrophic contours, provides an alternative to direct wind-generated longshore currents.

<sup>15</sup> A further consequence of this formula is that, if the phase speed,  $c$ , lies between  $U_1$  and  $U_2$ ,  $\mathcal{F}_1$  and  $\mathcal{F}_2$  have opposite signs. With no incoming energy from  $+\infty$ , then,  $\mathcal{F}_1 < 0$ , and net energy must flow away from the interface on both sides of it. This is known as "overreflection" of an incident wave.

Small-scale roughness on the bottom acts in a distinct way on mesoscale flows, probably providing an augmented drag owing to both its small-scale geostrophic wake and lee Rossby-wave and internal-wave generation. Bretherton and Karweit (1975) have emphasized this role of the roughness.

### K. Applications

The theory has been presented in an idealized form, but its extensions bear on the oceanic case with stratification, topography, and lateral boundaries. There the eddy flux of vorticity into a fixed, elemental region yields an average stress curl which can then drive a large-scale Eulerian circulation in the classical manner. The result analogous to equation 36 for a single-layer ocean, with mean potential vorticity  $Q(x, y)$  is that the potential vorticity flux-divergence may be rewritten to give

$$\frac{\partial}{\partial t} \nabla^2 \langle \psi \rangle + J(\langle \psi \rangle, Q) = \frac{\partial}{\partial x_i} \left( \kappa_{ik} \frac{\partial Q}{\partial x_k} \right)$$

where  $\kappa_{ij} = \int_0^t R_{ji}(\tau | \mathbf{x}) d\tau$ ,  $R_{ij} = \langle u_i(t) u_j(t + \tau) \rangle$ ,  $u_i = (\partial \psi / \partial x_2, -\partial \psi / \partial x_1)$ . Here  $\langle \psi \rangle$  is the ensemble-averaged flow, and  $Q(x, y)$ ,  $\kappa_{ij}$  are assumed slowly varying in space, relative to the particle excursions. If  $\kappa_{ij}$  is identified with the eddy diffusivity, then this becomes Welander's (1970) formulation, which was based heuristically on a down-gradient diffusion of vorticity. Unlike Welander (1970), Green (1970), and Rossby (1947), however, we suggest that the time-dependent theory, with  $\kappa_{ij}$  allowed to vary wildly in space, is likely to be of interest for the ocean. Over times greater than an eddy period, but less than the climatological time scale, a pulsing of eddy energy can drive temporary "mean" flows with the diffusivity either positive or negative; in free initial-value problems described earlier, in fact, the area-averaged diffusivity vanished.

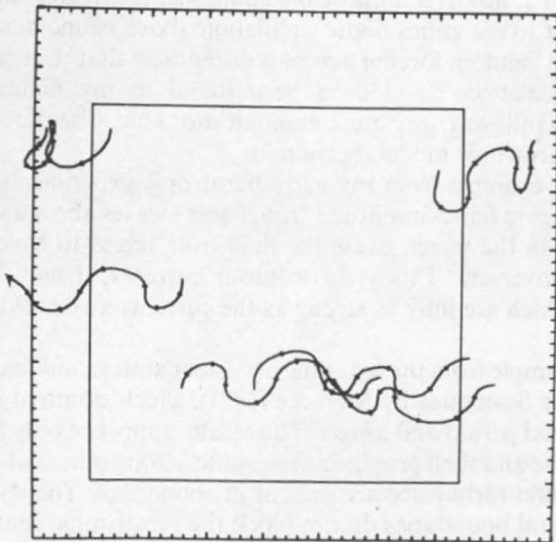


Fig. 55. Two examples of eddy-induced mean circulation in a homogeneous model. (a) The Lagrangian paths of particles in finite-strength waves above a sinusoidally corrugated bottom lie east-west along depth contours.

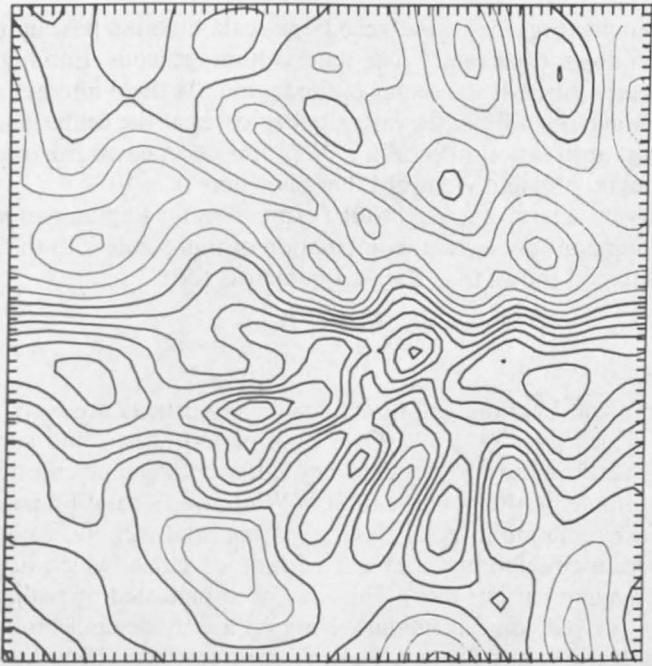
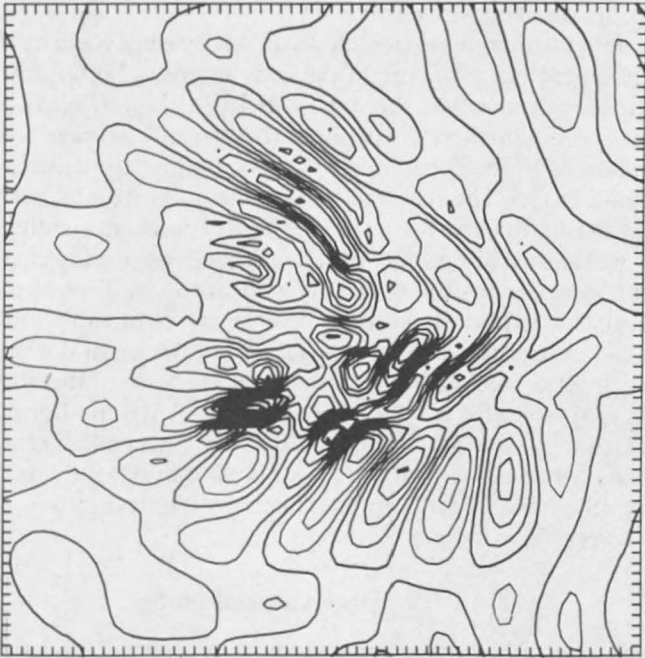
$\Psi$  $\zeta$ 

Fig. 55. (b) an initial cluster of eddies near the center interacts and radiates, developing a large-scale eastward jet in the center, westward flow at the periphery (full lines are positive  $\psi$  here). The vorticity field shows the small-scale tilted troughs, the vehicle of vorticity flux.

As an example (Fig. 55*b*) witness the large-scale Eulerian flow induced in a simple  $\beta$  plane spin-down experiment. The fluid is homogeneous. Initially a small cluster of eddies is prescribed at the center of the region. As these interact and radiate into the surrounding, quiet fluid, the intensity decreases at the center and increases elsewhere. Direct application of equation 36 promises an eastward zonal-mean flow at mid-latitudes ( $\kappa < 0$ ) and westward flow elsewhere ( $\kappa > 0$ ).

The eddy-stress term is related to the expression for Lagrangian mean flow, given at the beginning of this section; combination of that result with the above turbulent vorticity equation shows that, if  $\kappa_{ij}$  is symmetric, then

$$\left\langle \frac{\partial \zeta^E}{\partial t} \right\rangle + \left\langle \frac{D \zeta^L}{Dt} \right\rangle = -2\beta \langle v^E \rangle.$$

The Eulerian and Lagrangian rates of change of vorticity are equal but *opposite* for ensembles which have  $\langle v^E \rangle = 0$ . Over brief periods, floats and current meters will tend to register the same vorticity tendency, but over long times, the opposite tendency.

As an example, in the configuration of Whitehead's rotating paraboloid, it turns out that the circulation integral about a *moving* fluid contour is equal and opposite to the Eulerian circulation about a fixed latitude circle (which itself often is equal to the Lagrangian particle drift). This may be appreciated by realizing that the area enclosed by a dyed contour, initially lying on a latitude circle, must decrease if the fluid is displaced in any fashion. Kelvin's theorem then yields *eastward* circulation about this moving contour, but all particle motion (in free latitudes), and the Eulerian momentum, are directed westward.

In addition to the time-dependent flows driven by eddy vorticity flux, the discovery of quasi-permanent fine structure in the eddy intensity both in the models and the ocean, tremendously increases the stress curl,  $(\partial/\partial x_i)[\kappa_{ik}(\partial Q/\partial x_k)]$ .

In a stratified ocean these ideas apply to vertically averaged vorticity flux. The vigorous diffusivity of the upper-level flow may, in this case, drive abyssal circulation, as in Holland's model. The required vertical flux of horizontal momentum has been discussed by Bretherton and Karweit (1975). An experiment yielding mean circulation in this way was shown in Fig. 43*e*; the advancing front of eddy energy in this "propagation" run yielded a positive diffusivity with strong gradient, and created westward zonal-average flow in both shallow and deep layers. In other regions being drained of their eddy energy, the diffusivity was *negative* and the mean flow eastward.

The vorticity-flux theory gives dynamical significance to the observed diffusion of water-mass properties, for instance, the silicate in Antarctic Bottom Water, and the salt in the Mediterranean outflow. In addition, the direct measurement of Lagrangian diffusion can now be made with neutrally buoyant SOFAR floats (Freeland, Rhines, and Rossby, 1975); the spreading of the cluster with time (Fig. 64) gives a first estimate of 1500-m-level diffusivity,  $\approx 8 \times 10^6 \text{ cm}^2/\text{sec}$ .

## 9. Observational Notes

Observations of unsteady currents are now widespread, and we may anticipate a rapidly improving picture of their geographical distribution. For a sample, Hamon (1968), and Boland and Hamon (1970) have recorded eddies and pulsations in the East Australia Current; Mazeika (1973) and Koshlyakov and Grachev (1973) have described eddies in the North Equatorial Current; Bernstein and White (1975) have produced time sequences of thermocline eddies in the eastern North Pacific; Swallow and Bruce (1966) and Bruce (1973), describe a "separation bubble" in the Somali

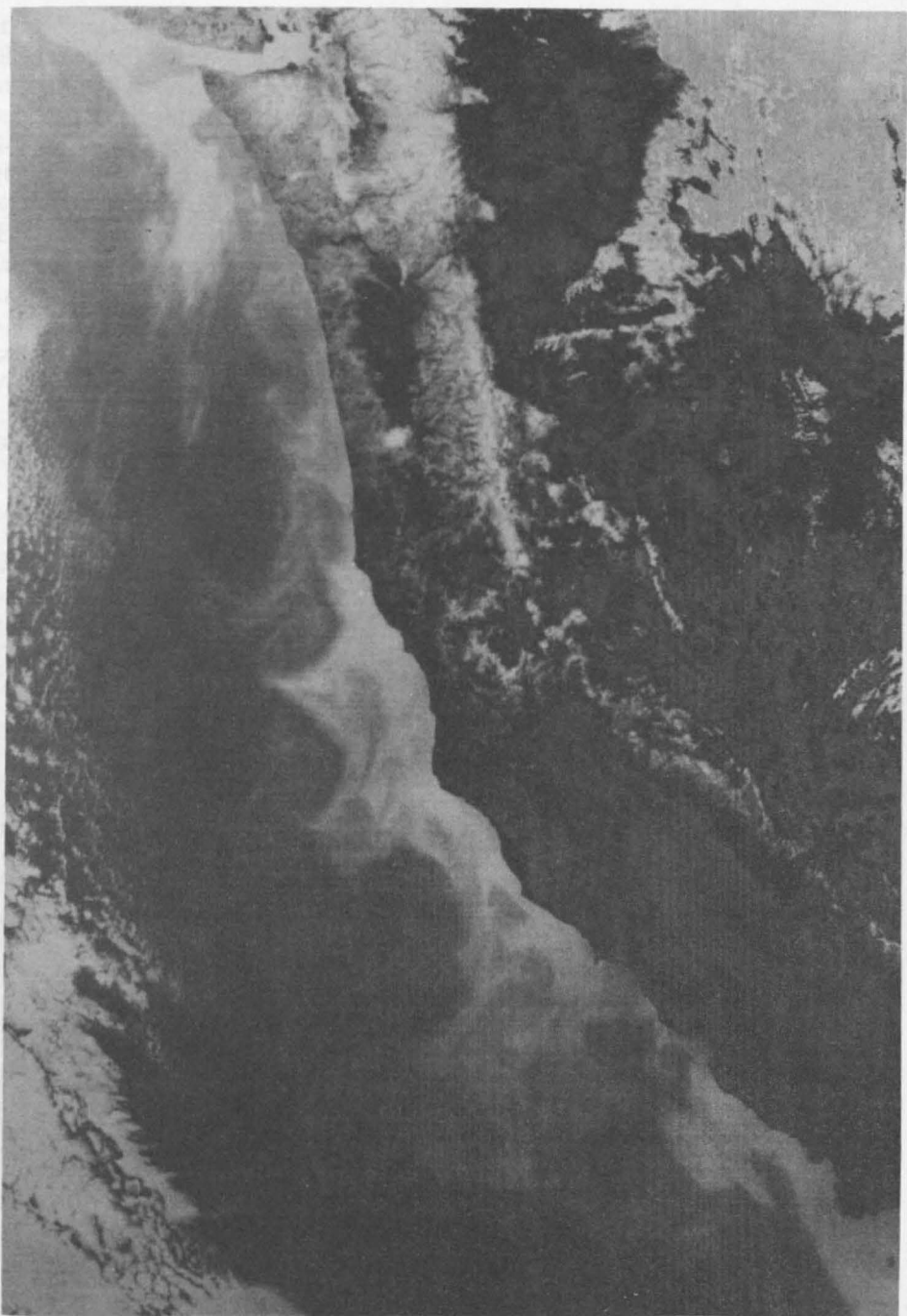


Fig. 56. Sea-surface temperature patterns along the west coast of the United States (from the NOAA-II satellite, courtesy of NOAA-National Environmental Satellite Service). Darker areas are warm, light areas cold. Sept. 11, 1974, after an intense period of coastal upwelling.

Current; Düing, Katz, and the GATE group (private communication) have found the Atlantic Equatorial Undercurrent to be oscillating on a large scale; Foster (1972) has seen gross irregularities in the Antarctic Circumpolar Current at the Drake Passage (where the net inferred transport was westward during the current meter experiment!); the MEDOC Group (1970) found eddies to occur after violent, meso-scale, deep convection in the western Mediterranean; and Swallow and Hamon (1960) and Gould (1971) report variable currents in the eastern North Atlantic and Bay of Biscay. As in the atmosphere, the meandering and pulsation of intense currents appears as eddy energy if time averaging is used, yet there is some distinction between such dynamics, and those of detached, freely moving eddies and waves in the ocean interior.

Surely the most dramatic evidence for eddies is the infrared photographs of the sea-surface temperature field, from earth satellites. Figure 56, from the NOAA series of satellites, shows billowlike patterns at the edge of cold coastal water lying off Oregon and California. Can these be the instabilities of the cold, southward coastal current? The temperature structure of the separated Gulf Stream (Fig. 57)



Fig. 57. The Gulf Stream near Cape Hatteras from a NOAA satellite, April 28, 1974. Woods Hole Oceanographic Institution's Site D is found to the left side of the prominent eddy just north of the Stream (black dot).

shows the distinctness of transition between shelf, slope, Gulf Stream, and Sargasso Sea water masses, giving life to these classical water-mass divisions. Active entrainment of cold water by warm eddies appears at the shelf edge (cf. Fig. 15) and a cold eddy seaward of the Gulf Stream entrains warm water from the stream near Cape Hatteras. Site D, the source of current records (Fig. 13), is indicated. It is remarkable that, amidst this chaos, linear wave theory continues to have qualitative truth (Sections 4 and 8). At Hatteras, the southward flowing shelf water is also entrained into the Gulf Stream, and but occasionally penetrates the crescent-shaped bays farther south. The crispness of these patterns reemphasizes the inability of geostrophic flow to cascade energy to small scales, in the efficient sense of 3D turbulence. Even though surface frontogenesis is no doubt occurring, and sharpening the temperature gradients, the picture lacks the fuzziness that we see in a laboratory turbulent jet, rich in energy over a broad range of scales.

Finally (Fig. 58), surface traces of eddies have appeared in mid-ocean. Dr. Legechis of NOAA has enhanced the signals (the satellites were designed for meteorology, not

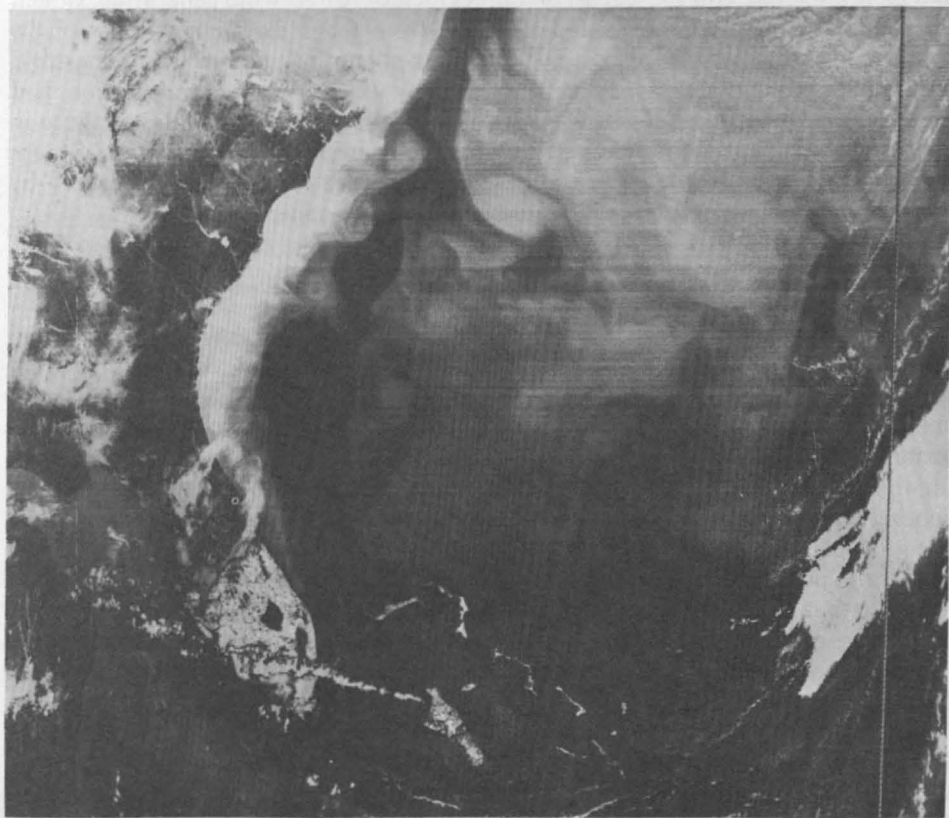


Fig. 58. NOAA-satellite view of the Sargasso Sea, April 1, 1974, enhanced by Dr. Legechis. Eddies are visible (at least in the original) not only near the Florida Current, but in open ocean. The MODE experiment occurred beneath the prominent north-south tongue of warm water in the right-center. Observed structure suggests that thermocline eddies should be made visible on the surface by the action of their velocities, more than their own temperatures. A cold, cyclonic Gulf Stream ring is visible, entraining warm water from the Stream. The gray shades cover a  $9.1^{\circ}\text{C}$  temperature range (darker = warmer), while black is  $2.1^{\circ}\text{C}$  range above this, and white represents all other temperatures, whether cold or hot.

oceanography), and finds warm and cold tongues hundreds of kilometers in scope with a clear imprint of horizontal advection. This picture reveals the organic reality of the mid-ocean north-south temperature gradient (which on climatological maps is so smooth). It is suggestive of down-gradient mixing by thermocline eddies. The connection with the deeper density field is unknown, as is the strength of the subtropical front suggested by the picture. Here at the top of the mixed layer, one can imagine the white imprint of cold windstorms continually being distorted by lateral stirring of the thermocline eddies. Elsewhere, entrainment appears by a cold eddy (the same as in Fig. 57) near the Gulf Stream, and billows occur on the shoreward side of the stream (see Rao, Strong, and Koffler, 1971), which were associated with momentum convergences by Webster (Section 8). A great deal of activity, perhaps with pulse-like variations of the Florida Current, occurs on the Blake Plateau.

### A. Sources

With improved observation, the sources and sinks of eddy energy will become more and more apparent. Our present list of sources includes direct wind generation, violent instabilities of intense currents and radiation from them, slower instability of the gentle mid-ocean currents, flow past rough topography and irregular coastline, occasional sinking of cold water, enhancement by western-boundary reflection, and possible driving by internal-wave stresses. The analogy of the dynamics to those in the atmosphere appears rather weak here, for the sources of energy seem to be more sparsely distributed in the ocean, and the domain itself is far bigger, measured by deformation radii and propagation rates, than the atmosphere.

### B. Dissipation

A crucial, unknown aspect of the long-term distribution of energy is the dissipation process. For example, the nature of interaction between mesoscale eddies and internal waves is uncertain even as to sign (Müller, 1974, predicts that internal waves drain energy from eddies, whereas other, more deterministic theories like critical-layer absorption may suggest the opposite). Again the ocean and atmosphere are very dissimilar, internal waves being far weaker than the large-scale flows in the atmosphere. The reason may be the absorptive nature of the stratosphere (owing to the effect of decreasing density in the kinematic viscosity), and less efficient generation at the ground. The ocean bottom, on the other hand, probably has an albedo of at least  $\frac{1}{2}$ , and turbulence and wind waves at the surface are a potentially strong source.

Dissipation by lateral friction is far weaker than classical eddy coefficients would suggest. The very nature of geostrophic turbulence, by its inability to extend vortex lines indefinitely, is to avoid such dissipation. The deep valley in frequency spectra between periods of a day and a few weeks (e.g., Rhines, 1973) attests to the lack of a homogeneous cascade, local in  $(\omega, k)$  space, between geostrophic and ageostrophic flow. Bottom friction, from conventional drag laws, is very slight, a few percent of 1 dyne/cm<sup>2</sup> in mid-ocean, giving a spin-down time exceeding 500 days. [Lee-wave drag exerted by topography of a few kilometers' lateral extent, may be far more significant (Bell, 1975).]

Once again the analogy between atmosphere and ocean breaks down in comparisons of the boundary drag and dissipation. The atmospheric lower boundary layer is  $O(1 \text{ km})$  thick, fully 10% of the depth of the troposphere. Perhaps one-half of the energy dissipation occurs there (Kung, 1967). This suggests a rapid spin-down of

atmospheric energy ( $e$  folding, say, in 3–6 days compared with an inertial time scale  $L/U \sim 1$  day for  $L \sim 1000$  km,  $U \sim 10$  m/sec). In the ocean, on the other hand, active three-dimensional turbulence does not seem to exist in regions thicker than  $O(10$  m), or 0.2% of the fluid depth.

Yet a crude estimate of overall dissipation time for oceanic kinetic energy is the ratio of vertically integrated kinetic energy density, to the rate of working by wind stress,  $\tau$ , or  $\rho \int |\mathbf{u}|^2 dz / \tau U_s$ , where  $U_s$  is a subsurface downwind current. For  $U_s = 10$  cm/sec,  $\tau = 1$  dyne/cm, and currents of 10 cm/sec above the thermocline and 4 cm/sec below, this yields a time of 19 days: a very short time in view of the paucity of three-dimensional turbulence, and one comparable with the inertial time scale  $L/U$  ( $\sim 5$ –20 days). The presence of severe intermittency may make such an estimate meaningless, but it suggests the need to search for the sinks as well as the sources of energy.

### C. MODE; Velocity

Some further data from the MODE experiment, discussed by Schmitz et al. (1975), is of more than casual interest here. Two site moorings were maintained for longer than 2 yr: MODE "east" ( $28^\circ 10'N$ ,  $68^\circ 35'W$ ) over hilly topography and, 100 km to the west, MODE "center" ( $28^\circ 00'N$ ,  $69^\circ 40'W$ ), above the Hatteras abyssal plain. Daily current vectors at three levels (filtered of internal waves) (Figs. 59, 60) show the usual decrease in time scale with depth. The energy level also decreases downward across the thermocline, yet rises slightly below 1500 m. The series are quite regular, yet there are occasional bursts of unusual activity. The 1500-m and 4000-m levels are visually coherent in the vertical, but not the horizontal. There appears, particularly at 1500 m, an eastward decrease in eddy-energy density. At the 4000-m eastern site, an unusually strong mean current flows at 2 cm/sec to the south-southwest. The presence, some 15 km to the southeast, of a dominant ridge topography ( $35$  km  $\times$   $5$  km  $\times$   $500$  m high) may not be incidental. This deep mean flow is known from other measurements to be of small lateral extent. The appearance of these noticeable gradients in intensity over small lateral separations, and of small-scale, deep, mean flows was a dominant feature of the rough bottom simulations (Section 7).

### D. Zonal Bands

At 500 m (note the rotated coordinates, Fig. 60), on several occasions, a strong burst of zonal flow appears at both moorings. This coherence over 100 km is unusual (it does not appear below the thermocline) and is suggestive of the anisotropy found to be so persistent in the computer experiments, when they were sufficiently energetic (Figs. 20b, 23d, 25d). There is some indication of a sympathetic pulse of energy in the deep water at these times.

There is evidence in other forms of zonally banded currents, from a variety of sources; P. Richardson and collaborators have recently followed SOFAR floats, depths 700–1100 m, in the region  $32^\circ N$  to  $36^\circ N$ , attempting to lay them within Gulf Stream rings. The trajectories, as well as showing some loops, followed long zonal excursions, westward and occasionally eastward, at an average velocity of about 5 cm/sec. Yoshida (1970) and Bryan (private communication) suggest that tropical regions exhibit banded currents, more extensive than the usual equatorial system. (Yoshida describes five or six distinct jets in the Pacific,  $20^\circ N$  to  $30^\circ N$ .) One must of course be wary of contours drawn from north-south sections widely spaced in longitude. Recalling Whitehead's experiment, we remark that any permanence in the



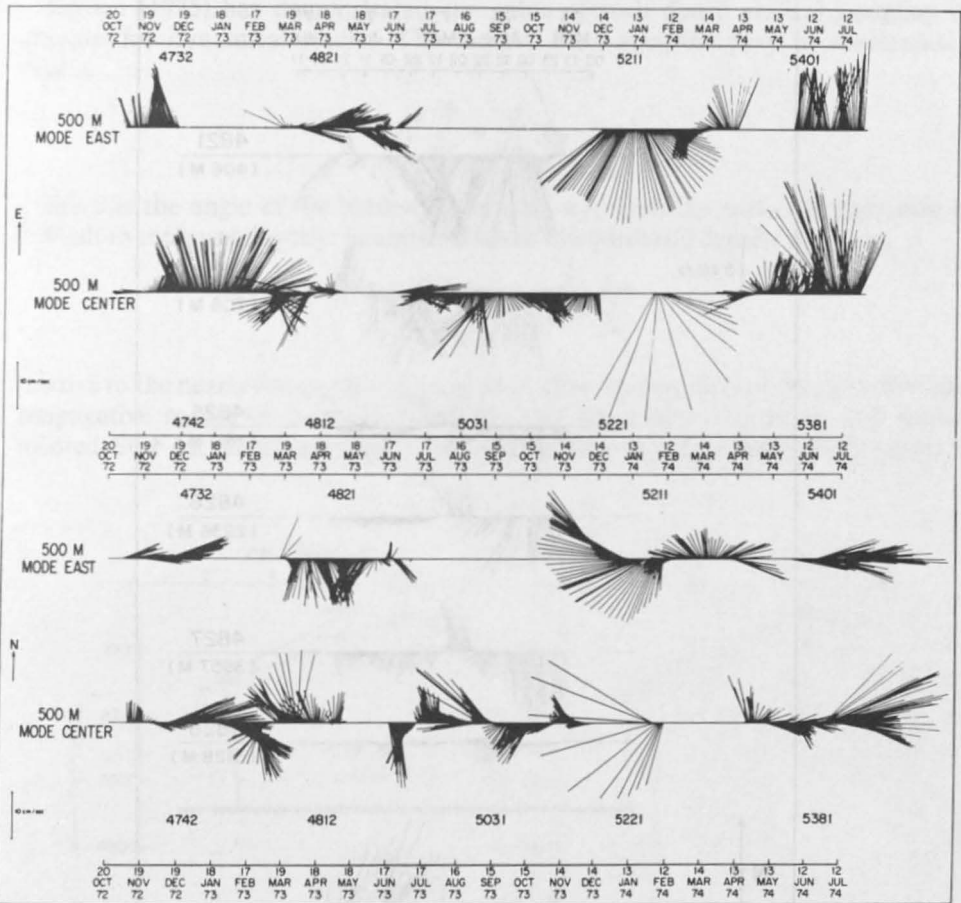


Fig. 60. Records from site moorings as in Fig. 59, 500-m level, plotted two ways (east = up, then north = up). Bursts of strong, zonal energy occur, coherent over 100 km (recall banded structures which recur in the numerical models, e.g., Figs. 23, 40).

forcing pattern will yield permanent bands, whereas in our free spin-down experiments a banded appearance occurred by chance, with the growth or decay of  $\langle \eta^2 \rangle$  in a given region. G. Williams' (private communication) experiments very likely involve the same physics, in a model of Jupiter's atmosphere.

A shorter sequence with dense vertical coverage is from the intensive period of the experiment (Fig. 61). The upper portion is excerpted from the record at MODE-east, in the rough area. It shows the kind of waxing and waning of vertical coherence that appeared, with nonlinear "capture" followed by topographic scattering, in the simulations, Fig. 37c. A period of southward flow (the eastern side of a warm thermocline eddy) begins at almost all levels; yet it gives way, below, to the shorter time scales natural to the deep water. The deepest level, 100 m above the sea floor, is grossly out of step; we suggest that it is dominated by fine-scale topographic oscillations, frontal activity (where thermal gradients intersect the boundary), and perhaps occasional intrusion of the bottom mixed layer.

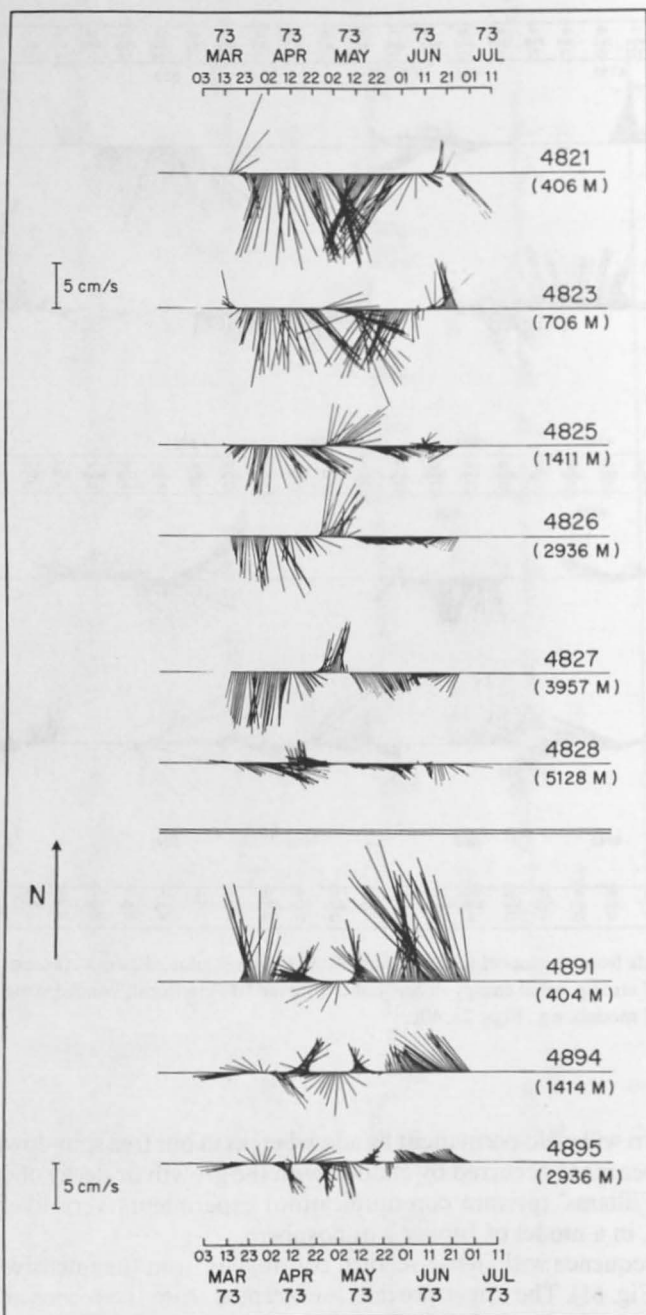


Fig. 61. Two short records from MODE showing well the vertical current structure, mooring 482 ( $28^{\circ}9'N$ ,  $68^{\circ}39'W$ ) and 489 ( $29^{\circ}35'N$ ,  $70^{\circ}W$ ). The more quickly varying yet weaker currents in the deep water and brief episodes of great vertical coherence are commonplace.

Bryden (1975) has demonstrated the value of such dense vertical sampling of currents for dynamical studies. The thermal-wind equation may be manipulated to give

$$|\mathbf{u}_H|^2 \frac{\partial \theta}{\partial z} = \frac{g}{f\rho_0} \mathbf{u}_H \cdot \nabla \rho$$

where  $\theta$  is the angle of the horizontal current,  $\mathbf{u}_H$ , from the east. The right side is difficult to measure directly. Its importance in the adiabatic density equation,

$$\frac{\partial \rho}{\partial t} + \mathbf{u}_H \cdot \nabla \rho = -w \frac{\partial \rho}{\partial z}$$

relative to the nearly linear, right term, gives a direct comparison of the advective and propagative nature of the eddy field. [Moored temperature recorders and instrumented SOFAR floats measure  $\partial \rho / \partial t$  and  $\partial \rho / \partial t + \mathbf{u}_H \cdot \nabla \rho$ , respectively (given a

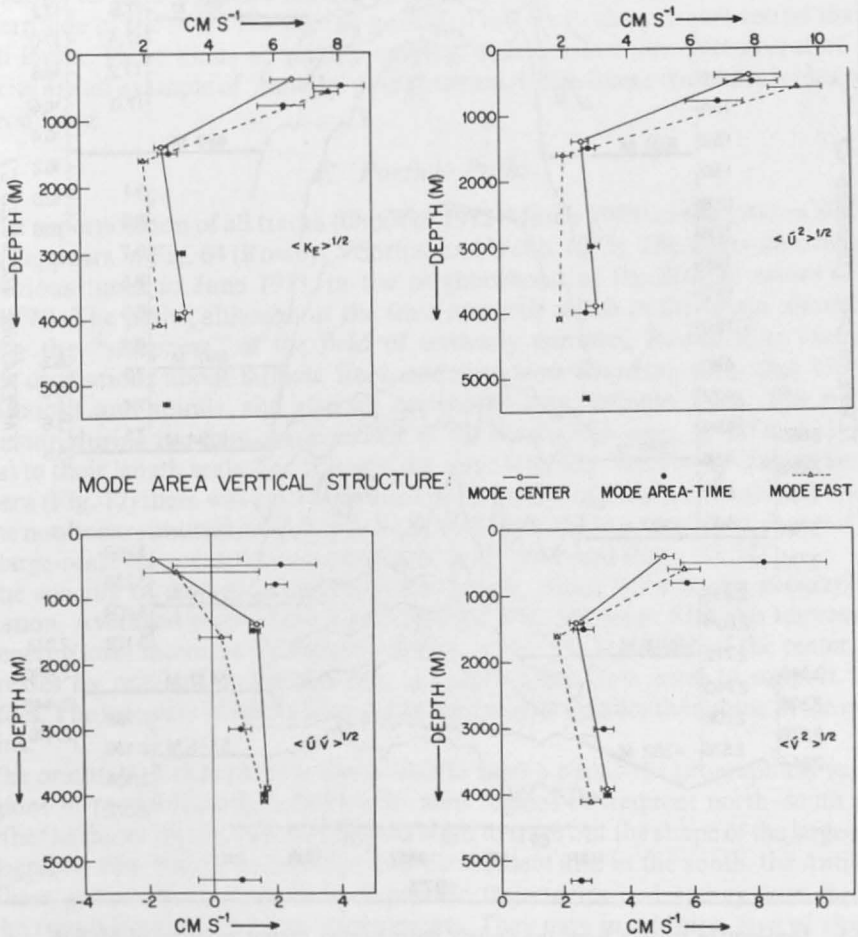


Fig. 62. Three representations of the average vertical current structure, from the two site moorings and the brief, spatially intense MODE experiment.

$T$ - $S$  relation). In all, they provide three determinations of the three terms in the equation.] Bryden concluded that, for a few weeks in MODE-I, the horizontal advection of density was well-correlated with, and comparable in magnitude to, the local time-derivative of density. This is consistent with the nonlinear picture of an eddy field.

The lower section of Fig. 61 shows perhaps a more classical structure of a slowly varying thermocline eddy, superimposed upon fast oscillations which are themselves more highly coherent in the vertical. This record was taken 170 km north of the MODE center.

In the time-averaged vertical structure (Fig. 62), the minimum in speed at 1500 m is visible, with a slight increase toward greater depth. If we adopt this profile to a

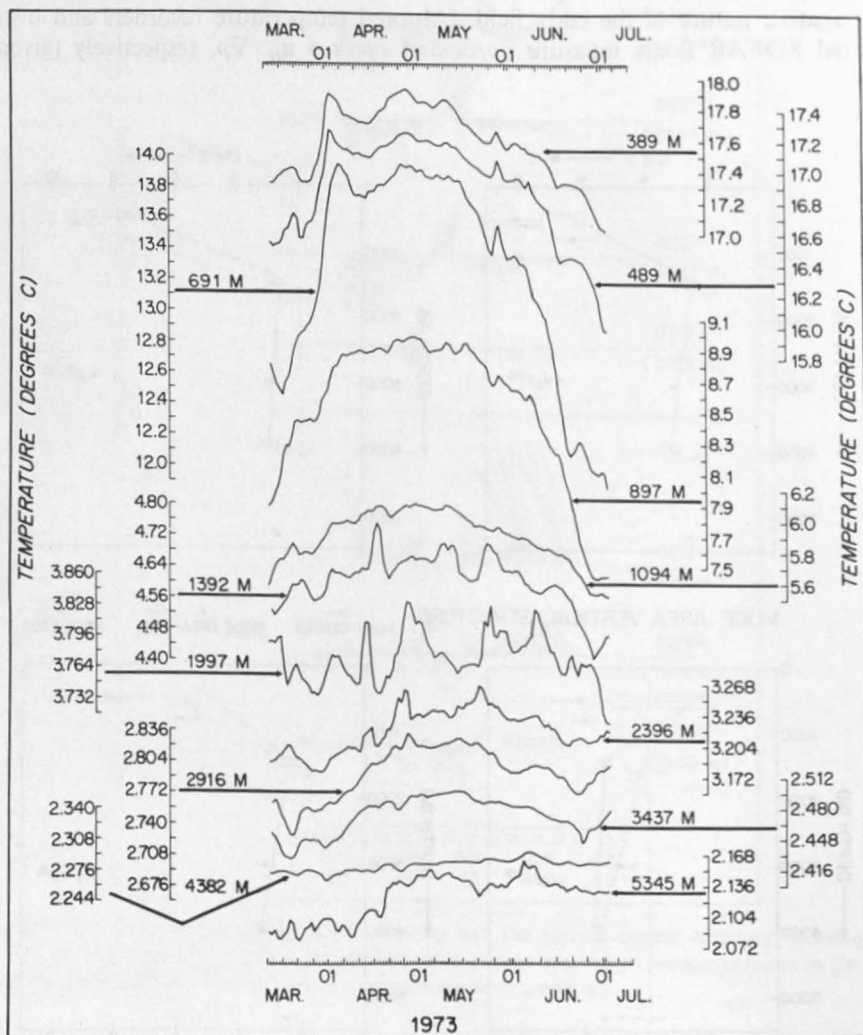


Fig. 63. Temperature records from the densely instrumented central mooring of MODE, courtesy of Drs. Schmitz and Wunsch. Time scales far shorter than those of linear, classical Rossby waves are present here.

two-layer model,  $U_2/U_1 \approx 0.4$ , and  $\varepsilon/\delta$ , based on 5 cm/sec rms current (the vertical average) and 200-m rms topographic height, yields  $\varepsilon \approx 0.02$ ,  $\delta \approx 0.05$ ,  $\varepsilon/\delta \approx 0.4$ . Referring to Fig. 36, this agrees satisfactorily with the simulated  $U_2/U_1$ . The dependence of the simulated structure on the manner of supplying the energy, however, requires study. The computer experiments, despite their spontaneous fine structure, suggest that the Hatteras abyssal plain is too narrow ( $\sim 150$  km) at this latitude to allow the fluid to respond to it; one cannot apply Fig. 36 to such a small region.

#### D. Temperature

The MODE center was heavily instrumented, also, for temperature (Schmitz et al., 1975; Wunsch, 1975). Figure 63, the pressure-corrected time series, shows a rapid warming, extending nearly to the ocean bottom, followed by a more gradual cooling. The noisy signal at mid-depth is characteristic of salty Mediterranean water, undergoing active mixing with its surroundings. There is unusual noise just above the bottom, where the currents were also observed to be special. It is easy to imagine a simple, sharp-edged thermocline eddy from this figure, but in fact the temperature rise seems to be a frontlike feature embedded in the more gradual and extensive western side of the eddy. During the arrival of this front, the currents veered sharply at all levels. These kinds of quickly varying, interlocked fields of temperature and velocity are an example of "mobile" fine structure, which linear dynamics is incapable of producing.

#### E. Particle Paths

The superposition of all tracks (October 1972–March 1974) of the 1500-m SOFAR floats appears in Fig. 64 (Rossby, Voorhis, and Webb, 1975). The floats were released at various times to June 1973, in the neighborhood of the MODE center ( $28^\circ\text{N}$ ,  $69^\circ 40'\text{W}$ ). The paths, although at the *least* energetic depth of the ocean, show most clearly the "steepness" of the field of unsteady currents. Rather than executing slight oscillations about latitude lines, added to slow Sverdrup drift, they undergo wild hooks and spirals, and also an occasional long, straight track. The particle excursion during the time characteristic of the deep eddies (say, 10–20 days) is fully equal to their length scale, and this sets the wave steepness near unity. Yet within this pattern (Fig. 12) there was clear westward propagation of phase; a ubiquitous feature of the nonlinear simulations was in fact the westward phase progression, except where the large-scale ( $L > L_p$ )  $f/h$  contours were badly distorted (Figs. 20, 24).

The spacing of daily fixes indicates the speeds, which have strong geographical variation. Averaged plots of the kinetic energy (Fig. 65) agree with this impression; the energy level increases by a factor of three in the 500 km south of the center, and decreases by one-half in 300 km east of center. Later data seem to support these profiles. The intensity of eddies thus varies on scales far smaller than those of the ocean basins.

The orientation of the tracks seems also to have a persistent geographical variety. Regions of predominantly zonal tracks abut regions of frequent north–south flow. Farther to the north and south, the paths seem to trace out the shape of the large-scale topography (the Blake Outer Ridge and Escarpment and in the south, the Antilles).

These geographical gradations of particle trajectories and energy were familiar in the rough bottom numerical experiments. They may in addition give us clues to the source of the deep eddies. One sees the nearby Florida Current (Fig. 58), and the western boundary undercurrent (which has been recorded directly beneath the looping

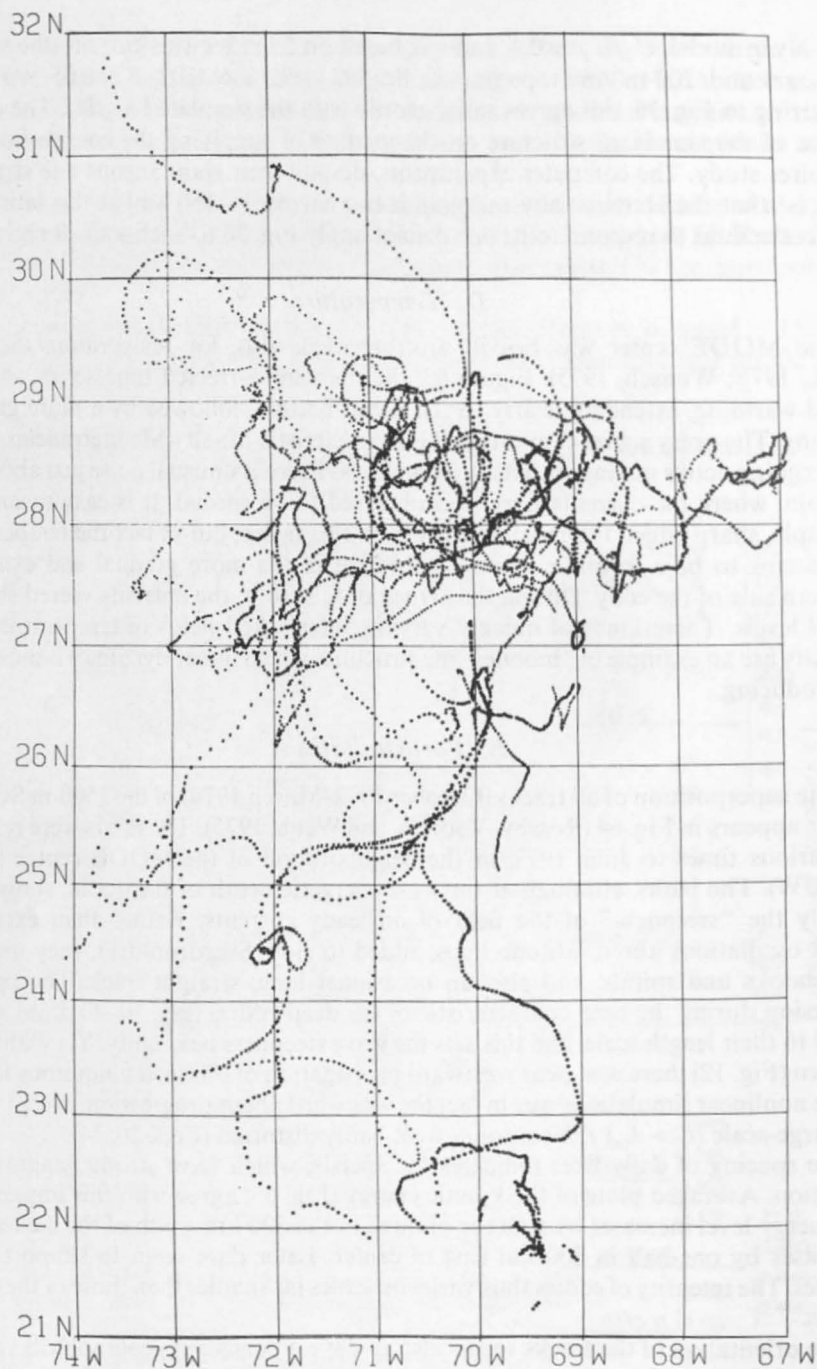


Fig. 64. The superposition of all trajectories, October 1972–March 1974 from neutrally buoyant SOFAR floats at 1500 m (from Rossby et al., 1975), daily positions plotted. A geographical variation in energy, as well as in the turbulent character of the flow, is evident.

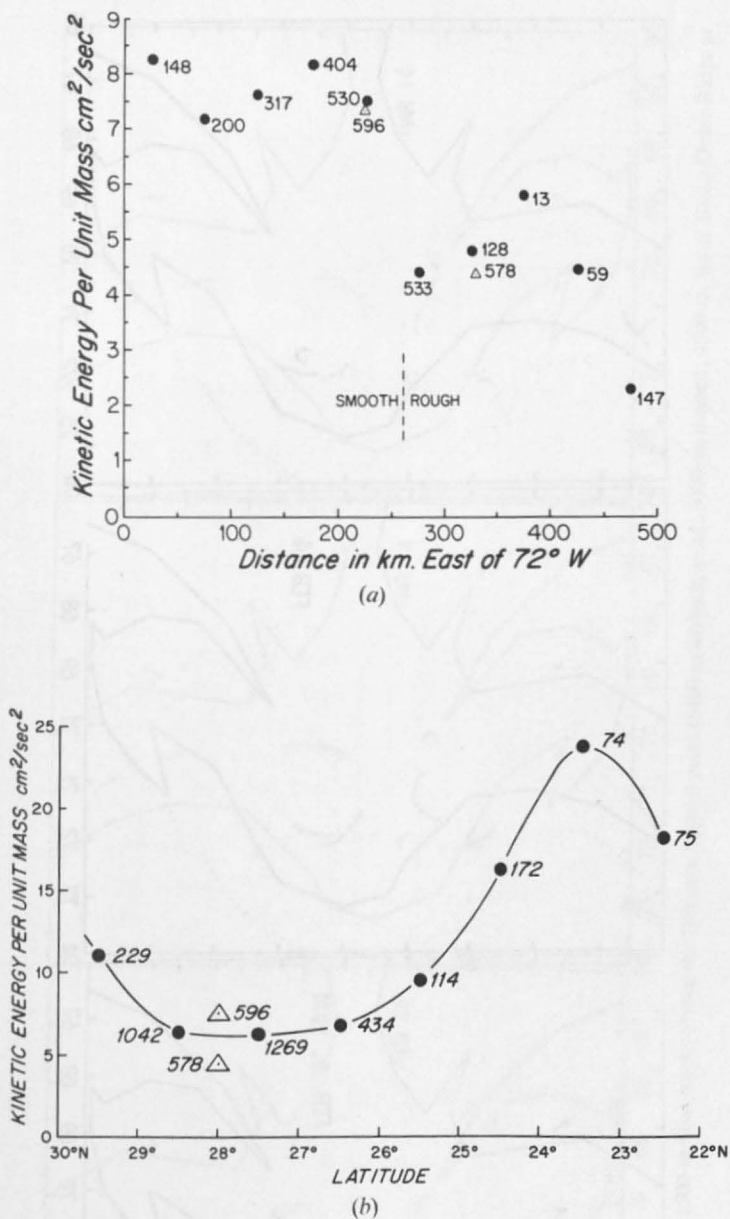
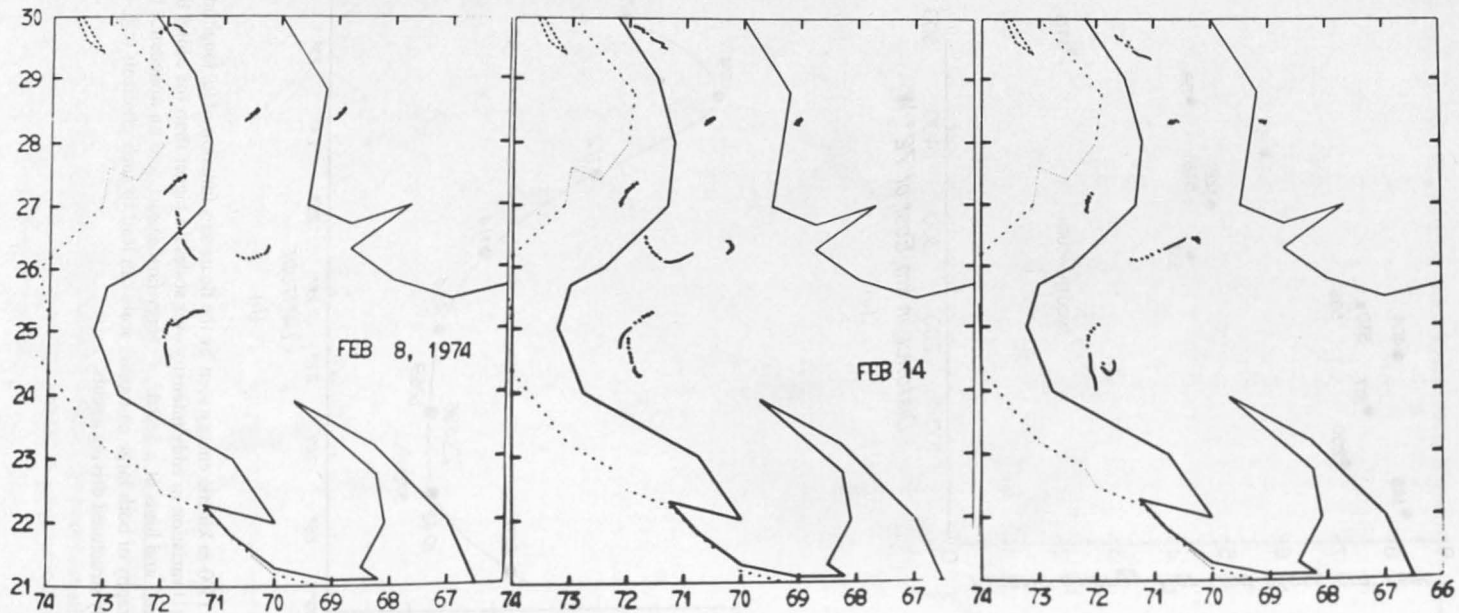


Fig. 65. Average 1500-m kinetic energy seen by the floats as a function of (a) longitude and (b) latitude. This permanent  $O(1)$  variation in eddy intensity over scales no bigger than the eddies themselves forms a fixed "fine structure," and hints at a dearth of energy farther east, and an abundance to the north, west, and south. Topography of both large and small scale can lead to such gradients (e.g., Figs. 41, 43f), but so also could highly structured driving agents.



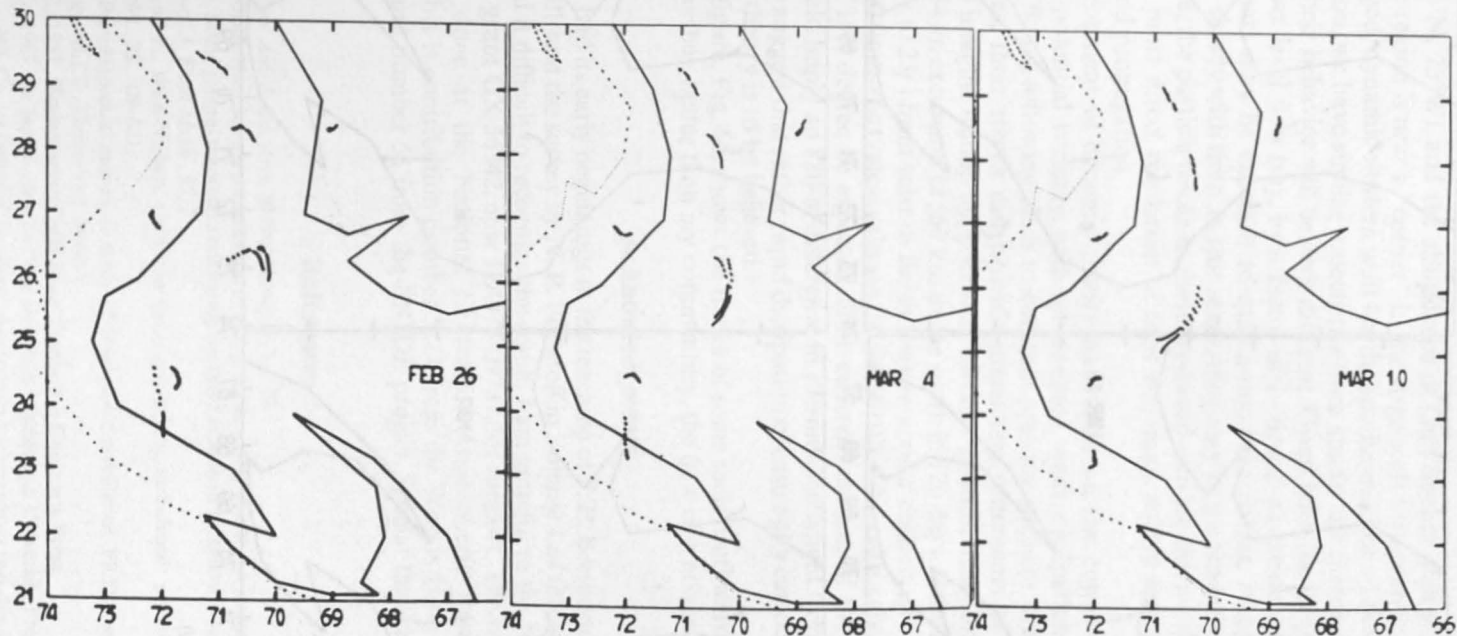


Fig. 66. Sequence of 1500-m float tracks above the Hatteras abyssal plain (5400-m isobath, solid; 5000-m, dashed; 4500-m, tip of Blake Outer Ridge at northwest corner).

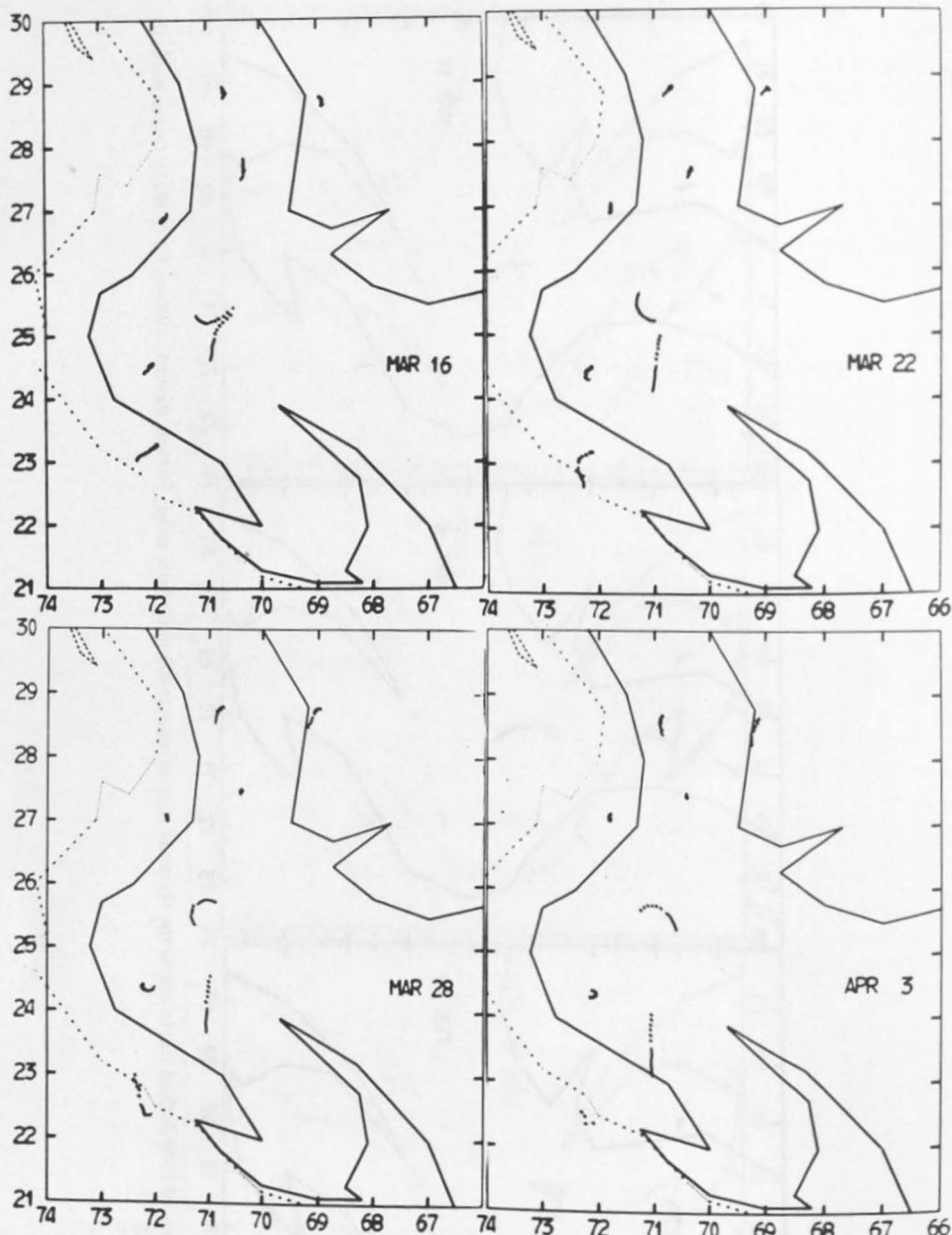


Fig. 66. (Continued)

tracks at 30°N, 73°W), and the abundance of Gulf Stream energy to the north. In addition the region is near a "corner" in the large-scale topography, which probably forms a jagged, dynamic western wall for the subthermocline eddies.

When, soon, we have similar trajectories from amidst the thermocline eddies (say, at 500 m), their behavior will be very different. Given both the longer Eulerian time scale of upper-level flow (say, by a factor of 2–3), and its greater speed (a factor of 2–5), the floats may be expected to race around the eddies, mapping them while they change slowly with time. In this sense, they may be particularly "cost effective." Furthermore, the particle tracks in these westward-moving thermocline patterns will provide the most direct resolution of their dynamics, subtly apportioned between advection and propagation.

The development of dynamic theory has rested on the conservation of quasi-geostrophic potential vorticity, with an assumed, weak dissipation. If these quasi-Lagrangian floats, following close to constant pressure surfaces, are sufficiently like fluid particles, their tracks can provide immediate statements of dynamics; it is attractive to imagine testing the potential vorticity relation using float clusters. One sees in Fig. 64 an excursion of 550 km to the south in 120 days. If the change in planetary vorticity ( $0.23f$ ) from start to finish were to appear entirely as relative vorticity, it would be 10 times the typical value in the field ( $0.02f$ )! Nor can a change in isopycnal thickness of this degree be expected. (For coherent motion of the subthermocline water, it would imply an 880-m difference in thermocline height from start to finish.) One is left to suggest that rather rapid dissipation of enstrophy can occur, if the quasi-geostrophic theory is to be believed.

The final figure, Fig. 66, shows the tracks of some such southward journeys of the floats. It describes, better than my commentary, the flow of a nonlinear ocean.

### Acknowledgments

This work had its early beginnings in the teaching of F. P. Bretherton, the papers of M. J. Lighthill, and the survey by N. P. Fofonoff in Volume 1 of this series. They may, however, find it difficult to recognize the result. I am grateful to the National Science Foundation, grant GX-36342, now IDO73-09737, for support. The computer experiments were done at the National Center for Atmospheric Research, Boulder, Colorado. This is contribution number 3371 from the Woods Hole Oceanographic Institution, and number 51 from the MODE project. Special thanks to MLLR and BPG.

### References

- Bache, A. D., 1846. *Am. J. Sci. Arts*, **30** (90) (1860), 313–329.
- Baer, F., 1972. An alternate scale representation of atmospheric energy spectra. *J. Atmos. Sci.*, **29**, 649–669.
- Ball, F. C., 1963. Some general theorems concerning the finite motion of a shallow rotating liquid lying on a paraboloid. *J. Fluid Mech.*, **17**, 2.
- Barros, V. R. and A. Wiin-Nielsen, 1974. On quasi-geostrophic turbulence: a numerical experiment. *J. Atmos. Sci.*, **31**, 609–621.
- Bass, A., 1974. Pseudospectral numerical study of geostrophic turbulence. Ph.D. thesis, Department of Meteorology, M.I.T., Cambridge, Mass.
- Batchelor, G. K., 1953. *Homogeneous Turbulence*. Cambridge University Press.
- Batchelor, G. K., 1967. *An Introduction to Fluid Dynamics*. Cambridge University Press.
- Batchelor, G. K., 1969. Computation of the energy spectrum in homogeneous two-dimensional turbulence. *Phys. Fluids*, **12**, II, 233–238.
- Bell, T. H., 1975. Topographically generated internal waves in the open ocean. *J. Geophys. Res.*, **80**, 320–327.

- Bernstein, R. L. and W. B. White, 1975. Time and length scales of baroclinic eddies in the central North Pacific Ocean. *J. Phys. Oceanogr.*, **4**, 613-624.
- Boland, F. M. and B. V. Hamon, 1970. The East Australian Current, 1965-1968. *Deep-Sea Res.*, **17**, 777-794.
- Brekhovskikh, L., K. Federov, L. Fomin, M. Koshlyakov, and A. Yampolsky, 1971. Large-scale multi-buoy experiment in the tropical Atlantic. *Deep-Sea Res.*, **18**, 1189-1206.
- Bretherton, F. P., 1969. On the mean motion induced by internal gravity waves. *J. Fluid Mech.*, **36**, 785-803.
- Bretherton, F. P., and M. Karweit, 1975. Mid-ocean mesoscale modelling. *Proc. Durham Conf. Numer. Methods Oceanogr.* In press.
- Brown, W., W. Munk, F. Snodgrass, H. Mofjeld, and B. Zetler, 1975. MODE bottom experiment. *J. Phys. Oceanogr.*, **5**, 75-85.
- Bruce, J. G., 1973. Large-scale variation of the Somali Current during the southwest monsoon, 1970. *Deep-Sea Res.*, **20**, 837-846.
- Bryden, H., 1975. Horizontal advection of temperature for low-frequency motions, *Deep-Sea Res.*, submitted.
- Charney, J. G., 1971. Geostrophic turbulence. *J. Atmos. Sci.*, **28**, 1087-1095.
- Crease, J., 1962. Velocity measurements in the deep water of the western North Atlantic. *J. Geophys. Res.*, **67**, 3173-3176.
- Deacon, M., 1972. *Scientists and the Sea, 1650-1900, A study of Marine Science*. Academic Press, New York.
- Dickenson, R. E., 1969. Theory of planetary-wave zonal flow interaction. *J. Atmos. Sci.* **26**, 73-81.
- Dickenson, R. E., 1970. Development of a Rossby-wave critical level. *J. Atmos. Sci.*, **27**, 627-633.
- Elliassen, A., and E. Palm, 1960. On the transfer of energy in stationary mountain waves. *Geof. Publ.*, **22** (3), 1-23.
- Fofonoff, N. P., 1954. Steady flow in a frictionless homogeneous ocean. *J. Mar. Res.*, **13**, 517-537.
- Foster, L., 1972. Current measurements in the Drake Passage. Ph.D. thesis, Dalhousie University.
- Freeland, H., P. Rhines, and T. Rossby, 1975. Statistical observations of the trajectories of neutrally buoyant floats in the North Atlantic. *J. Mar. Res.*, **34**, 69-92.
- Fuglister, F. C., 1960. *Atlantic Ocean Atlas of temperature and salinity profiles and data from the International Geophysical Year of 1957-58*. Woods Hole Oceanographic Institution Atlas Series. Vol. I. Woods Hole, Mass., 209 pp.
- Fuglister, F., and L. V. Worthington, 1951. Some results of a multiple ship survey of the Gulf Stream. *Tellus*, **3** (1), 1-14.
- Fultz, D., and P. Frenzen, 1955. A note on certain interesting ageostrophic motions in a rotating hemispherical shell. *J. Meteorol.*, **12**, 332-338.
- Gill, A. E., J. S. A. Green, and A. J. Simmons, 1974. Energy partition in the large-scale ocean circulation and the production of mid-ocean eddies. *Deep-Sea Res.*, **21**, 499-528.
- Gould, W. J., 1971. Spectral characteristics of some deep current records from the eastern North Atlantic. *Phil. Trans. Roy. Soc., London A*, **270**, 437-450.
- Green, J. S. A., 1970. Transfer properties of the large-scale eddies and the general circulation of the atmosphere. *Quart. J. Roy. Meteorol. Soc.*, **96**, 157-185.
- Greenspan, H. P., 1968. *The Theory of Rotating Fluids*. Cambridge Univ. Press.
- Hamon, B. V., 1968. Spectrum of sea level at Lord Howe Island in relation to circulation. *J. Geophys. Res.*, **73**, 6925-6927.
- Hasselmann, K., 1967. A criterion for nonlinear wave stability. *J. Fluid Mech.*, **30**, 737-739.
- Hogg, N. G., 1973. On the stratified Taylor column. *J. Fluid Mech.*, **58**, 517-537.
- Holland, W. R. and L. B. Lin, 1975. On the generation of mesoscale eddies and their contribution to the oceanic general circulation, I and II. *J. Phys. Oceanogr.*, **5**, 642-669.
- Hough, S. S., 1898. On the application of harmonic analysis to the dynamical theory of the tides, II. On the general integration of Laplace's dynamical equations. *Phil. Trans. Roy. Soc., A*, **191**, 139.
- Howard, L. N. and P. G. Drazin, 1964. On instability of a parallel flow of inviscid fluid in a rotating system with variable Coriolis parameter. *J. Math. Phys.*, **18**, 83-99.
- Howard, L. N. and W. Siegmann, 1969. On the initial-value problem for rotating stratified flow. *Stud. Appl. Math.*, **48**, 153-169.
- Huppert, H. E. and K. Bryan, 1975. Topographically generated eddies, preprint.
- Jeffreys, H., 1926. On the dynamics of geostrophic winds. *Quart. J. Roy. Meteorol. Soc.*, **52**, 85-104.
- Kenyon, L., 1964. *Nonlinear Rossby Waves*. Summer G.F.D. Program, Woods Hole Oceanographic Institution.

- Kim, K., 1975. Instability and energetics in a baroclinic ocean. Ph.D. thesis, W.H.O.I./M.I.T. Joint Program in Oceanography.
- Koshlyakov, M. N. and Y. M. Grachev, 1973. Mesoscale currents at a hydrophysical polygon in the tropical Atlantic. *Deep-Sea Res.*, **20**, 507–526.
- Kung, E. C., 1967. Diurnal and long-term variations of the kinetic energy generation and dissipation for a five-year period. *Mon. Weather Rev.*, **95**, 593–606.
- Kraichnan, R. H., 1967. Inertial ranges in two-dimensional turbulence. *Phys. Fluids*, **10**, 1417–1428.
- Lighthill, M. J., 1967. On waves generated in dispersion systems by travelling forcing effects with application to the dynamics of rotating fluids. *J. Fluid Mech.*, **27**, 4.
- Lighthill, M. J., 1969. Dynamic response of the Indian Ocean to west of the southwest monsoon. *Phil. Trans. Roy. Soc. A*, **265**, 45–92.
- Longuet-Higgins, M. S., 1964. Planetary waves on a rotating sphere. *Proc. Roy. Soc., A*, **279**, 446–473.
- Longuet-Higgins, M. S., 1975. The response of a stratified ocean to stationary or moving wind systems. *Deep-Sea Res.*, **12**, 923–973.
- Longuet-Higgins, M. S. and A. E. Gill, 1966. Resonant interactions between planetary waves. *Proc. Roy. Soc., A*, **299**, 1–145.
- Mazeika, P. A., 1973. Circulation and water masses east of the Lesser Antilles. *Dtsch. Hydrogr. Z.*, **26**, 51–73.
- McCartney, M. S., 1975. Inertial Taylor columns on a beta-plane. *J. Fluid Mech.*, **68**, 71–95.
- McWilliams, J., 1974. Forced transient flow and small-scale topography. *Geophys. Fluid Dyn.*, **6**, 49–79.
- McWilliams, J. and G. Flierl, 1975. Optimal quasi-geostrophic wave analysis of MODE array data, preprint.
- MEDOC Group, 1970. Observation of formation of deep water in the Mediterranean Sea, 1969. *Nature*, **227**, 1037–1040.
- Meincke, J., 1971. Observation of an anticyclonic vortex trapped above a seamount. *J. Geophys. Res.*, **76**, 7432–7436.
- Miles, J., 1974. On Laplace's tidal equation. *J. Fluid Mech.*, **66**, 241–260.
- Monin, A., V. M. Kamenkovich, and V. G. Kort, 1974. *The Variability of the Ocean*, Gidrometeosdat Leningrad (in Russian).
- Monin, A., and A. M. Yaglom, 1972. *Statistical Hydromechanics*. M.I.T. Press.
- Morse, P., and H. Feshbach, 1953. *Methods of Theoretical Physics*. McGraw-Hill, New York.
- Müller, P., 1974. On the interaction between short internal waves and larger scale motion in the ocean. *Hamb. Geophys. Einzelschr.*, **23**.
- Needler, G. and P. H. LeBlond, 1973. On the influence of the horizontal component of the earth's rotation on long-period wave. *Geophys. Fluid Dyn.*, **5**, 23–46.
- Orlanski, I. and C. Cox, 1973. Baroclinic instability in ocean currents. *Geophys. Fluid Dyn.*, **4**, 297–332.
- Parker, C. E., 1971. Gulf Stream rings in the Sargasso Sea. *Deep-Sea Res.*, **18**, 981–993.
- Pedlosky, J., 1965. A note on the western intensification of the oceanic circulation. *J. Mar. Res.*, **23**, 207–209.
- Pedlosky, J., 1965. A study of time-dependent ocean circulation. *J. Atmos. Sci.*, **22**, 267–272.
- Phillips, N. A., 1963. Geostrophic motion. *Rev. Geophys.*, **1**, 123–171.
- Phillips, N. A., 1966. Large-scale eddy motion in the western Atlantic. *J. Geophys. Res.*, **71**, 3883–3891.
- Phillips, N. A. and A. Ibbetson, 1967. Some laboratory experiments on Rossby waves with application to the ocean. *Tellus*, **19**, 81–88.
- Pillsbury, J. E., 1890. The Gulf Stream—a description of the methods employed in the investigation and the results of the records, App. 10. Rep. Supt. U.S. Coast Geod. Surv. 1890, pp. 461–620.
- Platzmann, G., 1974. Normal mode of the Atlantic and Indian Oceans. *Univ. Chicago Dept. Geophys. Sci. Tech. Rept.* 25.
- Prandtl, L., 1952. *Essentials of Fluid Dynamics*. Hatner, New York.
- Rao, P. K., A. Strong, and R. Koffler, 1971. Gulf Stream meanders and eddies as seen in satellite infrared imagery. *J. Phys. Oceanogr.*, **1**, 237–239.
- Rhines, P. B., 1969. Slow oscillations in an ocean of varying depth, parts I, II. *J. Fluid Mech.*, **37**, 161–205.
- Rhines, P. B., 1970. Edge-, bottom- and Rossby waves in a rotating, stratified fluid. *Geophys. Fluid Dyn.*, **1**, 273–302.
- Rhines, P. B., 1971a. A comment on the Aries observations. *Phil. Trans. Roy. Soc., A*, **270**, 461–463.
- Rhines, P. B., 1971b. A note on long-period motions at Site D. *Deep-Sea Res.*, **18**, 21–26.
- Rhines, P. B., 1973. Observations of the energy-containing oceanic eddies, and theoretical models of waves and turbulence. *Boundary Layer Meteorol.*, **4**, 345–360.
- Rhines, P. B., 1975. Waves and turbulence on a  $\beta$ -plane. *J. Fluid Mech.*, **69**, 417–443.

- Rhines, P. B. and F. P. Bretherton, 1974. Topographic Rossby-waves in a rough-bottomed ocean. *J. Fluid Res.*, **61**, 583–607.
- Rossby, C. G., 1947. On the distribution of angular velocity in gaseous envelopes under the influence of large-scale mixing processes. *Bull. A.M.S.*, **28**, 53–68.
- Rossby, T., A. Voorhis, and D. Webb, 1975. A quasi-Lagrangian study of mid-ocean variability using long-range SOFAR floats. *J. Mar. Res.*, **33**, 355–382.
- Saunders, P. M., 1971. Anticyclonic eddies formed from shoreward-meanders of the Gulf Stream. *Deep-Sea Res.*, **18**, 1207–1219.
- Schlee, S., 1973. *The Edge of an Unfamiliar World, a History of Oceanography*. E. P. Dutton, New York.
- Schmitz, W. J., Jr., J. R. Luyten, and W. Sturges, 1975. On the spatial variation of low-frequency fluctuations in the western North Atlantic: I. Along 70° west longitude. Submitted to *J. Mar. Res.*
- Schroeder, E. and H. M. Stommel, 1969. How representative is the series of Panulirus stations of monthly mean conditions off Bermuda? *Progr. Oceanogr.*, **5**, 31–40.
- Smagorinsky, J., 1963. General circulation experiments with the primitive equations, I, the basic experiment. *Mon. Weather Rev.*, **91**, 99–167.
- Smith, R., 1971. Ray theory for topographic Rossby waves. *Deep-Sea Res.*, **18**, 477–483.
- Starr, V. P., 1953. Note concerning the nature of the large-scale eddies in the atmosphere. *Tellus*, **5**, 494–498.
- Starr, V. P., 1968. *Negative Viscosity Phenomena*. McGraw-Hill, New York.
- Steinberg, L., 1973. Numerical simulation of quasi-geostrophic turbulence. *Tellus*, **25**, 233–246.
- Stommel, H. M., 1957. A survey of ocean current theory. *Deep-Sea Res.*, **4**, 149–184.
- Suarez, A. A., 1971. The propagation and generation of topographic oscillations in the ocean. Ph.D. thesis, Department of Meteorology, M.I.T.
- Swallow, J. C. and B. V. Hamon, 1960. Some measurements of deep currents in the eastern North Atlantic. *Deep-Sea Res.*, **6**, 155–168.
- Swallow, J. C. and J. G. Bruce, 1966. Current measurements off the Somali coast during the southwest monsoon of 1964. *Deep-Sea Res.*, **13**, 861–888.
- Taylor, G. I., 1915. Eddy motion in the atmosphere. *Phil. Trans. Roy. Soc., A*, **240**, 1–26.
- Taylor, G. I., 1921. Diffusion by continuous movements. *Proc. London Math. Soc.*, **2** (XX), 196–212.
- Thompson, R., 1971a. Topographic Rossby waves at a site north of the Gulf Stream. *Deep-Sea Res.*, **18** (1), 1–19.
- Thompson, R., 1971b. Why there is an intense eastward current in the North Atlantic, but not the South Atlantic. *J. Phys. Oceanogr.*, **1**, 235–237.
- Thompson, R. and J. R. Luyten, 1976. Evidence for bottom-trapped topographic Rossby waves from single moorings. *Deep-Sea Res.*, in press.
- Thomson, C. W., 1868. *The Depths of the Sea*. 2d ed. McMillan and Co., London.
- Thompson, R. E., 1975. Propagation of planetary waves over random bottom topography. *J. Fluid Mech.*, **70**, 267–286.
- Veronis, G., 1970. Effect of fluctuating winds on ocean circulation. *Deep-Sea Res.*, **17**, 421–434.
- Veronis, G., and H. M. Stommel, 1956. The action of variable wind stresses on a stratified ocean. *J. Mar. Res.*, **15**, 43–45.
- Webster, F., 1965. Measurements of eddy fluxes of momentum in the surface layer of the Gulf Stream. *Tellus*, **17**, 239–245.
- Welander, P., 1970. Lateral friction in the ocean as an effect of potential vorticity mixing. *Geophys. Fluid Dyn.*, **5**, 101–120.
- Whitehead, J. A., Jr., 1975. Mean-flow driven by circulation in a  $\beta$ -plane. *Tellus*, **27**, 358–364.
- Wiin-Nielsen, A., 1962. On transformation of kinetic energy between the vertical shear flow and the vertical mean flow in the atmosphere. *Mon. Weather Rev.*, **90**, 311–323.
- Wunsch, C., 1975 private communication.
- Yoshida, K., 1970. Subtropical countercurrents: band structures revealed from CSK data. In *The Kuroshio—A Symposium on the Japan Current*. J. C. Moor, ed. East-West Center Press, Honolulu, pp. 197–204.